Aix Marseille Université

Thèse de Doctorat

ED352 Physique et Sciences de la Matière

Centre Interdisciplinaire de Nanoscience de Marseille (CINaM)/AMU-CNRS, UMR 7325

Thèse présentée pour obtenir le grade universitaire de docteur

Discipline : Biophysique

Ranime Alameddine

Nanostructuration bio-chimique de substrats mous pour l'étude de l'adhésion et de la mécanique cellulaire.

Nano-patterning soft substrates with bio-chemically contrasted nano-dots to study cell adhesion and mechanics.

Soutenue le 09/12/2016 devant le jury :

Composition du Jury:

Manuel	Thery	CEA	Rapporteur
Christophe	Vieu	Université de Toulouse	Rapporteur
Helene	Delanoe Ayari	ILM	Membre de jury
Olivier	Margeat	CINaM	Membre de jury
Rudolf	Merkel	IHRS BioSoft	Membre de jury
Anne	Charrier	CINaM	Directrice de thèse
Kheya	Sengupta	CINaM	Directrice de thèse

Résumé

Durant les dernières décennies, de plus en plus de types de cellules se sont révélées capables de sonder leur environnement mécanique par l'application de forces par l'intermédiaire de protéines d'adhésion sur leur surface. Ce phénomène appelé "Mecanosensing" est lié à l'adhésion et la mécanique cellulaire, et est souvent étudié grâce à l'interaction des cellules avec des substrats artificiels. Mecanosensing devient un domaine de recherche en pleine émergence, grâce au développement de techniques expérimentales permettant de changer l'élasticité de la matrice et de mesurer précisément les interactions cellules-substrats. Dans des études distinctes, les technologies de bio-nanostructuration ont fourni des outils pour mimer l'état physiologique et pathologique des cellules ainsi que pour les manipuler. Des surfaces chimiquement structurées avec une répartition des ligands spécifiques ont montré une forte influence sur l'adhésion et la mécanique cellulaire. Cependant, la relation entre les deux phénomènes n'a pas été beaucoup explorée, en partie parce que la fonctionnalisation de substrats mous s'est révélée être un défi technique.

Pour résoudre ce problème, nous avons développé une technique simple et rentable nommée "reverse contact printing", afin de fabriquer des plots de protéines sub-microniques sur un élastomère d'élasticité contrôlée, le polydiméthylsiloxane (PDMS). Pour cela, des substrats de verre sont d'abord chimiquement fonctionnalisés par des molécules arrangées de façon contrôlée sur la surface (protéines), en utilisant la technique de «colloidal bead self-assembly». Le motif est ensuite transféré sur la surface d'une couche de PDMS uniforme supportée sur une lame de verre en amenant les deux surfaces en contact. Après séparation, le motif de protéines est transféré à la surface du PDMS. La technique a été validée pour différents types de protéines (Bovine serum albumine (BSA), biotine-BSA et neutravidine), ainsi que pour différents types de PDMS (Sylgard 184, Q gel 920 et CY52-276) d'élasticité allant de 3 kPa à 7 MPa. Mon travail de thèse a focalisé sur la standardisation et la compréhension du procédé de transfert. Nous avons montré que le greffage d'une espèce moléculaire, telle qu'un fluorophore, sur la protéine à transférer, ainsi que la nature chimique de la surface du PDMS peuvent influencer fortement le succès du transfert. Le degré d'hydrophobicité, ainsi que la présence de groupes ioniques à la fois sur l'élastomère et la protéine sont des facteurs moléculaires importants qui régissent le transfert. A l'aide de mesures de forces réalisées par AFM nous avons mesuré l'élasticité du PDMS, ainsi que les forces de cohésion et d'adhésion effectives impliquées dans le processus. Nous avons identifié que la réussite du reverse contact printing technique est facilitée par le greffage de groupes chimiques

appropriés sur la protéine, et dépend du traitement de la surface du PDMS ainsi que de son élasticité. Nous avons également étudié l'adhésion cellulaire avec des lymphocytes-T sur des surfaces de PDMS d'élasticité variable. Nous avons montré que contrairement à la plupart des autres types de cellules, les cellules-T s'étalent davantage sur substrat mou (5 et 140 kPa) que sur dur (2 MPa), sur la gamme de dureté étudiée. Finalement nous avons réalisé des expériences pilotes d'adhésion cellulaire sur PDMS structuré, que nous comparons à d'autres réalisées sur du verre structuré et sur surfaces de PDMS fonctionnalisées de manière homogène.

Abstract

In the past decade, more and more types of cells have been shown to be capable of probing the mechanics of their environment by application of forces through adhesion proteins on their surface. This phenomenon called "Mechanosensing", is related to cell adhesion and mechanics, and is often studied through interaction of cells with well-defined artificial substrates. Mechanosensing is becoming a growing domain of research, thanks to the development of novel techniques where the substrate elasticity can be changed, and the cell-substrate forces can be exactly measured. In separate studies, bio-nanopatterning technology have delivered tools to closely mimic the physiological and pathological state of cell as well as to manipulate it. Chemically patterned surfaces with spatial ligand distribution strongly influences cell adhesion and mechanics. However, the cross-talk between the two phenomena has not been much explored, partly because patterned functionalization of soft substrates is a current engineering challenge.

To address this issue, we developed a simple and cost effective technique named "reverse contact printing" for fabrication of nanometric protein patches on PDMS (polydimethylsiloxane) elastomer of controlled elasticity. Glass substrates are first chemically patterned with large coverage of nano-scale protein dots via colloidal bead self-assembly. The pattern is then transferred to the surface of a flat PDMS layer supported on a glass cover-slide by bringing the surfaces in to conformal contact. After separation, the protein pattern is transferred to the PDMS surface. The technique was validated for different types of proteins (Bovine serum albumin (BSA), biotin-BSA and neutravidin), and for different types of PDMS (Sylgard 184, CY52-276 and Q gel 920), of elasticity ranging from 3kPa to 7MPa. My PhD work mainly consisted of deciphering the molecular mechanism that underlie this technique. We have shown that the rate of transfer crucially depends on the molecular groups on the protein, and on the nature of the PDMS surface. The degree of hydrophobicity as well as presence of ionic groups on both the elastomer and the protein are important molecular factors that govern the transfer. We used atomic force microscopy (AFM) force measurements to measure PDMS elasticity, as well as protein-substrate interactions to understand the molecular mechanism governing the transfer process. We have identified that a successful reverse transfer is facilitated by the grafting of appropriate chemical groups on the protein, and depends on the PDMS surface treatment and elasticity. In addition, we studied adhesion and mechanics of T- lymphocytes on PDMS of varying elasticity. We found that surprisingly, T-lymphocytes spread more on softer (5 and 140 kPa) than on harder (2 MPa) PDMS. In on-going pilot experiments, cells on patterned soft PDMS are compared to those on

patterned glass or homogeneous PDMS surfaces.

Remerciements

Je remercie avant tout la France pour la grande opportunité qu'elle m'a offerte de poursuivre mes études et réaliser ma vie; ce pays qui offre la culture, des possibilités d'études et de travail, plus que n'importe quel autre pays au monde.

Je tiens à remercier tous ceux qui m'ont aidé dans la réalisation de ma thèse. Il me serait impossible de terminer cette phase de ma vie sans le soutien et l'amitié de tous les gens que j'ai rencontré le long du chemin.

Je tiens à remercier Claude Henry et Frédéric Fages, de m'avoir accepté au sein de leur laboratoire, et qui m'ont fourni une atmosphère amicale, coopérative et riche en savoir scientifique. Je remercie également les directeurs de l'école doctorale, Mossadek Talby et Conrad Becker.

Je tiens à remercier les membres du jury, Dr. Helene Ayari Delanoe, Dr. Olivier Margeat, Pr. Rudolf Merkel, Dr. Manuel Thery et Pr. Chritophe Vieu pour leur intérêt dans mon travail.

Des remerciements pour tous les collaborateurs qui ont contribué à la réalisation de mon travail de thèse: Pierre Henri Puech et Laurent Limozin pour les mesures d'élasticité cellulaire, Nathalie Ferté pour les mesures d'angle de contact, Igor Ozerov, Frédéric Bedu ainsi que Romain Jeanette pour l'aide technique en salle blanche.

Je serais négligente si je ne remerciait pas Delphine Simon, Valérie Juvénal et Michele Francia pour leur assistance si nécessaire aux tâches administratives. De même Bruno Gély qui a fourni un soutien immédiat pour tous les problèmes informatiques que nous avons rencontré.

Des remerciements tous particuliers à Fuwei Pi, pour ses conseils, pour toutes les discussions scientifiques que nous avons échangé ensemble et pour son amitié. J'ai gagné beaucoup de ses connaissances et sa curiosité scientifique.

Un grand merci à Astrid Wahl pour son aide précieuse pour les expériences avec les cellules, pour les nombreuses discussions, pour partager généreusement et avec patience ses connaissances ainsi que pour sa belle amitié.

Je voudrais également remercier Kaoutar Bouzalmate, que j'ai eu l'occasion de diriger et qui sans relâche et avec beaucoup d'enthousiasme a abordé un projet difficile au cours de plusieurs mois.

Mes meilleurs remerciements à mes amis et collègues Emmanuelle, Scott, Ahmad, Pierre, Aya, Priya, Arif, Cecile, Jack, et Kamel pour la recherche que nous avons fait ensemble, pour des temps extraordinaires. C'était un grand plaisir de les rencontrer tous.

Merci Evelyne pour ton beau sourire, et pour la musique que nous avons partagé ensemble.

Je tiens a remercier tous les membres du laboratoire avec qui j'ai discuté et échangé des

Contents

List of Figures

List of Tables

List of Materials

- Glass cover slides : thickness = 170 microns, 24 x 24 mm, Assistant, Karl Hecht KG, Germany.
- Hellmanex III : Sigma Aldrich,France.
- Silica colloidal beads:
  - 2μm diameter,Polysctiences, Inc., Germany.
  - Microspheres-Nanospheres, Corpuscular, New-York.
- 1H,1H,2H,2H PerFluoroOctyl-TriChloroSilane (PFOTCS): Sigma Aldrich, France.
- 3-AminoPropy-TriEthoxySilane (APTES): Sigma Aldrich, France.
- CY 52-276 A and B: Dow Corning, Toray, Tokyo, Japan.
- Sylgard 184 A and B: Dow Corning, USA.
- Q Gel 920 A and B: Quantum Silicones, LLC Richmond VA.
- Pluronic F-68: Life technology, France.
- Pluronic F-108: Sigma Aldrich, France.
- Pluronic F-127: Sigma Aldrich, France.
- Bovine Serum Albumin (BSA): Sigma Aldrich, France.
- Albumin from Bovine Serum, fluorescein isothiocyanate conjugated (BSA-FITC): Life Technologies, France.
- Albumin from Bovine Serum, Texas Red conjugated (BSA-TR): Life Technologies, France.
- Albumin from Bovine Serum, biotin conjugate (bBSA): Sigma Aldrich, France.
- NeutrAvidin, biotin-binding Protein (Nav): ThermoFisher Scientific, France.
- Neutravidin, Texas Red conjugated (Nav-TR): Invitrogen , USA.
- NeutrAvidin, fluorescein isothiocyanate conjugated (Nav-FITC): Sigma Aldrich, France.
- Neutravidin, DyLight conjugate (Nav-Dylight): Life Technology, France.
- Mono-biotinylated anti-CD3 (Ortho-clone OKT3, Janssen-Cilag, USA) conjugated to ATTO 647 (Life Technology).
- Anti-CD3 multi-biotinylated mouse anti-human Clon: UCHT1 Beckman Coulter, France.
- Texas Red-X protein Labelling Kit: T-10244, Thermo fisher Scientific, France.
- Atto 488 protein labeling Kit: 38371, Sigma Aldrich, France.
- RPMI complete medium supplemented with 10% Fetal Bovine Serum and 1% GlutaMAX :Invitrogen.
- Phosphate buffer saline (PBS): Sigma Aldrich, France.
- Paraformaldehyde: Merck, France.

- Glutaraldhehyde: Sygma Aldrich, France.
- Phalloidin rhodamine labeled (dissolved in DMSO): Sigma-Aldrich, France.
- Phalloidin FITC labeled (dissolved in methanol): Life technologies, France.
- Triton X-100: Sigma, France.
- FITC fluorescently labeled mouse anti-human Anti-Vβ8 TCR:BD Bioscience, France.
- 6 μm spherical tips: SQUBE surface science support, Germany.
- 3-(2-Aminoethylamino)propyl]trimethoxysilane: Sigma Aldrich, France.

Chapter 1

Introduction

1.1 Cells

1.1.1 General concepts

In 1665, the term "cell" was given by Robert Hooke, in a biological context, to describe the microscopic structure of cork. Since then, technology has given us an increasingly complex view of the basic unit of life [1]. Cells are the building blocks of all living things. It is the basic structural, functional and biological unit of all known living organisms, and is capable of performing life functioning. It consists of a concentrated aqueous solution enclosed by a membrane and filled with biomolecules such as proteins and nucleic acids [1]. Cells size can vary between 1 micrometer and hundreds of micrometer in diameter. In spite of being small, a single cell is very complicated and is composed of biological structures, with sizes down to the nanometer scale (Figure 1.1). In fact, a cell is hierarchically complex, taking for example a DNA double helix, within the cell is approximately 10 nanometers (nm) wide, whereas the cellular organelle, called the nucleus, that encloses this DNA can be approximately 1000 times bigger (about 10 μm). Considering the complexity of a cell, we will describe some of its major components, essential for our study here, namely, the cell membrane, the cytoskeleton, and the extracellular matrix.
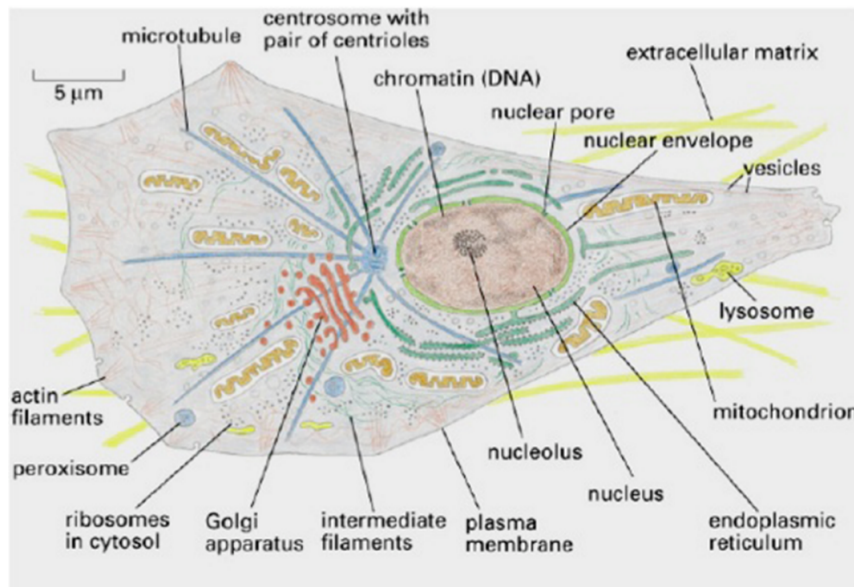
Figure 1.1 – **Schematic representation of the main structural element of a single animal cell.** Adapted from [2].

The cell membrane

The cell membrane or the plasma membrane, which is 3-9 nm thick [3][4][5], surrounds all living cells, and is, arguably, its most important organelle. It encloses and defines the cell. It acts as a boundary, holding the cell constituents together and regulating the passage of material into and out of the cell. All cell membranes have two major constituents, lipids and proteins. Ac-

cording to the "fluid-mosaic model" theory [6] (Figure 1.2), the plasma membrane is composed of a double layer of lipids which are fluid like organic oil, at body temperature, and where many diverse protein are embedded, while other simply adhere to its surface giving the membrane the look of a mosaic. While the lipids conserve the bilayer structure of the membrane, the proteins carry out the vast diversity of the membrane functions. In fact, proteins on the outside surface of the cell membrane can act as receptors by having specific binding sites where hormones or other chemicals can bind. The proteins that span the membrane are usually involved in transporting substances across the membrane, and the proteins on the inside surface of the cell membranes are often attached to the cytoskeleton, and are involved in maintaining the cell shape, or in cell motility. This binding then triggers other events in the cell. They may also be involved in cell recognition and signaling. The cell membrane is of a key importance in the cell adhesion process. The cell membrane carries the cell adhesion molecules (CAMs), that mediate binding interaction at the extracellular surface, and determine the specificity cell-cell and cell-extra cellular matrix (ECM) recognition. More detail will be elucidated in the cell adhesion section (section 1.1.2). Recent advances have shown that the membrane is more heterogeneous and dynamic than what was visualized in the fluid-mosaic model, but the basic structural notions remain.
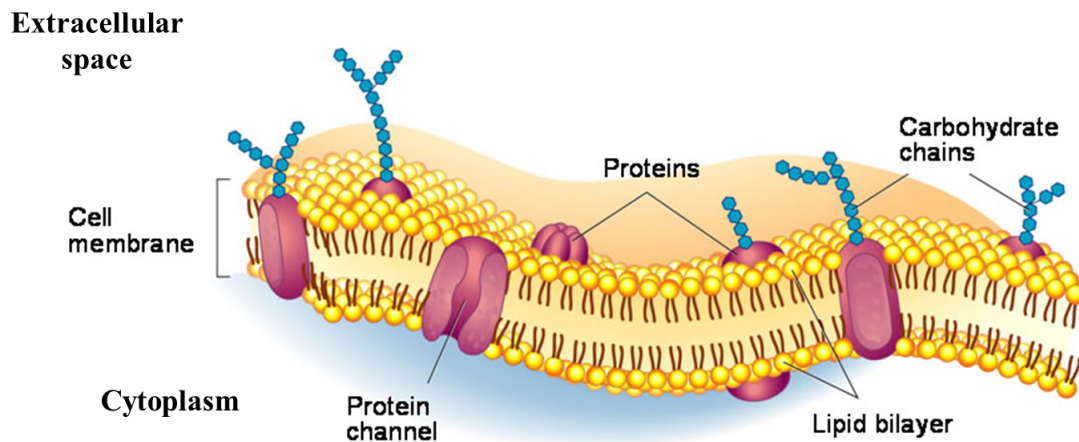
Figure 1.2 – **Fluid mosaic model of the plasma membrane.** Adapted from [7].

The cytoskeleton

The cytoskeleton is an interconnected network of filamentous polymers and regulatory proteins located in the cell cytoplasm, which influences the capacity of the cell to resist deformation, to change shape during movement and to transport intracellular cargo [8]. It organizes the contents of the cell; connects the cell physically and biochemically to the external environment; and generates coordinated forces that enable the cell to move and change shape. These constitute the key important functions of the cytoskeleton (see, for example [9] and references there in). The cytoskeleton is built on a framework of three types of protein filaments, that constitute the cytoskeletal polymers and control the shape and mechanics of cells. They are: the microtubules,

the actin filaments, and the intermediate filaments [1].

Here, we shall focus on actin filaments also known as microfilaments. They are two-stranded helical polymers of the protein actin. They are the thinnest filaments of the cytoskeleton. They appear as semi-flexible structures, much less rigid than microtubules, with a diameter of 5–9 nm. Depending on their association with different actin-binding proteins, they can be organized into a variety of linear bundles, two-dimensional networks, and three-dimensional gels. They can serve in a variety of functions in the cell such as cell-cell communications, filopodial protrusions, cell locomotion and changes in cell shape. Although actin filaments are dispersed throughout the cell, they are most highly concentrated in the cortex, just beneath the plasma membrane. This gives them the capacity of force generation when their growing end pushes against the cell membrane. Actin structure and dynamics closely associated with cell adhesion and mechanics, and is then important for this thesis.

The extracellular matrix

The extracellular matrix (ECM) constitutes an ensemble of extracellular molecules secreted by cells. It dispenses structural and biochemical support to the neighboring cells [10]. The extracellular matrix fills the spaces between cells and binds cells and tissues together. The composition of ECM varies between multicellular structures. However, the common functions of the ECM include cell adhesion, cell-to-cell communication and differentiation [11]. The major components of the ECM are water, proteins and polysaccharides. Each tissue has an ECM with a unique composition and topology that is generated during tissue development through a dynamic and reciprocal, biochemical and biophysical dialog between the various cellular components (e.g. epithelial, fibroblast, adipocyte, endothelial elements) and the evolving cellular and protein microenvironment. Indeed, the physical, topological, and biochemical composition of the ECM is not only tissue-specific, but is also markedly heterogeneous. In the context of adhesion, ECM receptors, such as integrins, mediate cell adhesion to the ECM [12][13]. Adhesion molecules couple the cytoskeleton to the ECM. Adhesion is also often linked to cell migration through the ECM [14][15].

1.1.2 Cell Adhesion

Tissues are viscoelastic and are made up of cells and ECM. The cells that make up tissues are adherent, attached to some combination of their neighboring cells and surrounding ECM. Many cell types require adhesion for survival [16][17][18]. Cell adhesion is the process by which cells interact and attach to a surface, substrate or another cell, mediated by interactions between molecules of the cell surface, the cell adhesion molecules (CAMs). Also known as adhesion receptors, CAMs, are proteins capable of binding to their counterpart in the extra cellular matrix or on a neighboring cell. Integrin binding to fibronectin is a prime example [19]. In connective tissue cells, through the binding, transient focal complexes are formed. If presented with proper ligands, focal complexes mature into focal adhesions [20] [21], which are micrometer size com-

plexes of proteins anchoring the cell cytoskeleton to the ECM via integrins, and are considered as important transducers of physical cues [22]. In fact, focal adhesions arise from integrin clusters that allow the assembly of the F-actin cytoskeleton and the generation of tension, resulting in cell spreading. The study of the transition from focal complex to focal adhesion, in an artificial system, requires spatial as well as chemical specificity. However, all cell types do not form focal adhesions to adhere. The example of T-cells will be discussed in section 1.2.3.

Cell adhesion plays an important role in cell growth, migration and differentiation. It is also involved in embryogenesis, maintenance of tissues integrity, immune response and cancer metastasis [23]. When a cell adheres and grows on a substrate, it senses, interprets, integrates, and responds to multiple chemical and physical features of the underlying adhesive substrate such as, the surface chemical composition, the wettability [24], the density and organization of the specific ECM protein [25], the topography [26], the roughness [27] and the stiffness [28].

In this section we will start by presenting general trends regarding the effect of roughness and surface wettability on cell spreading. Following that, we will present examples on the study of cell adhesion on micro and nano features and thus the influence of the substrate topography and the organization of the specific ECM proteins on cell adhesion.

1.1.2.1   Surface Wettability Effect on Cell Adhesion

Surface wettability (also referred to as hydrophobicity/hydrophilicity) is one of the most important factors affecting the cell response to implants (see for example [29], and references therein). Typically, when a surface is put in contact with a biological fluid or cell medium, before the cells have the time to arrive, the material surface is already coated with a monolayer of proteins. Hence, the cells do not "see" the material but see instead a dynamic layer of proteins. Since wettability affects protein adsorption [30] and since the presence of proteins allows cells to adhere to surfaces, wettability also affects cell adhesion [24][31]. However, observations regarding the effects of surface wettability on protein adhesion have not always been consistent.

In solution, proteins interact with water molecules, and tend to create a folded structure in order to lower the entropic penalty caused by the interaction between their hydrophobic side chains and water [32]. Generally, beside some exceptions [33], hydrophobic surfaces tend to adsorb more proteins, while hydrophilic surfaces tend to resist protein adsorption. This is because strong hydrophobic interaction is thermodynamically favorable for the proteins on hydrophobic surface, due to the large number of non polar and hydrophobic amino acids, generally occupying the interior of the protein folded structure, and also present in 40 to 50 % on the accessible area of the protein structure. This is in direct contrast to the large energy barrier created on the hydrophilic surface arising from strongly bound water molecules on the hydrophilic surface, thus leading to competition between water molecules and proteins, and resulting in decreased protein adsorption and conformational change. The process of adhesion of proteins to surfaces, induces conformational changes and reorientation of the proteins. Surface chemistry and wetta-

bility influence these conformational changes which can affect the protein activity and thus the cell adhesion (Figure 1.3).
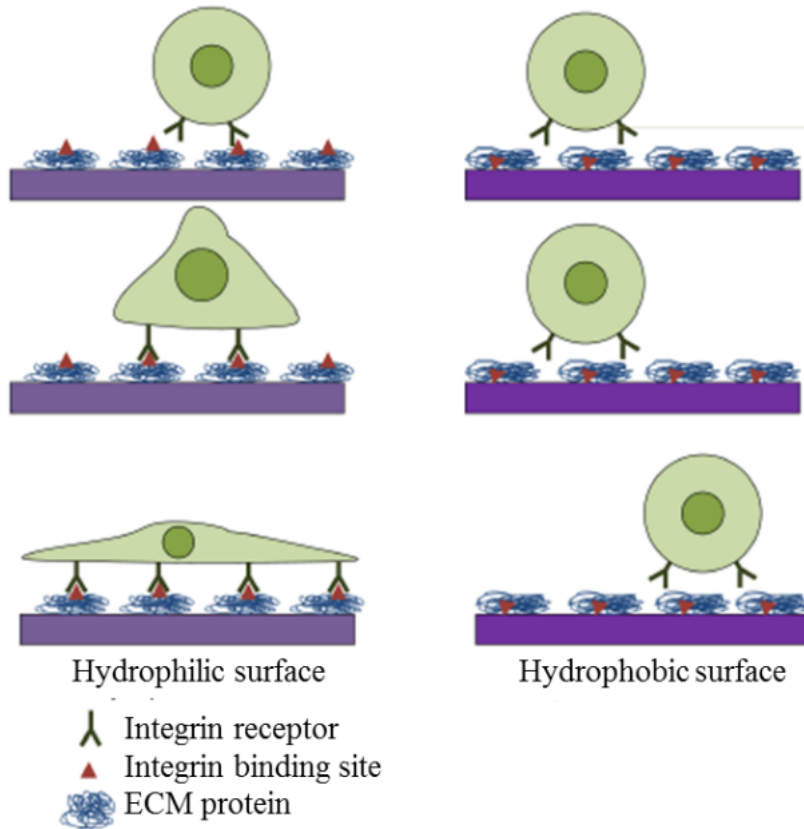
Figure 1.3 – **Changes in protein conformation and its affect on hydrophilic and hydrophobic surfaces.** Adapted from [34].

The wettability of a surface in part reflects its surface chemistry. Self assembled monolayers (SAMs) of alkanethiols on gold surfaces have been used as model surfaces to study cell adhesion behavior to artificial materials, since they can provide surfaces with different properties (wettability and chemistry) by using alkanethiols with different terminal groups (such as CH_3, OH, NH_2 and COOH). McClary et al. [35], showed that the COOH terminated SAM surface with contact angle of $17°$, yielded higher levels of fibronectin binding domain availability compared to the CH_3 terminated surface owing a contact angle of $108°$, and as a result, hydrophobic methyl terminated SAMs on gold, induced minimal cell attachment and could support spreading and formation of focal contacts by mouse fibroblasts. In contrast COOH terminated SAM surface has shown the formation of well defined focal contacts and stress fibers which reflects integrin attachment to ECM proteins. Similarly, Barrias et al. [36], also showed that fibronectin presents higher availability of binding domain on hydrophilic OH terminated SAM than on hydrophobic CH_3 terminated SAM, and when mixing OH and CH_3 terminated thiols, fibronectin adsorption decrease while increasing the percentage of OH terminated thiols, but the availability of the binding site increased also, leading to increased spreading and adhesion.

The effect of surface wettability on cell adhesion is not limited to SAMs and was also studied on polymer surfaces. Some studies have shown that the increasing of hydrophilic properties of polymers leads to increased cell spreading and adhesion [24], in contrast other studies report that the highest rate of cell adhesion and proliferation is observed on substrates with hydrophobic surfaces [37], or substrate with intermediate contact angle [38][39]. Polystyrene for example, has a hydrophobic surface, and showed an incapacity of many cell to spread and adhere. Decreasing its hydrophilicity by acid treatment or exposing to high energy ionizing radiation, leads to an increase in cell adhesion [40]. In contrast, polyethylene glycol, known for its high hydrophilicity, shows a low protein adsorption to its surface, and can not promote cell adhesion [41]. Mixing it with other more hydrophobic material was needed to decrease its hydrophilicity and thus, increase cell adhesion [42].

1.1.3 Surface Roughness Effect on Cell Adhesion

During cell-material interaction, the cells modify their behavior according to the surface characteristics of the material. In their natural environment, cells are exposed to many different types of surfaces, some of which are be rough, while others are smoother. Since the effect of surface topography on cell morphology is the consequence of the process of interaction between the extra-cellular matrix proteins adsorbed on the surface of the material, and related cell adhesion molecules, the surface roughness is an important factor in the study of cell adhesion. Often, it was demonstrated that an increase in surface roughness provides an increase in cell adhesion on both polymers [27][43] and metals [44]. Research has shown that surfaces with more topographical features and roughness will have more exposed area for protein to interact with [45]. Some other reports, suggested that an increase in surface roughness promotes higher availability of protein binding sites [46]. And some other associated the increase in roughness to the increase in hydrophobicity and thus, to the increase in cell adhesion. The response of cells to roughness depend on the cell type, cells are thought to respond better to surfaces which mimic their physiological environment. Rat osteoblast and human foetal osteoblastic cells, for example, showed increase spreading on rough surfaces in comparison with smooth one [47] [48]. Human osteoblastic cloned cells showed a decrease in proliferation rate in response to surface roughness [49]. It was also reported that rat cells generally follow surface orientation, while human osteoblasts do not follow any surface orientation [50]. Recently, studies on the influence of nano-structures were conducted [26][51], considering the fact that the natural environment of the cell, the ECM, is a nano-structured substrate [52][26]. It was shown that cells do respond to nano-topography [52].

1.1.4 Cells Adhesion on Chemically Patterned Substrates

The importance of adhesion geometry for the life and death of cells was first demonstrated in the early 1997, where Chen et al. used substrates that contained extracellular matrix-coated adhesive islands of decreasing size, to grow cells (Figure 1.4). They showed that cells shifted from growth to apoptosis on this substrates. They also demonstrated that cells vary their shape while

maintaining the total cell-ECM contact area constant, by decreasing the size and the spacing between the focal adhesion points (Figure 1.5) [53].
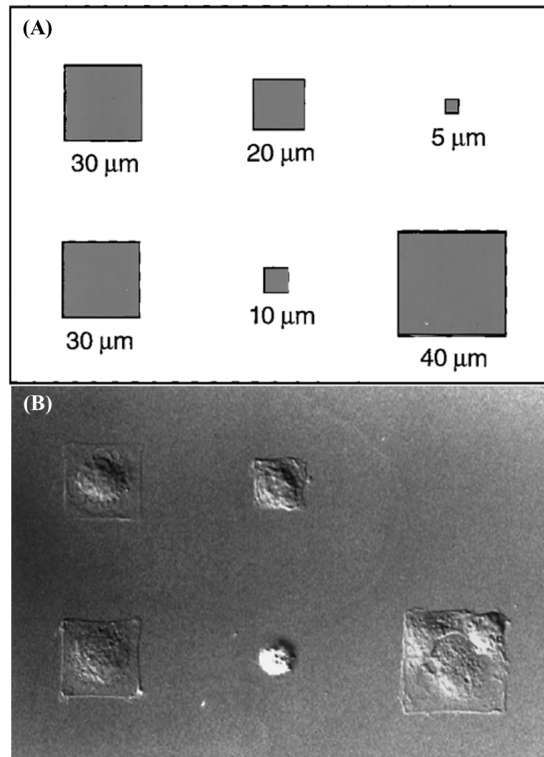
Figure 1.4 – **Effect of surface structuring on cells.** (A) Different sized square-shaped adhesive islands. (B) Final shapes of endothelial cells adhered to fibronectin coated islands. Cells were seen to adapt their shape and size to that of the adhesive islands. Adapted from [53].

Following this study, the location of focal adhesion (micrometer size complexes), began to be studied on surfaces patterned with microscopic islands of adhesion protein, to which the cells subsequently adhere [54]. Since then micro-patterning has been used extensively to investigate the sensitivity and response of a cell to specific micro-environmental cues [55] and has become a powerful tool to influence the behavior of cells [52].

Numerous studies have been done to investigate influence of micro-structure substrates on cellular processes. Thery et al. have used microcontact printing to finely control the spatial distribution of the ECM on the substrate. They demonstrated that HeLa cells, dividing on fibronectin coated micropatterns, orient their spindle relative to the pattern geometry [56]. In a following report, they studied the orientation of the mitotic spindle in HeLa cells on various fibronectin micropatterns. They demonstrated that by regulating torques that act on the spindle, the geometry of the adhesive pattern sets up the distribution of cortical cues that control spindle orientation [57]. Baily and colleague used micro-patterned substrates to study the regulation of protrusion shape during chemotactic responses of mammalian carcinoma cells. They plated rat mammary
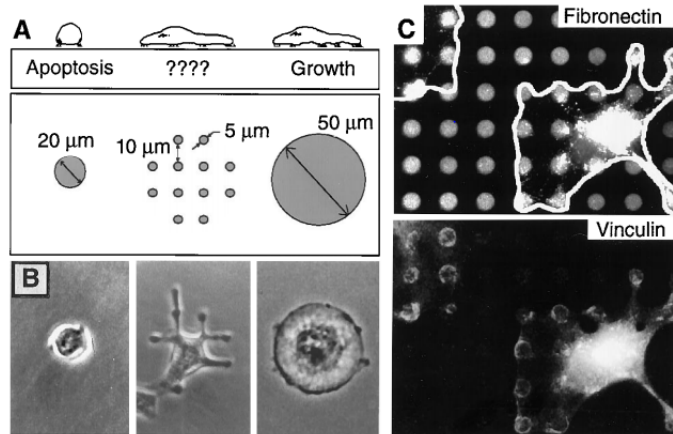
Figure 1.5 – **Cell-ECM contact area versus cell spreading as a regulator of cell fate.** (A) Substrates used to explore the shape variation of the cell independently of the cell-ECM contact area. (B) Phase contrast images of cell spreading on the patterns shown in (A). (C) Immunofluorescence staining of fibronectin or vinculin for cell spreading on micropatterned substrates. Adapted from [53].

carcinoma cells on gold coated glass cover-slips having 10 μm wide adhesive lanes. They saw that the cell attached only to the adhesive lanes, but lamellipod extension could occur independently of any contact with the substrate [58].

Spatz and co-workers, were the first to report one of the nano-structuring technique, so called block copolymer micelles nanolithography (BCML), which can lead to single integrin clustering in adhesion dependent cell [59][60]. Their method is based on the fabrication of hexagonal patterns of gold nanodots on a glass slide. The gold particles are separated by polyethylene glycol molecules (PEG) passivating the free glass and preventing nonspecific cell adhesion. The use of the hydrophilic PEG proves the importance of surface wettability on cell adhesion explained in section 1.1.2.1. Several studies using the BCMl have demonstrated a critical spacing of 50-70 nm, beyond which cells no longer recognize individual ligands as being clustered. Arnold et al. [51], for example, used this technique to design nano-patterned adhesive surfaces of gold nano-dots coated with RGD peptide, where the distance RGD-to-RGD could be precisely set. They demonstrated that a distance $\geq$ 70 nm between the dots leads to limited cell attachment and spreading and also reduces the formation of focal adhesion and actin stress fiber. In contrast a distance of $\leq$ 60 nm allows effective adhesion. In a related study, Elisabetta Ada Cavalcanti-Adam et al. wanted to see the extent to which cell spreading kinetics and adhesion stability depend on RGD ligand spacing [13]. They saw, that cells on substrate with 60 nm spacing RGD nano-pattern, reach a maximum spreading within 1-2 h after plating and are hardly migrating, comparably to cells on homogeneously coated RGD surfaces. In contrast, cells on 108 nm spaced nano-pattern, shows reduce spreading but enhanced motility. Other studies, such as the one done by Niepel et al. [61], used nano-sphere lithography to vary the size and distance of gold nano-structures on silicon to guide size and spacing of focal adhesion in fibroblast, in order to regulate their adhesion

and growth.

Micro-nano fabrication techniques have delivered tools to closely mimic the physiological and pathological states of the cell. These techniques offer easy ways to modulate the topography and density of the ECM proteins to control the local chemical environment for cell adhesion. Such techniques have become essential in the domain of cellular adhesion studies and will be discussed in section 1.3.

1.1.5 Cell Mechanics

Cellular signaling within living organisms is sustained by chemical and mechanical interactions mediated through a complex machinery involving the cytoskeleton, the cell membrane, and the macromolecules composing the extracellular matrix. All these elements associated with the forces generated by the cell and its surroundings play in concert to create dynamic materials with viscoelastic properties unique to each tissue. While historically, there has been significant attention on chemical regulators within the ECM, and their influence in cell fate was largely demonstrated, the role of mechanical environment was less well known.

In the recent years, it has become increasingly evident that the cellular response to environmental signals goes far beyond the ability of the cell to sense surface chemistry, and thus there has been focus on the cell environment mechanical properties, the spatial organization and the topographical data. Hence, it is now said that "*cells in vivo, are organized into tissues and organs that reside in complex mechanical environment*" [62]. At the cellular level, this mechanical environment consists of internal and external forces generated by, and applied to the cell. Further, the relative stiffness of the ECM is an important mechanical parameter for cell functions and behavior. All these factors were found to be essential in maintaining cell health and integrity [62][63] .

Mechanical forces are shown to play a major role in a wide range of biological and pathogenic processes [64][65], and mechanobiology is becoming an emerging field in biomedical research. A wide number of experiments were reported, on the capacity of the cells to sense the mechanical properties of their environment, called mechanosensing, by applying forces through adhesion proteins on their surface, and traducing the force into biochemical signals in response. It is now well recognized that cells respond actively to the stiffness of their underlying substrate. Hence, the study of cells on planar substrates are usually performed with non adhesive polyacrilamide (PAA) or polydimethylsiloxane (PDMS) coated with ECM proteins or ligands such as RGD.

Pelham and Wang in 1997, reported that the stiffness of PAA gels regulates focal adhesion formation and migration of cultured rat epithelial cells and 3T3 fibroblasts. They demonstrated a faster migration of cells on stiff substrates [66]. To sense the stiffness, cells generate and transmit forces to their substrate. It is in fact in the 1980's that the first experiments showing the ability of cells to sense the mechanical properties of their environment were conducted, and when

Harris et al. have had the idea to use a thin elastic substrate, which found to form wrinkles under cellular traction and thus provides visual informations about the capacity of the cells to sense stiffness [67] (Figure 1.6 a). However, due to the non linear response, quantitative information about the forces were difficult to obtain.
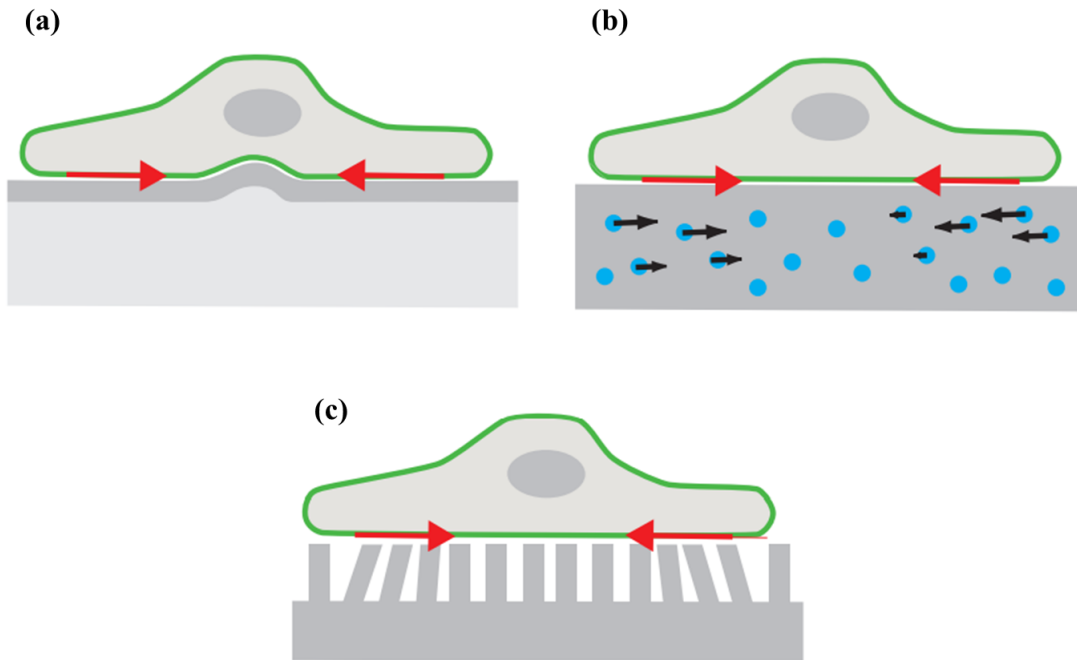
Figure 1.6 – **Schematic representation of different setups for traction force microscopy.**
(a) Thin films buckle under cell traction, therefore this setup is difficult to evaluate quantitatively.
(b) The standard setup are thick films with embedded marker beads. (c) Pillar arrays are local strain gauges and do not require any deconvolution; however, they also present topographical and biochemical patterns to cells. Adapted from [68].

Therefore, methods have been developed to quantify the traction forces generated by cells. This was first done by Dembo and colleagues, who developed the traction force microscopy. They used thin silicon films under tension and then thick polyacrylamide films, that show deformation under cell traction instead of wrinkling (Figure 1.6 b). Using specific methods, the deformation produced on the substrate by a migrating cell was converted into stress in the substrate, and the traction forces exerted by this migrating cell were detected [69][70]. These methods, ensure the fact that the cells have the capacity to apply forces on the substrate they interact with. Now, traction force microscopy is the most frequently used technique to quantify these forces. Other methods include the use of micro-patterned silicone elastomeric substrate [71] [72] [73], and the use of micro-fabricated post-arrays detectors [74][75][76] (Figure 1.6 c and 1.7).

All these techniques were based on strains, that the adherent cell created on the substrate, to calculate the traction forces. However, it is still not well understood if the cell senses their environment by applying a constant force (i.e stress) and extracting out the deformation (i.e. strain)
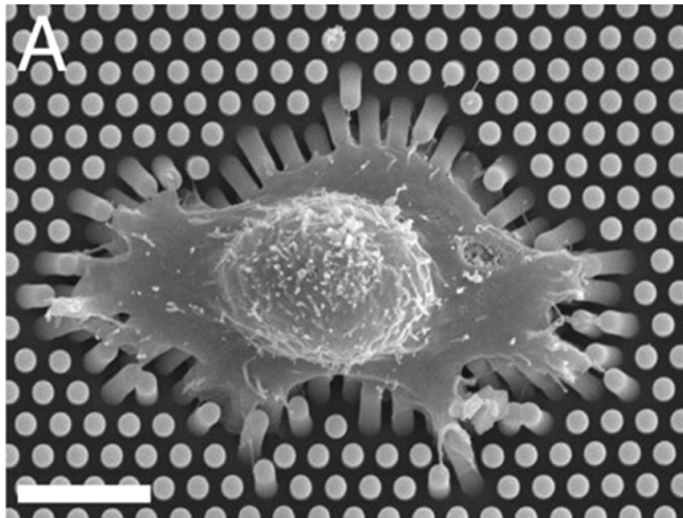
Figure 1.7 – **Scanning electron micrograph image of a rat embryonic fibroblast cell (REF 52) trying to hang and pull on a micropillar substrate.** Scale bare: 15 μm. Adapted from [77].

or vice versa. Theoretical models suggest that cells may maintain either an optimal stress or an optimal strain by readjusting their cytoskeleton organization and their contractile activity [78]. Recent traction force measurements on fibroblast cells on PAA gels with stiffness ranging from 6 to 110 kPa, suggested that cells switch from maintaining a constant strain on soft gels to maintaining a constant stress on stiffer substrates [79] [80]. However, whatever the experiment, care needs to be taken to choose the correct functionalization of the surface. In fact, the distance between anchoring points can influence cell fate [81], and if the ligands were not well attached to the substrate surface, cells risk pulling them out [79]. Furthermore, the thickness of the gel needs to be carefully chosen, since cells can sense the underlying stiff glass, if the gel is too thin [82].

The mechanical environment is now well recognized as an important factor in cell biology studies. Principally the matrix stiffness is shown to be a relevant parameter that modulates cell responses such as differentiation, adhesion, morphology, spreading and migration and even stiffness of the cell itself. Engler and colleagues, demonstrated that mesenchymal stem cells under stimulation, plated on chemically similar soft and stiff substrates, can differentiate into neurones and osteoblasts respectively [83]. Recent studies showed that stem cells can even remember the mechanical history of their environment [84]. Missirlis and Spatz demonstrated that fibroblast migration is regulated by the substrate elasticity, for hydrogel coated with ECM protein (fibronectin and vinculin). The cell migration is slower but more persistent on the stiffer substrate [85]. In contrast, Pelham and Wang demonstrated that fibroblasts migrate faster on stiff substrate [66]. Solon et al. showed that fibroblast cells increase their internal stiffness until they match that of their substrate [28]. Levental et al. showed that epithelial cells cultured on soft substrates appear softer than those grown on hard substrates [86]. Engler et al. have demon-

strated that cell differentiation can be tuned by substrate stiffness [87].

We have discussed the importance of matrix mechanics, and specially the matrix stiffness on individual cellular behavior and function. It was suggested that cells on substrates with the same stiffness as their native tissue environment adopt their physiologically relevant morphology [88]. Cells begin to behave abnormally, as the matrix stiffness deviates from some optimal stiffness range [63], thus, any modification or abnormal changes of matrix stiffness can contribute to the progression of various disease including cancer and fibrosis [89] [90]. Finally it is important to note that not all cell types are sensitive to substrate stiffness, and not all mechanosensitive cell types respond similarly to changes in stiffness. This can probably be related to the fact that the elastic modulus of each tissue is different, thus the response of the cell to the effective range of substrate elasticity depend on the tissue type from which the cell is derived [28].

1.2 Immune Cells

1.2.1 The Immune System

Because the human body provides an ideal environment for many microbes, that try to break in, through dermal contact, ingestion and inhalation. The immune system, which is a network of cells, tissue and organs, works to keep out these foreign invaders, or failing that, to seek out and destroy them. Another important activity of the immune system is to rid the body of its own cells that have become damaged or are abnormal. The immune system is typically divided into two categories: the innate immunity and the adaptive immunity.

Innate immunity, is the nonspecific and abrupt first response of defense that come into play immediately or within hours of an antigen appearance in the body [91]. It includes skin, chemicals in the blood, and immune system cells (e.g. neutrophils, macrophages and natural killer cells etc) that attack foreign cells in the body [92].

The adaptive immunity is unique in its specificity for distinct pathogens, it is able to create immunological memory and is more complex. Antigen presenting cells (APC) such as dendritic cells, B cells and macrophages are required for foreign antigen presentation. Following the antigen presentation, foreign pathogen are eliminated via antibody response from the humoral immune system (mediated by antibodies produced by B lymphocytes), or activation of effector cells (mediated by T-lymohocytes) [93].

The cross-talk between the innate and adaptive immune system contributes to an efficient recognition and clearance of pathogens, but dysfunctions of the immune system can lead to harmful immunologic responses including allergy, autoimmunity, and allograft rejection [94].

1.2.2 Antigen Presenting Cell

Cellular immune response is mediated by capturing, processing and presenting antigens for recognition by certain lymphocytes such as T-cells. Antigen presenting cells (APC) are the cells that perform these functions. Classical APCs include dendritic cells, macrophages and B cells. These cells are equipped with costimulatory molecules that allow for optimal signaling by T-Cells. They are strategically located in the T-cell-dependent areas of lymphoid tissues [95]. Their size varies between 15 and 30 μm. Either by phagocytosis or by receptor mediated endocytosis, they internalize very efficiently the antigen and proceed it into peptide fragments [96]. These fragments are then transported to the surface of the APC, where they bind to the major histocompatibility complex (MHC) molecules, forming the peptide MHC complex (pMHC). The MHC is responsible for displaying the antigen fragments at the surface of the APC cell, to be therefore recognized by the appropriate T-cells (Figure 1.8). The MHC is a set of cell surface proteins called the MHC proteins, which serve to enable the individual's immune system to distinguish its cells from foreign cells. This function of the immune system is called self-versus-nonself recognition. Antigen presentation allows for specificity of adaptive immunity and can contribute to immune responses against both intracellular and extracellular pathogens. It is also involved in defense against tumors. Actually, to target malignant cells, several cancer therapies involve the creation of artificial APCs. Some artificial APCs are derived from human cells; others are acellular, containing MHC proteins, co-stimulatory molecules and the necessary peptides [97][98].

Recent studies on APCs, have demonstrated that the pMHC of an infected cell presents clustered structure of 200-900 nm diameter, which are maintained for hours after their delivery to the plasma membrane of the cell, and prior to their contact with T-cell [100]. This finding was then expanded by showing that pMHC clustering also occur on professional APCs, such as the dendritic cells, and more importantly, by showing that cognate pMHC complexes are indeed contacting each other, forming a supra-molecular cluster [101].

In separate studies, focus has been on the visco-elastic properties of different APCs including, monocytes (M), dendritic cells (DC) and macrophages (MPH), untreated (Figure 1.9) and subjected to inflammatory conditions. The results shows that the viscoelastic properties, changes among different APC (M, storage modulus of 520 +90/-80 Pa; DC, 440 +110/-90 Pa; and MPH, 900 +110/-100 Pa), and also upon inflammatory treatments (storage moduli ranging from 190 Pa to 1450 Pa). These changes has been shown to correlate with changes in the composition and activity of the cell actomyosin cytoskeleton [103].

These findings accentuate the need to take into account the two discussed aspects of the APC: the rigidity and the presence of ligands in the form of clusters, when designing an artificial APC.
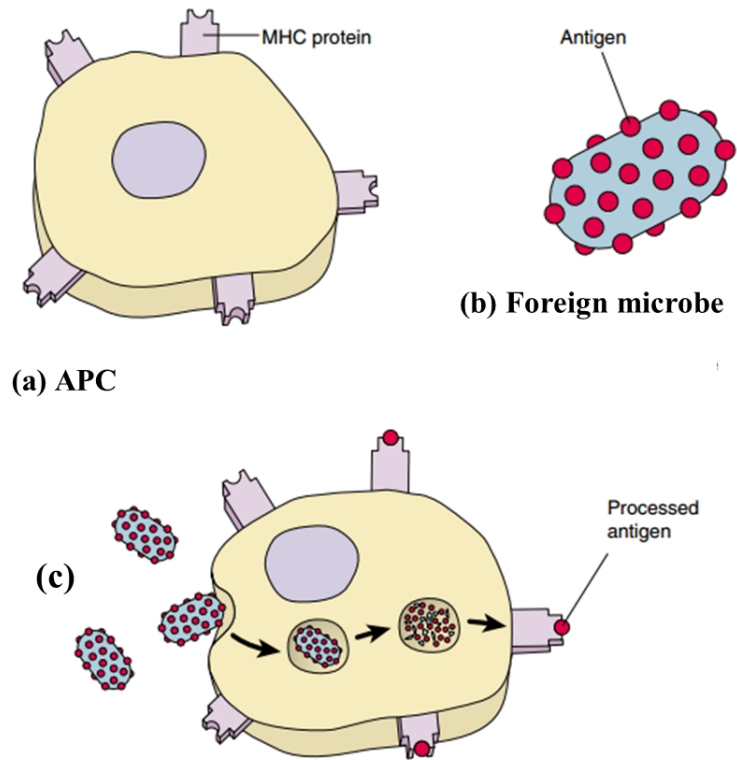
Figure 1.8 – **Antigens are presented on MHC proteins.** (a) MHC proteins at the surface of an antigen presenting cell. (b) Foreign microbes having antigens on its surface. (c) T-cells can bind to antigens only after the antigens are processed and complexed with MHC proteins on the surface of an antigen presenting cell. Adapted from [99]
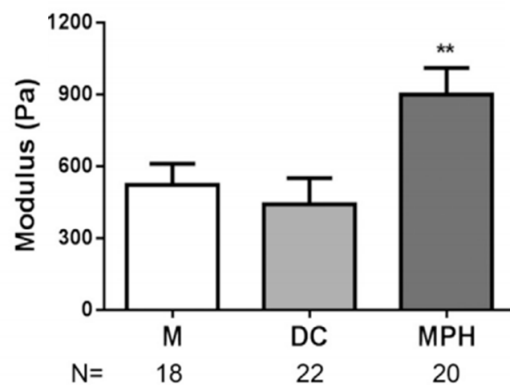
Figure 1.9 – **Storage modulus for human monocytes (M), dendritic cells (DC) and macrophages (MPH).** The storage modulus is a measure of the stiffness of a viscoelastic material and is proportional to the energy stored. "It is roughly equal to the elastic modulus for a single, rapid stress at low load and reversible deformation" [102]. $**p < 0.01$; N= number of cells tested, from at least three different donors. Adapted from [103].

1.2.3 T-Lymphocytes

The adaptive immunity defense mechanisms involve the action of lymphocytes cells, B and T lymphocytes. B-lymphocytes or B-cells (so called because they mature in the bone marrow), direct the humoral response, by secreting proteins called antibodies, which bind to and eliminate extracellular microbes. T lymphocytes or T-cells (which mature in the thymus) direct the cell mediated response and function mainly to identify and combat microbes that have learned to live inside cells (where they are inaccessible to antibodies). Depending on the subtype, T-cells, may play an important role in activating other kind of immune cells, destructing cells that have internalized pathogens, and preserving memory of an attacking pathogen.

1.2.3.1 T-Cell Receptor

The T-cell receptor or TCR is a molecule found on the surface of a T-cell. It is responsible for recognizing fragments of antigen as peptides bound to MHC molecules (pMHC). TCR is an heterodimers composed of two disulfide-linked polypeptide chains either α and β or γ and δ chains. The co-receptor known as CD4 is associated with the helper T-cell receptor (these cells can thus be indicated as CD4$^+$) and interacts only with the MHC-II proteins of another lymphocyte (Jurkat cell line used in this thesis is a CD4$^+$ cell line). The TCR associates with another cell surface molecule, cluster of differentiation 3 (CD3). CD3 consists of protein complex and is composed of four distinct chains CD3γ chain, CD3δ chain and two CD3ϵ chains. These chains associate with the TCR and the ζ-chain (zeta-chain) to generate an activation signal in T lymphocytes. The TCR, ζ-chain, and CD3 molecules together constitute the TCR complex (Figure 1.10).
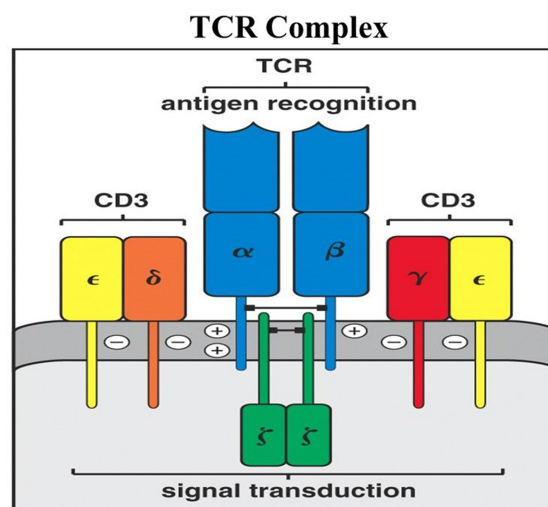
Figure 1.10 – **Schematic structure of the $\alpha\beta$ TCR complex.** A schematic drawing of a TCR, showing the TCR$\alpha\beta$ chains linked by a dilsulfide bond (black). Accessory CD3 molecules and the ζ-chains that mediate the signal transduction [104].

1.2.3.2 Interaction T-cell/APC

T-cells are highly migratory cells. They circulate through the blood, lymph and peripheral lymphoid organs [105]. Their size is about 10 μm. While migrating, the antigen receptors (TCRs) of T-cells search for membrane MHC protein that are bound to peptides derived from infection, pathogens or cellular transformation. The TCR comes in millions of slightly different forms, only one unique form will bind to a given kind of pMHC. Upon detection and recognition of such specific pMHC complex, the T-cell is arrested and forms a tight contact with the APC, with the help of stronger bonds between the LFA-1 (Lymphocyte function-associated antigen 1) on the T-cell and ICAM-1 (Intercellular Adhesion Molecule 1) on the APC (Figure 1.11), resulting, in the formation of the so-called immune synapse (IS) (Figure1.12), and activation of the T-Cell [106][107]. The activation occur only when the pMHC is recognized as "non-self" by the TCR. The interaction between TCR and pMHC triggers the IS formation. As a result, assembly of signaling, adhesive and scaffolding molecules at the cell contact zone is formed [108]. Any abnormalities affecting the synapse formation have a major impact on the immune system regulation and activation leading to immunological related pathologies such as T-cell lymphoma [107][109].
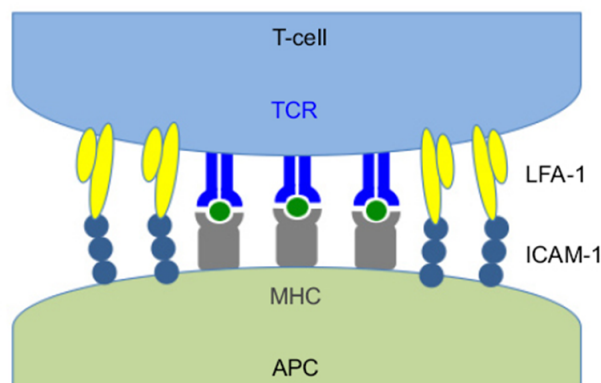
Figure 1.11 – **Interaction T-cell/APC and immunological synapse formation.** LFA-1 on the surface of T-cell binds with ICAM-1 expressed on APC, allowing the interaction of TCR with pMHC. Adapted from [110]

1.2.4 T lymphocyte/APC interface

While migrating in the secondary lymphoid organs, T-cells scan the surface of APCs for the presence of rare specific peptides on MHC complexes [105]. The contact surface at which T-cells recognize and activate in response to the pMHC complex is known as the immunological synapse or immune synapse. The concept of the immunological synapse goes back to the early 1980s; the name was chosen by M.Norcross to describe the specific T-cell/APC interaction in analogy to a neurological synapse or neuronal connections [111]. A mature IS was first imaged in T-cell/B-cell interaction [112], and soon after in T-cell/Supported Lipid Bilayer (SLB) interaction [108]. It has a bull's eye structure, that consists of three zones of concentric regions called supramolecular

activation cluster (SMAC). Each is enriched in different cell-surface and cytoplasmic molecules. However, the current view is that micro-clusters (μ-clusters) of molecules, rather than the IS itself is the key to T-cell activation.
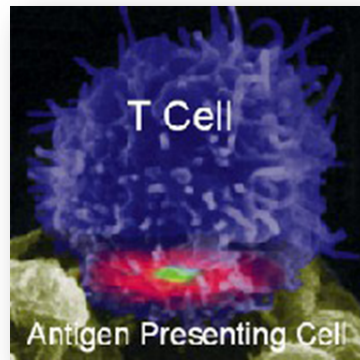
Figure 1.12 – **Interaction between a T-lymphocyte and an APC resulting in the immunologycal synapse formation.** A merge between an electron micrograph and a live-cell fluorescence micrograph to show the immunological synapse formation. It is indicated by the bull's-eye pattern of adhesion molecules (LFA-1/ICAM-1, red) and antigen receptors (TCR/pMHC, green) at the interface between a T lymphocyte (purple) and an APC (dark green). Adapted from [108].

Clustering and reorganization of membrane proteins, at the adhesive interface of a T-cell interacting with antigen presenting cells is seen to have a lot of influence on cell behavior including activation and signaling [108][113][114][115]. TCR and the integrins $\alpha_L\beta_2$ (LFA-1) at the interface of a T-cell adhering to an activating surface, are now well known to form μ-clusters [109][116][117]. In fact, thanks to hybrid systems of interaction between T-cell and SLB acting as surrogate APC [108], it was shown that the TCR μ-clusters migrate towards the center in an actin dependent manner [117][118], and form the central supramolecular activation cluster (cSMAC). Signaling molecules including ZAP-70 (receptor kinase involved in signaling), are also shown to form μ-clusters [119][120], which may colocalize with the TCR μ-clusters. Recently, it was found that micron or nano scale aggregates of TCR maybe pre-clustered on the membrane of T-cell [121][122]. Conversely, as discussed in section 1.2.2, the pMHC complex at the surface of APC is also clustered on the plasma membrane, prior the contact with T-cell [100] [101]. Therefore, it is relevant to study the adhesion and spreading of T cells on chemically contrasted substrates presenting micron and sub-micron scale clusters of ligands against the TCR complex.

Tissue cells are sensitive, on one hand to the stiffness of their environment and on the other hand also to the presentation of ligands in the form of clusters (see section 1.1.5 and 1.1.3). Interestingly, unlike the cells discussed before, the behavior of T-cells does not depend on the ligand spacing but on the ligand density [123] [124] [125]. Also there is contradictory report in

the literature on the behavior of T cells on soft substrates. Naive Mouse T-cells on polyacrylamide gels (PAA) with elasticity ranging from 10 kPa to 200 kPa are more activated on stiffer substrates [126]. In contrast, human T-cells on silicone rubber (PDMS) with stiffness ranging from 100 kPa to 5000 kPa show the opposite trend [127]. Recently it was shown that forces of about 100 pN can be exerted through the TCR complex [128] and preliminary evidence suggests that on PAA at least, more force is exerted on harder substrates [129]. However, the precise mechanisms of mechano-sensitivity of T cells are still not well established, and the development of soft patterned substrates is a requirement to further explore this phenomenon.

1.3   Technology for fabrication of biomimetic surfaces

1.3.1   Protein Adsorption to Biomaterials

Most of biological applications including tissue engineering, implemented devices, and cell based sensors and biosensors, employ the interaction of biological systems with synthetic material surfaces. The immobilization of active biomolecules or cells is required for biological studies, such as cell adhesion, cell proliferation and bio-molecular recognition. Protein adsorption phenomena is the first step in the acute biological response to artificial materials [130] [131]. However, due to the complexity and diversity of the interactions involved, the adsorption processes are complicated and difficult to predict and to control. In fact, protein is a complex molecule composed of sequences of amino acid chains that interact with each other to give the three dimensional structure of the protein, that determine its activity. Each amino acid contributes to the chemical and physical properties of the protein and thus to their adsorption properties. Proteins were described to have four different levels of structure (primary, secondary, tertiary and quaternary structure), multiple interaction sites and charged domains. They are also known to tend to denature and often attach with a random orientation on the surface. Certainly, a controlled orientation is required to ensure a correct interaction with other biomolecules or cells. Thus, the functional domain of the bounded protein must be located in a way that allows the interaction. In fact, the interaction of proteins with a solid surface, depends on several parameters including the chemical and physical properties of both the protein (protein size, concentration, charge and hydrophibicity distribution etc) and the material surfaces (e.g. hydrophilicity/hydrophobicity, chemical composition, surface charge, surface topography etc).

The main mechanisms of protein immobilization on a surface includes covalent binding to a functional surface and physical adsorption to a solid surface. Both strategies have been employed for bio-functionalization of surfaces.

1.3.2   Chemical Patterning

Micro/nano fabrication techniques were originally developed to manufacture integrated circuits [132] [133], but their applications are increasing in other fields including biology, biotechnology and biomedical science and engineering [134][135][136]. In the field of cell biology, combined

with surface chemistry and material science knowledge, micro/nano fabrication techniques have provided new tools to further explore and guide cellular processes such as adhesion, spreading, motility, and proliferation and thus explore the interaction of cells with their environment [135][137]. A wide number of techniques have been developed for producing patterned surfaces at the micro and nano scales. This techniques can be generally classified into two distinct approaches; "top-down" and "bottom-up" methods according to the process involved in creating the patterned surface [136] [137]. The *top-down* approach produces micro/nano scaled structures with specific shapes and characteristics starting from larger dimension [136], a simple way to illustrate a top-down method is to think of "carving a statue out of a large block of marble" [138]. This approach includes various methods of lithography (e.g. photolithography, colloidal lithography, nanoimprint lithography block copolymer lithography etc) [139]. In contrast, the *bottom up*, works in the opposite direction. It relies on assembling smaller building blocks into larger entities. The method resembles "building with Lego bricks" [138]. It includes methods such as chemical vapor deposition, sol-gel synthesis and molecular self-assembly (see, for example, [136] and references there in).

It is also relevant to note that patterning processes can be divided into serial and parallel techniques. In *serial techniques*, the patterning is performed by step by step processes, which reduce the writing speed (the area that can be exposed per unit time), and may be very long and costly. In contrast, in *parallel techniques*, a complete fabrication process is used to pattern large areas. Writing speed and resolution (i.e. the size of the smallest pattern feature that can be fabricated), are two important parameters characterizing the patterning techniques, which very often, are hard to reconcile, since the methods with very high resolution involve very slow writing speeds [140].

This section will be dedicated to describing the major fabrication techniques for preparing micro and nano patterns used in the field of cell biology and biophysics.

1.3.2.1 Photolitography

Traditionally, photolithography was used in the semiconducter industry for patterning metal in electronic microcircuits. Later, it was extensively used for patterning proteins and cells. To create a pattern on the surface of a substrate, photolithography requires the use of a photoactive polymer, a photoresist. Two standard type of photolitography exists: positive and negative (Figure 1.13).

In both cases it consists on the following steps: the substrate is coated by a photoresist (light sensitive organic polymer, such as PMMA or SU-8) on the surface, and then exposed to ultraviolet light through a mask containing the desired pattern.

For a positive resist, the area exposed to light will break down and be washed away and for a negative one, the opposite will happen. A negative resist is more resistant to solvent since it
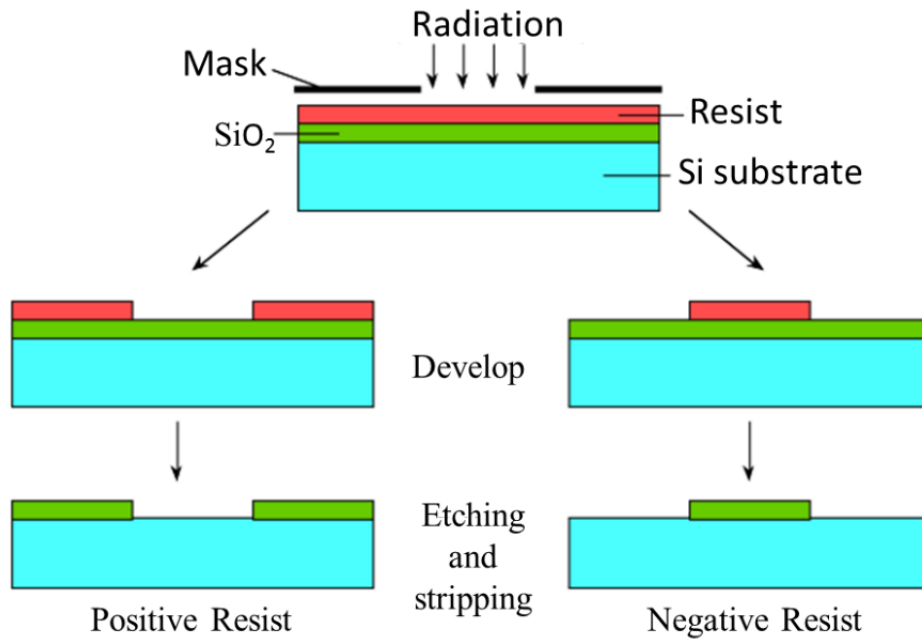
Figure 1.13 – **Photolitography using positive and negative photoresist.** Adapted from [141].

will be cross-linked. After developing, the pattern remains on the surface and the photoresist can act as mask or master for patterning material of interest. The photoresist is then removed to expose the remaining areas. This technique was extensively used to create cell adhesive and cell resistant micropatterns, for example by patterning amine terminated alkyl-silanes on a glass surface through the photoresist mask, than the non-amine coated surface, created after removing the photoresist, is backfilled with a cell repelling material such as methyl terminated alkyl silanes [142].

Protein patterns were also generated by photolithography, by immobilizing proteins on thiol terminated siloxane films that have been patterned by irradiation with UV light [143], and by covalently linking protein to photosensitive group [144]. Further, thin gold layers have been photolithographically patterned onto glass surfaces then the gold patterns were reacted with amine terminated alkyl-thiols, and the glass background with PEG-silanes [145].

In cell and protein patterning technologies, photolithography has become a dominating technique [146]. However this approach generally suffers from the need for clean-room based facilities which are expensive and/or inaccessible for many researchers. Photolithography by itself is also not well suited for introducing either chemical functionalities which may denature and deactivate biomolecules, or delicate ligands required for bio-specific adsorption onto surfaces. It also cannot be used to pattern non-plannar substrates. Photolithography can be used to produce patterns

with high resolution, which may be unnecessary for many application of patterning in cell biology. This has led to the development of other techniques for cell patterning.

1.3.2.2 Soft Lithography

Soft lithography has been developed as a complement for photolithography [147] [148] [149]. It solves many of the problems that arise in the application of microfabrication to biological problems [150]. The process of soft lithography can be separated in two parts. First, an elastomeric stamp with a defined patterned relief structures on its surface is fabricated. The fabricated stamp is then used for patterning desirable two or three dimensional micro/nano-scale patterns on different substrates.

The elastomeric stamp is typically prepared by cast molding process. It consists of pouring a prepolymer of the elastomer over a master with topological surface features, cured to induce cross-linking, and then peeled (Figure 1.14). PDMS is the most commonly used material for preparing the stamp, due to its transparency, low glass transition temperatures, low cost, biocompatibility as well as mechanical flexibility [132].
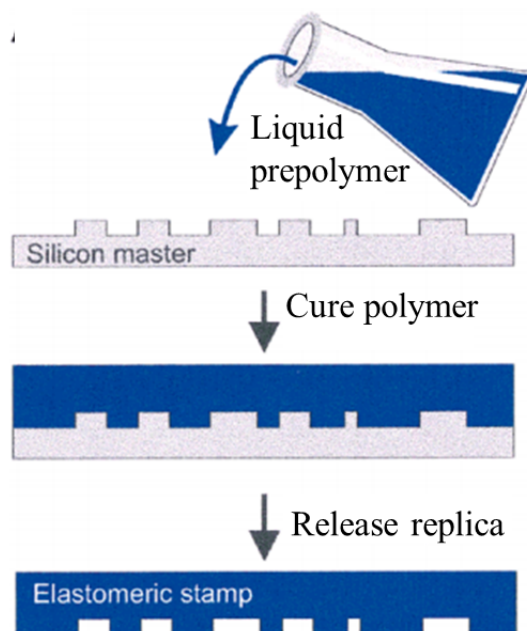
Figure 1.14 – **Overview of soft lithography process.** Adapted from [151].

Soft lithography does not require clean-room processing once the master is developed, which makes this technique cheaper, easy to use and available in biological laboratories. It is applicable to the complex and delicate molecules often dealt with in biochemistry and biology. Variety of different materials can be patterned using soft lithography, and both planar and curved substrates could be employed. Soft lithography can be divided into many categories including microcontact

printing, microfluidic patterning and stencil patterning.

1.3.2.3 Micro/Nano Contact Printing

Microcontact printing (μCP) was invented by the Whitesides group in 1993 [152] [133] [153]. It is a form of soft lithographic techniques. It transfers molecules to glass or gold surfaces using elastomeric stamps structured at micro or nano-scale. μCP is now an ubiquitous tool in different types of biological studies [153] [154] [53] [155] [133]. It consists of two consecutive steps: inking and printing. First, a silicon rubber stamp, is coated with a thin layer of material known as ink (such as proteins or alkanethiol), then the coated ink is dried by compressed nitrogen or air and transferred to another surface by conformal contact between the two surfaces [133] [132] [156]. Often the non-coated regions of the substrate are backfilled with another molecule. The advantages of this technique include its cost effectiveness, relatively simple fabrication process, ease of use, the possibility to pattern large area and high versatility [157] [55] [158]. Thus, it has been used to pattern a wide variety of materials, including colloid crystals [159], thermoplastics [160], biomolecules [53] [151] [161], metal [162], polyelectrolytes [163] and semiconductor nanoparticles [164].

In particular, μCP of proteins has helped the advancement of tissue constructs [166], biosensors [154] and cell biology research [167] [168]. Bernard et al. first used μCP to pattern proteins using an elastomeric stamp made of PDMS [169]. Since then, patterning proteins using these kind of stamps has become of interest in cell biology studies. One important particularity in μCP is the limited diffusion of proteins following the adsorption due to the absence of a viscous liquid ink during the printing [161]. This makes the proteins behave as globular particles immobilized on the stamp after adsorption and thus, transferred with good accuracy [170]. But one drawback of the method is that the protein is dried before stamping which may denature the protein.

The mechanism of transfer of the protein from the stamp to the substrate is still debated. Tan et al. found that as expected, microcontact printing of proteins occurs from low to high energy surface. In fact, they demonstrated that the transfer efficacy diminishes with the decreasing of the surface energy [171]. This was later confirmed by Kaufman et al. who found, using various stamp materials and surfaces, that transfer of protein must occur from low to high energy surfaces [170]. Following that, Ricoult et al. introduced the humidified microcontact printing which can transfer proteins adsorbed onto a stamp to both low energy and high energy surfaces due to the water vapor diffusing through the stamp. More studies are still needed to understand the molecular factors governing the transfer in proteins μCP.

μCP techniques, and their offshoots depend on the high affinity of the ink molecules for the target surface [172]. The transfer of molecules from the stamp to the substrate using μCP requires a higher attractive interaction of the molecules with the substrate than with stamp. The resolution obtained by microcontact printing is limited by diffusion of the printed molecules, both before and after contact (the ink tend to run), but also by the deformation and distortion
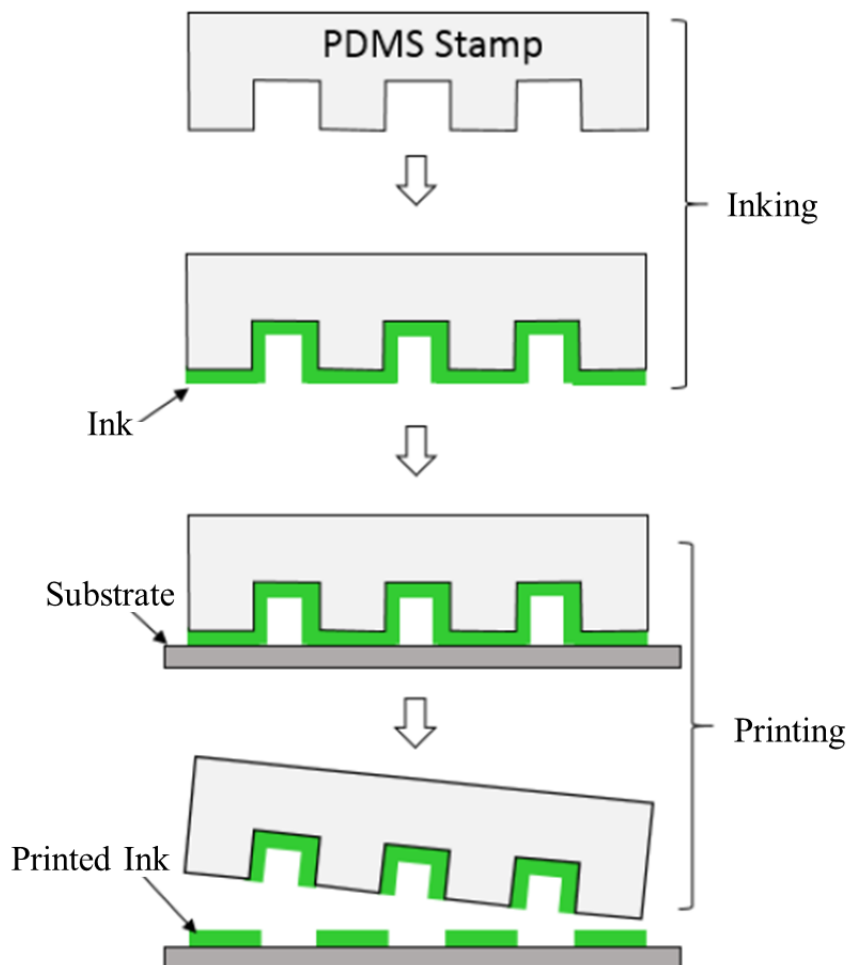
Figure 1.15 – **Schematic representation of the microcontact printing process.** Adapted from [165].

suffered by the elastomeric stamp which limit the smallest feature size [173]. Thus, one of the major challenges for μCP was to achieve the capability to print with high resolution, i.e. with lateral dimension lower than 100 nm. This was achieved by improving the stability of the PDMS, by fixing a stiff backplane to the stamp or by changing the chemical formulation of the stamp itself, in order to obtain a harder polymer. With these modification, it is now possible to print features as small as 50 nm [174] [138]. Hence, this technique has now been extended to the nano-scale and is called nano-contact printing [175] [176] [177].

μCP was historically associated with stamping self assemble monolayers (SAMs). SAM are ordered molecular assemblies formed spontaneously on surfaces by adsorption from a solution or gaz phase, and are organized into more or less, large ordered domains [178]. In some cases molecules that form the monolayers do not interact strongly with the substrate, but in other cases, the molecules consists of a head group that has a high affinity to the substrate and an-

chors the molecule to it [178]. In the latter case, the "head groups" assemble together on the substrate, while the "tail groups" assemble far from the substrate (Figure 1.16). The nature of
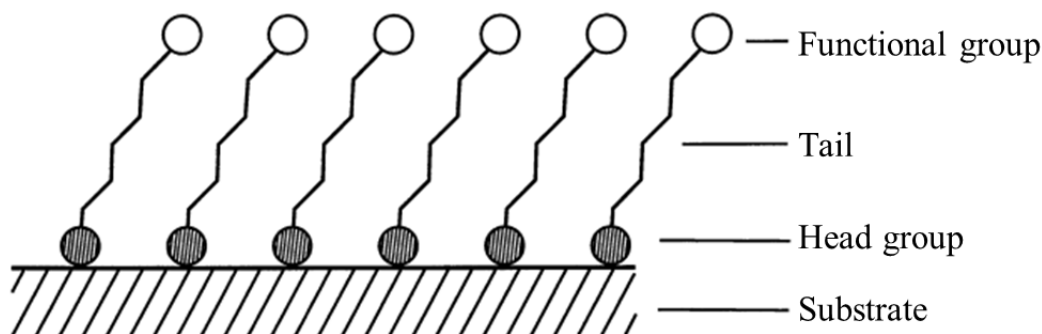
Figure 1.16 – **Schematic representation of SAM.** Shaded circle indicates chemisorbing head group and open circle end group, which can be chosen from variety of chemical functionalities. Adapted from [179].

the head group determines largely the properties of surfaces covered with the SAMs.

The adsorption of alkanethiols on gold, silver, copper, etc, form the most studied class of SAMs [180]. Besides, silane-based molecules, such as tricholorsilane and tetramethylsilane, can react with hydroxyl group on a substrate [181]. SAMs have been used as model surfaces studies involving biological components, since they can provide a range of chemical functionality at their interface with aqueous solution. Furthermore, by integrating with μCP, SAMs could be easily patterned with features down to 100 nm in size [178] [152], which enables selective immobilization of proteins and cells on substrate. Patterns of SAMs are created by printing either alkylsilane or hydrophobic alkanthiols onto a substrate. Hydrophilic molecules, such as silanated polyethylene glycol, are used to coat the remaining bare substrate in order to produce a bioinert SAM surrounding the hydrophobic areas. Proteins are then adsorbed to the hydrophobic regions creating protein patterns for cell studies [182].

1.3.2.4 Nanoimprint Lithography

Nanoimprint lithography (NIL) is an important top-down lithographic method for advanced nanostructure fabrication, it is based on the mechanical embossing principle. The concept of NIL is to use a hard master with 3D nanostructure to mould another material, which assumes its reverse 3D structure [138].

Two basic steps are required: in the first step a nanostructured mold is pressed into a thin resist (usually a heat or UV exposure curable monomer or a polymeric material) cast on a substrate. The mold is then removed (the adhesion of the resist with the template can be controlled by choosing the desired properties of the resist). The nanostructures are therefore duplicated in the resist which creates a thickness contrast pattern. The second step consists in removing the

residual resist present in the compressed area, by employing an anisotropic etching process, such as reactive ion etching RIE (Figure 1.17).
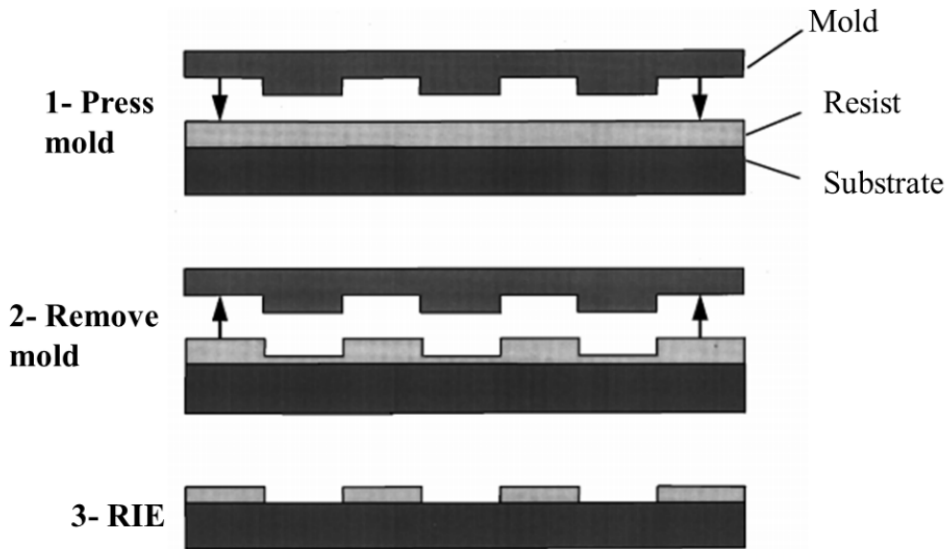
Figure 1.17 – **Schematic representation of NIL process.** Adapted from [183].

NIL methods can be classified into three categories: thermoplastic, photo and electrochemical nanoimprints methods. Thermoplastic NIL is the earliest form of NIL, developed by S.Chou's group in 1996 [183]. A high temperature is used to melt a thermoplastic substrate so that it can be embossed by a mold through applying a mechanical pressure. Photo NIL, involve the use of UV radiation to solidify a liquid precursor resist pressed against the mold. The electrochemical NIL involves an applied voltage that initiates electrochemical etching when the stamp is in contact with the metal surface.

NIL has been demonstrated to be a successful nano-patterning technique due to its high resolution that could reach sub-5 nm [184], high-throughput, low cost, and yet simple fabrication process. Its high resolution and high throughput make it a very useful technique for applications requiring precision patterning of nanoscale structures on large areas. NIL has been used to fabricate biomedical devices for tissue engineering and drug delivery [185] and also for biomolecule immobilization at the nanoscale.

Schwartzman et al. have developed a process based on NIL, to fabricate nanoscale bioarray chips where ligand spacing, density and number can be independently varied, in order to study cell adhesion [186]. They proceed as follows: a nano-structured mold was transferred to a glass substrate using NIL into a poly-methyl methacrylate (PMMA) film. A titanium layer was then deposited by e-beam evaporation while the sample is held at a certain angle relative to the metal vapor flux. Following that an oxygen plasma descum is held to remove the residual PMMA
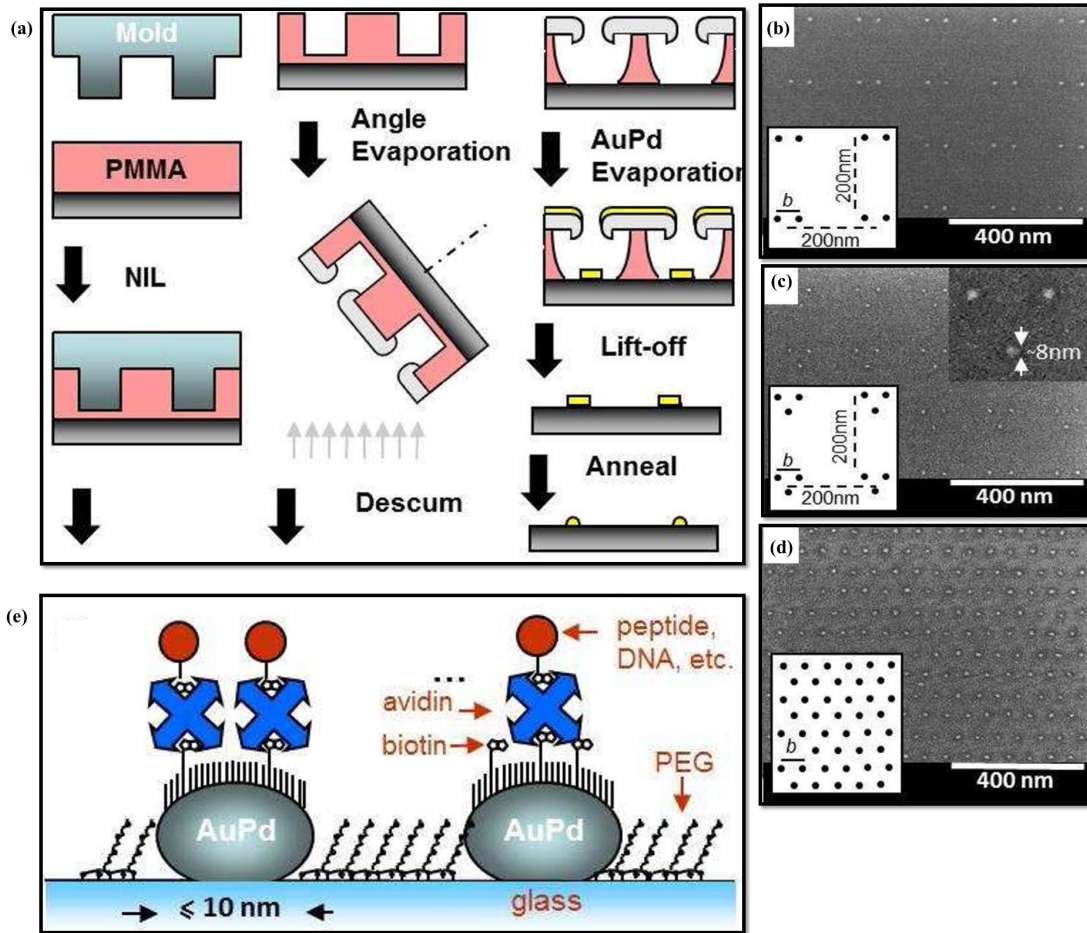
Figure 1.18 – **Fabrication of the nanoscale bioarrays chips.** (a) Schematic fabrication of AuPd nanodot arrays. (b-d) SEM of arrays of sub-10 nm functionalized nanodots arranged in dimers, trimers and extended hexagons. (e) Biofunctionalisation scheme of AuPd nanodots. Adapted from [186].

left after the imprint step. As a result, a robust motif for the definition of the final pattern is obtained. Following that, a thin film of AuPd is deposited by e-beam evaporation, followed by lift off done by immersion in boiling acetone. Finally a thermal annealing step is added to transform the size and the shape of the patterned AuPd dots (Figure 1.18 a). Scanning electron microscopy (SEM) of the pattern obtained at the end of the process is shown in figure 1.18 b-d. The AuPd nanodots pattern were then functionalized with a mixed monolayer of thiolated polyethylene glycol (PEG) and thiolated PEG-biotin, and the surrounding bare glass was passivated with PEG silane against non specific binding of proteins. Finally the protein of interest are bounded to the biotin (Figure 1.18 e) [187][186]. This present a successful strategies for creating biochemically funtionalized nanodots, with a high and accurate resolution for biological studies. However, it relies on the functionalization of gold nanodots and thus is limited by the biochemistry and optical properties of gold which make difficult the use of advance optical imaging such as total internal reflection fluorescence microscopy (TIRFM) and reflection interference contrast

microscopy (RICM) [124].

1.3.2.5 Dip-Pen Nanolithography

Dip-pen nanolithography (DPN) is a scanning probe based lithography technique developed by Mirkin's group in 1999 where it was used for transferring thiol molecules to a freshly prepared gold surface [188]. DPN can be used to deposit molecules and materials on surfaces with sub-50 nm resolution. This technique relies on using an ink coated atomic force microscope (AFM) tip, to "write" patterns directly on different substrates with a variety of materials including polymer [189], proteins [190], DNA [191], peptides [192], bacteria [193] and so on. The AFM probe is coated with a thin film of the material of interest by immersing the cantilever in a solution or by evaporation. The material molecules are then deposited onto a substrate surface during the contact between the coated tip and the substrate (Figure 1.19).
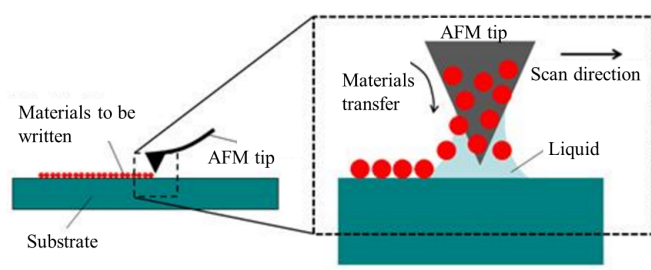
Figure 1.19 – **Schematic illustration of dip-pen nanolithography.** Adapted from [194].

The process of DPN is highly influenced by several parameters including: environmental conditions (i.e. humidity and temperature), chemical and physical properties of substrate surface (e.g. roughness, grain size), the reactivity of the ink with the substrate and tip coating procedures. The transport of ink-molecules, as well as the contrast of the AFM image are regulated by the surface roughness.

DPN is considered as one of the most flexible methods in terms of choice of molecules and surfaces [195], and has been successfully used in various applications including biosensor, and few cell biology studies such as cell signaling, activation, adhesion and migration [196] [195] [197]. However, even after massive parallelization [188] [190], DPN remains a time-consuming technique for extensive use in biology laboratory, and requires the use of specialized facilities and inks with special properties.

1.3.2.6 Block Copolymer Micelles Nanolithography

Block copolymer micelles nanolithography (BCML), is a straightforward strategy to generate periodic nano-scale structures over large areas or "structures where nanometer-sized objects are separated by nanoscopic length scales" [198]. A block copolymer molecule contains two or more polymer chains (blocks) attached by a covalent bond. Di-block copolymers consist of two polymer

chains chemically different [199]. Block copolymers are characterized by their intrinsic tendency to self assemble into ordered domains at the nanoscale. BCML uses micelles of self-assembled block copolymers with a large solubility difference between their hydrophilic and hydrophobic segments. In aqueous conditions, the block copolymers assemble into nano-scale double layered micelles, with a hydrophilic core segregated from the bulk solution by a hydrophobic region. These hydrophilic cores can be loaded with salt precursors (e.g., metal salts or oxides) by complexation or protonization of the precursors to the functional groups in the polymer chains [200]. The micelles are then allowed to self assemble in hexagonally close-packed patterns on surfaces, by spin coating the solution on a substrate or dipping the substrate into the solution. Once assembled, the salt precursors are reduced and the desired metal nanoparticles embedded in the micelles block copolymer matrix are obtained. The last step of this process consists of the removal of the block copolymers by means of a hydrogen, oxygen, or argon plasma treatment in order to obtain ordered metallic nanoparticle arrays .
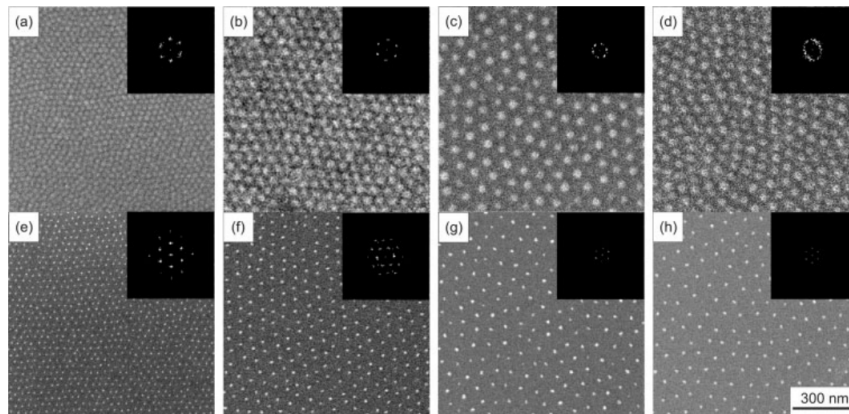
Figure 1.20 – **SEM images of micellar monolayer (a-d) and Au nanoclusters arrays after hydrogen plasma treatments of the corresponding monomicellar films (e-g), prepared from different block copolymers.**; (a, e) PS(190)-b-P2VP(190); (b,f) PS(500)-b-P2VP(270); (c, g) PS(990)-b-P2VP(385); and (d, h) PS(1350)-b-P2VP(400). polystyren(x)-block-poly(2-vinylpyridine)(y) = PS(x)-b-P2VP(y); x and y indicate the number of units per block. Adapted from [201].

BCML was mostly employed for the production of surfaces patterned with gold (Au) nanoparticles [202]. 1-15 nm gold particles organized in a quasi-hexagonal pattern are obtained without any particle enlargement. A tunable inter-particle spacing of 10-200 nm is realized. In fact the distance between the nano-particles on the surface could be finely tuned by varying the molecular weight of the block copolymer. This was demonstrated by Glass et al. as it is shown in figure 1.20 [201].

BCML method is applicable to a large number of substrates which only need to be stable against the plasma process and resistant to the solvent of the block copolymer. Previous studies have shown a successful application of this technique on several types of substrates such as glass,

silicon, titanium, diamond, sapphire and mica [200] [203] [204]. The gold nanoparticles fabricated with this techniques can be used for the immobilization of different kind of molecules [205]. This technique can be used as platform for bio-analytical devices by a biofunctionalization with enzymes, DNA, or peptides. It can be also used in cell biology studies, where the lateral distance between the biomolecules can be controlled by controlling the distance of immobilized nanoparticles. This allows the study of the influence of clustering or density on cell adhesion [206]. Lohmueller et al [203] reported a couple of protocols where the particle size could be tuned independently from the interparticle spacing, and this by combining BCML with electroless deposition (Figure 1.21). Without any particle enlargement, the average size of gold particles obtained by BCML is around 1-15 nm [200] [201] [204]. However, electroless deposition can enlarge the particle size up to approximately 50 nm [203].
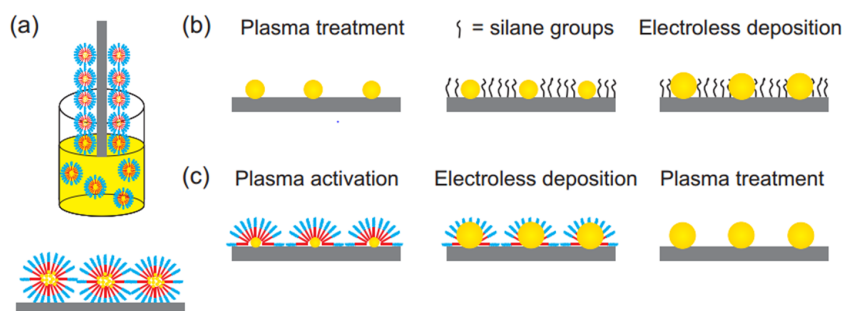
Figure 1.21 – **Electroless deposition strategy to increase the nanoparticle sizes.** (a) Formation of a micellar monolayer by dip-coating. (b) The particles are stabilized by embeddingthem into a hexadecyltrimethoxysilane (HTMS) layer. (c) A remaining polymer shell arising from the block copolymer allows for gold nanoparticle enlargement by electroless deposition without loosing the high order of the array. Adapted from [203] [207].

In conclusion, BCML represents a successful and versatile technique to generate uniform and periodic nano-scale structures over large areas. It was extensively used to generate gold patterned surfaces, where the gold nanoparticles size could be varied independently of the interparticle spacing, for application in cell biology. It was also adapted to soft substrates [208] [209]. However, this technique relies on selective functionalization of preformed gold nanodots and is therefore limited by the biochemistry and optical properties of gold, which render unpractical the use of advanced optical imaging technique such as total internal reflection fluorescence microscopy (TIRFM) or reflection interference contrast microscopy (RICM), which are essential in cell biology studies.

1.3.2.7 Nanosphere lithography

Nanosphere lithography (NSL) also known as natural lithography [210], colloidal lithography [211], or shadow nanosphere lithography [212], was first reported by Fisher and Zingsheim in 1981. They presented the use of a suspension of colloidal sphere with diameter of 312 nm to form an ordered monolayer on a glass plate, which will be use as a lithographic mask for preparation of platinum (Pt) nanostructures. However, the focus of their work was on replication of

submicroscopic patterns using visible light, and not realization of lithographic colloidal masks [213]. One year later, Deckman and Dunsmuir extended the idea of this technique and showed that a monolayer of nanospheres can be used both as a "deposit material" or as a "lithographic mask" [210]. Since the pioneering works of Fisher et al. and Deckman et al., new approaches have been developped to improve the NSL method, in order to fabricate colloidal masks with better quality and more sophisticated nanostructures depending on application.
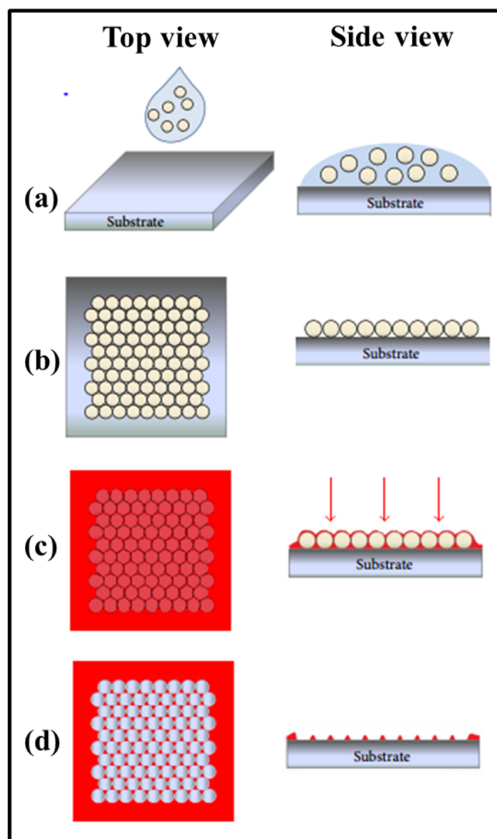
Figure 1.22 – **Schematic illustration of nanosphere lithography.** (a) Cleaning of the substrate and deposition of the colloidal suspension. (b) Self assembly of the colloidal suspension on the substrate. (c) Deposition of the material of interest. (d) Removal of the spheres. Adapted from [214].

Using this technique, regular and homogeneous arrays of nanoparticles are produced. The process begins with self assembly of a nanosphere mask (e.g polystyrene or silica) onto a substrate, followed, upon drying, by deposition of a material(s) through the holes of the ordered nanosphere mask. The mask is then removed by sonication in an adequate solvent or by stripping. An array of ordered nanodots on the surface of the substrate is formed. The supporting substrate underneath the nanospheres could be glass, mica, silica and copper, and the deposited material could be noble metal, semiconductor materials, magnetic materials, polymers and proteins.

The nanosphere diameter determines the size and inter-spacing distance of the NSL produced nanoparticles, thus the dot size could not be varied independently of the dot spacing, which in cellular study is an important requirement. To overcome this problem, a suggestion was the heat treatment of polystyrene beads [215] [216], but this process was difficult to control and till now no biological studies were reported using this process. Another suggestion was to use reactive ion etching in order to reduce the bead size, but the defect of this strategy is that it is applicable for areas of few tens of microns only [211]. Following that Pi and colleagues, reported a NL based technique, creating nanodots whose size could be tuned independently of the spacing, and used this strategy to pattern glass as well as soft PDMS (the method will be explained in more details in section 1.3.4.2.3).

NSL has been shown to be a powerful process with a wide potential of interest for the field of nano and microfabrication, it is an effective technique for high throughput fabrication of various arrays of periodic structures.

1.3.3 Soft substrates

1.3.4 Polymers

Polymers are substances whose molecules have high molar masses and are composed of a large number of small repeating units (called monomers). Monomers are usually connected by covalent chemical bonds and have a wide range of physical and chemical properties. Polymers properties can be easily tailored for specific technological and scientific applications, they can be also easily fabricated in a variety of shapes. This gives the polymers an advantage over ceramics and metals for use as biomaterials. The microscopic properties of polymers are specially related to their microstructure and to the physical arrangement of the repeating units along the backbone of the chain. Thus polymeric materials could fall into linear, branched or cross-linked architectures. Polymers could be produced with a wide range of physical and chemical properties which make them good materials for choice in biological applications.

1.3.4.1 Hydrogels

Hydrogels are popular materials for biological applications since they exhibit properties like that of natural soft tissue and have tunable properties. The first application of hydrogel in the medical sector was published in 1960, when Wichterle and Lim introduced the hydrophilic networks of cross-linked poly(2-hydroxyethyl methacrylate) (pHEMA) as soft contact lens material [217]. Since then, hydrogels were considered as promising biomaterials for application in biomedical sectors. The most frequent definition for hydrogels was given by Peppas, according to, hydrogels are three dimensional, hydrophilic, polymeric networks capable of imbibing large amounts of water or biological fluids which make them resemble to a large extent, biological tissues. Their polymeric networks are comprised of homopolymer or copolymers that are insoluble due to the presence of physical cross-links (chain entanglements or crystallites), or chemical cross-links (tie-points, junctions), or association bonds including hydrogen bonds or strong van der Waals interactions

between chains [218].

Hydrogels can be separated into two groups based on their natural or synthetic origins. The hydrogel technology may be applied to biomedical implants [219] , tissue engineering [220], diagnostics [221], food additives [222], drug delivery systems [223], barrier materials to regulate biological adhesion [224] and contact lenses [225].

In the context of cell biology, forming hydrogels typically involves either encapsulation of viable cells within the material or fabrication of substrates using molds that are later seeded with cells. Hydrogel formation involves the transition of liquid precursor solutions into solid materials, which can be achieved using either physical (noncovalent) or chemical (covalent) crosslinking to assemble the hydrogel components [226]. The mechanical stiffness of hydrogels was used in several biological applications including apoptosis, proliferation, differentiation, cell adhesion and traction force. Therefore, the creation of hydrogel system with varying stiffness was desirable to provide suitable mechanical environment for different cell types, and to extend the study of substrate elasticity effect on cells. The advantage of these gels include the fact that they produce a linear deformation in response to a wide range of stress and show a rapid and complete recovery on removal of the stress. In addition the rigidity of the gels can be easily manipulated by varying the concentration of the bis-acrylamide crosslinker. Polyacrylamide hydrogels are clear and non-fluorescent, which facilitate microscopic visualization of cellular processes. Furthermore, it is possible to covalently link proteins of interest to the otherwise nonadhesive substrate surface. PA have been widely used to create substrates with elastic moduli in the range of 0.1 kPa to 100 kPa, covering the range of many types of soft tissues in the body [83] [66] [227] [228] [229]. PA gels were also used to measure the intracellular traction forces of cells. In such technique fluorescent beads- embedded polyacrylamide gels, and the cultured cells on the substrate generated traction forces that deformed the gel structure. The deformation are then detected by the movement of the embedded beads. Even though this technique improved our knowledge of traction response in cells, it could not determine the location and direction of point forces, and the magnitude of the force which was difficult to calculate [67] [230]. These limitations were overcome by use of high density elastomeric micropost force sensor. This opened a route to experimentally investigate the force transmitted by the cell to its environment [231] [232] [233] [234].

1.3.4.2 Elastomers

The different elastomers, natural and synthetic, could be produced with a wide range of chemical, physical and mechanical properties (stiffness, strength, heat resistance, density) and even price, which allows for great selection and matching of elastomer structural and mechanical properties for scientific and technological applications. For biological applications, polydimiethylsiloxane (PDMS), organosilicone elastomer, has been extensively used as a material to study cell behavior because of its biocompatibility and the tunable mechanical properties that cover a wide range of biological tissue stiffness [235] [236].

1.3.4.2.1 Polydimethylsiloxane (PDMS)

PDMS is an elastomeric compound, easy to deform and release from features of a mold without damage. PDMS is used to reproduce with high fidelity microfluidic channels or other features with micron scale dimensions [237] and can even form structures which feature sizes down to 100 nm [152] [238] [239], for example for molds and stamps for nano-imprint lithography [149] [240]. It offers a long list of beneficial properties. It is a material that is fairly inexpensive, optically transparent, non toxic, permeable to gases, durable, non fluorescent, biocompatible, chemically inert, easy to mold into (sub)micrometer features, can easily bond to itself or to glass and have a high modulus of elasticity [241] [242] [243]. Unsurprisingly therefore, PDMS is a widely used material in multiple fields of applications including microfluidics [244][241] [245], biomaterials [246], tissue engineering [152], and medical applications as intraocular lenses, breast implants and cardiac valves. Besides its well-known superior elasticity and flexibility in mechanical applications, it is the biocompatible material aspect of PDMS which makes it attractive as a substrate for cell arrays fabrication [247] and fundamental cellular studies [235] [127], that is of most interest in this work.

1.3.4.2.2 Surface Modification of PDMS

Despite the many advantages that PDMS present for cell biology studies, including deformability and permeability of gas, using PDMS in biology studies can present problems. In fact, PDMS is known to be extremely hydrophobic and chemically inert, due to the closely packed methyl groups on its surface. Thus, its use in biology is limited, since most of biological experiments are performed in aqueous media. Moreover cell adhesion is inhibited on hydrophobic materials which limit the use of PDMS in devices which are dependent on adherent cells [248]. To overcome this limitations, biologically active PDMS were created by modification of its surface through passive coating or covalent linkages.

Passive coating technique modify PDMS surface by depositing materials such as protein, lipid bilayers and polyelectrolytes [163]. The deposition techniques include chemical vapor deposition [249], Langmuir-blodgett film formation and diffusion from solutions. Passive coating is simple and quick, however it relies on weak physical interactions to adhere the material of interest to the PDMS surface, which make the coating unstable and easily damaged. Covalent modification could improve these difficulties and increase the stability of the coatings. Covalent coating include silanization, to create covalently linked coating, by first oxidizing the PDMS surface than exposing it to a chemical silanizing agent [250].

1.3.4.2.3 Nano-patterning of soft substrates

Hard surfaces like glass or silicon are mechanically very different from the physiological state of cells. Therefore, chemically patterning soft substrates is generating a lot of interest in the domain of cell biology, to create surfaces that better mimic the real environment of the cell. But so far, to our knowledge there is only one available technique to do so. This technique is

based on patterning soft hydrogels by employing BCML (see section 1.3.2.6) for the production of surface patterned with gold nanoparticles on a solid template, then transferring the pattern to a polymeric hydrogel [208] [209] [251] [252]. These nanoparticles are used for immobilization of active biomolecules. However, this technique is limited by the optics and chemistry of gold, as well as being applicable only to hydrogels. In our group, Pi and colleagues, reported a NL based technique, creating nanodots whose size could be tuned independently of the spacing, and used this strategy to pattern glass as well as soft elastomer (PDMS). They proceeded as follows: a primary silica bead mask was self-assembled on an hydrophilic glass substrate, resulting in two dimensional monolayer of colloidal beads, then a secondary aluminum mask was deposited by sputtering, resulting after removing of the beads, a well defined array of pits giving access to the glass substrate for further deposition. They observed that by tuning the thickness of the deposited aluminum layer, the later size of the pits could be tunned. The resulting substrate was further bio-functionalized with proteins and used to study T-cell adhesion or to transfer the protein pattern to the surface of soft PDMS elastomer by contact printing [253]. This technique removes the constraint of using gold particles, and provides a powerful tool for cell biology studies. The strategy demonstrated by Pi et al. is the starting point of this thesis.

1.4 Thesis outline

Studies have demonstrated that cells are mechanosensitive, behaving differently on stiff or soft substrates. It was also shown that cells are able to respond to the nanoscale organization of active biomolecules. To enable systematic inquiry into this, micro/nano fabrication methodologies have become key methods to design model substrates that mimic spatial aspects of the cell microenvironment, and permit a deep study into cell behaviors including cell adhesion and mechanics. However, there is only one unique study reported in literature where cell behavior on soft patterned substrate could be explored [13]. Here rat embryonic fibroblast cells (REF52) were imaged in epi-fluorescence on substrates with varying ligand clustering and elasticity, showing that for the considered cell type and parameter range, increasing ligand clustering and increasing stiffness tends to influence adhesion in a similar manner.

The aim of this thesis was to develop elastomer substrates with both controlled elasticity and chemical patterning, and to explore T-cell adhesion and activation on these substrates.

The thesis is presented in six chapters which are organizing as follows:

Chapter one is dedicated to the "state of the art and literature review".

Chapter two describes the materials, methods, and protocols used and developed in this work.

Chapter 3 presents a step by step description of the printing technique that I developed. It consists of reverse transfer of protein patterns adsorbed onto a glass surface to a variety of soft elastomer surfaces with different elasticity.

Chapter 4 reports the efficiency of the patterning method. First, the elasticity of the elastomer is characterized using force measurements carried out with atomic force microscopy. Then the transfer of different proteins to a variety of silicone based elastomer surfaces is characterized in terms of dot size, contrast and transfer ratio. The chapter ends by proposing a molecular

mechanism governing the protein transfer, based on quantifying the effective force of adhesion of the protein on glass and PDMS using AFM force curves.

Chapter 5 concerns T-cell responses to homogeneously functionalized and patterned soft substrates. Parameters such as cell adhesion area, actin cytoskeleton organization, and TCR and ZAP-70 distribution are studied.

Chapter 6 concludes the manuscript with a summary of the thesis. It highlights the main points of the project, and includes a discussion on the limitation of the patterning technique that I developed and possible routes for improvements as well as suggested directions for future work.

Chapter 2

Materials and Methods

2.1 Glass substrates

Glass cover slides (Thickness = 170 microns, Assistant, Karl Hecht KG, Germany, 24 x 24 mm), were used as substrates for preparing protein nano-dot arrays, and as support for polydimethylsiloxane (PDMS) elastomer layers.

Two different cleaning procedures were used in order to prepare the glass cover-slides:
Cleaning Procedure with surfactant solution: Square glass cover slides were placed in a Teflon holder, put in a glass crystallizer and submitted to the following cleaning protocol:
- Ultra-sonication in 2% (v/v) aqueous solution of Hellmanex III (Sigma Aldrich, France) for 30 minutes at 40 ˚C.
- Rinsing 5 times with ultra-pure water (resistivity of 18.2 MΩ.cm, Elga, UK).
- Again Ultra-sonication in 2% Hellmanex solution for 30 minutes at 40 ˚C.
- Rinsing 10 times with ultra-pure water.
- Ultra-sonication in ultra-pure water (2 times, 30 minutes, 40˚C) with repeated 10 times rinsing.
Cleaning Procedure with oxygen plasma: Glass cover-slides were put inside a Nanoplas DSB3 (France) oxygen plasma cleaner, equipped with a SEREN R 301 radio frequency power supply (200 W; ≈ 2.3 Torr; Ar, 0.75 sccm; O_2, 1.5 sccm, SEREN IPS, USA) and cleaned for 15 minutes at room temperature.

Glass slides cleaned using one of these two procedures, were kept immersed in ultra-pure water protected from dust using aluminum foil for maximum 48 hours. Note that this two procedures renders the glass ultra-hydrophilic (contact angle less than 3˚). Such high hydrophilicity is essential for the next step of bead mask formation (see section 3.1.1)

2.2 Organosilanes

A silane that contains at least one silicon-carbon bond (e.g., Si-CH3) is an organosilane. The carbon-silicon bond is very stable and non polar, and in the presence of an alkyl group it gives rise to low surface energy and hydrophobic effects. Organo-functional silanes are molecules carrying two different reactive groups on their silicon atom so that they can react and couple with very different materials, e.g., inorganic surfaces and organic resins via covalent bonds and often via a polymeric "transition" layer between these different materials (Figure 2.1).
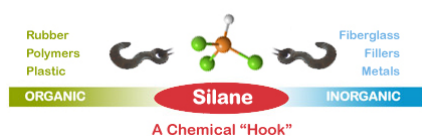
Figure 2.1 – **Silane as a coupling agent.** Adapted from [254].

Two kinds of organosilane were used in our experiments: 1H, 1H, 2H, 2H PerFluoroOctyl-TriChloroSilane (PFOTCS), and (3-AminoPropyl)-TriEthoxySilane (APTES). PFOTCS was used

as a hydrophobic place-holder to graft a passifying polymer. APTES was used as certain kinds of functionalization of elastomers. The two silane were purchased from Sigma Aldrich, France.

1H, 1H, 2H, 2H PerFluoroOctyl-TriChloroSilane (PFOTCS)
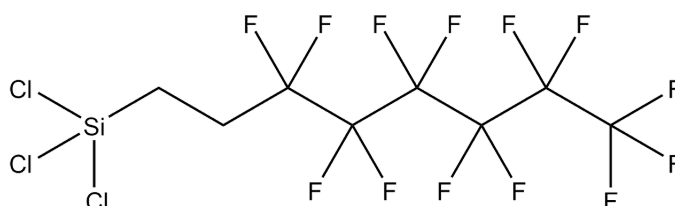
Figure 2.2 – **Chemical structure of 1H, 1H, 2H, 2H PerFluoroOctyl-TriChloroSilane (PFOTCS).** Source: Sigma Aldrich.

PFOTCS is a liquid chemical with molecular formula $CF_3(CF_2)_5CH_2CH_2SiCl_3$ (Figure 2.2), its molecules form self-assembled monolayers. It was used due to its capacity to anchors on oxide surfaces with its trichloro-silane group, and therefore to reacts with free silanol groups on the surface of the hydrophilic glass cover-slides, forming a regular covalent bond with a low interfacial free energy due to its heavy fluorinated tail group (Figure 2.3).
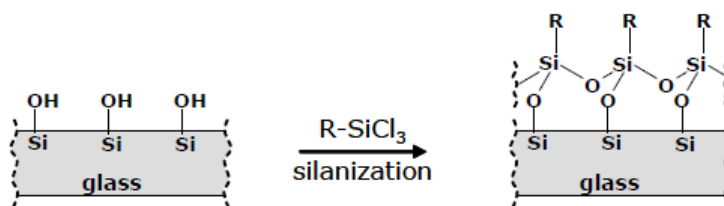
Figure 2.3 – **Schematic representation of the reaction between silanol groups of an hydrophilic glass substrates and trichloro-silane groups of PFOTCS (R= $CF_3(CF_2)_5CH_2CH_2$).** Adapted from [255].

(3-AminoPropyl)-TriEthoxySilane (APTES)

APTES is an amino-silane frequently used in the process of silanization, the functionalization of surfaces with alkoxy-silane molecules. It is a silane coupling reagent with 3-aminopropyl group at one end, which terminates in a primary amine and silane reactive portion on another end with tri-ethoxy group (Figure 2.4). The chemical formula of APTES is $(H_2N(CH_2)_3Si(OC_2H_5)_3)$, with molecular weight 221.37g/mol, it is a clear liquid with density 0.946 g/mL at 25°C [256]. APTES was used to incorporate amine functionality at the polydimethylsiloxane (PDMS) surface. This opens a route for facile functionalization of the modified PDMS surface with small organic molecules or biomolecules (such as proteins). The interest of the APTES molecule is that it can bind to the substrate forming a covalent bond, and can be bio- functionalized at the same time.
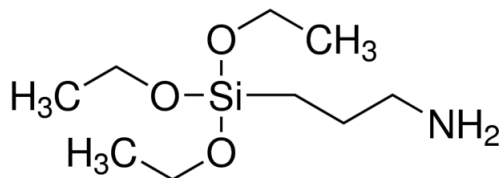
Figure 2.4 – **Chemical structure of APTES.** Source: Sigma Aldrich.

2.3 Silicon elastomers/gels

Polymers are substances whose molecules have high molar masses, and are composed of a large number of small repeating units (called monomers) that can be linked together to form long chains, or macromolecules. Silicones are macromolecules comprised of a polymer backbone of alternating silicon and oxygen atoms, siloxane bonds (Figure 2.5), with organic side groups, such as methyl, phenyl or vinyl, attached to silicon. The number of repeating units, can range from zero to several thousand. By adjusting -Si-O- chain lengths, the functionality of the side groups and the cross-linking between molecular chains, silicones can be synthesized into an almost infinite variety of materials, each with unique chemical properties and performance characteristics.
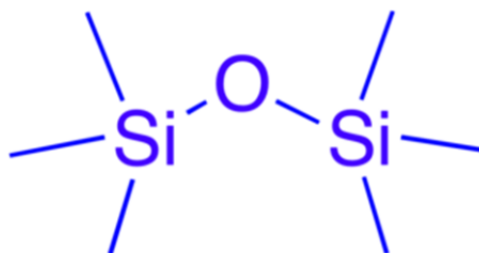
Figure 2.5 – **Chemical structure of a siloxane unit.** Adapted from [257]

2.3.1 Chemistry of PDMS

PDMS belongs to the family of silicones polymers. Silicones have a Si-O-Si backbone to which, different organic groups can be attached through Si-C linkage giving silicones the general formula $[-OSiR'R-]_n$ (where R and R' refers to the organic side groups and n is an integer denoting the number of repeating units). The presence of both the organic groups attached to an inorganic backbone gives silicone unique properties [258]. The Si-O bond renders silicones to be highly flexible material because of its long bond length, and a long bond angle that allows for ease changes in conformation. PDMS trimethylsiloxy terminated, are the most common type of silicone polymers, they have two methyl groups attached to each silicone atom, the structure is shown in figure 2.6.

PDMS is available commercially as two-part base/current agent kit, forming an elastomeric material after cross-linking. Sylgard 184 A and B is the most common silicone used in research and industry. Sylgard 184 silicon networks are prepared via hydrosilylation reactions between vinyl

$$CH_3 - \underset{\underset{CH_3}{|}}{\overset{\overset{CH_3}{|}}{Si}} - O - \left(\underset{\underset{CH_3}{|}}{\overset{\overset{CH_3}{|}}{Si}} - O \right)_n - \underset{\underset{CH_3}{|}}{\overset{\overset{CH_3}{|}}{Si}} - CH_3$$
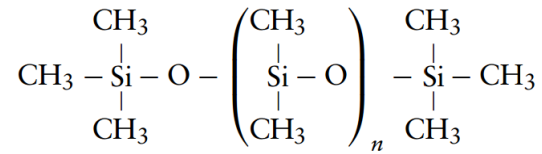
Figure 2.6 – **PDMS chemical formula.** n is the number of repeating monomer [SiO(CH_3)$_2$] Adapted from [259].

groups in the base, and Si-H groups in the cross-linkers, and this in the presence of a platinum catalyst, which results in Si-C bond as shown in figure 2.7.
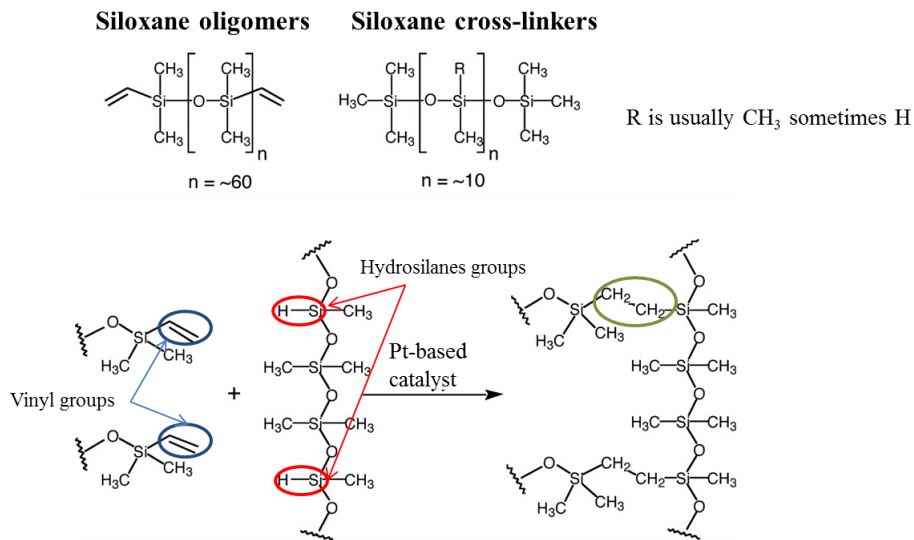
Figure 2.7 – **Reaction scheme for platinum catalyzed PDMS curing.** Adapted from [260].

The mixture of the two products will causes a cross-linking reaction that leads to obtain solid PDMS. This cross-linking reaction will starts immediately after mixing the two components together. It can take place also at room temperature, but elevated temperature accelerates the process. Because of the multiple reaction sites on both of the base and the cross-linker, a three dimensional polymeric network is formed during cross-linking (see figure 2.7). Moreover, the elasticity of cross-linked PDMS can be modulated by changing the mixing ratio of the base and curring agent.

The majority of silicone elastomers, including Sylgard incorporate fillers, which acts to reinforce the cross-linked matrix. The addition of this reinforcing fillers reduces silicones stickiness, increases its hardness and enhances its mechanical strength [259].

Among silicones materials, we used in this research project, polydimethylsiloxane, also known as PDMS, silicon rubber or Dimethicone.
Three different types of PDMS were used, they can be classified into two category:

Silicone elastomers:

- Sylgard 184 A and B (Dow Corning, USA), called Sylgard.

Silicone Gels:

- Q Gel 920 A and B (Quantum Silicones, USA), called Q Gel.

- CY 52-276 A and B (Dow Corning, Tokyo, Japan), called CY.

Silicone elastomers are cross-linked linear silicone fluids or gums with a three dimensional structure. They contain reinforcing fillers that interact with the base polymer to increase the strength of the elastomer, and also extending fillers that help reduce the material cost. Instead, silicone gels are essentially lightly cross-linked silicone fluids, and as silicone elastomers, they have a three-dimensional structure. However, silicone gels have fewer reactive sites and higher molecular weight starting material which allows for more entanglement, and contrary to silicone elastomers they do not contain fillers.

2.3.2   Preparation of the PDMS layers

PDMS layer was prepared using the spin coating method, which is a common method to produce a thin, uniform polymer film on a planar substrate. In the spin coating process, a certain amount of the polymer solution is deposited on the substrate, and the substrate is then accelerated rapidly to the desired rotation rate. Liquid flows radially, owing to the action of centrifugal force, and the excess is ejected off the edge of the substrate [261]. Final film thickness and other properties depends on the nature of the polymer (viscosity, drying rate, surface tension, etc.), and the parameters chosen for the spin process. Factors such as final rotational speed, acceleration, and fume exhaust contribute to define the properties of the coated films. Here a POLOS, single substrate spin coater, Spin 150i/200i was used at a typical speed of 2000 rpm and for 60 seconds. The PDMS layer is subsequently backed at an appropriate temperature on a hot plate for a certain duration.
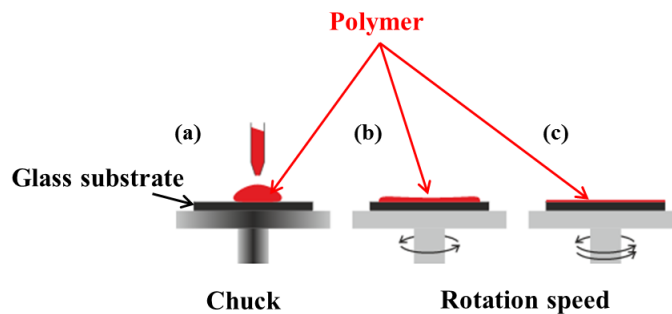
Figure 2.8 – **Schematic representation of the spin coating process.** (a)The substrate is fixed on a holder (chuck), well-centered on it, and a drop of the polymer is dispensed in the middle of the substrate. (b) The substrate is spun at a constant speed. (c) Centripetal acceleration causes the resin to spread up to, and eventually off, the edge of the substrate leaving a thin film of resin on the surface.

The specific protocols are as follows:

CY:

- Base and curing agent, part A and B, were mixed in a 1:1 ratio by mass.

- The mixture was kept for some minutes at room temperature until the bubbles disappeared.

- $\simeq$ 2ml portion of the liquid silicone mixture was dispensed on a glass substrate cleaned by hellmanex cleaning procedure (see section 2.1) using a plastic pipette.

- Spin coating was carried out at 2000 rpm for 60 seconds.

- The samples were then cured at 100 ˚C for 20 minutes.

Sylgard:

- Base and curing agent, part A and B, were mixed in a 10:1, 35:1 or 58:1 ratio by mass.

- The mixture was kept for 30 minutes in a vacuum desiccator in order to eliminate bubbles.

- $\simeq$ 2ml portion of the liquid silicone mixture was dispensed on a glass substrate cleaned by hellmanex cleaning procedure (see section 2.1) using a plastic pipette.

- Spin coating was carried out at 2000 rpm for 60 seconds using a spin coater.

- The samples were then cured at 125 ˚C for 20 minutes

Q Gel:

- Base and curing agent, part A and B, were mixed in a 1:2 or 1:0.95 ratio by mass.

- The mixture was kept for some minutes at room temperature until the bubbles disappeared.

- $\simeq$ 2ml portion of the liquid silicone mixture was dispensed on a glass substrate cleaned by hellmanex cleaning procedure (see section 2.1) using a plastic pipette.

- The sample was cured at 100 ˚C for 2 hours.

Following these procedure, a PDMS layer, supported on a glass substrate was obtained. The thickness was measured to be between 5 and 9 μm depending on the type of the PDMS used and the mixing ratio (see section 2.3.5).

Note that it is important to use a clean glass cover-slides for PDMS deposition, because small air bubbles are sometimes produced at the boundary between cover-slides and silicones in case of imperfect cleaning of the cover-slide. The procedure to produce glass supported PDMS substrate is described, step by step, in Appendix A.1.1.

2.3.3   Chemical Structure of PDMS

Sylgard 184 is the most common liquid silicone used in research and industry. It is a poly-dimethyl based silicone material (Figure 2.9 a), which contains reinforcing fillers (e.g, silica) that interacts with the base polymer and increase the strength of the material [262]. This gives the Sylgard a wide range of elasticity when changing base to cross-linker ratio. In comparison with Sylgard, the Q gel is a polydimethyl, methyl-phenyl based material (Figure 2.9 b) and has 5.5% phenyl polymer in its chain. In fact, the ratio of methyl to phenyl groups in the polymer control the refractive index in the range of $n_D = 1.4$ to 1.6 [263]. For Q Gel it's 1.49 [264]. CY is a polydimethyl based material, which contains no additive or fillers, but includes low molecular siloxane D4-D10 (cyclic poly-dimethylsiloxane polymers) (Figure 2.9 c) [265] that gives it the
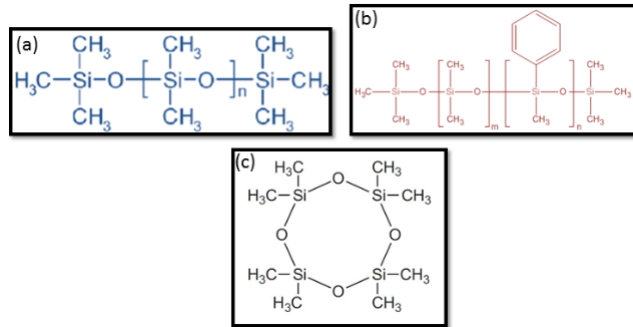
Figure 2.9 – **Chemical structure of different silicone material.** a- Poly-dimethyl based silicone material (Sylgard and CY 52-276). b- poly-dimethyl, methyl-phenyl based silicone material. c) D4: example of cyclic poly-dimethylsiloxane polymers).

characteristics of low viscosity and high volatility. Table 2.1, represents the differences in some typical properties of the three types of PDMS used in our research.

	Sylgard	Q gel	CY
Class	Silicon elastomer	Silicone Gel with controlled volatility	Soft, resilient silicone gel
Viscosity (cp)	A: 5100	A: 1455	A: 975
A= Base, B= Cross linker	B: 3500	B: 1645	B: 825
Refractive Index @ 589nm	1.4118	1.49 [264]	1.4 [266]

Table 2.1 – **Typical properties of the three PDMS types** [267][268][269].

2.3.4 Plasma treatment of PDMS

Plasmas can be conceptualized as a fourth state of matter. As energy is supplied, solids melt into liquids, liquids vaporize into gases, and gases ionize into "plasmas" – an extremely reactive gas. Free electrons, ions, radicals, and UV generated in the plasma can impact a surface with energies sufficient to break the molecular bonds on the surface of most polymeric substrates. This creates very reactive free radicals on the polymer surface which, in turn, can form, cross-link, or in presence of oxygen – react rapidly to form various chemical functional groups on the substrate surface. Polar functional groups that can form and enhance bond ability include carbonyl (C=O), carboxyl (HOOC), hydroperoxide (HOO-), and hydroxyl (HO-) groups. Even small amounts of reactive functional groups incorporated into polymers can be highly beneficial to improving surface chemical functionality and wettability. Oxygen plasma treatment is the most common method to hydrophilize PDMS substrates because it is fast, benign and effective [262]. We used air plasma treatment to render the surface of our PDMS hydrophilic. In this process, hydrogen atoms are first abstracted from the PDMS chains to generate radicals within the PDMS chains located at the surface. Some of these carbon radicals in the polymer chain combine with the radicals formed in the plasma to form functional groups. The other carbon radicals, when exposed to the air, and due to the presence of oxygen in air, will form oxidized species on the surface. Thus, the methyl groups oxidize, forming polar functional group mainly silanol group (SiOH) at the PDMS surface [270] (Figure 2.10).
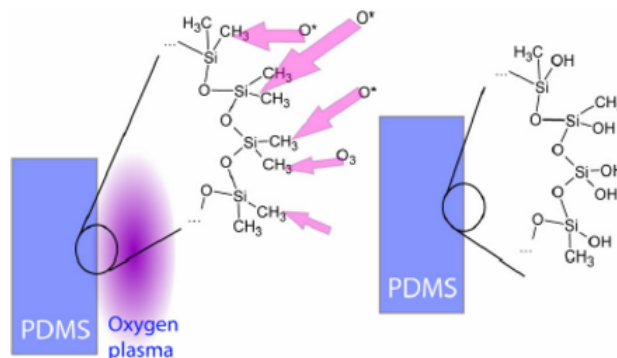
Figure 2.10 – **Surface modification of PDMS with plasma treatment.** Silanol groups SiOH are introduced at the surface of the PDMS rendiring it hydrophilic.

However plasma treatment of PDMS, presents two main drawbacks, hydrophobic recovery and surface cracks. A lot of studies have documented the hydrophobic recovery mechanism. These studies shows that the recovery mechanisms include reorientation of the polar groups from the surface to the bulk, condensation of surface silanols groups, diffusion of pre-existing low-molecular-weight (LMW) species from the bulk to the surface [271] [272] and also that the recovery rate is affected by storage condition such as temperature, humidity, incomplete cross-linking and the solvent use for the storage.

In our experiment, all PDMS samples subjected to plasma treatment, were oxidized using a Harrick plasma cleaner (Harrick scientific products), with pressure of 2.6 Torr, and 30 W power for 15 seconds. This conditions showed no cracks on the PDMS surface. The plasma treated PDMS substrates were used directly after the treatment to prevent the hydrophobic recovery and to take advantage of the hydrophilicity. The plasma treated PDMS substrates are either used as target substrate for the contact printing or further chemically functionalized with APTES and glutaradehyde (see section 3.2.2.1).

2.3.5   PDMS thickness measurement

PDMS thickness was measured using a Dektat XT, Bruker profilometer equipped with a stylus of 12.5 μm radius of curvature. Profilometer drags a diamond stylus, with a diameter of a few micrometers, laterally across a sample while maintaining a constant force. The stylus moves up and down with changing topography; this movement is recorded and used to determine surface height variations. In our experiments, PDMS sample was prepared as described in section 2.3.2, then gently scratched with a pair of tweezers and the height of the profile was measured across the scratch, leading to the measurement of PDMS thickness.

2.3.6   PDMS contact angle measurement

Contact angle measurements were done to characterize the hydrophobic/ hydrophilic properties of the surface of different types of PDMS substrates. Sessile drop method was used to measure

PDMS Type	Mixing Ratio (W/W)	Curing temperature (°C)	Curing Time (min)	Thickness (μm)
Sylgard	10:1 35:1 58:1	125	20	9 ± 1 8 ± 0.3 8 ± 0.1
CY	1:1	100	20	8 ± 1
Q Gel	1:2	100	60	8 ± 0.8

Table 2.2 – **Summary table of different PDMS layer preparation and the corresponding thickness.** Thickness value are averages of thickness measurements done on at least 2 samples and at least three scratches on each sample.

the contact angle, it is based on the investigation of the shape of a liquid drop lying on the solid surface. The image of the drop is then analyzed and thus the contact angle is determined. An optical contact angle measuring instrument (OCA20, Data physics instrument GmbH, Germany) was used to perform the measurements. Water was always used as measuring liquid. In fact, a water droplet of 5 or 1μL, in the case of native or plasma treated PDMS respectively, was placed on the surface of the sample and the focused drop was analyzed after $\pm$ 10 seconds with the aid of DataPhysics SCA 20 software. Measurements were executed on three samples, and at least on three different regions for each sample. The average value was used as result, the standard deviation as error. All contact angle measurements were performed 30 minutes after the surface treatment.

In our study, the glass supported PDMS substrates were first characterized by AFM to mechanically determine the stiffness (see section 2.8.1), and then were used for reverse contact printing of proteins patterns(see section 3.2.3), or were further homogeneously functionalized with proteins for the study of T-cells adhesion (see section 2.6).

2.4 Poloxamer

A copolymer is a type of polymer where two or more different monomer subunits are linked together to form a polymer chain. The copolymer material used in this research project is a poloxamer known by the trade name Pluronic. Pluronic is a nonionic tri-block copolymer in the form of white, waxy, free-flowing granules that are practically odorless and tasteless [273]. Chemically, Pluronic is α-Hydro-ω-hydroxy $poly(oxyethylene)_x$ - $poly(oxypropylene)_y poly(oxyethylene)_x$ block copolymer. It consists of two **hydrophilic** ethylene oxide chains **(PEO)** that sandwiched one **hydrophobic** propylene oxide chain **(PPO)** [274]. The chemical structure is given below (Figure 2.11):

At low concentration (10^{-4} - 10^{-5} %), Pluronic form mono-molecular micelles, but higher concentrations result in multi-molecular aggregates consisting of a hydrophobic central core with their hydrophilic polyoxyethylene chains facing the external medium [273].
In this research project three types of Pluronic were used:
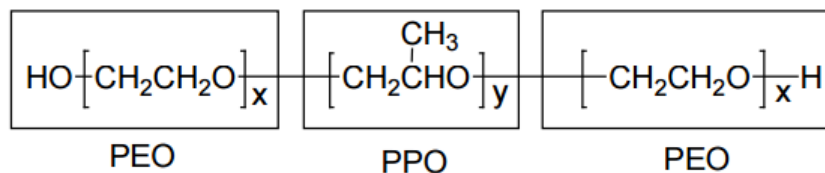
Figure 2.11 – **Tri-block structure of Pluronic block copolymer.** x= z = ethylene oxide portion, y= propylene oxide portion. Adapted from [275].

- Pluronic F-68 (Life technology, France)
- Pluronic F-108 (Sigma Aldrich, France)
- Pluronic F-127 (Sigma Aldrich, France)

The "F" designation refers to the flake form of the product.

The three Pluronic types are freely soluble in water, the main difference between them is the variety of the length of the polymer blocks constituting the Pluronic (see table 2.3). In this project, pluronic was used in liquid form as an intermediate step for creating the protein patch arrays on glass, therefore to prevent non specific adhesion of protein outside the pattern. It was also used to passivate non patterned areas on PDMS. In order to do that, several concentrations were tried (Table 2.3).

Polymer	PEO (x)	PPO (y)	Concentration (in ultra-pure water)
F 68	75-85	25-40	2%,4%,6%,10%
F 108	137-146	42-47	2%,4%
F 127	95-105	54-67	1%

Table 2.3 – **Different types of poloxamer and their concentrations, used in this project.** X is the number of PEO monomers and y is the number of PPO monomers.

2.5 Proteins and fluorophores

In this project, several types of proteins (Table 2.4) were used for fabrication of protein nano-dots arrays on glass and PDMS substrates, or to contribute to the adhesion of T-lymphocytes cells on different surfaces. The needed concentration of protein was prepared from a solution stored at -4° C , and was used directly or stored in the refrigerator for maximum two days. Phosphate buffer saline (pH = 7.4; molarity = 150 mM) (PBS, Sigma Aldrich, France) was dissolved in deionized water to a concentration of 1X, and used for the storage and the rinsing of all the proteins. The important proteins are discussed below:

BSA	Bovine serum albumin
bBSA	Bovine serum albumin coupled to biotin
BSA-TR	Bovine serum albumin texas-red conjugated
BSA-FITC	Bovine serum albumin fluorescein isothiocyanate conjugated
Nav	Neutravidin (un-conjugated)
Nav-TR	Neutravidin texas-red conjugated
Nav-FITC	Neutravidin fluorescein isothiocyanate conjugated
Nav-dylight	Neutravidin dylight conjugated
Anti-CD3	Anti-cluster of differentiation 3
bBSA-TR	biotin-bovin serum albumin, texas red conjugated
bBSA-Atto	biotin-bovin serum albumin, Atto 488 conjugated

Table 2.4 – **Abbreviations list of the different proteins.**

2.5.1 Bovine Serum Albumin (BSA)

Bovine serum albumin (BSA) is often used as blocking reagent for cell and other proteins types. It is a molecule whose advantages are to be passive, functional, robust, stable and easy to deposit in micro-contact printing and has no negative effect in many biochemical reactions. Here we used:
- Un-conjugated bovine serum albumin (BSA).
- BSA coupled to fluorescein isothiocyanate (BSA-FITC).
- BSA coupled to texas-red (BSA-TR).
- BSA coupled to biotin (bBSA).
All the types of BSA proteins used were purchased from Sigma Aldrich, France, and used either as is or, for bBSA, was conjugated to a dye (see section 2.5.6.1).

2.5.2 Neutravidin-Biotin interaction

Biotin is a relatively small molecule (244.3 Daltons), that can be conjugated to many proteins (such as BSA) without significantly altering their biological activity. The highly specific interactions of biotin with biotin-binding proteins make it a useful tool in assay systems designed to detect and target biological analytes. During our study, we choose to use neutravidin (Nav) as a biotin binging protein. Several forms of neutravidin were employed:
- Un-conjugated neutrAvidin (Nav, ThermoFisher scientific, France).
- Neutravidin, Texas Red conjugated (Nav-TR, Invitrogen, USA).
- NeutrAvidin, Fluorescein isothiocyanate conjugated (Nav-FITC, Sigma Aldrich, France).
- Neutravidin, Dylight conjugated (Nav-Dylight, Life technology, France).

2.5.3 Anti-CD3

Anti-CD3 is a monoclonal antibody that binds to the CD3 moiety on the surface of T-Cells. Biotinylated anti-CD3 was used in order to bind to the neutravidin via the biotin, and to further target the TCR complex. Two types of anti-CD3 were employed:

- Mono-biotinylated anti-CD3 (Ortho-clone OKT3, Janssen-Cilag, USA) conjugated to ATTO 647 (Life Technology). (For more detail about the process of biotinilation and Atto 647 labelling see ref [276]).

- Multi-biotinylated anti-CD3, mouse anti-human Clone (UCHT1 Beckman Coulter, France)

2.5.4 Fluorophores

Fluorophores, fluorescent probes or simply dyes are the category of molecules capable of undergoing electronic transitions that ultimately result in fluorescence. Fluorescence is the result of a three-stage process that occurs in a fluorophore molecule. This process is illustrated by the simple electronic-state diagram (Jablonski diagram) shown in Figure 2.12.

A photon of energy $h\nu_{EX}$ is supplied from an external source such as an incandescent lamp or
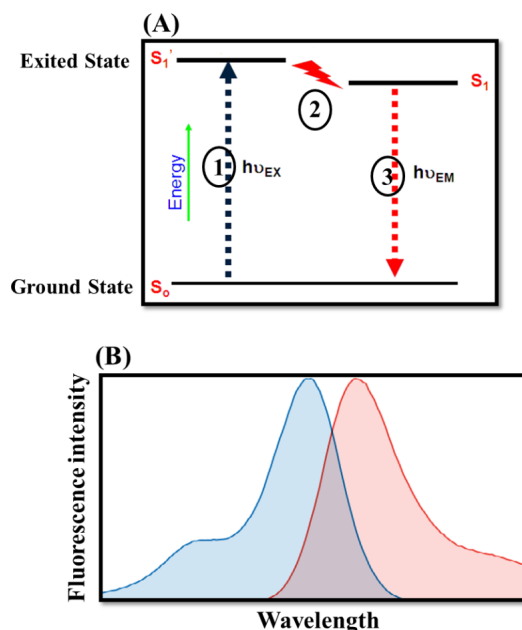
Figure 2.12 – **Principle of fluorescence.** A- Jablonsky diagram; B- General diagram of the excitation (blue) and emission (red) spectra for a fluorophore. Adapted from [277]

a laser and absorbed by the fluorophore, creating an excited electronic singlet state (S_1').
The excited state exists for a finite time (typically 1–10 nanoseconds). During this time, the fluorophore undergoes conformational changes and is also subject to a multitude of possible interactions with its molecular environment.The energy of S_1' is partially dissipated, yielding a relaxed singlet excited state (S_1) from which fluorescence emission originates. However, not all the molecules initially excited by absorption (Stage 1) return to the ground state (S_0) by fluorescence emission, other processes may also depopulate S_1. The fluorescence quantum yield, which is the ratio of the number of fluorescence photons emitted (Stage 3) to the number of photons

absorbed (Stage 1), is a measure of the relative extent to which these processes occur. Finally, a photon of energy $h\nu_{EM}$ is emitted, returning the fluorophore to its ground state S_0. Due to energy dissipation during the excited-state lifetime, the energy of this photon is lower, and therefore of longer wavelength, than the excitation photon $h\nu_{EX}$. The excitation and photon emission from a fluorophore is cyclical, and until the fluorophore is irreversibly damaged (photo-bleached), it can be repeatedly excited. Because fluorophores can there for emit numerous photons through this cycle of excitation and emission, fluorescent molecules are used for a broad range of research application. In our experiments, we used several flurophores including Atto 488, Texas Red (TR), Dylight 647 (dylight), Fluorescein Isothiocyanate (FITC), Alexa Fluor 647, Rhodamine and Atto 647 (see details in section 2.5.5).

2.5.5 Fluorofores used

In our experiments, we used several organic dyes to visualize proteins. BSA and Nav were bought in a labeled state, anti-CD3 labeled with biotin and Atto 647 was a gift from Rjat Varma, and bBSA was labeled in house. Here, i will describe the two dyes used for in home labeling.

2.5.5.1 Atto 488 dye
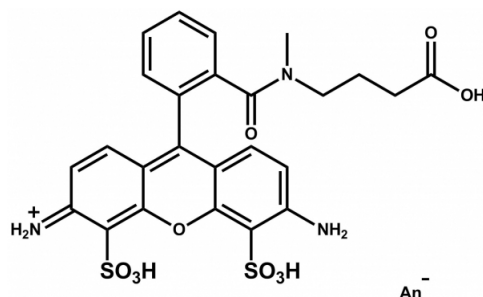
Figure 2.13 – Chemical structure of atto 488 dye, adapted from [278].

Atto 488 dye (Figure 2.13) is characterized by its excellent water solubility, strong absorption, high fluorescence yield, very little aggregation, net charge of -1 and exceptional thermal and photo-stability [279]. It has a maximum absorption at 501 nm and emission maximum of 523 nm. The presence of free carboxy groups can let us bind it to amino group of the bBSA via N-hydroxysuccinimidyl-esters (NHS) (more details in section 2.5.6.1).

2.5.5.2 Texas red dye (TR).

Texas red dye (Figure 2.14) is a red fluorescent dye, it fluoresces at about 615 nm and the peak of its absorption spectrum is at 589 nm. It is commonly used conjugated to antibodies and proteins for cellular imaging applications. It dissolves very well in water as well as other polar solvents, e.g., dimethylformamide, acetonitrile. It is usually a mixture of two monosulfonyl chlorides as seen in figure 2.14, or with the SO_3 and SO_2Cl groups exchanged. TR can be easily bought in a form of NHS-esters. It is activated with sulfonyl chloride for covalent attachment to
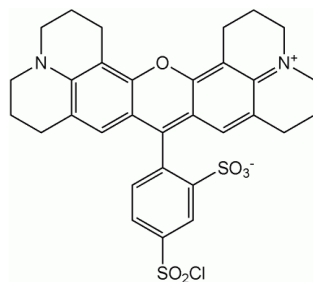
Figure 2.14 – Chemical structure of Texas Red dye, adapted from [280].

primary amines of antibodies, protein and other molecules (more details in section 2.5.6.1). In our experiments, TR was used to visualize BSA and Nav and also, for in home labeling of bBSA.

2.5.5.3   Other Dyes

Other fluorophores such as fluorescein isothiocyanate (FITC), Atto 647, alexa fluor 647 (alexa 647) and rhodamine were also employed in our study.

FITC (Figure 2.15) is a derivative fluorescein, one of the most popular fluorochrome ever designed, and has enjoyed extensive application in immuno-fluorescence labeling. FITC has excitation and emission spectrum peak wavelengths of approximately 495 nm/519 nm, and like most of the fluorochromes, it is prone to photo-bleaching. Due to this problem, derivative of fluorescein such as alexa fluor 488 have been tailored for various chemical and biological applications where greater photostability, higher fluorescence intensity, or different attachment groups are needed. In our experiments, FITC was used to visualize BSA and Nav, and also to label actin in the cells.

  Alexa 647 is a bright, far-red-fluorescent dye, it absorbs light maximally at 650 nm and fluoresce
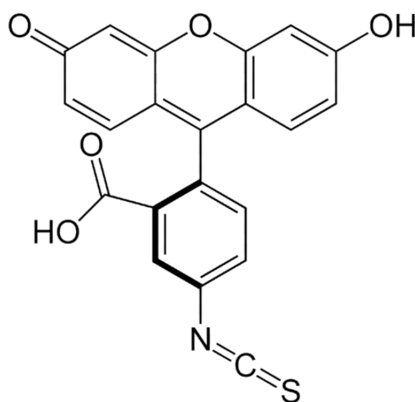
Figure 2.15 – Chemical structure of FITC dye, adapted from [281].

with a peak around 665 nm. Alexa 647 dye, is characterized by high fluorescence quantum yield and high photostability, which allow detection of low-abundance biological structures with great sensitivity. Here, Alexa 647 was used to label ZAP-70

Atto 647 belongs to a new generation of fluorescent labels for the red spectral region. It absorbs

at 645 nm and fluoresce at 669 nm. It is characterized by strong absorption, excellent fluorescence quantum yield, good solubility high photostability, it is a cationic dye that carries a net electrical charge of +1 after coupling to a substrate. It is specially used in the area of life science, for labeling , e.g. of DNA, RNA and proteins. In our project, atto 647 dye was used labeled to anti-CD3.

Rhodamines dyes are supplements to fluoresceins, as they offer longer wavelength emission maxima and provide opportunities for multicolor labeling or staining. Rhodamines exhibit higher photostability than fluorescein. Here rhodamine was used attached to phalloidin, to label actin in the cell.

2.5.6 Fluorophore Coupling

2.5.6.1 Labeling protocol of BSA biotin conjugated with fluorophores.

Bovine Serum Albumin (BSA) coupled to biotin was labeled either with TR or Atto 488 dye using a fast and easy Protein Labeling kit (Texas Red-X protein Labeling Kit, T-10244, Thermo fisher Scientific France or Atto 488 protein labeling Kit, Sigma, France).

The two dyes have a succinimidyl ester (NHS-ester) moiety that reacts efficiently with primary amines of proteins to form stable dye–protein conjugates (Figure 2.16).
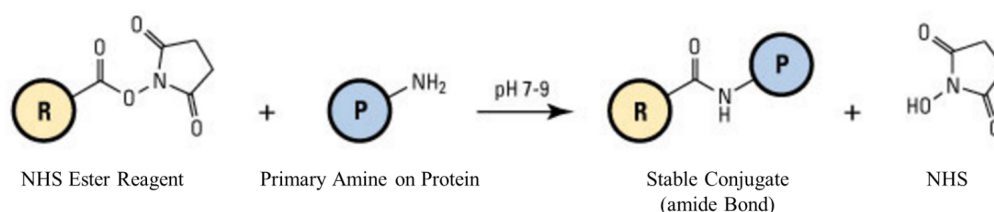
Figure 2.16 – **NHS ester reaction scheme for chemical conjugation to a primary amine.** (R) represents a labeling reagent or one end of a cross linker having the NHS ester reactive group; (P) represents a protein or other molecule that contains the target functional group (i.e., primary amine). Adapted from [282].

The labeling protocol can be summarized in three steps (Figure 2.17):

Step 1: Protein Preparation
A solution of 2 mg/ml of bBSA in PBS buffer is prepared.

Step 2: Labeling Reaction
- Sodium bicarbonate, pH∼8.3 is added to the protein solution in order to raise the pH of the reaction mixture. NHS reacts efficiently at pH 7.5 - 8.5.
- In case of TR dye, addition of DMSO (dimethylsulfoxide) to the vial containing the reactive dye is required, in order to help dissolve the hydrophobic TR reactive dye into the aqueous protein solution, thereby increasing the efficiency of the reaction.
- The protein solution is transferred to the vial of the reactive dye.
- The reaction mixture is stored at room temperature.

Step 3: Purification of the labeled Protein

A gel filtration column is used in order to achieve good separation of the protein-dye-conjugate from excess free dye. Solvent flow in the column is achieved by gravity only, there's no need to apply pressure.
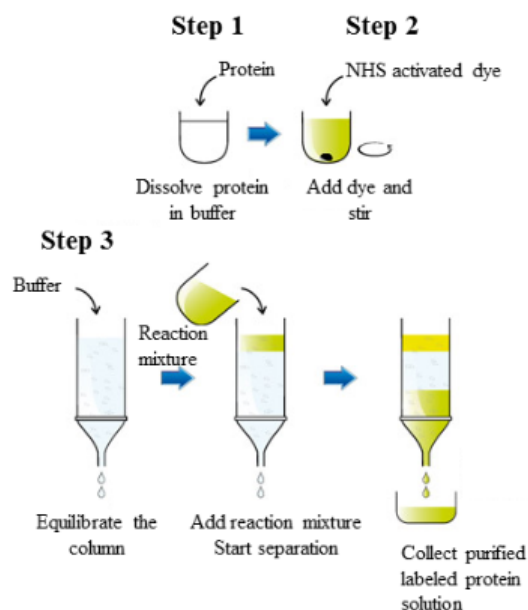
Figure 2.17 – Illustration of fluorescent labeling of biotin-BSA protein using Atto 488 or TR dye [283].

2.5.6.2 Determination of the degree of labeling

An Ultra violet spectrophotometer (UV/VIS spectrophotometer: Varian, Cary 5000, UV-VIS-NIR) was used to measure the absorbance of the conjugates, in order to calculate the degree of labeling (Dye/Protein ratio; D/P), and the labeled protein concentration.

The conjugate solution was diluted in PBS buffer so that the maximum absorbance measure is between 0.5 and 1 A.U.

The absorbance of the conjugate solution was measured at the wavelength maximum of the protein (λ_P) and of the dye (λ_D).

The D/P molar ratio is then calculated as follow:

$$D/P = \frac{A_{\lambda D} \times \epsilon_P}{[A_{\lambda P} - (A_{\lambda D} \times CF)] \times \epsilon_D} \qquad (2.1)$$

The final protein concentration can be calculated as follows:

$$C_P(mg/mL) = \frac{A_{\lambda P} - (CF \times A_{\lambda D})}{\epsilon_P} \times MW_P \times Dilution factor \qquad (2.2)$$

$A_{\lambda D}$: Absorbance (A) of the dye solution measured at the wavelength maximum (λ_D) for the dye molecule.

$A_{\lambda P}$: Absorbance (A) of the protein solution measured at the wavelength maximum ($\lambda_P = 280$ nm) for the protein molecule.

ϵ_P: molar extinction coefficient of the protein at 280 nm ($M^{-1}.cm^{-1}$); e.g. the molar extinction coefficient of bBSA is 44973.11.

CF: Correction factor; adjusts for the amount of absorbance at 280 nm caused by the dye.

ϵ_D: molar extinction coefficient of the dye at λ_D [$M^{-1}.cm^{-1}$]; e.g., the molar extinction coefficient of Atto 488 is 90000 at 498 nm, and 80000 for the TR dye at 595 nm).

MW_P: molecular weight of the protein (66.430 g/mol for biotin-BSA).

In our experiments, the protein-dye conjugate was diluted 1/10 in phosphate buffer saline. The value of the obtained absorbance, the calculated protein concentration and D/P molar ratio are resumed in table 2.5.

Dye	λ_D (nm)	ϵ_D	CF	$A_{\lambda P}$ (A.U.)	$A_{\lambda D}$ (A.U.)	C_P(mg/mL)	D/P
Atto 488	498	90000	0.1	0.124	0.496	0.27	3.34
TR (first batch)	595	80000	0.18	0.154	0.36	0.68	2.31
TR (first batch)	595	80000	0.18	0.154	0.29		1.58

Table 2.5 – **Results of UV absorbance measurements.**

2.6 Substrates for Cell experiments

2.6.1 Positive control

PDMS supported on a square glass cover-slide was prepared as described in section 2.3.2, placed inside a home made round chamber (Figure 2.18) and functionalized as follows:

- Incubate 800 μl of bBSA at a concentration of 100 μg/ml in PBS on the PDMS sample for 2 hours at room temperature (RT)(in the case of CY and Q gel) or at 37°C (in the case of Sylgard).

- Rinse 5 times with PBS.

- Functionalize with 800 μl of Nav-TR at a concentration of 4 μg/ml in PBS, for 45 minutes at RT.

- Again rinse 5 times with PBS.

- Incubate 800 μl of multi-biotinylated anti-CD3 at a concentration of 2 μg/ml in PBS for 45 minutes at RT.

- Rinse five times with PBS.

2.6.2 Negative Control

Negative controls were performed for homogeneously functionalized and patterned substrates, in order to determine weather cells adhere only in presence of specific ligands or adhered to

substrates via unspecific interactions.

For homogeneously functionalized substrates, negative control was performed as follows:
- Incubate 800 μl of bBSA at a concentration of 100 μg/ml in PBS, on the PDMS substrate
(prepared as describe in section 2.3.2) for 2 hours, at room temperature (RT)(in the case of CY
and Q gel) or at 37°C (in the case of Sylgard).
- Rinse 5 times with PBS.
- Functionalize with 800 μl of Nav-TR at a concentration of 4μg/ml in PBS, for 45 minutes at
RT.
- Rinse 5 times with PBS (0.1% BSA).

2.7 Cell Experiments

The cells used here are Jurkat T-cells (Clone E6-1, ATCC). Jurkat is an immortalized line of
human T lymphocyte cells. It was demonstrated that signaling requirement for Jurkat T-cells
was fulfilled by ligation of the TCR with CD3 antibodies, and that the CD3 subunits mediated
signal transduction across the plasma membrane, thus the study of Jurkat T-cell activation could
be done using anti-CD3 monoclonal antibodies instead of using a cognate antigens.

2.7.1 Chamber used for cell experiment

For cells, round, home made chambers (Figure 2.18), cleaned with surfactant cleaning procedure
(see section 2.1) were used. These chambers were designed to facilitate and optimize substrate
functionalization steps, cell fixation and labeling, and can be easily manipulated on the micro-
scope.
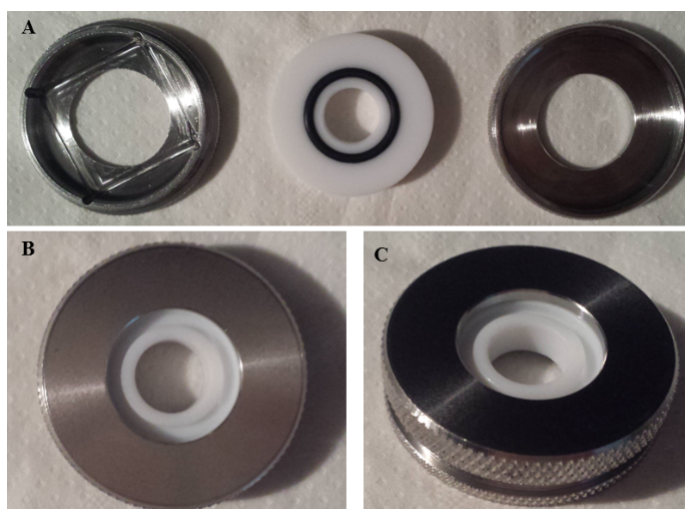
Figure 2.18 – **Chamber used for cell experiments.** A- Unmounted home made open chamber.
B- Upper view of mounted chamber. C- Side view of mounted chamber.

2.7.2 Cell culture and splitting

Jurkat E6 T-lymphocytes were cultivated in RPMI complete medium supplemented with 10% Fetal Bovine Serum and 1% GlutaMAX (Invitrogen). Splitting is realized every two days in order to let the cell concentration quadruple between two splits, and last splitting was done 24 hours before experiments to ensure a concentration of 0.6 million cells/ml at the moment of the experiment.

2.7.3 Cell Preparation

Prior to any experiment, the observation media consisting of PBS + 0.1% BSA is heated in a water bath to 37°C. 1 ml of the cell were taken out from the culture flask using a serological pipette, placed in an eppendorf tube, and centrifuged at 1600 rpm during 4 minutes. Supernatant is removed and the cell pellet is suspended in PBS + BSA 0.1% at 37°C, 5% CO_2.

The steps required for the deposition of the cells on the substrate of interest, are as follow:

- Place the substrate inside a home-made round chamber.

- Rinse five times with the pre-heated observation medium (PBS + 1% BSA).

- Add 800 μl of the observation medium.

- Place the chamber in a water bath at 37°C, for 15 minutes so that it takes the temperature of the cell.

- Take out the chamber from the incubator.

- Remove 400 μl of the observation medium from the chamber.

- Add 200 μl of cells to the chamber.

- Incubate the sample containing the cells for 20 minutes (on controls) or 30 minutes (on patterned PDMS), at 37°C, 5% CO_2 in order to let the cells adhere to the substrate.

2.7.4 Cell fixation

2% paraformaldehyde (Merck, France) in PBS solution is pre-heated to 37°C, and is gently introduced into the chamber (care should be taken to minimize detachment). The sample is then incubated during 15 minutes at 37°C, and washed carefully 10 times with PBS.

2.7.5 Post-fixation labeling

2.7.5.1 Actin labeling

The actin marking was done using phalloidin fluorescently labelled with:

1- *Rhodamine* (dissolved in DMSO, Sigma-Aldrich, France), by incubation of the cells, directly after the fixation step, with 20μg/ml of phalloidin rhodamin conjugated, for 30 minutes at room temperature and then washing 10 times with PBS.

2-*FITC* (dissolved in methanol, Life Technologies, France). In this case, after the fixation step,

and before the labeling, an additional step is required. It consists on incubating the cells in 0.1 % Triton X-100 (Sigma, France) for 4 minutes in order to permeabilize the cell membrane, then to wash 5 times with PBS. Next, the labeling can take place by incubating the cell with 20 μg/ml of Phalloidin-FITC conjugated, during 20 minutes at room temperature, then rinsing 10 times with PBS.

2.7.5.2 TCR labeling

Before labeling the TCR, and after cell fixation a blocking step is required to prevent any non specific adhesion of the marker. In order to do that, the substrate is incubated with 500μg/ml of BSA at 4°C overnight (or two hours at room temperature). After this step, cells are incubated, during 30 minutes at room temperature, with FITC fluorescently labeled mouse anti-human Anti-Vβ8 TCR, (5 μg/ml) (BD Bioscience, France), then washed 10 times with PBS.

2.7.5.3 Phosphorylated ZAP-70 labelling

After the step of cells fixation, and before labeling the ZAP-70, two additional steps were required. First, blocking step as in the case of TCR (incubation with 500μg/ml of BSA at 4°C overnight (or two hours at room temperature), then a membrane permeabilization step which consists on incubation of the sample in 0.1% Triton X-100 for 4 minutes. Finally, the cover-slides were incubated in 0.03 μg/ml of Alexa-Fluor 647 Mouse Anti-ZAP70 (PY319)/Syk (PY352) Clone 17A/P-ZAP70 (RUO) overnight at 4°C and washed 10 times with PBS.

2.8 Force Measurement using Atomic Force Microscopy and Spectroscopy

Atomic force microscopy (AFM) was invented in 1986 by Binnig, Gerber and Quate [284] to broaden the usefulness of its precursor scanning tunneling microscopy (STM) [285] to insulating samples. The AFM is best known for its ability to create three-dimensional images with resolution down to the nanometer and Angstrom scales, which has made it an essential tool for imaging surfaces in applications ranging from semiconductor processing to cell biology. In addition to this topographical imaging, another major application of AFM is force spectroscopy, it is able to exert and measure forces on the order of pico-newtons. This features provides the ability to probe nano-mechanical and other fundamental properties of sample surfaces, including obtaining a local adhesive or elastic properties of a surface, measuring modulus variation across a sample surface and probing molecular interactions [286]. Figure 2.19 shows a schematic of an AFM system with its general components and their functions.

2.8.1 AFM Force Spectroscopy

AFM Force spectroscopy involves the direct measurement of forces between the tip and the sample surface as a function of the distance between the two. The result is called a force-distance curve. The deflection of the cantilever is monitored as the tip (or the sample) is moved towards
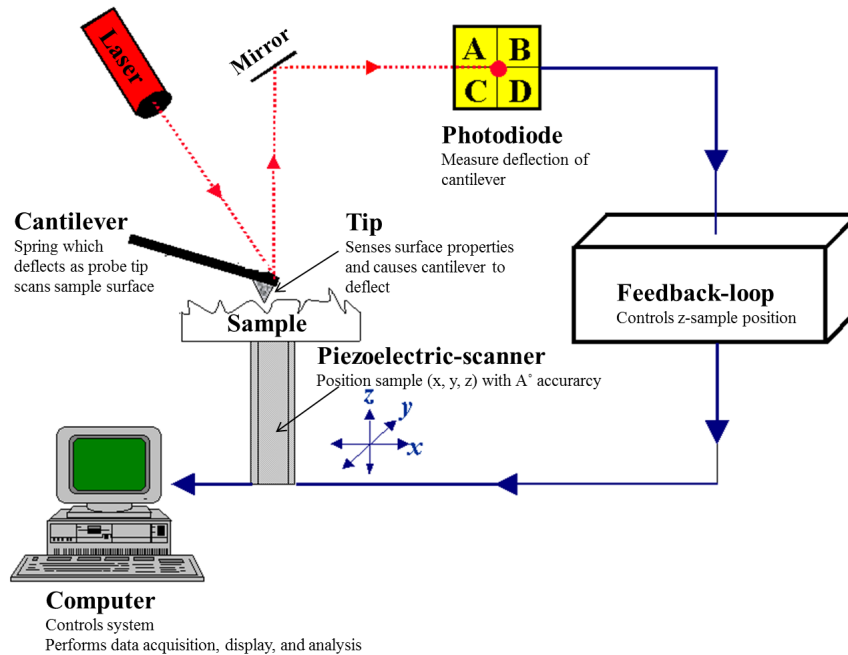
Figure 2.19 – **Schematic of an atomic force microscopy system.** The atomic force microscope senses the physical properties of a sample by passing a sharp probe on a cantilever over the sample, and detecting deflections in the cantilever using reflections from a laser beam. From [287].

and away from the sample (or the tip), and then is plotted as a function of piezoelectric displacement which gives the force-distance curve. This technique can be used to measure the long range attractive or repulsive forces between the tip and the sample surface, elucidating local chemical and mechanical properties of the sample surface such as adhesion, elasticity, dissipation energy due to material deformation and, bond rupture forces could be measured.

To help examine the basics of AFM force measurements, figure 2.20 shows a typical "force-versus-distance" curve or force curve, for short:

The horizontal axis (X-axis) is the vertical distance moved by the sample stage.

The vertical axis (Y-axis) is the deflection of the cantilever as the sample surface is moved towards the tip, contacts and pushes against the tip and then away from the tip.

The black curve is the approach cycle and the red curve is the retract cycle.

The different sections of the curves are defined as follows:

a-b: The surface approaches the cantilever, initially the forces are too small to give a measurable deflection of the cantilever, and the cantilever remains in its undisturbed position. Therefore the curve is flat.

b-c: The attractive forces (usually Van der Waals, and capillary forces in air) overcome the cantilever spring constant and the tip jumps into contact with the surface. The cantilever is deflected downwards and the force is negative.

c-e: The sample surface continues to approach the tip, until the tip is in contact with the surface (point d: the cantilever is not deflected, and the force is zero). As the sample surface is brought
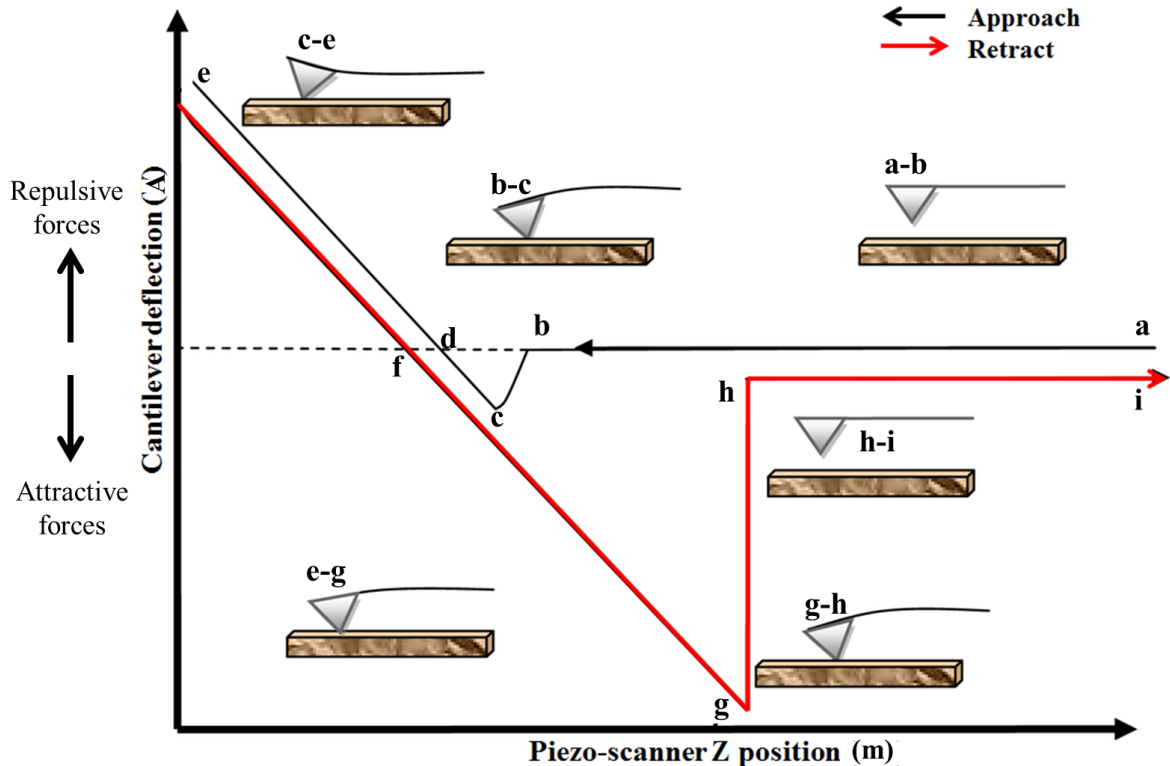
Figure 2.20 – **A typical AFM force-distance curve.** The curve depict the interaction of the AFM tip with the sample surface. A single approach(black) - retract(red) cycle of the AFM tip is recorded as a deflection voltage against piezo position. Adapted from [288].

closer to the tip, the force exerted by the tip on the surface will increase which will lead to a deflection of the cantilever and/or an indentation of the tip into the surface in the case where the cantilever is sufficiently stiff.

e-g: The cantilever is withdrawn, adhesion or bonds formed during contact with the surface cause the tip to adhere to the sample(f-g).

g-h: The spring force of the cantilever overcomes the adhesion forces and the cantilever pulls-off.

h-i: The cantilever is moved upwards to its undeflected or non-contact position.

2.8.2 Calibration of the cantilever deflection

In the experimental measurement, the force distance curve is given in term of cantilever deflection in Ampere (A) versus piezo displacement in meter (m) (Figure2.20). It is important to convert the cantilever deflection from (A) to (m) and then to unit of force in order to be able to determine the young modulus of the sample of interest (in our case: PDMS). To do that, a force curve between a cantilever and a bare hard substrate is recorded. Therefore, the deflection will be equal to the displacement, and the slope of the recorded curve will give us the deflection sensitivity (measurement of the deflection of the tip in meters for a given displacement of the cantilever).

The deflection of the cantilever in m is then determined as follow:

$$\delta_c(m) = \alpha \times \delta_c(A) \tag{2.3}$$

where δ_c is the deflection of the cantilever and α is the deflection sensitivity.

2.8.3 Calibration of the Cantilever Spring Constant

After calculating the sensitivity, it is relevant to determine the exact value of the cantilever spring constant. In fact, the cantilever spring constants can vary greatly from the values quoted by their manufacturers. The manufacturers often specify the spring constant in a wide range that may span values up to four times smaller and four times larger than the nominal value. This is because the techniques used to fabricate the probes can result in substantially different cantilever dimensions, especially thickness, from wafer to wafer and smaller variations within a single wafer, which demonstrate the need for independent calibrations. A number of ways to calibrate AFM cantilevers have been described in the literature: Thermal noise method [289], calculation from cantilever geometry [290], added mass method [291], calibration using a reference cantilever [292] and more on. Each of this method is subject to some limitations, and if experiments are compared where different methods are used, differences of maybe 10-20% can be expected. In our study, we applied the calibration against a reference cantilever or the thermal noise method.

2.8.3.1 Calibration using reference Cantilever

In this method of calibration, a lever of known spring constant (reference cantilever) attached to a sample substrate is mounted on the piezoelectric translator and the unknown cantilever is mounted as normal in the AFM. The cantilevers are approached to each other so that they just overlap at the end, and a force curve is performed. If Z_c is the deflection of the cantilever and Z_p is the height position of the piezoelectric translator (Figure 2.21) (the zero is when the tip of the cantilever just touches the reference cantilever and the cantilevers are not yet deflected) then the spring constant is given by:

$$K_c = k_r \frac{Z_p - Z_c}{Z_c} = k_r \frac{1 - Z_c/Z_p}{Z_c/Z_p} \tag{2.4}$$

Here K_r is the spring constant of the reference cantilever and k_c is the spring constant of the cantilever needed to be calibrated. Practically, Z_c/Z_p is the slope of the force curve obtained on the reference cantilever in the contact regime [293].

Difficulties with this method include the fact that reference levers with spring constants near that of the cantilever to be calibrated must be available. It is obviously also essential that the spring constant of the reference levers is well determined, and care must be taken to position the AFM cantilever so that it contacts the end of the reference lever, therefore the AFM must be
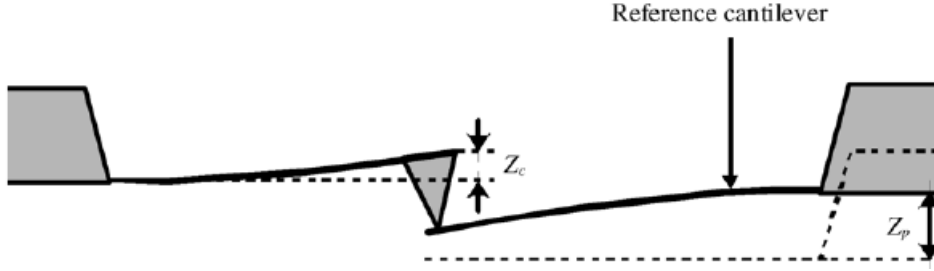
Figure 2.21 – **Calibration against reference cantilever.** The unknown spring constant of a cantilever can be determined by pressing it against a reference cantilever (on the right) and measuring its deflection Z_c for a given movement of the piezoelectric translator Z_p [293].

equipped with good optical imaging system, so that the cantilevers can be well aligned (Figure 2.22).

Figure 2.22 – **Cantilever alignment.** Alignment of the AFM cantilever against the reference cantilever. From [294]

2.8.3.2 Calibration using thermal noise method

Cantilevers are susceptible to fluctuate because of the thermal vibrations from the environment. The thermal noise method is based on measuring this free fluctuations of the cantilever. Therefore, the thermal environment of the cantilever is known, and the deflection of the cantilever can be measured accurately, so the balance between them can be used to calculate the spring constant. In our study, the root mean square of the thermal deflection (RMS) was used for the calibration of the spring constant. For this, the cantilever is suspended away from any solid surface, and a time interval of the deflection signal is registered with the laser ON and with the laser OFF (Figure 2.23). The noise power that is related to thermal noise is given by [295]:

$$(U_{th})^2 = <U_{ON}{}^2(t)>_{rms} - <U_{OFF}{}^2(t)>_{rms} = RMS_{OFF} - RMS_{ON} \qquad (2.5)$$

The reason to acquire data with the laser off is to estimate and subtract electronic noise that is not related to the thermal noise of the cantilever motion. Without substraction, it will be implicitly assumed that all measured noise (that is, also electronic noise) is thermal noise.

The thermal noise method appeals to the equipartition theorem, which states that the energy in any free mode of a system has to be equal to the thermal energy due to the absolute temperature
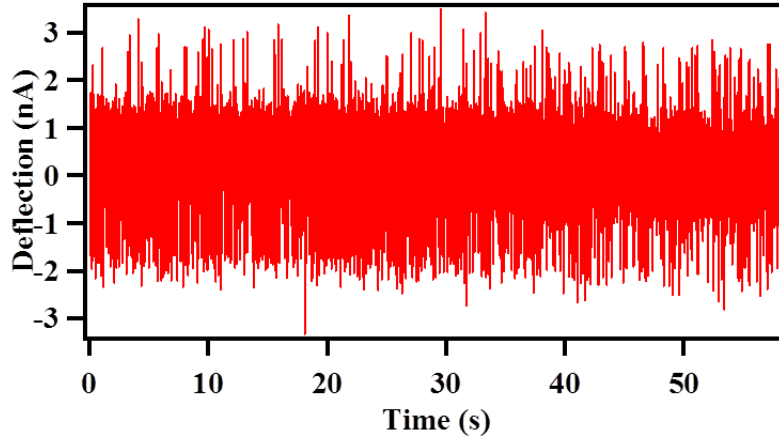
Figure 2.23 – **Thermal noise analysis.**

of the system, $1/2\ K_B$T, where K_B is the Boltzmann constant. The measured energy in the resonance is given by the spring constant and the average value of the vertical deflection of the cantilever, here Z_c.

$$\frac{1}{2}K_B T = \frac{1}{2}K_c < Z_c{}^2 > \tag{2.6}$$

The cantilever elastic constant can then be determined as:

$$K_c = \frac{K_B T}{< Z_c{}^2 >} \tag{2.7}$$

The value of $< Z_c{}^2 >$ can be measured from the Lorentz fit to the frequency spectrum by monitoring the deflection over time and extrapolating the root mean square (RMS) of this deviation.

The primary advantage of the thermal noise method is easy to use, fast, can be made in air or in liquid and actually in-situ during an experiment. The thermal noise method is limited by the sensitivity of the device used to measure the noise in the deflection signal (stiffer cantilever suffer less thermal vibration), and its main drawback is the need of spatial correction factors to take care of special effects from the shape of the cantilever, details of the hydrodynamic damping etc. These factors could shift the accuracy of the spring constant value from 5 to 10% . Despite that, this method remains the best so far.

2.8.4   Force Measurements

In our study, force measurements using AFM were performed in order to determine the surface elastic modulus of cross-linked PDMS samples, to quantify the physiochemical interactions of proteins adhered to different substrates (glass and PDMS substrates), and to measure cell elasticity.

2.8.4.1 Elastic modulus of polymers

The traction or compression elastic modulus, which is also known as Young's modulus , is one of the most important materials properties. It is a number that measures an object or substance's resistance to being deformed (elongated or compressed) elastically when a force is applied to it. For an ideal elastic solid, Hooke's law expresses the Young's modulus, E, as:

$$E = \frac{\sigma}{\epsilon} \tag{2.8}$$

Here, σ is the Stress and ϵ is the strain. **The stress** is the force causing the deformation divided by the area to which the force is applied and **the strain** is the ratio of the change in some length parameter caused by the deformation to the original value of the length parameter that is: $\epsilon = \frac{(L - L0)}{L0}$. It is easy to understand that for the same strain, the larger the stress is, the stiffer the material is the larger the Young's modulus is. According to Hook's law, the elastic modulus is then the slope of the stress–strain curve of an object in the elastic deformation region and is specific for the material under investigation. In force measurement curves, Young's modulus is related to the elastic deformation of the sample in the contact regime during loading and unloading, and the stiffness of the sample is related to its Young's modulus by:

$$K_s = \frac{3}{2} a E_{tot} \tag{2.9}$$

with

$$\frac{1}{E_{tot}} = \frac{3}{4} \left(\frac{1 - \nu_s{}^2}{E_s} \right) + \left(\frac{1 - \nu_t{}^2}{E_t} \right) \tag{2.10}$$

Where ν_s, E_s, ν_t, E_t are the Poisson's ratio and the Young's moduli of sample and tip, respectively. E_{tot} is the reduced Young's modulus, and a is the tip–sample contact radius.

In most cases, the tip is much stiffer than the sample, therefore the deformation of the tip can be neglected and the stiffness K_s can be approximated by:

$$K_s = \frac{dP}{dh} = 2a \left[\frac{E_s}{1 - \nu_s{}^2} \right] \tag{2.11}$$

with P the loading force and h the deformation of the sample under the tip (indentation).

2.8.5 Young Modulus determination

AFM measurements imply nano-metric contact area (A_c) between the AFM probe and the studied samples, although A_c value cannot be measured directly by any imaging technique. Nevertheless, an accurate knowledge of the A_c value is extremely important if quantitative nano-mechanical parameters such as young's modulus are to be measured from experimental data. Several contact mechanics models, can be successfully applied to describe the elastic deformation, as a function of the nature of the sample (i.e. metals, organic bilayers, ceramics, polymers, and others) and the geometry of the tip (define the contact area) [296]. In our study, PDMS samples are homogeneous and have absolute elastic behavior. And the tips we are using have spherical geometry, and there diameter was verified by scanning electron microscopy. Thus, two

models have been chosen to be used:

- Hertz model

- JKR model

The **Hertz** model was developed in 1881 by Heinrich Hertz [297]. It provides with a calculated contact area (A_c) value, it considers both the tip and the sample as two spheres of radius R_1 and R_2 ($R_2 \to \infty$; as the substrate is a flat surface), that when in contact will create a stress that deform the sample. It assumes only that the deformation of the sample is elastic, and depends on the young's moduli of the materials; thus, it does not model the inter-penetration between surfaces during the indentation process nor any adhesion force (F_a) acting between the surface and the AFM tip [296] or any visco-elasticity properties. The interaction force is sketched in Figure 2.24 A.
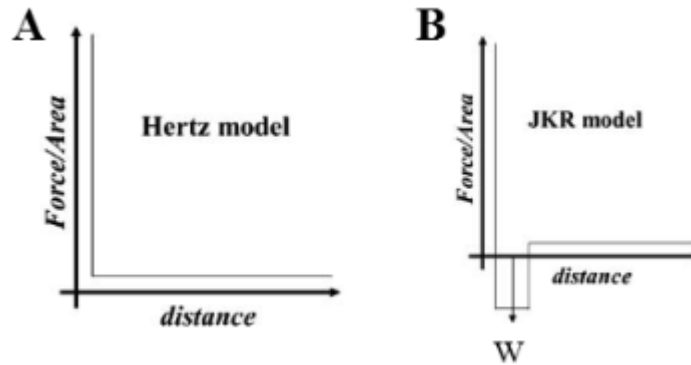
Figure 2.24 – **Interaction forces for A- Hertz, B- JKR model.** Hertz model does not consider any adhesion forces as both surfaces(tip and the sample) come closer. JKR model includes short range adhesion which is a function of the strength of the adhesion work per unit of area necessary to separate the two surface in contact, W [296].

When the maximum adhesive (pull-off) force (F_{ad}) is large enough in comparison with the maximum force (F_{max}) applied during loading, Hertzian analysis is no longer valid and models for adhesive contact of spheres should be invoked. These models include the JKR (Johnson–Kendall–Roberts – 1964-1971) model which is an extension of the Hertz model taking into account adhesive forces. This model applies to tips with large curvature radius and small stiffness (systems strongly adhesive). It accounts for the influence of Van der Waals forces within the contact zone, considers that the work per unit of area (W) (Figure 2.24 B) is necessary to separate the tip and the surface of study, and also that the attractive forces only take place when the two surfaces are in contact and no effect is noticed by the tip as it approaches the sample [296]. The model is applied to the retract curve only, and is valid only when the surface is much softer than the tip (assumption $E_{surface} < E_{tip}$).

Table 2.6 summarizes the relation between the contact radius a, the sample deformation δ, and the adhesion force F_{ad} for a spherical tip on a flat surface according to the Hertz and JKR theories. The young modulus of the sample can be calculated using these models by fitting the

force curve (force vs tip-sample separation) using E as a fit parameter.

	Hertz	JKR
a	$\sqrt[3]{\frac{RF}{E_{tot}}}$	$\sqrt[3]{\frac{R}{E_{tot}}(F + 3\pi RW + \sqrt{6\pi RWF + (3\pi RW)^2})}$
δ	$\frac{a^2}{R} = (\frac{F^2}{RE^2{}_{tot}})^{1/3}$	$\frac{a^2}{R} - \frac{2}{3}\sqrt{\frac{6\pi Wa}{E_{tot}}}$
F_{ad}	0	$\frac{3\pi RW}{2}$

Table 2.6 – **Relation between the contact radius a, the sample deformation δ, and the adhesion force F_{ad} for a spherical tip on a flat surface according to the Hertz and JKR theories.** R is the tip radius and W is the adhesion work per unit area. R is the radius of the spherical tip, F is the force exerted by the tip on the surface, and E_{tot} is the reduced Young's modulus defined in equation 2.5 [293].

In the course of this work, elasticity measurements were performed using AFM (NTEGRA system, NT-MDT,Russia) at room temperature in water. Spherical tips of spring constant stated between 0.02-0.77 N/m (SQUBE surface science support, Germany) were employed with diameter d= 6 μm. The colloidal cantilevers were, cleaned with oxygen plasma (10 W, 2 minutes) before utilization and functionalized with [3-(2-Aminoethylamino)propyl]trimethoxysilane from a gas phase for 15 minutes. The cantilever were then individually calibrated against a reference cantilever, owing a spring constant of 0.35 N/m. At least three samples were tested for each type of substrate and 100 curves were recorded at different locations for each sample, at minimum 4 distinct regions at the sample surface and under the same conditions. The AFM data were collected in term of tip deflection versus piezo-displacement and were analyzed using self-written routines in IGOR-Pro (Wavemetrics, USA), were they are converted to force (nanonewtons) versus tip-sample separation (nanometers), in order to apply the Hertz or JKR model for spherical indentation, and determine the young modulus. The final value of the young modulus, for each sample was obtained from the average of all the curves.

2.8.6 Pull-off force measurements

Pull-off force measurements were performed to determine the interaction between protein (BSA-biotin) and different PDMS and glass substrates. To do that, the AFM tip was first functionalized with the protein of interest, then a force curve was recorded (Figure 2.25). During the force measurement cycle, the tip is brought downward to the surface (approach trace) at constant velocity until it contacts and exerts a positive load on the surface, then it is retracted and moves back to its original position. During this retraction, a downward peak may occur in the retraction curve that indicates adhesion between the tip and the sample. The pull-off force was calculated as the difference between the initial position of the tip and the point where the tip is detached from the sample (Figure 2.25).
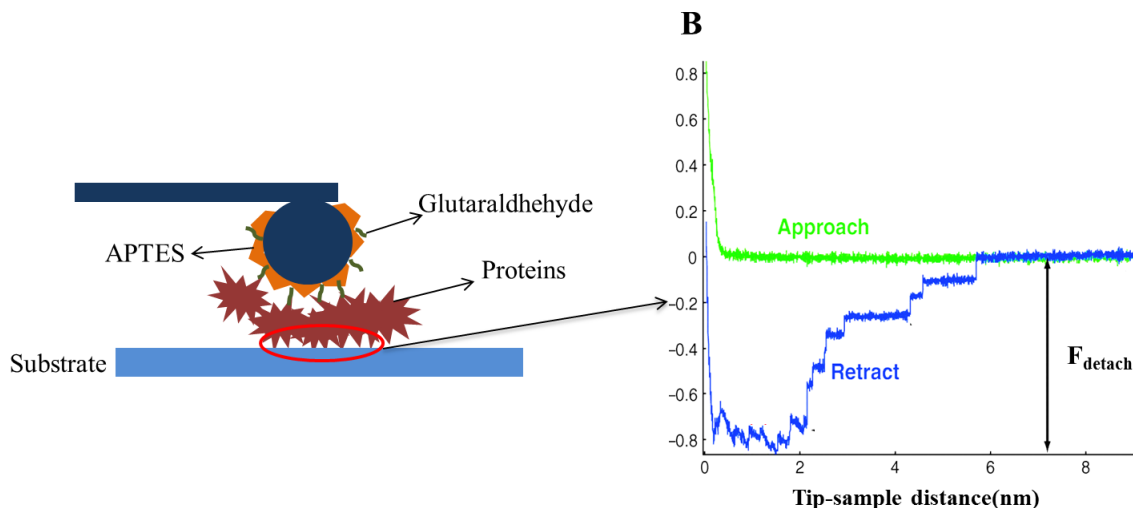
Figure 2.25 – **Principle of pull-off force measurements** A- Schematic representation of the functionalization of the AFM cantilever tip with the protein of interest (fluorescent bBSA). B- Representative curve of force versus distance of separation between the protein tip and the surface of interest during advance and retraction. Adapted from [298].

2.8.6.1   Functionalization of the AFM tip

To perform force measurements, the tips were functionalized with the protein of interest as follows; they were first cleaned/oxidized using an oxygen plasma (10 W, 2 minutes), after which they were functionalized with APTES from a gaz phase for 30 minutes at 70˚C. The amino-silanized tips were then activated by incubating in 0.5% v/v solution of glutaraldhehyde in water for 15 minutes at room temperature, and then carefully rinsed with ultra-pure water. The tips were then finally incubated in a solution of 50 μg/ml of the protein of interest (bBSA-atto or bBSA-TR) for 15 minutes, and rinsed with PBS to remove excess of protein. A schematic representation of the AFM cantilever tip functionalization is shown in figure 2.25 A.

Here, pull-off force measurements were performed using AFM (NTEGRA system, NT-MDT,Russia) at room temperature in air or in water. Spherical tips of spring constant stated between 0.02-0.77 N/m (SQUBE surface science support, Germany) were employed with diameter d= 6 μm. The colloidal cantilevers were individually calibrated using the thermal noise method. At least two samples were measured, and 100 curves were recorded at different locations for each sample at 2 distinct regions and under the same conditions. The AFM data were collected in term of tip deflection versus piezo-displacement and were analyzed using self-written routines in IGOR-Pro (Wavemetrics, USA), were they are converted to force (nanonewtons) versus tip sample separation (nanometers) in order to obtain the pull-off force. The final value of the pull-off force for each sample was obtained from the average of all the curves.

2.8.7 Cell elasticity measurements

AFM force measurements for cell elasticity, were conducted using a JPK Nanowizard atomic-force microscope (JPK Instruments, Berlin) on top of an Axiovert 200 inverted microscope (Carl Zeiss, Jena). The AFM head is equipped with a 15 μm z-ange linearized piezoelectric ceramic scanner and an infra-red laser. The set-up was used in closed loop, constant height feedback mode. Spherical tips of spring constant stated between 0.02-0.77 N/m and diameter d= 6μm (SQUBE surface science support, Germany) were employed. The cantilever was mounted and aligned on the AFM head, and the petri dish containing the adherent cells was placed on the AFM stage, and force measurements were conducted for 15 minutes at room temperature, before cell fixation. The sensibility and spring constant of each cantilever were calibrated prior to each experiment using built-in routines on the JPK software (the sensitivity is calculated by fitting a force curve taken on a hard substrate within the linear contact part, and the spring constant is determined using the thermal noise method). Once the calibration is complete, the desired set point force (the force to be applied to the sample) is entered. The approach and retraction speed were set to 2 μm/s and the maximum indenting force was set to 1 nN to avoid damage to cells. At least 3 force curves were collected for each cell, and at least 10 cells were measured for each sample. The recorded force-distance curve collected during indentation were fitted to Hertz model, using JPK SPM Data Processing 5.0.69 software, to extract information about the local elastic modulus of the cell. All operations were applied to the retraction curve since it normally contains no interaction like adhesion that make a determination of the contact point impossible.

2.8.8 Imaging with Atomic force microscopy

AFM imaging were carried out in tapping mode, in air and at room temperature, using NTEGRA system (NT-MDT, Russia). Silicon tips, NCSC 35 MicroMash, Bulgaria with a typical frequency of 120 KHz and less than 10 nm tip radius were used for imaging funtionalized glass substrates, and CSC 37 MicroMash, Bulgaria, with a typical frequency of 21 KHz,a spring constant stated between 0.35-1.2 N/m and less than 10 nm tip radius were used to image funtionalized PDMS substrates. Images were analyzed using NTEGRA Imaging analysis software packages (Nova 1.1) and were flattened in the scanning direction following standard practice.

2.9 Optical Microscopy

Different types of optical microscopy were used to both image and characterize patterns and to image cells. These include fluorescence based techniques; epi-fluorescence and total internal reflection fluorescence microscopy (TIRF-M), and a reflection based technique; reflection interference contrast Microscopy (RICM).

2.9.1 Epi-Fluorescence

Fluorescence microscopy is a special form of light microscopy that uses high intensity light source which excites a fluorescent species in a sample of interest. This fluorescent species in turn emits

a lower energy light of a longer wavelength that produces the magnified image. Here, epi-fluorescence microscopy was used extensively to image protein patterns fabricated on glass and PDMS substrates.
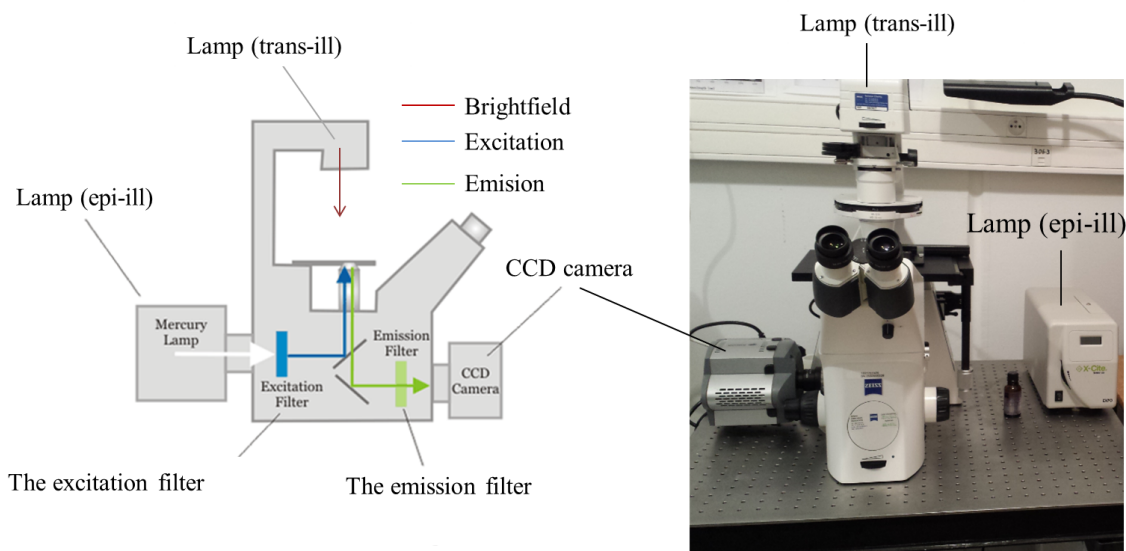
Figure 2.26 – A simple epi-fluorescence system.

A fluorescence microscope is equipped with a light source (usually a xenon arc or mercury vapor lamp) that emits light in a broad spectrum. An excitation filter is placed after the light source to narrows the wavelengths of the incoming light to only those used to excite the sample. The light then impinges on a dichroic mirror (beam splitter) and is reflected down through the objective lens and onto the sample. Fluorophores molecules within the specimen absorb the light and re-irradiate the energy at a longer wavelength, this is fluorescence. An objective lens collect this emitted fluorescent light, which then passes through the dichroic mirror. The reflected excitation light is blocked by an emission filter that transmits only the wavelengths of the emitted light from the sample. Finally, a CCD camera detects the fluorescence imaging and is usually connected to a computer screen, which shows the picture of the image.

In our experiments, epi-fluorescence images were performed using an inverted optical microscope (Axio Observer, Zeiss,Germany) equipped with an EM-CCD camera (iXon, Andor, North-Ireland) (Figure 2.26). Acquisition was performed using Andor IQ software. Excitation was done using a metal Halide lamp XCite 120 (Excelitas Technologies, USA). Epi-fluorescence images were taken using a high magnification oil immersion objectives (100X; N.A 1.4 or 100X; N.A 1.45, Zeiss Germany). For certain experiments (when using dylight fluorophore), another microscope, detailed in section 2.9.2 was used.

Filter cubes (all from Zeiss, Germany) used during imaging with epi-fluorescence microscope are summarized in table 2.7.

Images were done using the following camera settings:

Fluorophore	Filter set	Excitation (nm)	Beam splitter (nm)	Emission (nm)
FITC and Atto 488	17	485	510	515/65
	44	475	500	530/50
Texas red	45	560	585	630/75
	76	561	578	608
Atto 647	77	642	659	688

Table 2.7 – **Filter cubes used during imaging with epi-fluorescence microscope.**

1- For atto 488, FITC or TR dyes:

- Exposure time: 310 ms.

- Electronic gain: 2 or 50.

- Pre-Amp gain: 2.

- Pixel size: 0.08 μm.

2- For atto 647 dye:

- Exposure time: 200 ms.

- Electronic gain: 37.

- Pre-Amp gain: 4 .

- Pixel size: 0.08 μm.

2.9.2   Total internal reflection fluorescence Microscopy (TIRF-M)

Total internal reflection fluorescence (TIRF) is a special technique in fluorescence microscopy developed by Daniel Axelrod at the University of Michigan, Ann Arbor in the early 1980s [299]. TIRF allows us to excite fluorophores in an aqueous or cellular environment very near a solid surface (within $\leq$ 100 nm) without exciting fluorescence from regions farther from the surface [300]. TIRF is based on the surface-associated evanescent electromagnetic field that is created when light is internally reflected at a planar interface between two materials with different refractive indices.

2.9.2.1   Physical basis of TIRF

When light passes through the interface of two transparent media with different refractive indices, it is be partially refracted and partially reflected (Figure 2.27, light blue and yellow). Above a certain angle of incidence, the so-called critical angle, the light is completely reflected and a phenomenon called total internal reflection (TIR) occurs (Figure 2.27 blue and gray). TIR can only be observed if the light travels from a medium with a higher refractive index (n_1) (e.g. glass, n = 1.52) to a medium with a lower refractive index (n_2) (e.g. aqueous medium, n = 1.33) [299][301][302]. The critical angle (θ_c) of incident light, at which total internal reflection occurs, can be determined by Snell's law:

$$\theta_c = sin^{-1}(\frac{n_2}{n_1})$$

(2.12)
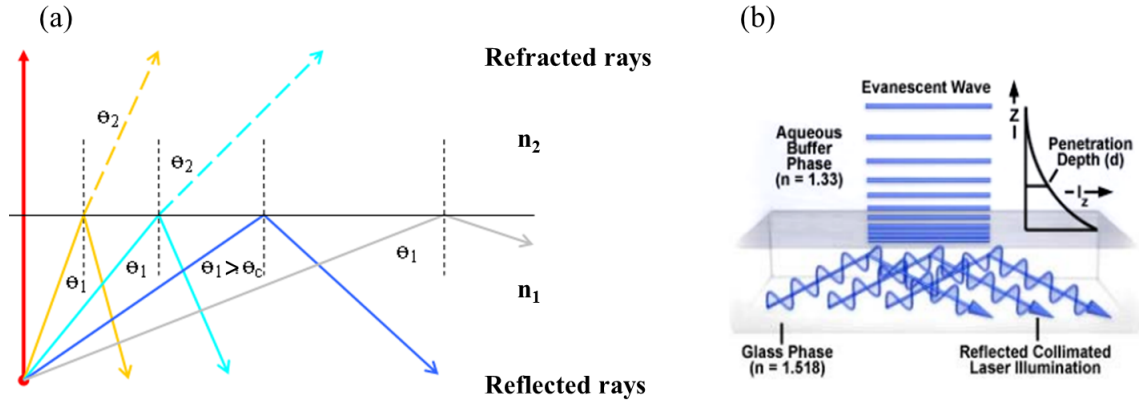
Figure 2.27 – **Representation of light propagating through two transparent media with different refractive indices.**(a) Representation of the reflection and refraction of a beam of light propagating from a medium with a refractive index n_1 to another medium with a refractive index n_2, where $n_2 < n_1$. No refraction occurs at an angle $\theta_1 > \theta_c$. (b) The evanescent wave illumination created in TIRF microscope reaches maximally few hundred nanometer into the specimen and its energy drops off exponentially. Adapted from [303].

In case that the angle of incidence is less than θ_c, most of the excitation light propagates through the sample; this is what occurs in epi-fluorescence. However, in the case of TIR (where $\theta_1 > \theta_c$) some of the incident energy penetrates through the interface, creating an electromagnetic field called the evanescent wave. This is the excitation field employed in TIRF microscopy (Figure 2.27 b). The evanescent wave then propagates parallel to the surface with an intensity I that decays exponentially (the penetration of the light wave is small) with perpendicular distance z from the interface. Therefore, a fluorophore that is closer to the interface is excited more strongly than a fluorophore that is further from the interface. The intensity of the evanescent field at any position z is described by:

$$I = I_0 exp(\frac{-z}{d}) \tag{2.13}$$

where I_0 is the intensity of the evanescent field at z=0; and d, is the depth of the evanescent field. In typical case, d is equal to 200 nm.

TIRF microscope has been intensively used in cell biology [299][300][301][302][304][305][113]. It has the advantage of permitting fast recording of high-definition images of features close to surface, without interference of light from the depth of the sample.

2.9.2.2 Materials and settings

In our experiments, TIRF microscope was essential particularly for imaging TCR and Zap, otherwise out of focus light made imaging impossible. Imaging was performed using an inverted microscope (Axio Observer Z1, Zeiss) equipped with an EM-CCD camera (iXon, Andor, Belfast, North-Ireland), and a laser with wavelength appropriate to the fluorophore used (488 nm, 639nm or 561nm). TIRF images were taken using a high magnification oil immersion objective (100 X;

N.A 1.45; Zeiss, Germany). Filter cubes (all from Zeiss, Germany) used during imaging with TIRF microscope are summarized in table 2.8:

Fluorophore	Filter set	Excitation (nm)	Beam splitter (nm)	Emission (nm)
FITC	17	485	510	515/65
Rhodamine	76 HE	561	578	608
Alexa fluor 647	77 HE	642	659	688

Table 2.8 – **Filter cubes used during imaging with TIRF microscope.**

2.9.3 Reflection Interference contrast Microscopy (RICM)

Currently, RICM is probably the most widely used non-fluorescent technique for imaging cell/substrate contacts. It is an interferometric technique that allows the determination of the vertical distance and of the contact area between the interfaces. RICM was initially devised by Adam Curtis in 1960, to study the interaction of cells with a glass substrate under water by using an optical microscope [306]. He named this technique "interference reflection microscopy" (IRM). Later, in the 1980's Sackmann and co-workers started applying the closely related technique of "Reflection Interference Contrast Microscopy" or RICM and demonstrated that the distances between a planar transparent substrate and optically well defined objects, like a colloidal bead or model membranes for example, hovering over the substrate can be well quantified by RICM [307][308][309]. The main advantage of RICM rely on the simplicity of the set up, as it can be implemented with relative ease and very little investment on a standard inverted microscope and specially, it does not require labeling of the sample.

2.9.3.1 Experimental Setup

A standard version of a RICM set-up consists of a light source, an inverted microscope equipped with an antiflex objective and a CCD camera. The optical configuration of the microscope for obtaining the RICM images is illustrated in figure 2.28. The incident light from a high pressure partially coherent mercury lamp, passes through a filter, a field diaphragm (FD), an aperture diaphragm (AD) that allows variation of the illuminating numerical aperture, and a polarizer, in order to produce monochromatic, linearly polarized incident light. The main beam splitter reflects this light, through the objective, and then through a quarter-wave retardation plate. This optical system converts the light from linearly polarized into circularly polarized light which is subsequently transmitted and reflected by the glass substrate and the object. The reflected light beam passes the quarter wave plate a second time, and becomes linearly polarized, with a switch on its direction of 90°with respect to the incident light. The change on the light direction allows to separate the reflected light by the samples from the stray light reflected on the components of the microscope, by means of crossed analyzer located in front of the detector. Finally, the CCD camera captures the image that represents the periodic variation of the intensity.
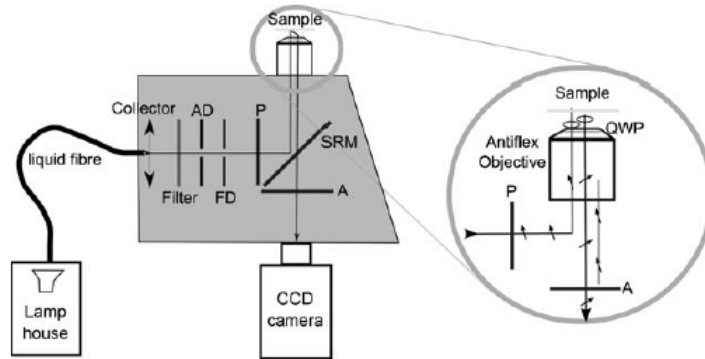
Figure 2.28 – **Typical experimental set-up and optical path for a standard RIC microscope.** AD: aperture diaphragm; FD: field diaphragm; QWP: quarter-wave plate; SRM: semi-reflecting mirror; P: polarizer; A: analyzer. The circular zoom illustrates the polarization of light with the antiflex method [310].
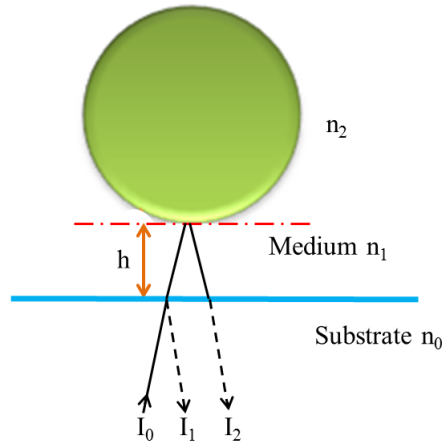
Figure 2.29 – **Schematic representation of the RICM working principle.** I_0 is the incident light, I_1 and I_2 are the reflected lights, h is the distance between the interacting surfaces and n_0, n_1 and n_2 are the refractive indexes.

2.9.3.2 Working principle

The working principle of RICM based on the interference of light reflected from different interfaces, is shown in figure 2.29. If we consider, a monochromatic incident ray I_0, that passes through a glass substrate having a refractive index n_0, then enters a medium having a refractive index n_1, will be reflected at the glass/medium interface to give rise to a transmitted ray I_1. It will then be reflected at the surface of an object of refractive index n_2, to give rise to the ray I_2. Rays I_1 and I_2 interact to create an interference image. The intensity at a given position in the image depends on the separation (h) between the two surfaces (the glass substrate and the object).

Initially, RICM suffered from some limitations, namely low contrast images caused by stray reflections (which come from outside of the test region, blur the fringes and make them difficult to

analyze), unwanted interference with reflections from the cell dorsal membrane and ambiguity between refractive index and substrate separation.These problems were later addressed by using polarization to eliminate unwanted reflections [311], employing a high illumination numerical aperture (NA) to defocus dorsal membrane reflections [312] and by illuminating with two different wavelengths [313] respectively. The approach suggested by Ploem (1975) [311] has been widely adopted, and antiflex objective lenses based on his technique are commercially available.

We used RICM principally to characterize cell adhesion area. In order to form an image of the attached cell, the linearly polarized incident light will be reflected by the glass surface, and then travel into the cell to be reflected by the cell membrane. When the membrane is close to the glass, the reflected light from the glass is shifted by half of a wavelength, so that light reflected from the membrane will have a phase shift compared to the reflected light from the glass phase and therefore interference occurs which results in a dark pixel in the final image. Instead, when the membrane is not attached to the glass, the reflection from the membrane has a smaller phase shift compared to the reflected light from the glass, and therefore they won't cause interference, which results in a bright pixel in the image. We can conclude that, if a cell adheres to the substrate at its periphery, there will be a difference in contrast between the part of the cell that adheres to the substrate (dark pixel) and the part that is not adhering (bright pixel). More the distance between the cell membrane and the substrate decreases, the intensity of the light increases and the pixel in the image is darker. In our study, cells were imaged using the same set up as for epi-fluorescence imaging (see section 2.9.1) in addition with a pre-filters (green 436 ± 17; blue 546 ± 11 nm), and cube composed of two polarizer perpendicularly oriented and a dichroic mirror. Objectives used were custom antiflex oil objectives with 100X; 1.46 NA or standard antiflex oil objective 63X; 1.25 NA (Zeiss, Germany), both of which include a built-in quarter-wave plate (QWP) located in front of the front lens (Zoom in Figure 2.28). The microscope was equipped with a motorized aperture diaphragm. Images were recorded with EM-CCD camera (iXon, Andor, Belfast, North- Ireland). Acquisition was performed using software Zen (Zeiss). Saved images were opened and processed with Image J/Fiji using macros written in-house (see section 2.10.2).

2.10   Image analysis

2.10.1   Analysis of the protein nano-dots images

Epi- fluo images of protein nano-dots on glass and PDMS substrates were analyzed manually or automatically, using a self-written macros in Fiji [S3]/imageJ v1.49d [314] and Igor Pro (Wave-Matrix,USA) software packages. The analysis performed to determine the lateral size of the protein nano-dots, the distance between the dots, the intensity inside and outside the dots, and also to estimate the contrast and the transfer efficiency.

2.10.1.1 Manual Analysis

To characterize the protein nano-dots islands, a radial profile of intensity representing the fluorescent intensity of the dots is realized (Figure 2.30). For this, a line is drawn through several dots of proteins aligned in the image field (Figure 2.30 white line in a), and an intensity profile corresponding to the drawn line is represented (Figure 2.30 b). From this intensity profile, several parameters are determined:

- The distance between two protein nano-dots array which was estimated from the distance between two peaks in the corresponding intensity profile.

- The lateral size or the width of the proteins dot expressed in terms of the diameter of the protein dot, was taken to be the full width at half-maximum of the peaks intensity value.

- The fluorescence intensity inside (I_{max}) and outside the dots (I_{min}), were estimated respectively from the peak of the intensity value for each dot, and the baseline around each dot (Figure2.30 b).
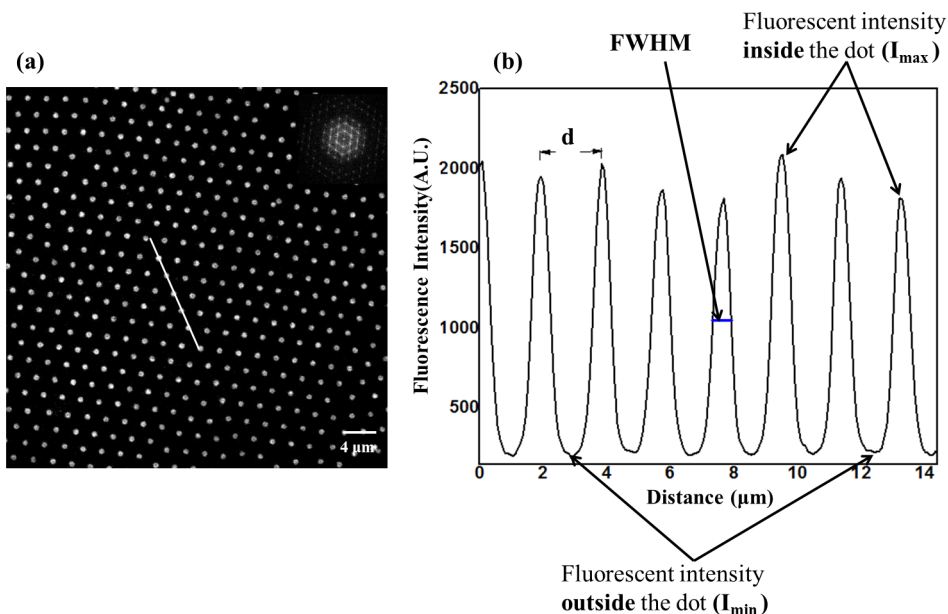
Figure 2.30 – **Manual characterization of the protein nano-dots.** (a) Epi fluorescence image of the proteins nano-dots pattern; inset display Fourier transforms of the image to emphasize the ordering of the lattice. (b) Intensity profile of the line drawn in (a); FWHM is the full width at half maximum, d is the distance between the dots.

2.10.1.2 Automatical Analysis

Each image field, containing hundreds of dots was segmented into appropriately sized windows around each dot and a median dot was constructed (Figure 2.31). The dot size was defined as the full width at half maximum (FWHM) of the intensity profile of the median dot.

The contrast which is a measure of the amount of protein in a dot as compared to outside the
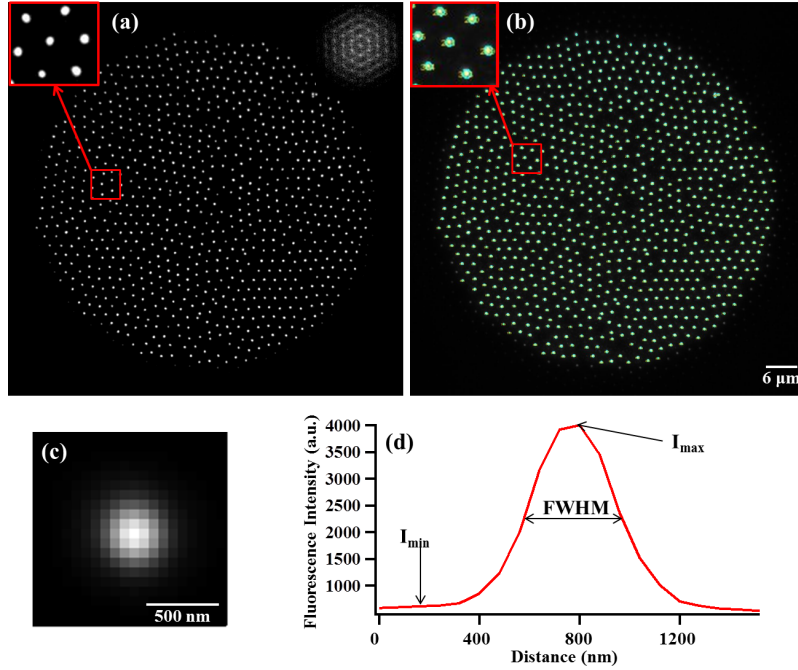
Figure 2.31 – **Segmentation of the dots and building of the median dot for quantification of the dot characteristics.** (a) Raw image with a zoom on a centered hexagonal unit. (b) Green ROIs segmenting the dots obtained by automated intensity thresholding. (c) The median dot obtained for the field. (d) Radial intensity profile of the median dot, indicating the full width at half maximum (FWHM) and the maximum intensity (I_{max}).

dot was also calculated, for this, the peak of the intensity profile (I_{max}) and the base-line around each profile (I_{min}) was calculated for each median dot and the contrast was defined as follow:

$$Contrast = \frac{I_{max} - I_{min}}{I_{max} + I_{min}} \tag{2.14}$$

The transfer ratio was calculated (separately for inside and outside) to estimate the transfer efficiency, and was defined as follows:

$$TransferRatioinside(TR) = \frac{I_{max}(elastomer)}{I_{max}(glass)} \tag{2.15}$$

$$TransferRatiooutside(TR) = \frac{I_{min}(elastomer)}{I_{min}(glass)} \tag{2.16}$$

2.10.2 Analyses of cell adhesion area

Cell adhesion area was analyzed based on RICM images of cells adhered on different surfaces, and using image J/Fiji macro written in house. The macro is based on applying a spatial variance filter with a radius of 8 pixels, followed by a thresholding step, which determines the cell contour and provides an accurate measurement of the contact area. The variance in intensity in the

feature-less background is much lower then the variance with and around the image of the cell. Thus a variance threshold can successfully identify the presence of a cell.
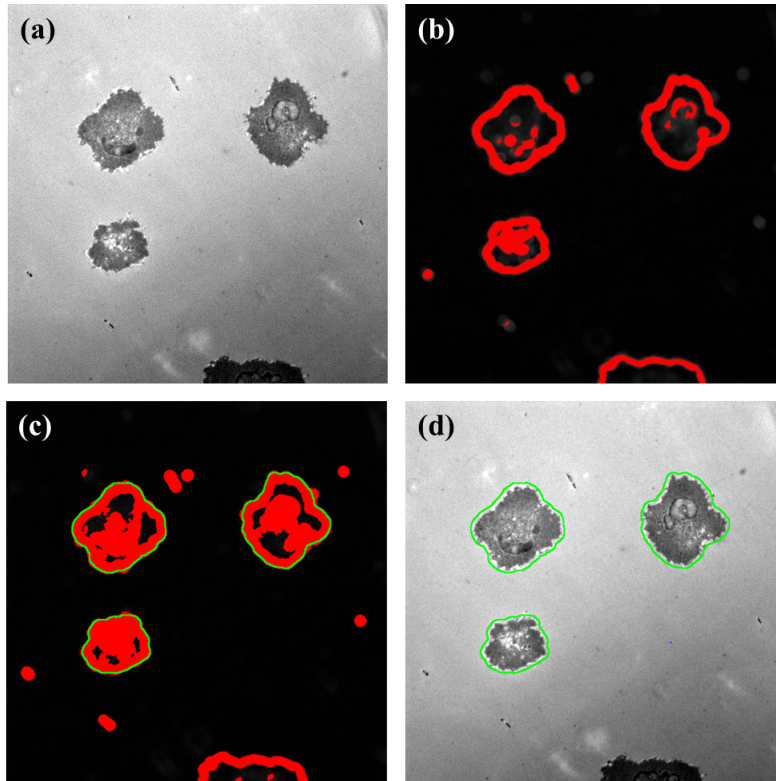
Figure 2.32 – **Steps involved in automatic calculation of cell adhesion area.** (a) The basic RICM image from which the cell-substrate contact region will be segmented. (b) Threshold determining the cell area. (c) Identification of the cell boundary. (d) Superposition of the initial RICM image and the cell boundary identified in (c).

Chapter 3

Patterning Protocol

Abbreviations list of the protein and the PDMS used:

BSA	Bovine serum albumin
bBSA	Bovine serum albumin coupled to biotin
BSA-TR	Bovine serum albumin texas-red conjugated
BSA-FITC	Bovine serum albumin fluorescein isothiocyanate conjugated
Nav	Neutravidin (un-conjugated)
Nav-TR	Neutravidin texas-red conjugated
Nav-FITC	Neutravidin fluorescein isothiocyanate conjugated
Nav-dylight	Neutravidin dylight conjugated
Anti-CD3	Anti-cluster of differentiation 3
bBSA-TR	biotin-bovin serum albumin, texas red conjugated
bBSA-Atto	biotin-bovin serum albumin, Atto 488 conjugated
Sylgard	Sylgard 184 A and B
Q Gel	Q Gel 920 A and B
CY	CY 52-276 A and B
p Sylgard	Sylgard after curing exposed to plasma
p Q Gel	Q Gel after curing exposed to plasma
p CY	CY after curing exposed to plasma
glu CY	CY after curing chemically treated with a process involving glutaraldhehyde
glu Q Gel	Q Gel after curing chemically treated with a process involving glutaraldhehyde

In this chapter, I will report a step by step description of the "reverse contact printing" technique. It consists of transferring protein patterns from glass to PDMS substrates. In brief, a glass cover-slide is chemically patterned with large coverage of nano-scale protein dots via colloidal bead lithography, and is brought in contact with the surface of a flat PDMS layer supported on glass cover-slide by manually applying a homogeneous pressure. After separation, protein pattern on PDMS is obtained.
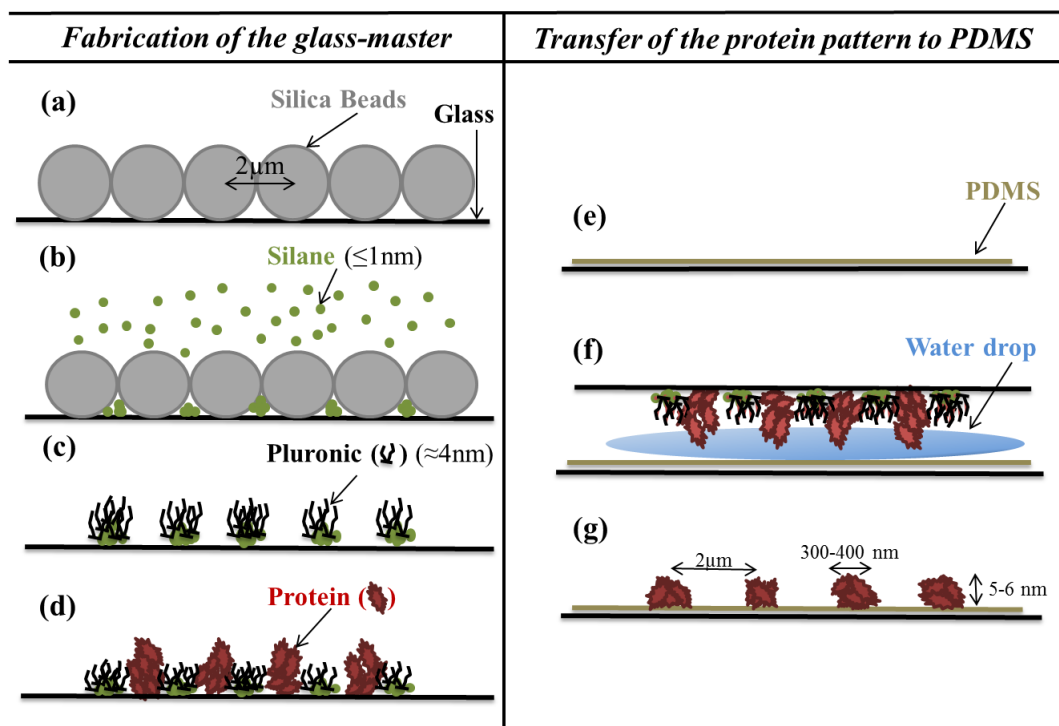
Figure 3.1 – **Schematic representation of the fabrication of protein nano-patterns on glass and soft substrates.** (a) Self-assembly of the colloidal bead mask on glass substrate. (b) Deposition of fluorosilane (PFOTCS) molecules from a gas phase through the bead mask. (c) Removal of the bead mask and grafting of a poloxamer (pluronic) to passivate the fluorosilane covered area. (d) Functionalization of the bare patches with the desired protein. (e) Thin layer of elastomer supported on glass cover-slide. (f) Transfer of the protein patches from glass to elastomer by "reverse contact printing" in presence of water. (g) Protein pattern on the elastomer.

3.1 Fabrication of pattern on glass master

In this section the steps required to make the protein nano-pattern on a glass substrate are described. Figure 3.1 (a-d), schematizes the protocol. In brief:

- A bead mask is formed on a cleaned glass cover-slide (a).
- The fluorosilane (Trichloro(1H,1H,2H,2H-perfluorooctyl)silane (see section 2.2), called (PFOTCS) is deposited through the bead mask from a vapor phase (b).
- On removal of the bead mask, the substrate is patterned with holes surrounded by a sea of

hydrophobic silane, which is then passivated with pluronic (see section 2.4) (c).

- The holes are filled with the protein of interest (d).

3.1.1 Fabrication of the colloidal bead mask

Suspension of silica colloidal bead micro-spheres with 2μm diameter was concentrated into 2:1 (v/v) with ultra-pure water and washed as follow:

- 1 ml of the bead suspension was placed in centrifuge tube.
- The tube containing the beads was centrifuged at 2000 rpm for 4 minutes to clear the supernatant.
- The supernatant were removed and discarded from the tube.
- The beads were resuspended in water and vortexed to re-disperse.
- This steps were repeated 6 times.
- The beads were cleaned and ready to be used.
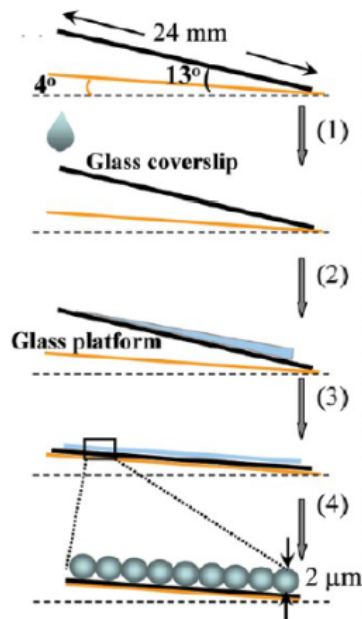
Figure 3.2 – **Steps of the colloidal bead self-assembly on glass substrate.** In step (1) a glass cover-slide is set at a controlled angle. In steps (2) and (3); a drop of the beads suspension is allowed to spread on the glass cover slide until it attends the bottom of the slide. In step (4) the edge angle of the glass cover-slide is decreased [215].

A glass platform with edge angle of 4° was placed on a standard laboratory work bench under ambient conditions. Then, a glass cover-slide, washed as described in section 2.1, was set on the platform at an angle of 13°. A 80 to 100 μl drop of washed silica suspension is allowed to spread on the cleaned glass substrate under gravity. When the spreading front of the suspension reaches the bottom of the glass cover-slide, we decrease the edge angle of the glass cover-slide to 4°, and we turn the glass cover-slide 90° from its position, every 10 seconds, 4 times. This is done to facilitate uniform spreading and prevents formation of multilayers or clusters. Decreasing the

edge angle and turning the glass cover-slide cause a back flow of the suspension which carries some of the beads and fill the defects formed during the first step. The slide is then kept on a plane surface for around 45 minutes, at room temperature to let the water evaporate. After drying, a large coverage area of ordered array of beads with a characteristic distance between neighboring beads (corresponding to the diameter of the beads) is generated. Figure 3.2 shows the steps of the colloidal bead self-assembly on the glass substrate.

The quality of the monolayer in terms of uniformity and the area covered, is influenced by the following factors:

- The hydrophilicity of the glass substrate which enables the liquid drop of beads to spread due to the high surface energy.

- The concentration and the volume of the micro-spheres suspension, which play a key role for particle absorption before draining and prevent formation of multilayers of beads after drying.

Figure 3.3 shows an example of the bead mask obtained, visualized with optical microscopy in transmitted light, using a 100X, 1.4 N.A. oil objective.
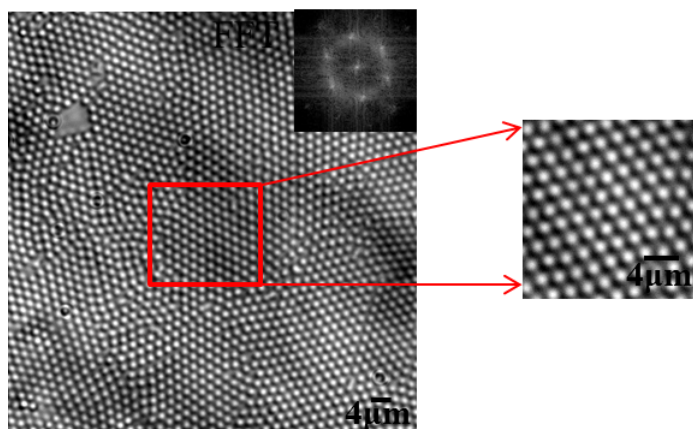
Figure 3.3 – **Optical microscopy (transmission bright-field) image of 2 μm silica colloidal bead mask on glass substrate.** Inset displays the Fourier transform of the image to emphasize the ordering of the lattice.

3.1.2   Silanization with PFOTS via Vapor Deposition

The colloidal bead monolayer served as a mask to deposit organosilane molecules on the glass cover-slide from a vapor phase. The silanization procedure was done with PFOTS by vapor phase deposition (VPD). High quality monolayers are known to be easier achieved by this technique in comparison from a solution [315]. This can be done by increasing the percent partial pressure of the organosilane within a closed system, achieved either by heating a closed container or by lowering the base pressure using a vacuum pump with an open source of the liquid organosilane inside. The organosilane is then deposited via chemisorption.

The VPD was performed as follows (Figure 3.4):

Figure 3.4 – **Schematic set-up of silanization procedure.** Vapor phase deposition of PFOTS by increasing the percent partial pressure of the organosilane within a close chamber (desiccator).

- Around 200 μl of PFOTS was placed in a petri dish in the bottom of the desiccator under the sample holder.
- The substrates with the bead monolayer were put on the sample holder.
- The desiccator was closed and connected to a vacuum pump.
- The system was pumped to approximately 100 mTorr, for around 30 minutes.
- The pump was shut, retaining the vacuum inside the desiccator.
- The system was placed on a hot plate and heated for one hour at 35°C, to maintain a constant temperature during deposition.
- The desiccator chamber was opened, and the silanized substrates were stored in a clean environment until the next step.
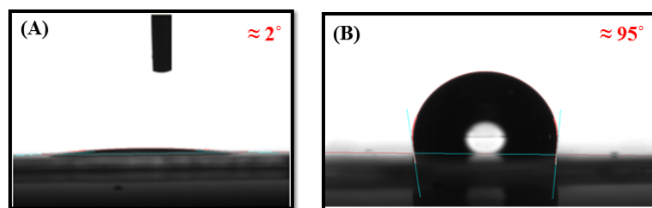
Figure 3.5 – **Water contact angle measurements on glass substrates.** (A) After cleaning with surfactant (before the silanization step). (B) After silanization with PFOTCS.

During the process of chemisorption, the trichloro-silane group of PFOTS reacts with trace amount of water to form intermediate silanol groups, which then react with the free hydroxyl groups on the glass surface, to covalently immobilize the organosilane. As a consequence of the

successful deposition of PFOTCS on the glass, the surface becomes hydrophobic, due to the presence of the heavy fluorinated tail group of the PFOTS (see section 2.2). This was tested by measuring the contact angle of a droplet of water on the silanized glass cover slide. Figure 3.5 (B) shows that the cover slide was rendered hydrophobic with a contact angle $\simeq 95°$. After the deposition of PFOTCS, the colloidal bead mask was removed by ultrasonic agitation of the glass cover-slide in water for 3 seconds, and the success of the silanization step was characterized at the molecular level, by imaging the glass substrate (after the removal of beads), using tapping mode AFM in air.

Figure 3.6 (a,c), shows the topography of the PFOTCS structures presenting nearly perfect ring shape with a spacing of 1.9 ± 0.1 μm between two rings corresponding to the size of the beads used (2 μm). Figure 3.6 (b,d), shows a zoom on a single ring and the corresponding height profile showing a distance of 250 ± 20 nm between the two peaks. These images show that the silane is preferentially grafted in a form of multi-layers along the line of contact between the bead and the glass cover-slide, thus forming rings. It is also expected to be grafted everywhere outside the ring (as indicated by the shading in figure 3.6 d) though the thin layer outside the ring is not clearly detectable here.
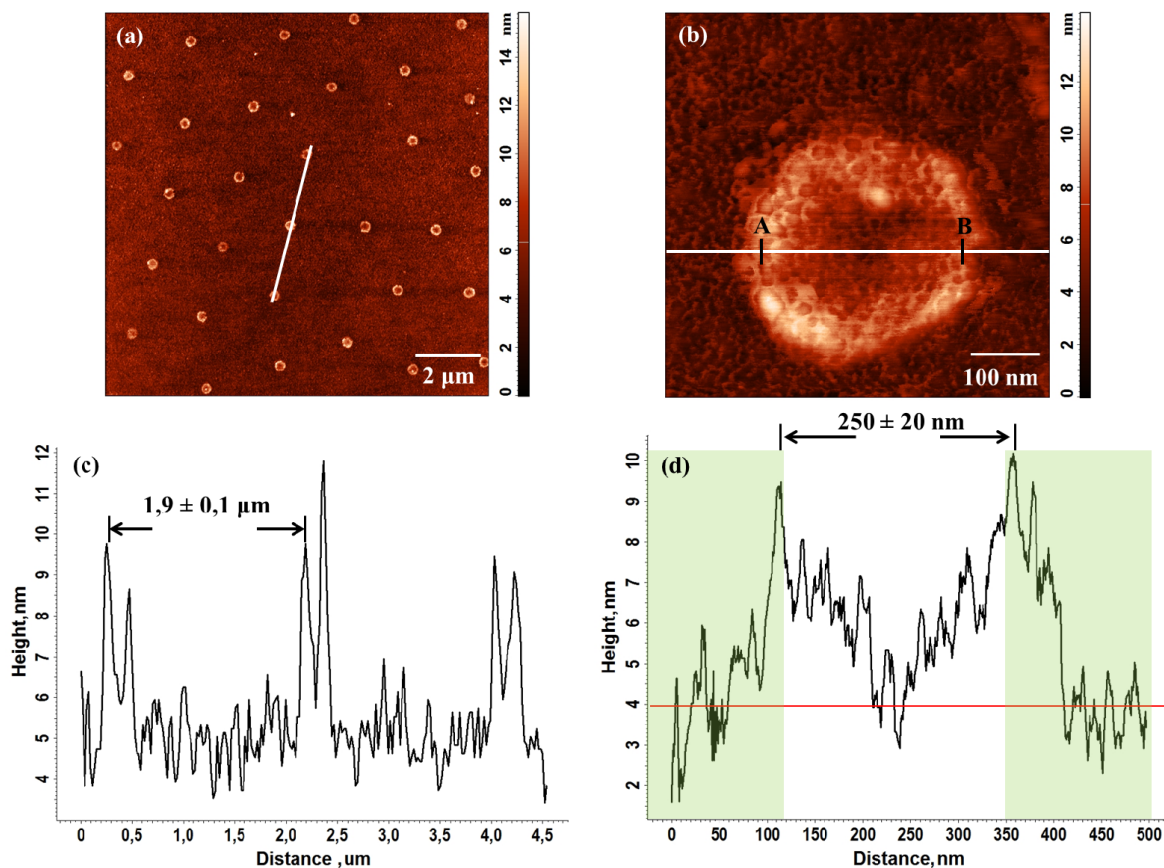
Figure 3.6 – **AFM imaging and analysis, corresponding to the grafting of PFOTCS.** (a) Tapping mode AFM image (in air) after PFOTCS grafting. (b) Zoom-in image of a single circle. (c,d) Corresponding height profile of the line drawn in a and b respectively.

3.1.3 Pluronic grafting and protein patterning

At the step of beads removal, the substrate is patterned with holes to the bare glass surrounded by a sea of PFOTCS. To proceed further with the functionalization, pluronic chains are grafted to PFOTCS, by incubating the silanized glass cover-slide in 1 ml of pluronic F68 10%, for one hour at room temperature, then rinsing three times with PBS solution. The pluronic copolymer will adsorb on the surface by interaction between its middle apolar polypropylene oxide segments (PPO) and the hydrophobic fluorinated tail group of the silane (PFOTCS). The polyethylene oxide segments (PEO) of the pluronic interact with water molecules and extend to the bulk aqueous solution. Pluronic will therefore acts as a blocking agent to reduce or eliminate non specific protein binding in the subsequent step of protein adsorption. The adsorption of pluronic to the chemically nano-patterned substrate produced defined regions with protein-adhesive and protein-rejecting characters. The protein repellent properties of pluronic have been reported in a number of studies [316] [317].

To demonstrate this concept, we functionalized the glass cover-slide, after the pluronic depo-

sition, with Nav-TR. Thus, it was incubated in 300 μl of 4 μg/ml Nav-TR for 30 minutes at room temperature, then rinsed 10 times with PBS. The protein molecules were directly adsorbed only on patches of bare glass corresponding to the contact sites of the micro-spheres in the original mask, thus forming an array of well organized protein patches corresponding to the original pattern of the silica beads micro-spheres. This can be seen in figure 3.7 a, which is an epi-fluorescence image of the Nav-TR pattern on glass. The white dots are the proteins and the black background corresponds to the pluronic. We can see from the intensity profile in figure 3.7 b, a distance of 1.89 $\pm$ 0.09 μm between two peaks, corresponding to the distance separating two dots of proteins, and matching well the diameter of the colloidal beads used (2 μm). We can also determine from the intensity profile, the proteins dot size, here 450 $\pm$ 40 μm as calculated from the full width at the half maximum of the intensity trace.
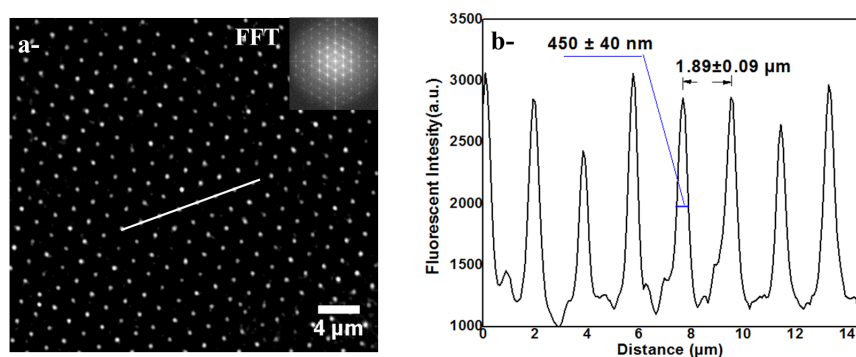
Figure 3.7 – **Epi-fluorescence images of protein pattern (Nav-TR) on glass substrate.** a- Epi-fluorescence image. b- Corresponding intensity profile of the line drawn in a. Inset display the Fourier transform indicating the ordering of the pattern.
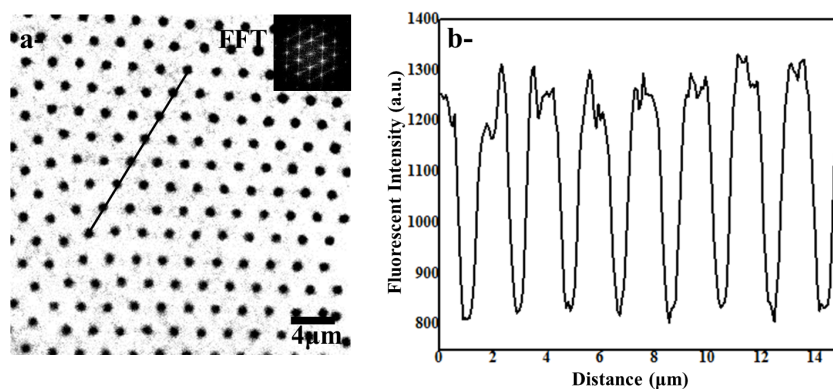
Figure 3.8 – **Epi-fluorescence images of proteins (Nav-TR) without the pluronic grafting step.** a- Epi-fluorescence image. b- Corresponding intensity profile of the line drawn in a. Inset display the Fourier transform indicating the ordering of the pattern.

In a separate experiment, the success of the pluronic binding step was tested. For this, all the steps of the protocol from the beads spreading to the functionalization with protein (Nav-TR),

were repeated, but this time without the pluronic grafting step. We obtain an inverted protein pattern (the protein molecules are everywhere on the silanized glass but not in the holes) as is seen from the epi-fluorescence image in figure 3.8. In fact, proteins are known to easily adsorb to hydrophobic surfaces. In the absence of pluronic, the presence of the fluorinated tail of the silane in between the holes, offers an hydrophobic surface attracting the proteins. In fact, the amount of protein going to the hydrophilic surface is much less then the massive amount going to the hydrophobic zones. Therefore, the hydrophilic dots look dark in a sea of bright background.
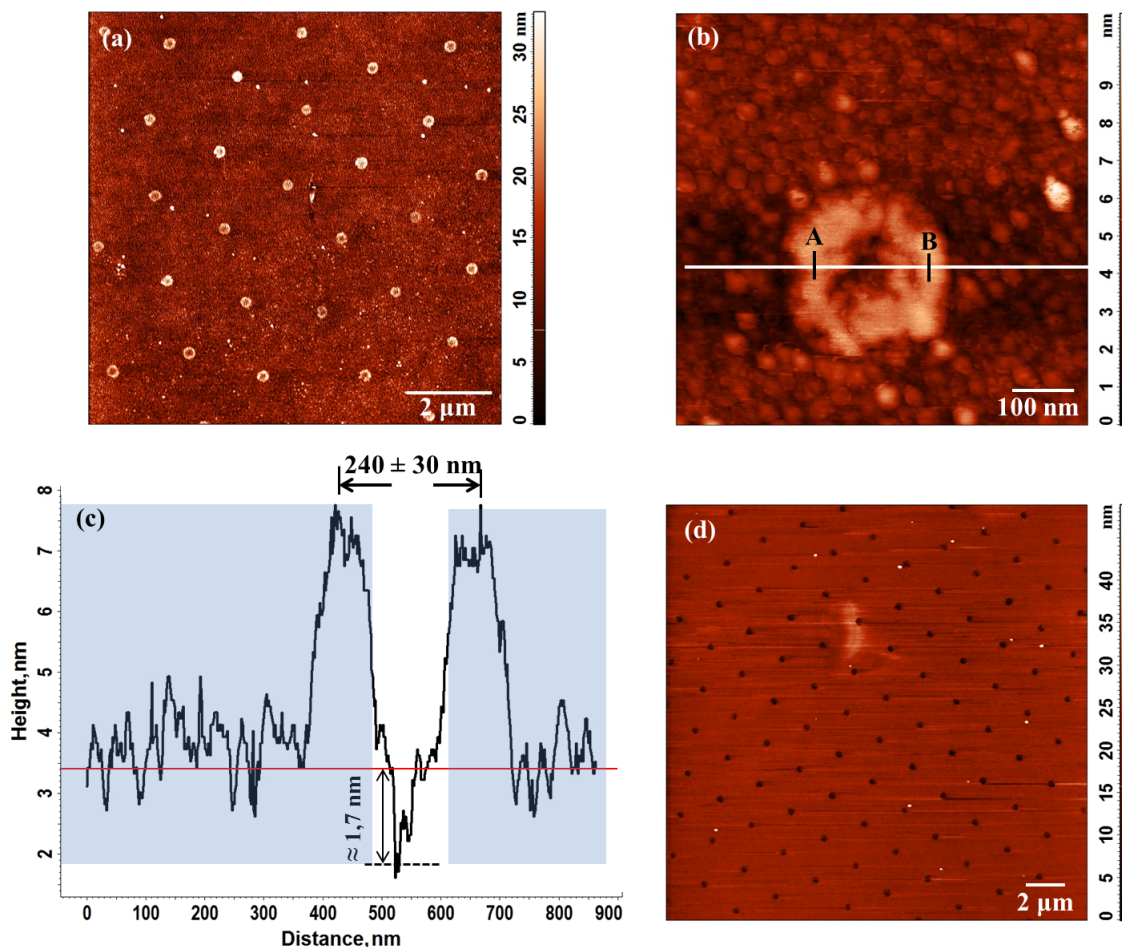
Figure 3.9 – **AFM images corresponding to the grafting of pluronic on the PFOTCS layer.** (a) Tapping mode AFM image (in air) after pluronic grafting. (b) Zoom-in image of a single circle. (c) Corresponding height profile of the line drawn in b. (d) Tapping mode AFM image (in water) after the pluronic grafting step.

To characterize the binding of pluronic at the molecular scale, AFM images in air were effectuated after the pluronic grafting step (Figure 3.9). Figure 3.9 (a,b), shows the presence of the ring shapes with a distance of 1.85 ± 0.1 μm corresponding to the pitch of PFOTCS ring array, and also to the diameter of the beads used (2 μm). The relative elevation of the area outside the ring (shading in figure 3.9 c) indicates successful pluronic grafting. The diameter of a single

ring is measured to be 240 ± 30 nm (Figure 3.9 c), and is in correlation with that found after the silanization step (250 ± 20 nm, Figure 3.6 d).

The pluronic grafting step was also imaged in water (Figure 3.6 d). The image shows perfect circular holes. No ring shape is observed as compared with the image taken in air.
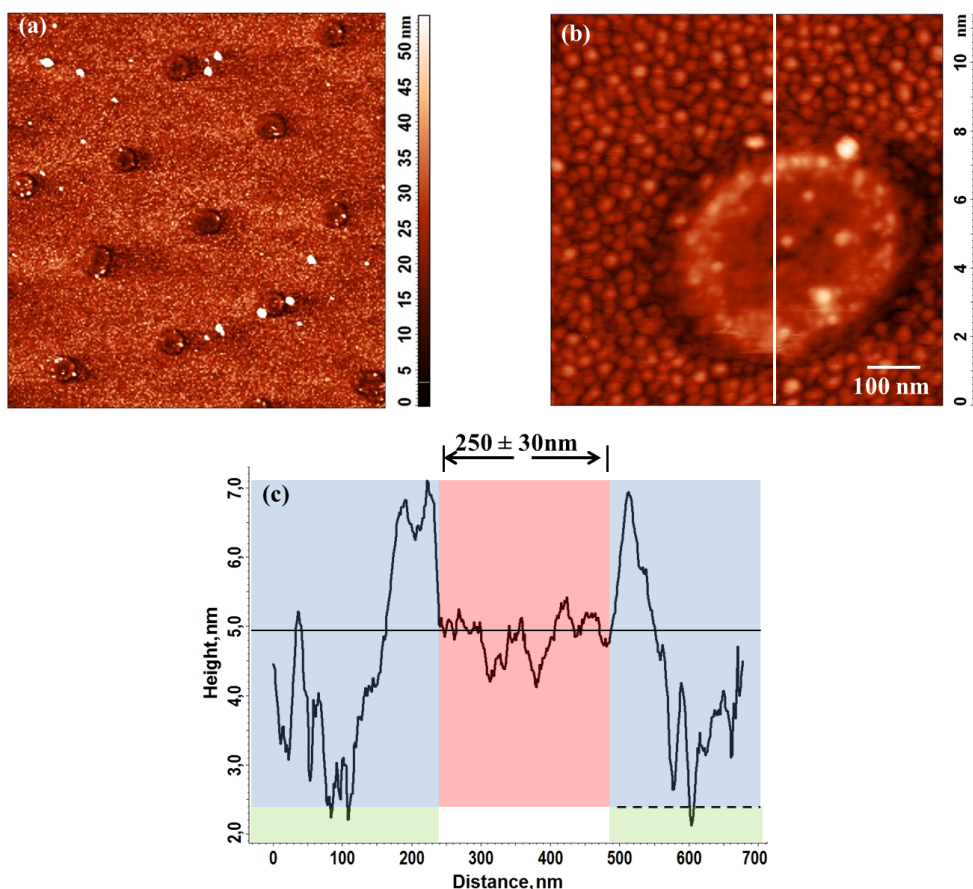
Figure 3.10 – **AFM images corresponding to the protein grafting step.** (a) Tapping mode AFM image (in air) after protein grafting. (b) Zoom-in image of a single patch. (c) Corresponding profile of the line drawn in b. Black line indicates the protein level, and black dashed line the height of pluronic grafted on PFOTCS.

Finally, the final step of the Nav-TR protein grafting was also imaged with AFM in air (Figure 3.10). The elevation of the level of the interior of the ring (shading in figure 3.10 c) indicates successful grafting. First, the height profile represented in figure 3.10 (c), shows a lateral size of the protein equal 250 ± 30 nm, measured as the distance between the two edges of the protein patch, and corresponds to the diameter of the protein. The black dashed line indicates the height of pluronic grafted on PFOTCS, and the black line indicates the Nav protein grafted on glass.

The technique of fabrication of the protein nano-pattern on glass substrates was validated for

several types of proteins (BSA-FITC, BSA-TR, bBSA, Nav-TR, Nav-FITC, fibronectin, bBSA-TR, bBSA-Atto), and for different types of pluronic (F-127, F-108 and F-68) used at various concentration (see section 4.4).

3.1.4 The use of the protein patterned glass substrates

The protein patterned glass substrates fabricated as described above, were either functionalized for experiments on T-cell adhesion (section3.1.4.1) or used as master for transfer of the pattern to the surface of elastomer (PDMS) substrate (section 3.2).

3.1.4.1 Functionalization of the protein patterned glass for T-Cell experiments

The protein patterned glass substrates were further used as support for experiments on T-lymphocytes adhesion. For that, glass patterned with bBSA-TR was fabricated as described in section 3.1, rinsed several times with PBS to eliminate excess of protein, then functionalized with 800 μL of non-fluorescent Nav at a concentration of 4 μg/ml for 30 minutes at room temperature, followed by 10 times washing with PBS, and incubation in 800 μl of 2 μg/ml anti-CD3 multi-biotinylated for 30 minutes at room temperature, and finally, thoroughly rinsed with PBS.

3.2 Patterning PDMS by Reverse Contact Printing

In this section, we will trace the "reverse contact printing" mechanism, consisting of the transfer of the protein nano-pattern created on glass (as described section 3.1), to the surface of native or functionalized silicone PDMS elastomer. We will start by describing the preparation of the PDMS substrate, followed by its surface modification. We will then report the transfer mechanism, and finally the functionalisation of the patterned PDMS substrate for experiments on T-cell.

3.2.1 Preparation of the PDMS layer

The various steps for obtaining the PDMS layer are described in detail in section 2.3 and appendix A.1. In brief a cleaned glass substrate is coated with a thin layer of PDMS by spin coating, and then cured appropriately. The thickness of the PDMS layer depends on the PDMS type and mixing ratio of the base and curing agent constituting the PDMS. We obtained a thickness of 8 $\pm$ 1 μm (Table 2.2). The PDMS substrates are used either native or in a certain experiments functionalized, as target surface for the protein transfer. Three types of PDMS were used, CY, Sylgard and Q gel (see section 2.3 for details).

3.2.2 Surface modification of PDMS

In some experiments, PDMS was oxidized by oxygen plasma treatment (see section 2.3.4) and either used directly or was subjected to a chemical treatment following the plasma.

3.2.2.1 Chemical treatment

In some experiments, PDMS substrate was chemically funtionalized in order to create an attractive surface for the proteins where strong and stable covalent linkage of the protein to the PDMS surface can be induced. For this, PDMS substrate was activated by oxygen plasma as described in section 2.3.4, creating free hydroxyl (OH) groups on its surface. The oxidized PDMS was then treated for 10 minutes with 10% (v/v) solution of APTES in absolute ethanol. Finally, the APTES treated PDMS was rinsed with 96% ethanol, dried, and functionalized with 8% (v/v) solution of glutaraldhehyde (called Glu) (1.06g/mL) in ultra-pure water, for one hour at room temperature, carefully rinsed using MQ water. In fact, APTES will bound to free OH groups on the PDMS, leaving primary amine (NH_2) groups on the surface. Glutaraldehyde is then subsequently used to reacts with the surface amine group, yielding an imine linkage (C=N) with one end aldehyde group in glutaraldehyde. The other end aldehyde group will reacts with the amine group in the protein by elimination of a water molecule (Figure 3.11). Surface treatment
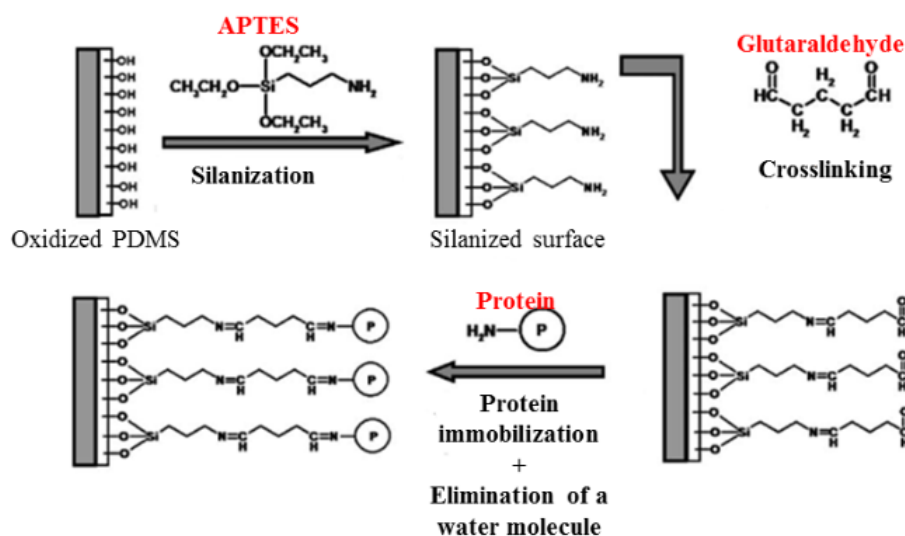
Figure 3.11 – **Schematic representation of PDMS surface modification.** Oxidized PDMS surface is chemically silanized with APTES, and then activated with glutaraldhehyde for subsequent functionalization with protein. Adapted from [318].

of PDMS with APTES and Glu was frequently reported [39][318][319][320]. It was demonstrated that this functionalization reduces the hydrophobicity of the native PDMS, minimizes the direct and weak interactions of proteins with the PDMS surface and overcomes the steric hindrance from the vicinity of the support, which is essential for stronger protein attachment.

3.2.3 Transfer

The protein patterned glass cover-slides described in section 3.1, were used as "masters" to transfer the protein patches to the surface of a thin layer of PDMS . The printing of the pattern from the glass to the PDMS substrate was performed in two steps (Figure 3.1 e-g):

- The patterned glass was brought in contact with the PDMS substrate wetted by a thin water layer, through adding a drop of water onto the PDMS surface (more details in section 4.2.2.3). When the two substrate in contact, a manual moderate pressure was applied. The pressure was seen to be robust and not very sensitive since the mechanism was tried by several experimenter.
- The two surfaces were left in contact overnight and separated the following day.
After separation, the protein pattern was transfered to the PDMS surface, and epi-fluorescence images were done to asses the quality of the transfer.

Different types of proteins (Nav-TR, bBSA, BSA-FITC, bBSA-TR, bBSA-Atto 488; see list of abbreviation at the beginning of chapter 3) were transfered to different PDMS substrates, the mechanism and the conditions governing the transfer will be depicted in the chapter 4.

3.2.4   PDMS controls for T-cell study

In addition to patterned PDMS, the followin substrates were used as controls for cell studies.

Positive Control (POS)
The patterned PDMS substrates were further used as support for pilot experiments on T-lymphocytes adhesion. For that, PDMS patterned with bBSA-TR was fabricated as described in section 3.2.3, then incubated in 800 μl of pluronic F-127 1% (v/v) in water for 30 minutes at room temperature in order to block unspecific protein adhesion. It was then rinsed three times with PBS, functionalized with 800 μL of Nav-dyelight or non-fluorescent Nav at a concentration of 4 μg/ml for 30 minutes at room temperature, followed by 10 times washing with PBS, and incubation in 800 μl of 2 μg/ml anti-CD3 multi-biotinylated for 30 minutes at room temperature, and finally, thoroughly rinsed with PBS.

Negative Control(NEG)
For patterned substrates, negative control was performed as follows:
- Incubate 800 μl of F 127 1% on the native PDMS substrate for one hour at RT.
- Rinse 5 times with PBS.

Chapter 4

Characterization and Mechanism of the transfer process

In the previous chapter, I introduced the reverse contact printing protocol, which can transfer pattern of proteins adsorbed onto a glass surface to a variety of PDMS surfaces. To further investigate the efficiency of the patterning technique that I developed, I will begin by characterizing the different PDMS substrates used in this protocol, in term of chemical structure, wettability and elasticity. Then I will describe the transfer of different proteins on a variety of PDMS substrates in terms of dot size, contrast (before and after the transfer) and transfer ratio. I will finish by proposing a molecular mechanism governing the protein transfer.

4.1 Characterization of PDMS substrates

As I already presented in section 2.3 and 3.2, various types of PDMS materials with great variability in surface properties (Sylgard 184, Q Gel 920 and CY 52-276), were used in this work. This section will be dedicated to describe the differences between this three types of PDMS in terms of wettability and elasticity.

4.1.1 Contact angle measurement on PDMS

Contact angle of a water droplet on PDMS was measured 30 minutes after substrate preparation, with the sessile drop method (see section 2.3.6). Table 4.1 summarizes the water contact angle values obtained for the different samples.

The water contact angle of the different native PDMS substrates were 104°, 116° and 122° for Sylgard, Q Gel and CY respectively (Figure 4.1 a-c). Therefore PDMS can be considered as having an hydrophobic surface. The CY shows the highest contact angle.

	Native	Plasma treated
Sylgard (10:1)	104° ± 4	3° ± 1
Q Gel (1:2)	116° ± 4	35° ± 6
CY(1:1)	122° ± 3	13° ±3

Table 4.1 – **Water contact angle measurements of different native and plasma treated PDMS samples.**

Contact angle measurements were also done following the surface modification of the PDMS substrates with oxygen plasma (see section 2.3.4). Measurements show a decrease in the contact angle value as follows, 3°, 35° and 13° for Sylgard, Q Gel and CY respectively (Figure 4.1 d-f). This can be related to the fact that during oxygen plasma treatment, methyl groups at the surface of PDMS are removed and replaced by chemical species like hydroxyl groups, which are negatively charged dipoles producing an hydrophilic behavior of the surface (see section 2.3.4). Given that, water is a dipole with certain affinity to the hydroxyl groups and therefore the drop formed on the modified PDMS surfaces exhibits a smaller contact angle [321].

4.1.1.1 Interpretation

Given the differences in the composition of the different PDMS types (CY, Q Gel and Sylgard) elucidated in section 2.3.3, we hypothesize that the increased contact angle of the native Q Gel
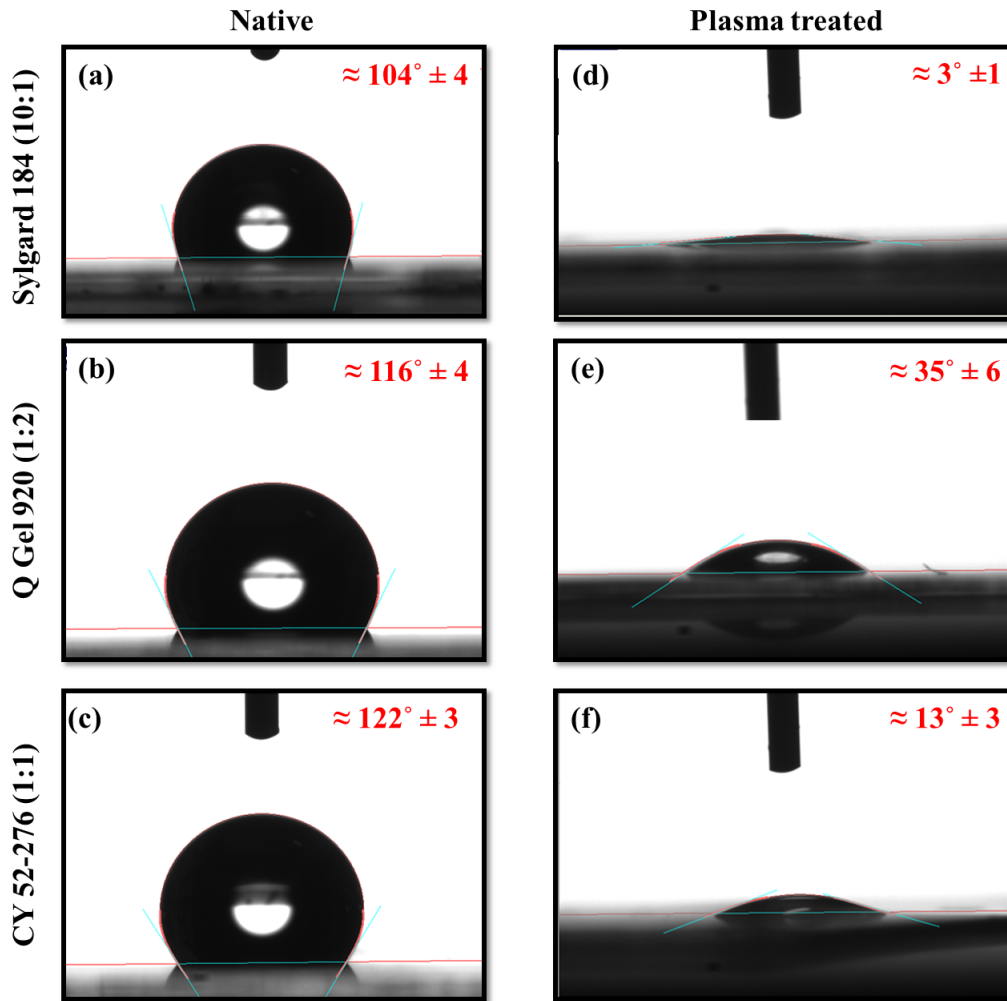
Figure 4.1 – **Droplet contact angle on different PDMS substrates.** On native (a-c), and plasma treated (30W, 15 seconds) (d-f), sylgard, Q Gel and CY respectively.

(116°± 4) in comparison with the native Sylgard (104°± 4) noticed in section 4.1.1, is due to the presence of phenyl groups in the Q Gel chains. This groups are non polar hydrophobic groups. The contact angle obtained for the plasma treated Q Gel (35°± 6), corresponding to the highest hydrophobicity among all the treated PDMS studied, can be attributed to the fact that the phenyl groups present in the Q Gel tend to resist oxidation [322]. Finally, in the case of CY (122°± 3), which is more hydrophobic than the Sylgard (104°± 4), it needs more plasma power for the same exposure time or vice-versa, to obtain a wettability compared to the plasma treated Sylgard. However, for the same plasma power and exposure time, plasma treated CY exhibit a higher contact angle in comparison with the treated Sylagrd.

4.1.2 Elasticity measurement

AFM nano-indentation experiments were performed on the different PDMS substrates under water. All the values reported are averages from measurements done on at least three samples for each type of substrate, and 100 curves were recorded at different locations for each sample, at minimum 4 distinct regions at the sample surface and under the same conditions, in order to determine the Young's modulus. The data obtained from the nano-indentation experiments were fitted with the Hertz (in case of no adhesion) or JKR (in case of adhesion) model (see section 2.8.5). The contact point was chosen to be at zero distance from the sample, thus, the point where the force begins to increase.

4.1.2.1 Indentation Depth

One of the major problem for elasticity measurement in the case of a soft and thin sample is that the AFM tip can largely compress the sample, and "feel" the underlying stiff substrate. Consequently, the extracted Young's modulus is increased and the sample appears stiffer than it is in reality. To elucidate this problem, force-distance curves were recorded at different indentation depth in the PDMS sample.

Figure 4.2 A represent a typical force curve registered on the CY (1:1) PDMS. We observe that the loading and unloading curves are perfectly superimposed, indicating an elastic behavior. Using Hertz Model for data fitting, the elasticity of the PDMS sample was calculated at different indentation depth, and a graph of elastic modulus versus indentation depth was produced (Figure 4.2 B). From this graph, we could identify a plateau region where elasticity values remained relatively constant. We observe that when the indentation depth is a small fraction of the PDMS film thickness, being 8 μm, the Young's modulus is relatively low. As the indentation depth increases, the measured Young's modulus also increases, due to the increasing influence of the very stiff glass substrate (E $\sim$ GPa) supporting the PDMS layer, which starts to couple in mechanically and affects the measurements. Thus, we note a constant value from initial tip-sample contact until 500 nm depth, followed by an increase of the Young's modulus 30 times greater for indentations between 500 nm and 3 μm, to attain a value 10^3 times greater for indentations above 50% of the film thickness (data not shown in the figure). To minimize the influence of the glass substrate, only the portion of the indentation curve, up to 500 nm was used for the analysis (note that in the field of nano-indentation, it is common practice to assume that indentations which are less than 10% of the film thickness are mostly independent of substrate influences). The value measured at this indentations matches, what was previously reported for this type of PDMS [266][323][324]. As the constant region was obtained for indentation $\leq$ 500 nm, all measurements in this project were done for a maximum indentation of 500 nm.
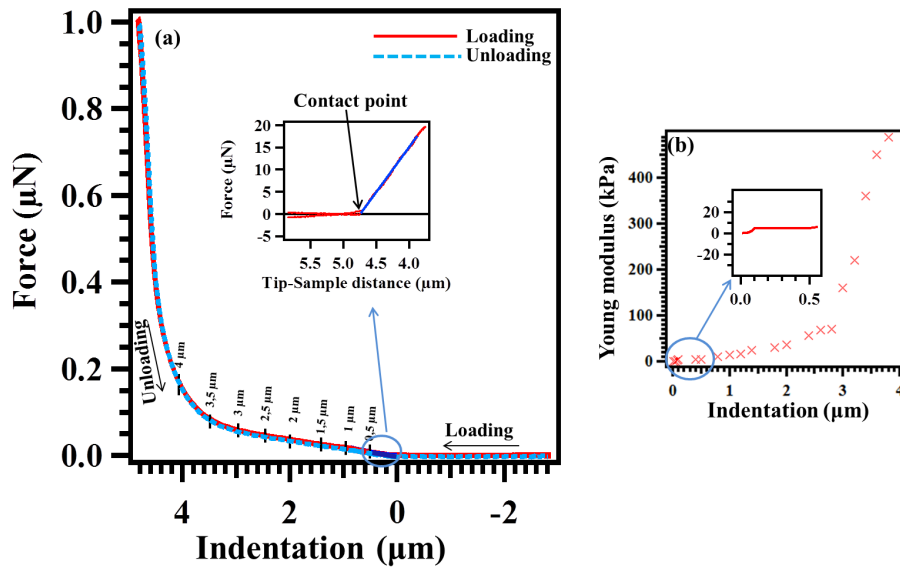
Figure 4.2 – **A typical force versus displacement curve on the PDMS (CY52-276 (1:1))
surface.** a- Force-distance curve showing a loading and unloading curves perfectly superimposed,
the black lines on the curve indicate the value of the indentation depth were the Young's modulus
was measured. b- Effect of indentation depth on Young's modulus calculation. In this example,
a plateau region of reliable elasticity values is present between 100 nm and 500 nm depth, and
the final indentation depth is 4 μm.

4.1.2.2   Surface Stiffness of PDMS

The elastic response of a material is its ability to recover its initial shape following mechanical
deformation. From the contact regime of a force-displacement curve, it is possible to draw in-
formations about the elastic behavior of the material. For an ideal elastic material, during the
advance, the tip deforms the sample by a depth of δ, the sample then regains its shape during
the retract, exerting on the tip the same force.

Figure 4.3 (a), shows a force curve recorded on glass substrate used as a sample with "infi-
nite hardness" to calibrate the AFM. The sharp transition observed in the curve indicates that
a clean AFM tip (here, silica colloidal tip) is approaching a clean support (here glass), and that
both the materials are mechanically stiff. We also see that the loading and unloading curves
are atop of each other, with no hysteresis, which means that the AFM system has been set up
properly, and the AFM tip and sample are not contaminated.
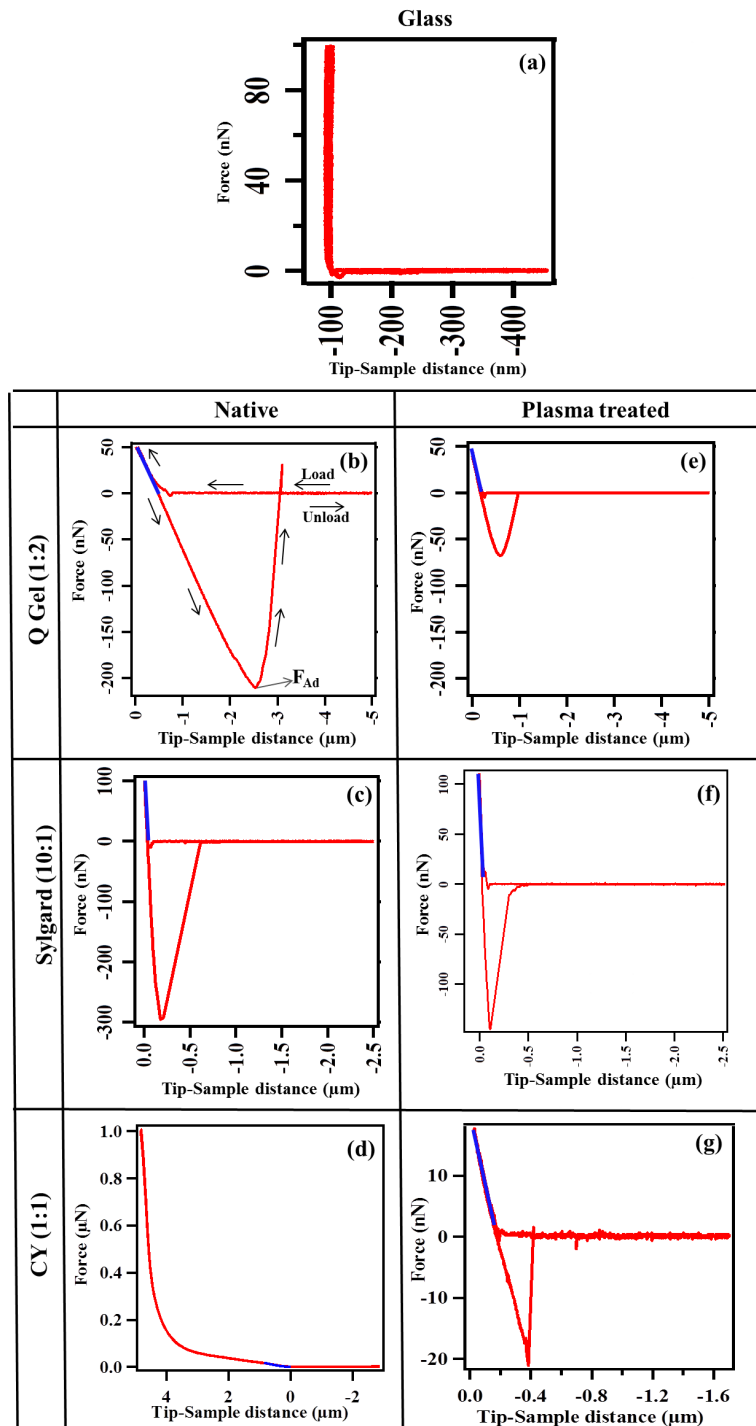
Figure 4.3 – **Force-distance curves on glass and different PDMS substrates.** Force
curves on (a): Glass. (b-d): native Q Gel, Sylgard and CY respectively, (e-g): Plasma treated
Q Gel, Sylgard and CY. The blue curves represent the fit curves. Note the differences in scale
between the curves.

Figure 4.3 (b-g) shows, force curves recorded on different native and plasma treated PDMS sam-

ples. We perceive that the loading and unloading curves overlap and show no hysteresis for all the samples, confirming the elastic behavior of our PDMS, and indicating that PDMS does maintain this behavior also after plasma treatment of its surface.

Force-distance curves were analyzed (as described in section 2.8), for both qualitative and quantitative data about a material's stiffness. The stiffer a material, the steeper the force-distance curve is. To obtain quantitative data about the surface, contact mechanics models were used to fit the curves. Hertz model, was applied in case where no adhesion between the tip and the sample is present. When large adhesive force is observed in the curve, JKR model was used (see section 2.8.5). From the fit (blue lines in the figure 4.3), the Young's modulus was calculated for the different PDMS substrates. The values are reported in the table 4.2, showing a stiffness range of about 3 kPa to 7 MPa.

	Native (kPa)	Plasma Treated (kPa)
Q gel (1:2)	20 ± 3	120 ± 4
Sylgard (10:1)	2440 ± 500	7300 ± 900
CY (1:1)	3 ± 1	260 ± 10

Table 4.2 – **Elasticity measured from AFM force curves.** The average value of the Young's modulus (in kPa) and the corresponding standard deviation are reported. At least three samples were tested for each type of substrate and 100 curves were recorded at different locations for each sample, at minimum 4 distinct regions at the sample surface and under the same conditions.

In a previous study, it was demonstrated that the degree of cross-linking, and also the condition used to cross-link PDMS can have an effect on the polymer Young's modulus [325]. In order to avoid any experimental effect on the Young's modulus, both native and plasma treated polymer samples, were from the same PDMS mixture, and baked at the same time. Thus, the differences seen in Young's modulus for native and plasma treated samples, can only be attributed to the surface treatment. Measurements show that the Young's modulus of the plasma treated PDMS is substantially higher than native PDMS which is consistent with previous reports [326] [327].

4.1.3 Visco-elastic behavior of PDMS

The elastic behavior of our PDMS was discussed in the previous paragraph, while the viscoelastic behavior can exist and sometimes can not be identified by the force curves alone. For this reason, we performed a viscoelastic characterization of our substrates, by the study of the variation of Young's modulus versus the indentation rate. The viscous property is associated with time-dependent relaxation of PDMS upon indentation and, thus, its contribution to indentation measurements is frequency dependent. Indentation speeds varying from 0.2 μm/s to 20 μm/s were investigated.

Figure 4.4 shows the representative elastic response of different PDMS substrates to a systematic change in the indentation speed. JKR model was applied to derive the elastic modulus of all
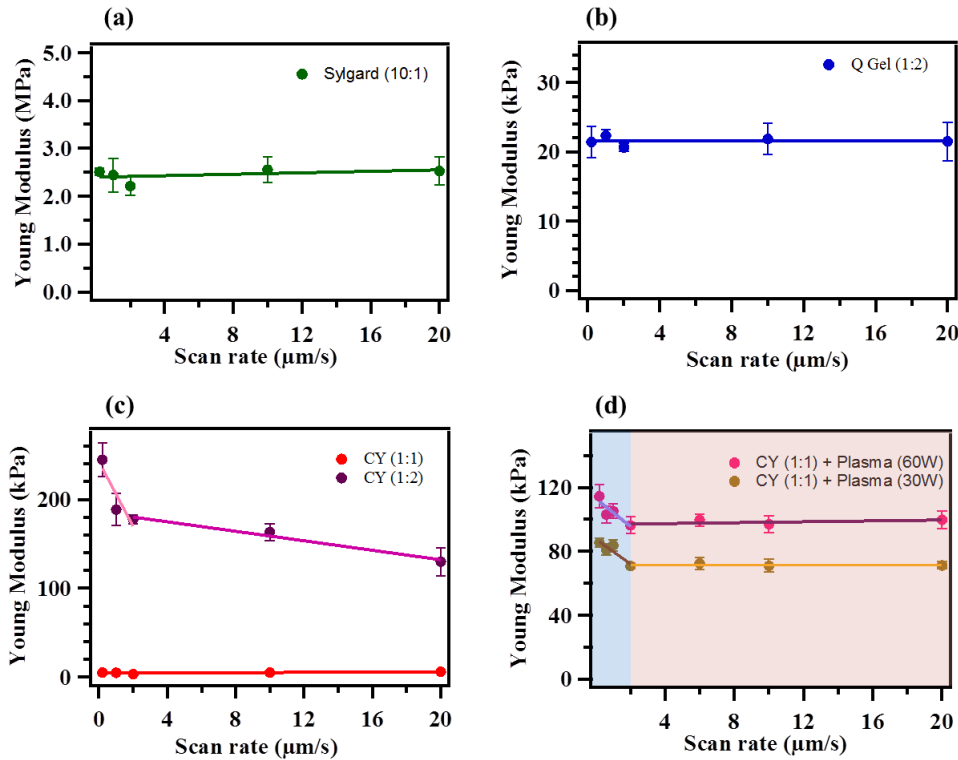
Figure 4.4 – **Influence of indentation rate on elastic modulus of different PDMS
substrates.** (a) On Sylgard. (b) On Q gel. (c) On CY with ratio of (1:1) or (1:2) between base
and cross-linker. (d) On CY (1:1) treated 15 seconds with plasma at a power of 30 W or 60 W
directly after spin coated and without previous baking. 3 samples were tested for every case, and
at least 100 curves at different location on the sample were recorded for each scan rate. Lines
show fit between points. Error bars show standard deviation.

the substrates except for the native CY (1:1) where hertz model was applied. Native Sylgard
(10:1), Q gel (1:2) and CY (1:1) (Figure 4.4 (a,b and c red line) show no significant change in
the Young's modulus over the range of speeds tested. CY (1:2) (Figure 4.4 c purple line) shows
a continuous decrease of its Young's modulus with the increasing of the scan rate, indicating a
viscous behavior. This is confirmed by the hysteresis that appears between the load and unload
curve in figure 4.5, which implies deformation on the substrate.These anomalies were soon seen
for CY (1:4) (data not shown). Thus we decided not to use CY (1:2) or CY (1:4) for patterning
experiments, since future modelization of the force exerted by the cells on visco-elastic substrates
is complicated.

In the previous section 4.1.2.2, we observed that plasma oxidation of PDMS increases its stiff-
ness. Considering the case of CY (1:1), the plasma treated PDMS elasticity (260 ± 10 kPa)
was ≈ 90 times greater than the native one (3 ± 1 kPa). In order to obtain lower elasticity
after plasma treatment, we tried to oxidize the sample directly after the step of spin coating, by
eliminating the baking step (see section 2.3.2). Figure 4.4 d, shows the Young's modulus of these
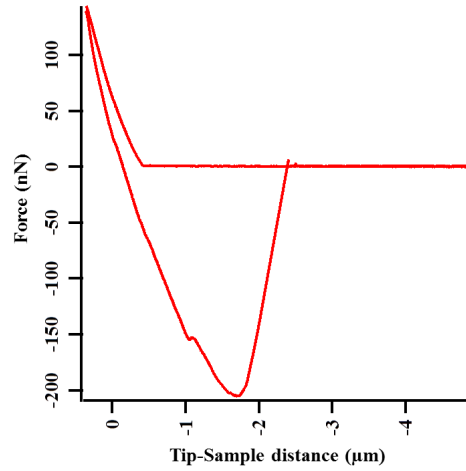
Figure 4.5 – **Force-distance curves on CY (1:2)**.

kind of substrates as a function of scan rate variation. We observe for scan rate < 2 μm/s, the
Young's modulus decreases with the decreasing of the scan rate, showing a viscous behavior (as
indicated by blue shading in figure 4.4 d). For scan rate > 2 μm/s, no significant modifications
of the Young's modulus with the increasing of the scan rate (brown shading in figure 4.4 d).
We think that the plasma treatment did not permits a total cross-linking of the PDMS. We de-
cided to not use this technique, because a deeper study of the mechanism was felt to be necessary.

From these results, we concluded that indentation speed did not affect the resulting values
of elasticity over the range tested (for all the substrates except for the CY (1:2) and CY (1:4)
(results not shown)). As the smallest standard deviation in of Young's modulus was observed for
a scan rate of 2 μm/sec, this was selected as the indentation speed for all the AFM measurements
reported henceforth.

4.2 Observation and characterization of fluorescent pro-
tein nano-dots on glass and PDMS substrates

This section will be dedicated to the observation of different types of fluorescent protein patterns
on glass, and after transfer to different PDMS surfaces, using epi-fluorescence microscopy. This
will be followed by quantification and characterization of the pattern transfer in terms of dot
size, contrast and transfer ratio.

4.2.1 Characterization of nano-patterned glass substrates

biotin BSA (bBSA) protein, in its original state or labeled either with Atto 488 or Texas Red
dyes (henceforth called: bBSA, bBSA-Atto and bBSA-TR respectively); fluorescent BSA (BSA-
TR or BSA-FITC) and fluorescent neutravidin (Nav-TR) proteins, were used to pattern glass

substrates as describes in section 3.1. In this section, I report the characterization of fluorescent
bBSA patterns fabricated on glass in terms of width and contrast.

4.2.1.1   Patterning glass with bBSA proteins
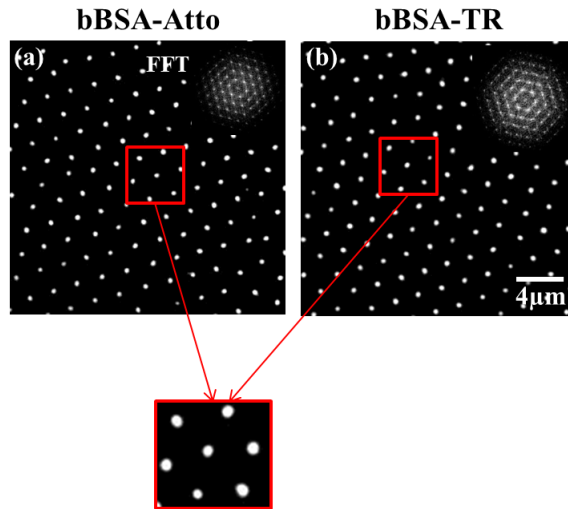
Figure 4.6 – **Epi-fluorescence images of fluorescent bBSA nano-patterns on glass substrates.** (a) bBSA-Atto. (b) bBSA-TR. Fluorescent bBSA dots formed an uniform array with hexagonal lattice. Insets display Fourier transforms of the corresponding images to emphasize the ordering of the lattice.

Fluorescent bBSA patterns were fabricated on glass using the protocol described in section 3.1.
Figure 4.6 shows epi-fluorescence images of bBSA-Atto and bBSA-TR patterns on glass. The fluorescent bBSA patterns are shown to form regular arrays with a hexagon lattice. Epi-fluorescence images are characterized in terms of width and contrast. For that, each image field containing hundreds of dots, is segmented into appropriately sized windows around each dot and a median dot is constructed (see section 2.10.1.2). The scatter dot plot represented in figure 4.7, shows the width and contrast of 10 median dots for each sample. The size of the dots is expressed as the full width at half maximum of the intensity profile of the median dot. The contrast is defined as indicated in equation 4.1:

$$\frac{I_{max} - I_{min}}{I_{max} + I_{min}} \tag{4.1}$$

I_{max} being the peak of the intensity profile for each median dot and I_{min} the baseline around each profile (see section 2.10.1.2).

We observe that the **width** of bBSA-Atto does not vary inside a sample, the best standard deviation (sd) being for sample 3 ($\pm$ 12) and the worst for sample 5 ($\pm$ 35), however a slight variation is observed between samples with a cumulated standard deviation of $\pm$ 56. In the case of bBSA-TR, we also remark very low variation of the width inside a sample with the lowest sd being for sample 3 ($\pm$ 14) and the highest for sample 1 ($\pm$ 38). A slight variation between
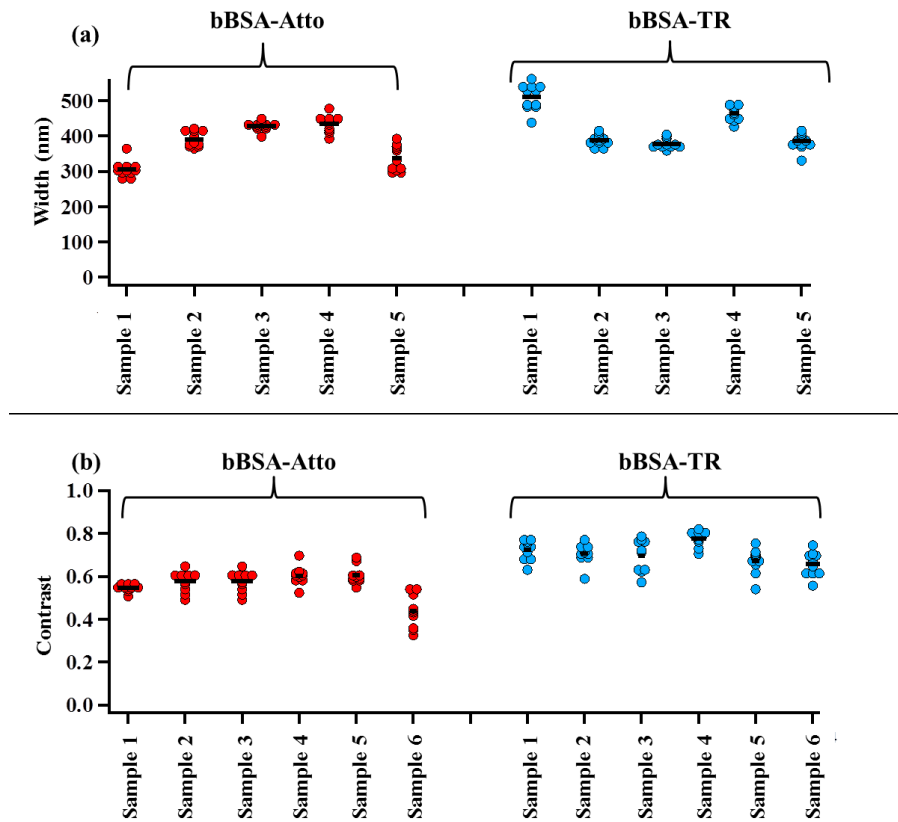
Figure 4.7 – **Scatter-dot plots of width (a) and contrast (b) from epi-fluorescence images of fluorescent bBSA patterns on glass.** At least 10 median dots for each sample, and 6 samples for each case are presented. Bar = median value.

samples is remarked, with cumulated sd = ± 59.

The **contrast** is seen to be stable inside a sample, for both bBSA-Atto and bBSA-TR, with the highest sd being of a value of ± 0.077 for sample 6 and ± 0.076 for sample 5; for bBSA-Atto and bBSA-TR respectively. The cumulated sd being of ± 0.06 for bBSA-Atto and ± 0.15 for bBSA-TR.

The glass cover-slides patterned with bBSA, were either functionalized with fluorescent neutravidin and used as masters for patterning-functionalization of PDMS substrates (see section 4.2.1.2), or served as support for experiments on T-cell adhesion (see section 4.2.1.3).

4.2.1.2 Functionalization of the bBSA patterned glass for transfer

The glass patterned with bBSA were functionalized with 300 μl of 4 μg/ml of fluorescent neutravidin (Nav-TR) for 30 minutes, rinsed with PBS, then transfered to the surface of native (see section 4.2.2.4) or functionalized (see section 4.2.4.2) PDMS. Figure 4.8 shows neutravidin patterns on glass attached either to a bBSA-Atto pattern, or to a pattern of non-fluorescent bBSA
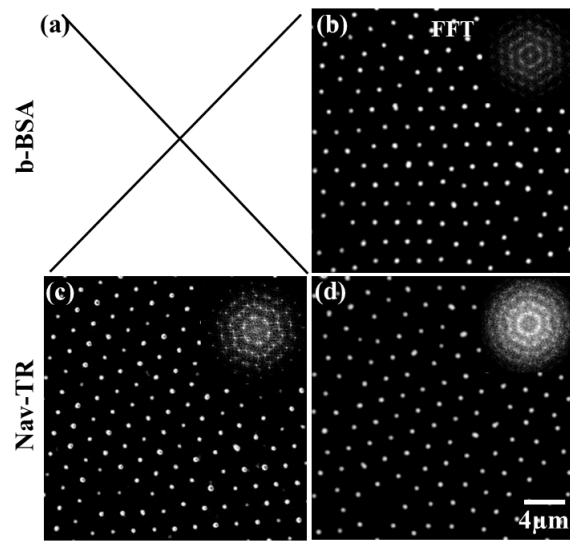
Figure 4.8 – **bBSA patterns functionalized with Nav-TR on glass.** Dots of bBSA : (a) non fluorescent (cannot be imaged without any fluorophore attached), (b) labeled with Atto 488 (bBSA-Atto). Functionalization of the non fluorescent and Atto labeled bBSA dots with Nav-TR (c,d respectively). Insets display Fourier transforms of the corresponding images to emphasize the ordering of the lattice.

on glass.

4.2.1.3 Functionalization of the bBSA patterned glass for T-cell experiments

The bBSA patterned glass slides were used as support for experiments on T-cell adhesion. For
this, bBSA glass patterns were functionalized with Nav-TR, which in turn were incubated with
anti-CD3. The anti-CD3 is expected to bind strongly and uniformly to the neutravidin, and we
ascertained that, indeed it is patterned similarly to the underlying neutravidin dots (Figure 4.9).
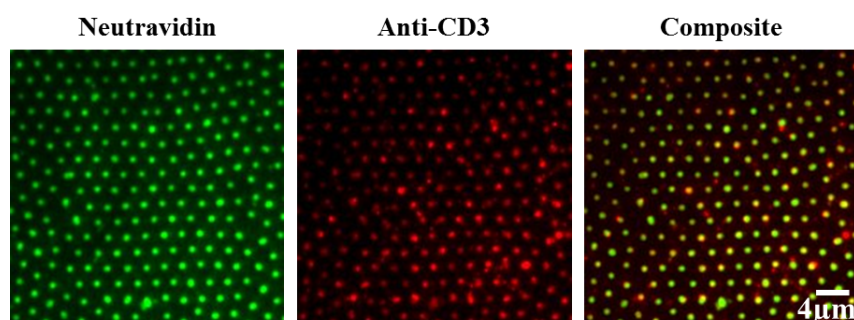
Figure 4.9 – **Anti-CD3 dots on glass.** Neutravidin dots were functionalized with fluores-
cent labeled anti-CD3. The sample were imaged using epi-fluorescence microscopy in the Alexa
488 channel for neutravidin (green dots) and the Atto 647 channel for anti-CD3 (red dots).
The composite image shows good correspondence between the two channels as indicated by the
preponderance of yellow.

4.2.2 Transfer of protein nano-patterns from glass to native PDMS surface.

This section will be devoted to the characterization of the transfer of different fluorescent protein
nano-patterns from glass to untreated PDMS surfaces.

4.2.2.1 Transfer of bBSA

bBSA functionalized either with Atto 488 (bBSA-Atto) or with TR (bBSA-TR) patterned on
glass substrates as described in section 3.1, were transferred to the surface of one of two different
PDMS substrates: Q Gel (20 kPa) or Sylgard (2 MPa) using the reverse contact printing proto-
col.

To verify the successful transfer, the nano-patterned surfaces were imaged, then characterized
by epi-fluorescence microscopy. Figure 4.10 shows epi-fluorescence images of the patterns before
and after transfer to PDMS. Visual inspection of the images shows that bBSA-Atto failed to
transfer to Sylgard (Figure 4.10 a,b), however the pattern exists but is so feeble that it can
not be detected without amplification of camera gain settings (Figure 4.11). A good transfer is
observed on Q Gel (Figure 4.10 c,d), the protein pattern was found to be similar to the one on
glass. In the case of bBSA-TR, successful transfer is observed on both Sylgard (Figure 4.10 e,f)
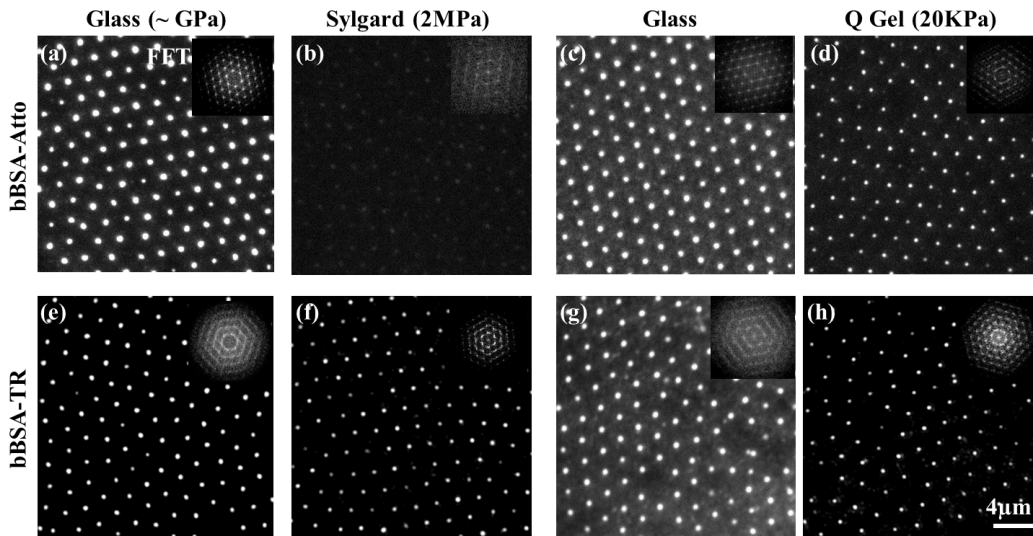
Figure 4.10 – **Epi-fluorescence images of nano-patterns of bBSA labeled with TR or Atto 488 on glass or native Sylgard or Q Gel.** (a,c) bBSA-Atto on glass before transfer, (b,d) the same transferred to native Sylgard and Q Gel respectively, (e,g) bBSA-TR on glass before transfer, (f,h) the same transferred to native Sylgard and Q Gel respectively. Insets display Fourier transforms of the corresponding images to emphasize the ordering of the lattice. Care was taken to ensure same camera and image display conditions for all images.
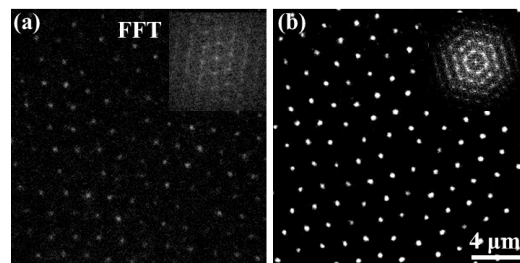
Figure 4.11 – **Transfer of bBSA-Atto on Sylgard imaged with two different camera settings.** Before and after amplification of the camera gain settings (a, b respectively). Image reproduced in figure 4.10 b.

and Q Gel (Figure 4.10 g,h).

Insets in figure 4.10, refer to Fast Fourier transforms (FFT) of the pattern images, showing the ordering of the lattice. We observe that FFT's of the dots for all glass and PDMS images exhibit several diffraction orders indicating that spatial ordering is long range.

The dots are characterized locally by quantification of the epi-fluorescence images in terms of dot size or width and, contrast. As discussed in section 2.10.1, in order to obtain the width and the contrast, first, a median dot is constructed, to obtain a typical dot for every type of patterned surface. Then the width of the dot is expressed as the full width at half maximum
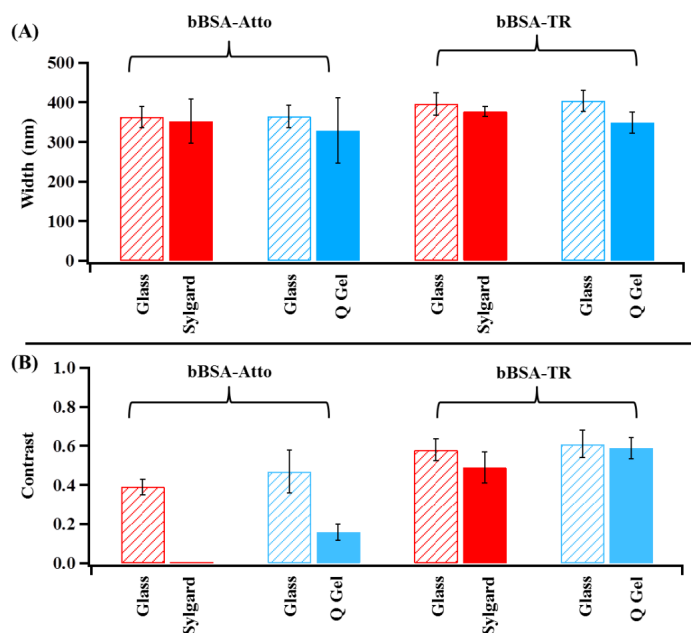
Figure 4.12 – **Quantification of fluorescent bBSA nano-dots from epi-fluorescence images in terms of dot size and contrast before and after the transfer from glass to PDMS.** Values are medians and error bars are median absolute deviation, both averaged over at least 3 independent samples, 6 fields for each sample, and hundreds of dots for each field. (A) Dot-size (FWHM of the intensity profile). (B) Contrast of the dots with respect to the background.

	Glass	Sylgard	Glass	Q Gel
bBSA-Atto	364 ± 27	353 ± 55	364.7 ± 28	329 ± 82
bBSA-TR	396 ± 27	377 ± 13	404.5 ± 26.6	349 ± 27

Table 4.3 – **Summary table of bBSA-Atto and bBSA-TR dot size on glass and after transfer to native Sylgard or Q gel.**

of the intensity profile of the median dot, and the contrast is defined as described in section 4.2.1.1 or equation 4.1. All the values presented in this study represent the average of different fields and samples of the median value in each fields. At least, 3 independent samples for each case, 6 fields for each sample, and hundreds of dots in each field are used for the calculations.

Figure 4.12 A, shows the **width** of bBSA-Atto dots to be 364 ± 27; 353 ± 55 and 329 ± 82 on glass, Sylgard and Q Gel respectively, and in the case of bBSA-TR dots to be, 400 ± 27; 377 ± 13 and 349 ± 27 on glass, Sylgard and Q Gel respectively (Table 4.3). These measurements imply that for both bBSA-Atto and bBSA-TR the dot size is conserved after transfer, onto both untreated Sylgard and Q Gel.

Figure 4.12 B, shows the **contrast** of the dot, which is a measure of the amount of protein in a dot as compared to outside the dot. The contrast was calculated for the dots on glass and after

	Glass	Sylgard	Glass	Q Gel
bBSA-Atto	0.39 ± 0.04	≈ 0	0.47 ± 0.11	0.16 ± 0.041
bBSA-TR	0.58 ± 0.055	0.49 ± 0.08	0.61 ± 0.07	0.59 ± 0.054

Table 4.4 – **Summary table of bBSA-Atto and bBSA-TR dot contrast on glass and after transfer to native Sylgard or Q Gel.**

the transfer to PDMS. We observe a decrease of the contrast for all the cases, implying that the amount of protein transferred from within the dots is not identical to the transfer outside the dots. In fact, for bBSA-Atto on Sylgard, the contrast is ≈ 0, which confirms that no transfer occurs. For transfer to Q Gel a decrease of 65 % is noticed for the contrast after transfer. In the case of bBSA-TR a decrease of 15% is observed for the contrast after transfer to Sylgard and for 3% after transfer to Q Gel (Table 4.4). This measurements confirm the success of the transfer in all the cases except for bBSA-Atto on Sylgard, and the best transfer being for bBSA-TR on Q Gel (Table 4.4).

Another way to characterize the transfer, is the determination of the **transfer ratio**, which is calculated as $I_{max}(elastomer)/\ I_{max}(glass)$; and corresponds to the quantification of the amount of transfer of protein molecules inside the dots, irrespective of the transfer outside, or $I_{min}(elastomer)/\ I_{min}(glass)$; and corresponds to the quantification of the amount of transfer of protein molecules outside the dots (in the region passivated with pluronic), irrespective of the transfer inside.

Figure 4.13 shows the transfer ratio of fluorescent bBSA on untreated Sylgard (2 MPa) and Q Gel (20 kPa), from inside (A) and outside (B) the dots. As we already noticed, no transfer occurs for bBSA-Atto on Sylgard, instead a transfer ratio of $\approx 0.38 \pm 0.03$ is observed for bBSA-Atto on Q Gel. In the case of bBSA-TR transfer occurs on both Sylgard and Q Gel. The best transfer being for bBSA-TR on Q Gel $\approx 0.6 \pm 0.14$ (Table 4.5). Table 4.6 shows the amount of proteins transfered from the region passivated with pluronic.

	Sylgard	Q Gel
bBSA-Atto	≈ 0	0.38 ± 0.03
bBSA-TR	0.31 ± 0.066	0.6 ± 0.14

Table 4.5 – **Summary table of transfer ratio from inside the dots, of bBSA-Atto and bBSA-TR on native PDMS.**

	Sylgard	Q Gel
bBSA-Atto	≈ 0	0.8 ± 0.018
bBSA-TR	0.57 ± 0.033	0.6 ± 0.06

Table 4.6 – **Summary table of transfer ratio from outside the dots, of bBSA-Atto and bBSA-TR on native PDMS.**
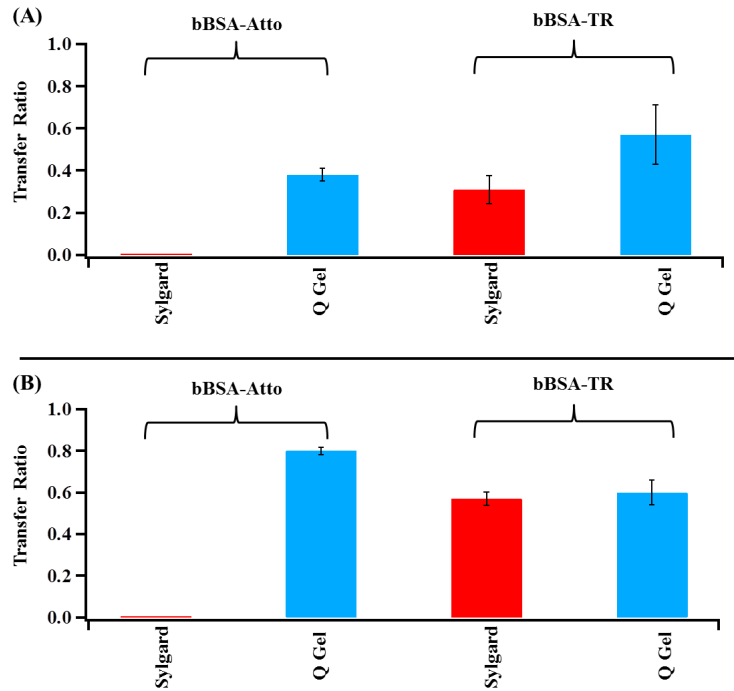
Figure 4.13 – **Transfer Ratio of fluorescent bBSA on native PDMS.** Transfer ratio inside
a dot (A), and outside the dots (pluronic covered zones) (B).
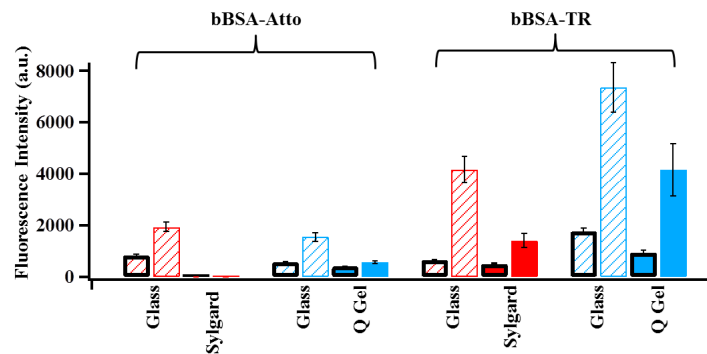
Figure 4.14 – **Fluorescence intensity of fluorescent bBSA dots before and after trans-
fer from glass to PDMS.** Bars represent the peaks of the intensity profile I_{max} (red and
blue bars) and the baseline around each profile I_{min} (black framed bars). Note that the bBSA-
TR patterns on glass (red and blue dashed bars), were fabricated from two different batches of
bBSA-TR which explains the difference in the intensity observed.

Figure 4.14 shows the **averaged fluorescence intensity** inside the dots, I_{max}, and outside the
dots, in the region passivated with the pluronic, I_{min}, before and after transfer from glass to
PDMS. The fluorescence intensity is correlated with the quantity of proteins bound to the sub-
strate. In the ideal case, there should be no proteins adsorbed in the passivated region and even if
there is some protein adsorbed, their should be no transfered to the PDMS, which is not the case.

We observe, for **bBSA-Atto**, the amount of proteins outside the dots is 0.3 times the amount inside the dots for the glass substrates, this amount increase to 0.7 on Q gel substrates. This means that the amount of protein transfered from the outside of the dots was higher than that transfered from within the dots. When observing **bBSA-TR** on glass substrates, the amount of protein outside the dots is 0.2 times that of inside the dots, for Sylgard it is 0.35 and for Q gel 0.22. We can conclude that better patterns are obtained for bBSA-TR, on both glass and PDMS substrates. In fact, the presence of proteins outside the dots, could be due to unspecific interaction coming from the presence of multilayers of beads, instead of mono-layers, formed during the self-assembled beads mono-layers deposition step. The multilayers will prevent the silane to deposit on the bare cleaned glass during the second step of silanization. This will influence the grafting of pluronic and open a route to unspecific deposition of proteins. We can also note that the amount of protein absorbed and transferred depends strongly on the quality of the pluronic layer (see section 4.4).

4.2.2.1.1 Functionalization of bBSA-TR PDMS pattern for Cell experiments

Since the best transfer to native PDMS, was observed for bBSA-TR on Q Gel, it was further functionalized with fluorescent neutravidin and then with anti-CD3 as describe in section 3.2.4, to be further used for T-Cell experiments. Figure 4.15 shows fluorescent Nav patterned similarly to the underlying bBSA-TR dots.
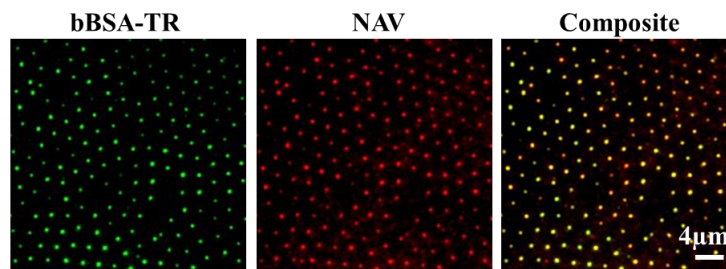
Figure 4.15 – **Nav-dyelight dots.** bBSA-TR dots were functionalized with fluorescent labeled neutravidin. The sample was imaged using epi-fluorescence microscopy in the Alexa 488 channel for bBSA-TR (green dots) and the atto 647 channel for fluorescent neutravidin (red dots). The composite image shows good correspondence between the two channels as indicated by the preponderance of yellow.

4.2.2.1.2 General characterization of bBSA-TR pattern on Q gel

We also studied, the variation of the width and contrast for bBSA-TR pattern on Q Gel, inside the same sample and between different samples (Figure 4.16). We observe that the **width** varies slightly inside a sample, the highest standard deviation being observed for sample 1 (sd = $\pm$ 19.86) and the lowest for sample 6 (sd = $\pm$ 9). A negligible width variation between samples
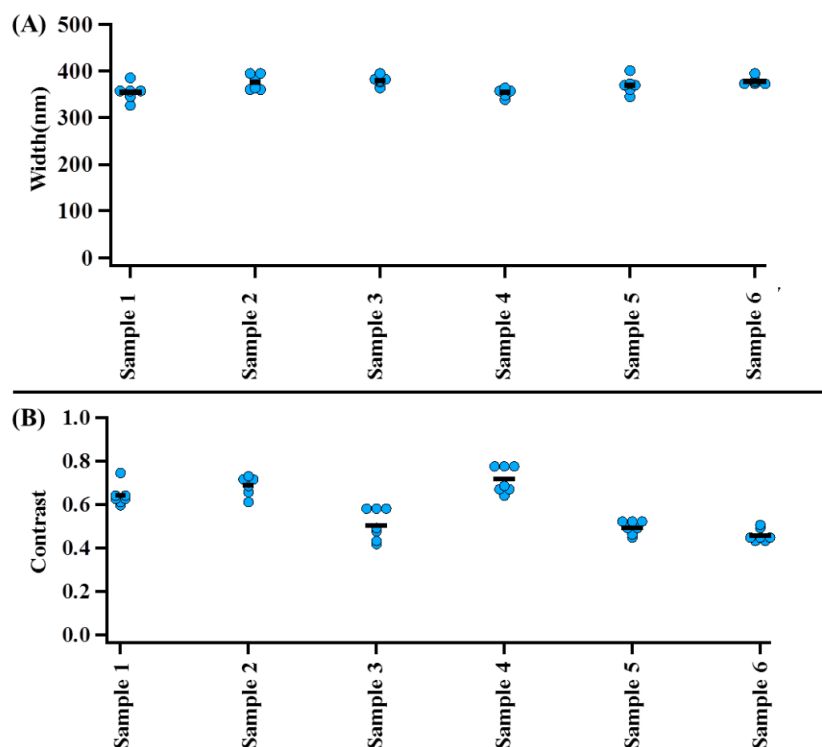
Figure 4.16 – **Scatter-dot plots of width (A), and contrast (B) from epi-fluorescence
images of bBSA-TR patterns on Q Gel.** At least 6 median dots for each sample are
presented. Bar = median value.

is noticed (sd = $\pm$ 11.5). For the **contrast**, variations are presented inside a same sample and
also between samples. Sample 3, shows the highest standard deviation being $\pm$ 0.07 and the best
sample was sample 6 where sd decrease to $\pm$ 0.028. The sd between samples was $\pm$ 0.1. This
variation of contrast is related to the quality of the glass master before the transfer. Thus, when
fabricating the glass master, the first step of beads deposition is a very delicate step, where in
some cases during deposition, multi-layers of beads can form instead of mono-layers, and this
can create unspecific binding of proteins outside the holes in some regions of the sample as was
explained in section 4.2.2.1, which are then transferred to the PDMS creating variation in the
contrast.

4.2.2.1.3   Transfer of non fluorescent bBSA

bBSA (not conjugated to any fluorophore), was transfered to native Q Gel and CY PDMS.
Since its presence can not be directly imaged in fluorescence microscopy, due to the absence of
an attached fluorophore, it needs to be revealed by functionalization with fluorescent neutravidin
after the transfer to the PDMS surface (see section 3.2.4). Therefore the characterization of
bBSA in terms of width, contrast and transfer ratio, in this case, is not possible.
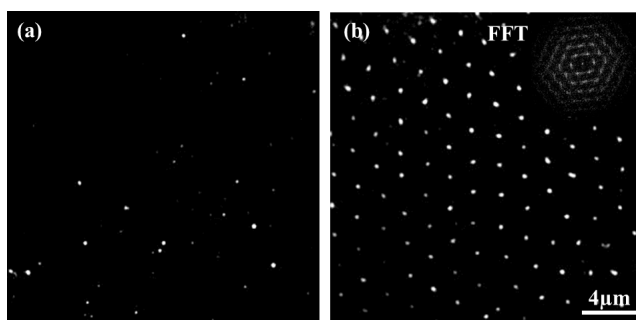
Figure 4.17 – **Nav-TR pattern on PDMS revealing the quality of the transfer of non
fluorescent bBSA.** (a) On CY, (b) on Q gel.

Figure 4.17 shows Nav-TR on CY and Q Gel. bBSA transfered to the surface of CY PDMS
failed, no pattern was observed after functionalization with Nav-TR. On Q Gel, possible transfer
is revealed with the presence of Nav-TR pattern, however the transfer was not reproducible, one
sample out of five tried, shows a pattern on not more than 20% of the sample surface.

4.2.2.2 Transfer of Texas Red labeled neutravidin

Neutravidin Texas Red (Nav-TR) nano-patterns were created on glass substrate, and transfered
to the surface of Q gel with and without adding a drop of water during the transfer step (see
section 3.2.3). Well organized neutravidin patterns were observed on glass (Figure 4.18 a-c) be-
fore the transfer. However, when no water is added during the transfer, Nav-TR showed changes
in shape in 70% of the samples (Figure 4.18 d) after transfer to Q Gel, and the rest 30 % gave
acceptable patterns (Figure 4.18 e). Instead when a drop of water is added, a successful transfer
is observed in all the cases (Figure 4.18 f).

Quantification of the epi-fluorescence images of the neutravidin patterns showing conformational
changes after transfer to Q gel are reported in Figure 4.19. The parameters here are averages
calculated from 6 samples with at least 5 fields each, and hundreds of dots in each field. An
increase in the **dot size** is noticed, passing from 406 ± 30 on glass to 536 ± 85 on Q Gel
($p<0.001$) (Figure 4.19 a). The **contrast** decreases from 0.55 ± 0.14 on glass to 0.2 ± 0.05
on Q gel (Figure 4.19 b). Finally, the **transfer ratio** calculate from the fluorescence intensity
(Figure 4.19 c), as $I_{max}(QGel)/I_{max}(glass)$, was around 0.24 ± 0.06. The contrast and transfer
ratio measurement prove that the transfer works reasonably. These kind of patterns were also
obtained on Sylgard (2 MPa) and CY (1 kPa) (data not shown). However, Nav patterns on
native PDMS were not further used for cell experiments, because subsequent functionalization
with a biotinylated protein (anti-CD3), after a pluronic blocking step failed. We think, this is
due to the fact that neutravidin was not anymore functional due to drying.
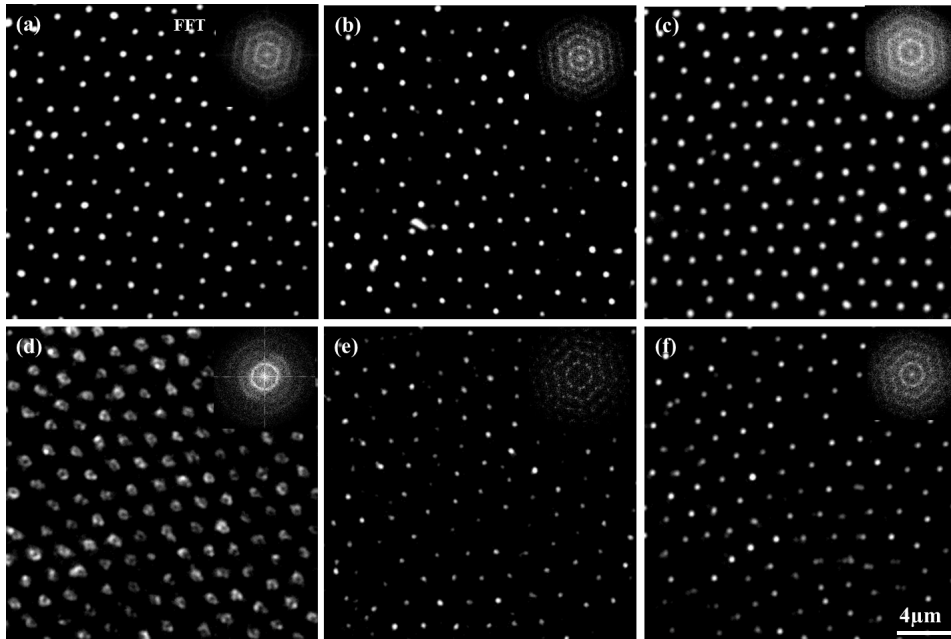
Figure 4.18 – **Epi-fluorescence images of Nav-TR pattern on glass (a-c) and the corresponding pattern on Q Gel (d-f).** Insets display Fourier transforms of the corresponding images to emphasize the ordering of the lattice.
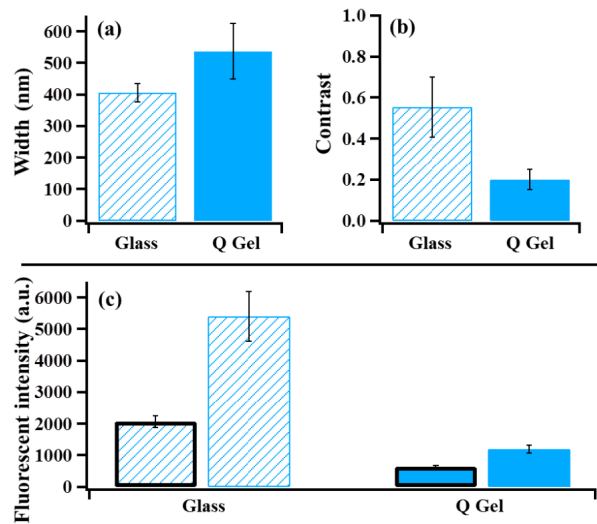
Figure 4.19 – **Quantification of the epi-fluorescence images of the Nav-TR patterns obtained on glass and after transfer to Q Gel, in terms of width and contrast.** (a) Dot-size (FWHM of the intensity profile). (b) Contrast of the dots with respect to the background. (c) Fluorescence intensity of the Nav-TR dots, represented as the peak of the intensity profile I_{max} (blue framed bars) and the baseline around each profile I_{min} (black framed bars) on glass and after transfer to PDMS.

4.2.2.3 Effect of adding a water layer between the two surface in contact during the transfer

Micro-contact printing of protein has been always shown to take place when transferring from a low free energy hydrophobic surface (usually PDMS), to a high energy hydrophilic surface (usually a cleaned glass surface) [328]. This was characterized by Tan et al. who found that, transfer efficacy decreases as the free energy of the surface diminishes, and fails completely on low energy hydrophobic surfaces [171]. This constituted one of the limitations of the micro-contact printing technique. Later on, Ricoult and colleagues introduced the humidified micro-contact printing technique based on adding water in proximity to proteins adsorbed on hydrophilized stamps, and showed that the printing of proteins on both high (hydrophilic) and low (hydrophobic) energy surfaces is enabled by the water vapor diffusing through the stamp. To explain that, they used a molecular simulation of a RGD peptides which was sandwiched between low energy PDMS and SiO_2. They found that in the absence of water, a close interaction takes place between RGD and both PDMS and SiO_2. When water molecules are included, they are trapped between the peptide and SiO_2 and prevent the adhesion of the peptide to the SiO_2 [161]. Based on this findings, we found that working in wet condition during the transfer of the protein patterns from the glass master to the PDMS is important for the success of this step.

4.2.2.4 Transfer of bBSA functionalized with Texas Red labeled neutravidin

Non fluorescent bBSA patterns on glass, were functionalized with Nav-TR as described in section 4.2.1.2, and transfered to the surface of native Q gel. The pattern was correctly transfered as seen in the epi-fluorescence images (Figure 4.20). However, further functionalization of the pattern with a biotinylated protein, failed. We think that during the transfer from glass to the PDMS substrate, the Nav-TR was physically attached to the PDMS exposing the bBSA to the surface, which explain the unsuccessful binding of the biotinylated protein.
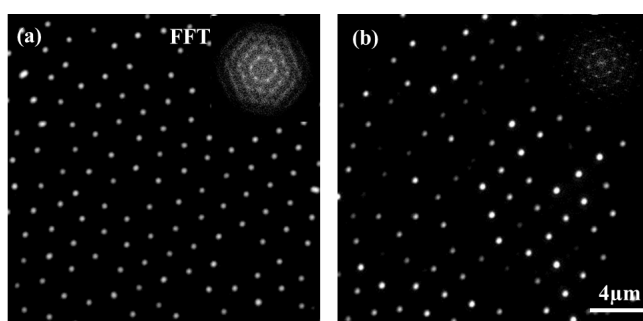
Figure 4.20 – **Epi-fluorescence images of Nav-TR attached to a pattern of non-fluorescent bBSA on glass (a) and the corresponding pattern after transfer to Q Gel (b).** Insets display Fourier transforms of the corresponding images to emphasize the ordering of the lattice.

4.2.2.5   Transfer of fluorescent BSA

Patterns of BSA (non-biotinylated) conjugated to fluorescein isothiocyanate (called BSA-FITC)
or to Texas Red (called BSA-TR) were fabricated on glass and transferred to the surface of
untreated PDMS. In the case of BSA-FITC, no transfer occurs. In the case of BSA-TR, good
transfer was observed on Sylgard and Q Gel PDMS. The transfer was successful for three different
Sylgard stiffness 30 kPa, 140 kPa and 3 MPa [215], and for 20 kPa Q Gel.

4.2.3   Transfer of protein nano-patterns from glass to plasma treated PDMS surface

Sylgard (10:1) with an elasticity of 2 MPa and Q Gel (1:2) 20 kPa, were treated with plasma as
described in section 2.3.4. Following the plasma treatment, the elasticity of the PDMS increased,
becoming 7 MPa for the Sylgard and 120 kPa for Q Gel (details in section 4.1.2.2). The plasma
treated PDMS's will be called p Sylgard and p Q Gel.
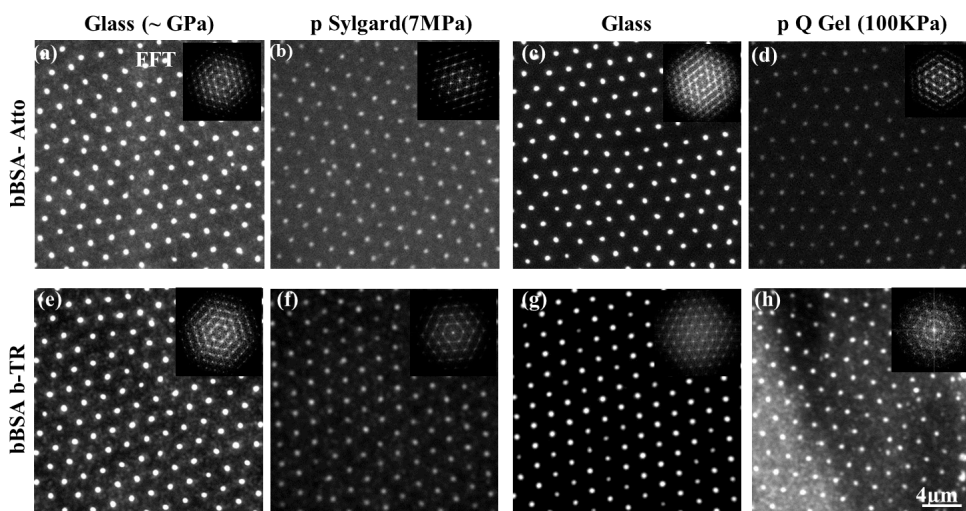
Figure 4.21 – **Epi-fluorescence images of nano-patterns of bBSA conjugated to TR or
Atto 488 on glass and plasma treated Sylgard or Q Gel PDMS.** (a,c) bBSA-Atto on glass
before transfer, (b,d) the same transferred to p Sylgard and p Q Gel respectively. (e,g) bBSA-TR
on glass before transfer, (f,h) the same transferred to p Sylgard and p Q Gel respectively. Insets
display Fourier transforms of the corresponding images to emphasize the ordering of the lattice.
Care was taken to ensure same camera and image display conditions for all images.

Looking over the epi-fluorescence images (Figure 4.21), we observe that both bBSA-Atto and
bBSA-TR transferred well on p Sylgard and p Q Gel. The dot size and contrast calculated
as described in section 4.2.2.1, are reported in figure 4.22 and tables 4.7, 4.8. The parameters
presented are averages calculated from at least 3 samples, with at least 6 fields each and hundreds
of dots in each fields. We notice a slight increase of the **dot size**, for both bBSA-Atto and bBSA-
TR after the transfer to the plasma treated PDMS. This increase was shown to be statistically
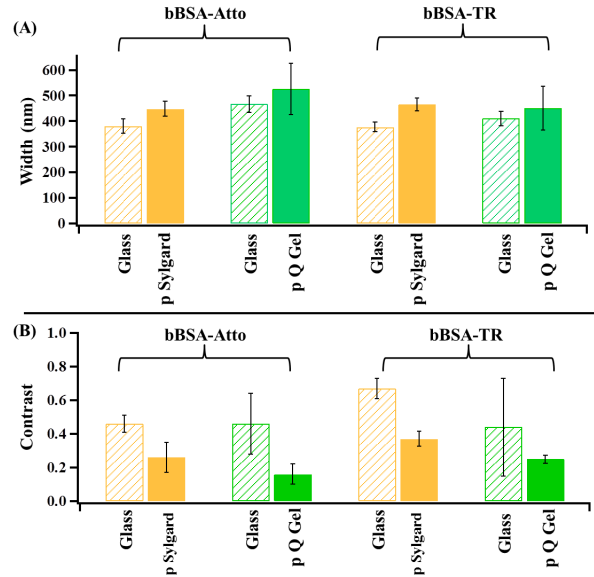
Figure 4.22 – **Quantification of fluorescent bBSA nano-dots from the epi-fluorescence images in terms of dot size and contrast before and after the transfer from glass to plasma treated PDMS.** Values are medians and error bars are median absolute deviation, both averaged over at least 3 independent samples, 6 fields for each sample, and hundreds of dots for each field. (A) Dot-size (FWHM of the intensity profile). (B) Contrast of the dots with respect to the background.

	Glass	p Sylgard	Glass	p Q Gel
bBSA-Atto	380 ± 28	448 ± 29	467 ± 32	526 ± 101
bBSA-TR	377 ± 19	465 ± 25	411 ± 28	451 ± 86

Table 4.7 – **Summary table of bBSA-Atto and bBSA-TR dot size on glass and after transfer to plasma treated Sylgard or Q Gel.**

	Glass	p Sylgard	Glass	p Q Gel
bBSA-Atto	0.46 ± 0.05	0.26 ± 0.09	0.46 ± 0.18	0.16 ± 0.06
bBSA-TR	0.67 ± 0.06	0.37 ± 0.044	0.44 ± 0.29	0.25 ± 0.024

Table 4.8 – **Summary table of bBSA-Atto and bBSA-TR contrast on glass and after transfer to plasma treated Sylgard or Q Gel.**

	p Sylgard	p Q Gel
bBSA-Atto	0.6 ± 0.056	0.46 ± 0.048
bBSA-TR	0.36 ± 0.042	0.33 ± 0.044

Table 4.9 – **Summary table of transfer ratio inside the dots, of bBSA-Atto and bBSA-TR transferred to plasma treated PDMS.**

significant (T-test: p<0.001) (Figure 4.22 A, table 4.7).

The **contrast**, is systematically diminished upon transfer. The best contrast after transfer is shown to be for bBSA-TR on p Sylgard (0.37 ± 0.044). Contrast measurements confirm the
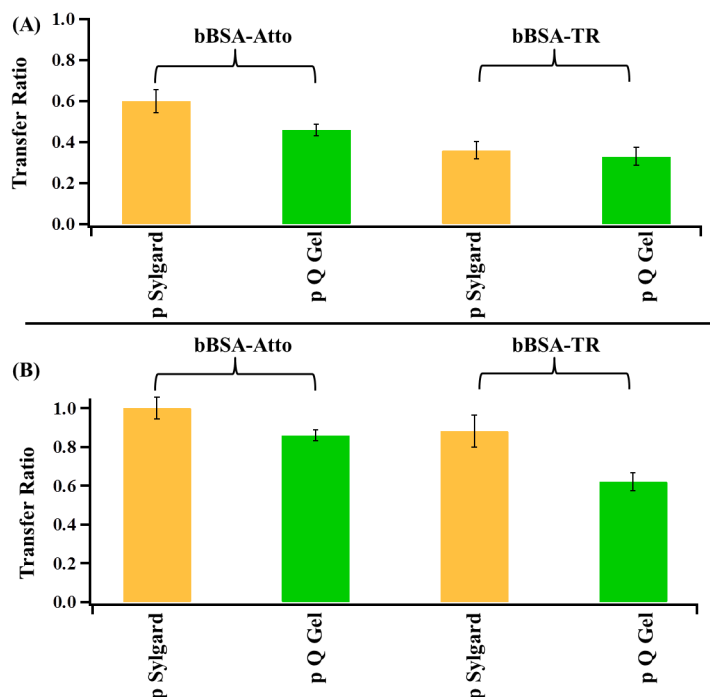
Figure 4.23 – **Transfer ratio of fluorescent bBSA inside the dots(A), and outside (B) the dots.**

	p Sylgard	p Q Gel
bBSA-Atto	1 ± 0.035	0.86 ± 0.027
bBSA-TR	0.88 ± 0.082	0.62 ± 0.046

Table 4.10 – **Summary table of transfer ratio outside (pluronic covered zones) the dots, of bBSA-Atto and bBSA-TR transferred to plasma treated PDMS.**

success of the transfer for all the cases (Table 4.8). The **transfer ratio** was also calculated as described in section 4.2.2.1. Figure 4.23 shows the transfer ratio of fluorescent bBSA on p Sylgard and p Q Gel, from inside (A) and outside (B) the dots. The transfer is seen to be better for bBSA-Atto on p Sylgard and p Q Gel, being respectively 0.6 ± 0.056 and 0.46 ± 0.048, than for bBSA-TR being 0.36 ± 0.042 on p Sylgard and 0.33 ± 0.044 on p Q Gel (table 4.9). Table 4.10 shows the amount of proteins transferred from the region passivated with pluronic.

Figure 4.24 shows the averaged fluorescence intensity inside the dots (I_{max}), and outside the dots, in the region passivated with pluronic (I_{min}), before and after transfer from glass to the plasma treated PDMS. As we already discussed in section 4.2.2.1, there should be no proteins adsorbed in the passivated region and even if there is some, there should be no transferred to the PDMS, which is not the case.
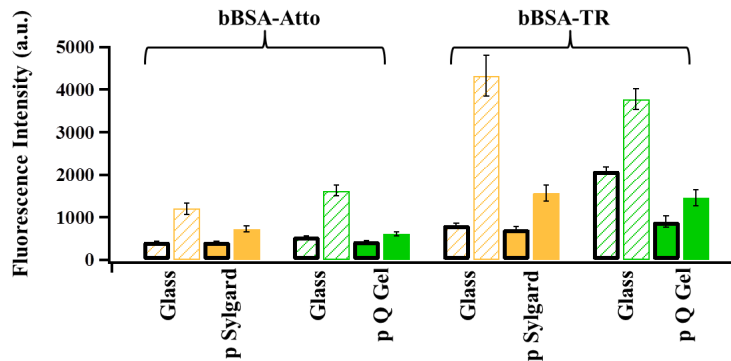
Figure 4.24 – **Fluorescence intensity of fluorescent bBSA dots before and after transfer from glass to plasma treated PDMS.** Bars represent the peaks of the intensity profile, I_{max} (yellow and green framed bars), and the baseline around each profile, I_{min} (black framed bars).

4.2.3.1 Functionalization of bBSA-Atto PDMS pattern for cell experiments

Since the best transfer to plasma treated PDMS, was observed for bBSA-Atto on p Q Gel, it was further functionalized with fluorescent neutravidin and then with anti-CD3 as describe in section 3.2.4 to be further used for T-Cell experiments. Figure 4.25 shows successful binding of Nav on bBSA-Atto.
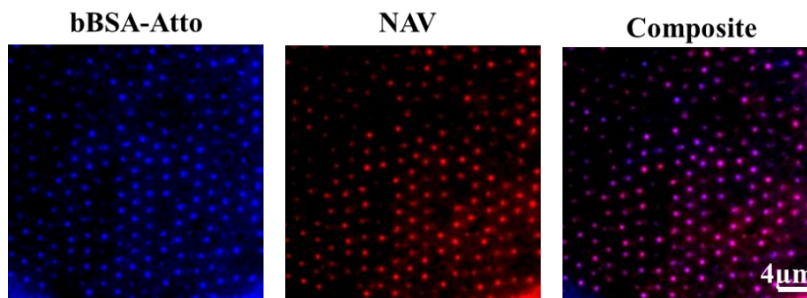
Figure 4.25 – **Nav-dyelight dots.** bBSA-Atto dots were functionalized with fluorescent labeled neutravidin. The sample were imaged using epi-fluorescence microscopy in the Alexa 488 channel for bBSA-Atto (blue dots) and the atto 647 channel for neutravidin (red dots). The composite image shows good correspondence between the two channels as indicated by the preponderance of pink.

4.2.3.2 Transfer of fluorescent BSA

BSA (non- biotinylated) labeled with FITC (BSA-FITC) was transfered to the surface of plasma treated Q gel. The transfer works properly with a transfer ratio of 0.57 (Figure 4.26).
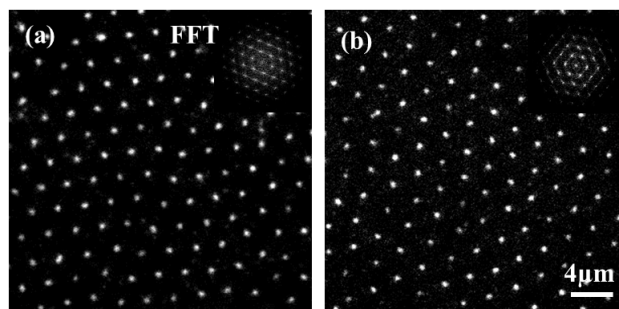
Figure 4.26 – **Epi-fluorescence images of BSA-FITC transfered from glass (a) to plasma treated Q Gel (b).** Insets display Fourier transforms.

4.2.4 Transfer of protein nano-patterns from glass to functionalised PDMS surface

In separate experiments, plasma treated CY and Q Gel PDMS elastomer (p CY and p Q Gel), were functionalized with APTES and glutaraldhehyde as described in section 3.2.2.1 (henceforth we will be calling them glu CY and glu Q Gel). Different proteins were transfered to their surface.

4.2.4.1 Transfer of Nav-TR

Nav-TR patterns were allowed to transfer to functionalized PDMS (glu CY and glu Q gel) using the reverse contact printing protocol. Observation of the epi fluorescence images (Figure 4.27), show that the Nav-TR nano-dots were readily transfered to the surface of the elastomer.
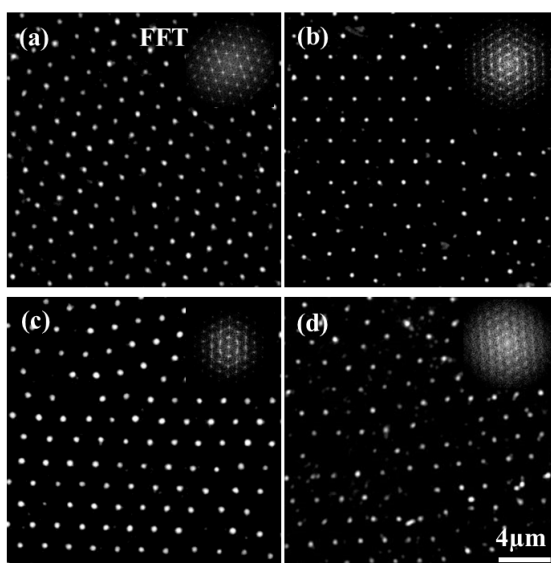
Figure 4.27 – **Epi-fluorescence images of Nav-TR transfered from glass to functionalized PDMS.** (a,b) Images on glass. (c,d) Images on glu CY and glu Q gel respectively. Insets display Fourier transforms.

Width and contrast were calculated to characterize the pattern (Figure 4.28). **Dot size** seems to not change after the transfer (495 ± 58), and the **contrast** shows a decrease from 0.45 ± 0.1 on glass to 0.25 ± 0.1 on glu CY. **Transfer ratio** inside the dots was also measured and calculated to be 0.39 ± 0.24. After the transfer, glu CY Nav patterned was homogeneously functionalized with anti-CD3 for further use for T-Cell spreading experiments (Figure 4.29).
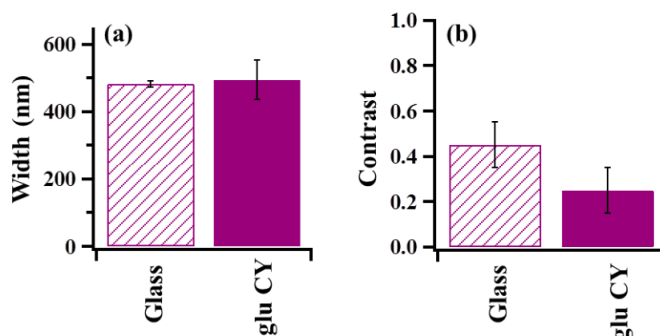
Figure 4.28 – **Quantification of Nav-TR nano-dots from epi-fluorescence images in terms of dot size and contrast before and after the transfer from glass to glu CY.** Values are medians and error bars are median absolute deviation, both averaged over 5 independent samples, each with at least 5 fields containing hundreds of dots. (a) Dot-size (FWHM of the intensity profile). (b) Contrast of the Nav-TR nano-dots on glass and glu CY with respect to the background.
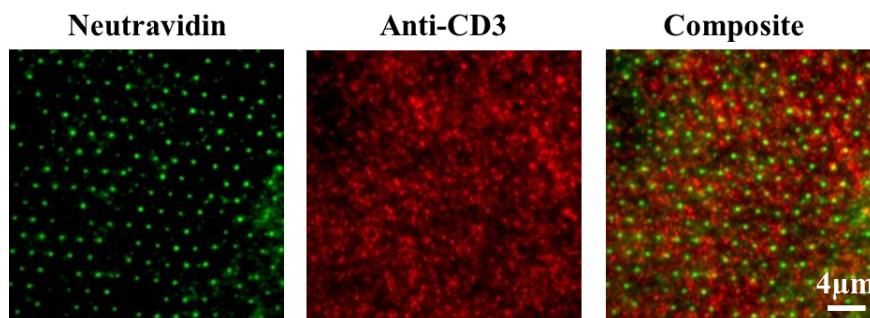
Figure 4.29 – **Anti-CD3 on Glu CY.** Neutravidin dots were functionalized homogeneously with fluorescent labeled anti-CD3. The samples were imaged using epi-fluorescence microscopy in the Alexa 488 channel for neutravidin (green dots), and the atto 647 channel for anti-CD3 (red). The co-localization is not satisfactory.

4.2.4.2 Transfer of other proteins

4.2.4.2.1 Transfer of bBSA

Non fluorescent bBSA patterns on glass were transfered to the surface of glu CY and glu Q

Gel. A very low and unreliable transfer was observed after revealing the pattern by function-
alization with Nav-TR (Figure 4.30). However, when patterns of bBSA are functionalized with
Nav-TR on glass and then transfered to the surface of functionalized PDMS, the transfer worked
easily (Figure 4.31). We think that during the transfer, the Nav-TR was physically attached to
the PDMS exposing the bBSA to the surface.
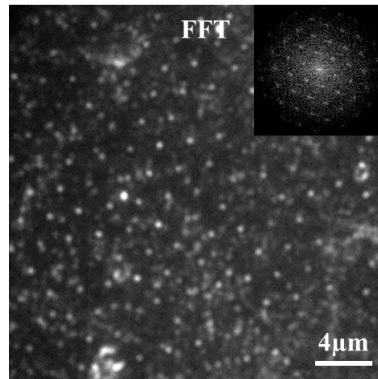
Figure 4.30 – **Epi-fluorescence images of Nav-TR pattern on glu CY revealing the
low quality transfer of non-fluorescent bBSA.**
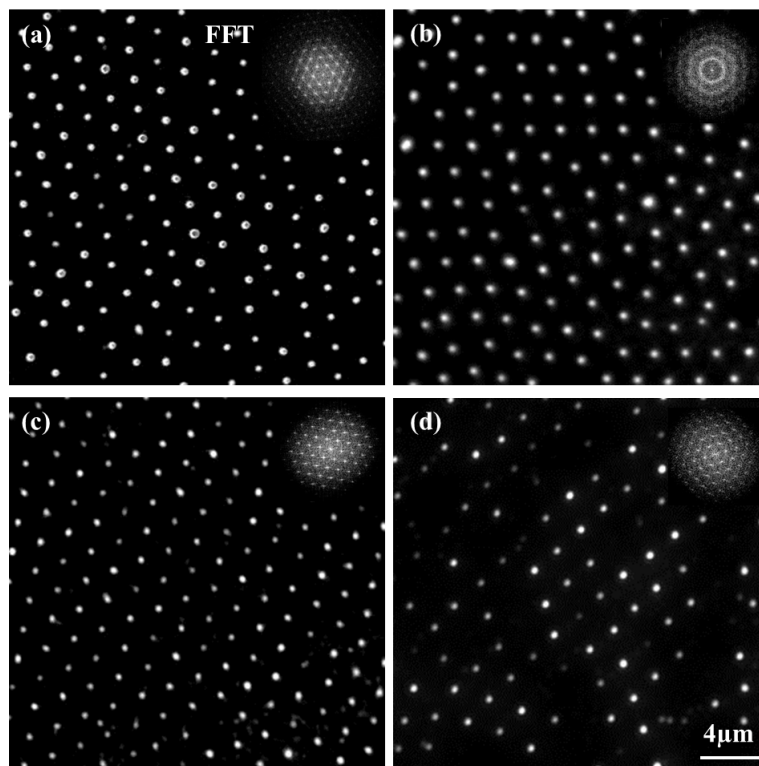
Figure 4.31 – **Epi-fluorescence images of Nav-TR pattern revealing the quality of
bBSA pattern on glass (a,b) and after transfer of the ensemble to the surface of
functionalized PDMS, glu CY and glu Q Gel(c,d respectively).**

141

4.2.4.2.2 Transfer of BSA-FITC

BSA-FITC failed to transfer to any of the glu functionalized PDMS.

4.3 Transfer on hard and soft Sylgard

Next, we tested the technique of reverse transfer on softer PDMS and explore the influence of stiffness on the quality of transfer.
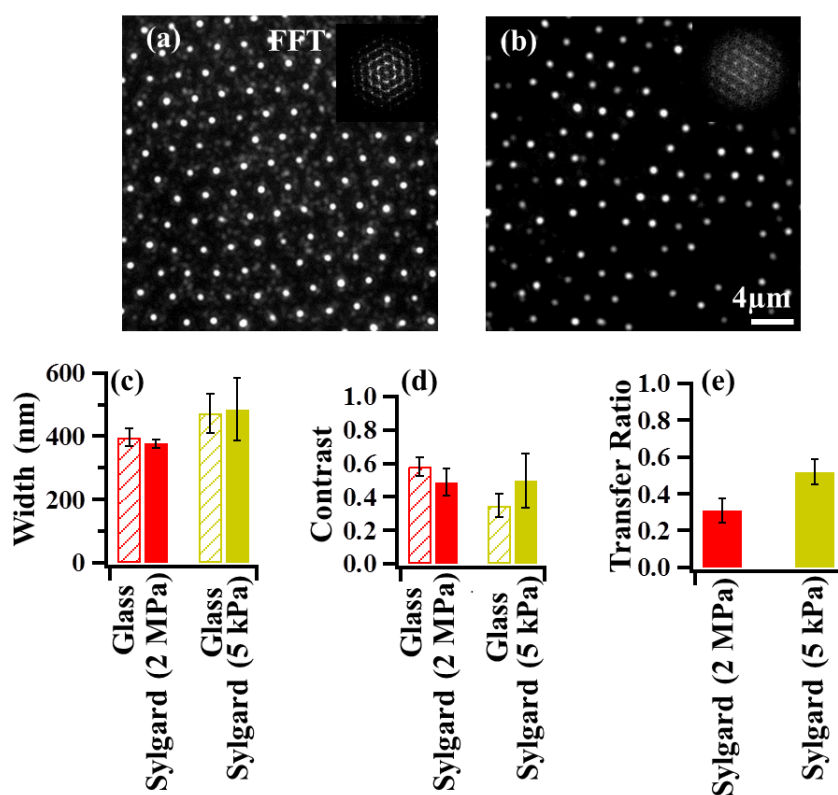
Figure 4.32 – **Comparison of the transfer on hard Sylgard (2 MPa) and soft Sylgard (5 kPa).** (a,b) Epi-fluorescence images of bBSA-TR on Sylgard 2 MPa and 5kPa respectively. care was taken to ensure same camera and image display conditions for all images. (c) Dot size (FWHM of the intensity profile). (d) Contrast of the bBSA-TR on glass and PDMS with respect to the background. (e) Transfer ratio of bBSA-TR on Sylgard 2 MPa and 5 kPa.

Figure 4.32 shows successful transfer of bBSA-TR on both 2 MPa and 5 kPa Sylgard. No variation in the **dot size** was observed before and after the transfer. The **contrast** shows a decrease when transfer to 2 MPa Sylgard and an increase when transfer to soft Sylgard, which means that in the case of the soft Sylgard, the amount of protein transferred from outside of the dots was negligible to that transfered from within the dots. Better **transfer ratio** was obtained for soft Sylgard (0.52 ± 0.07) when comparing with the hard one (0.31 ± 0.066).

4.4 Poloxamer influence on the transfer and the contrast
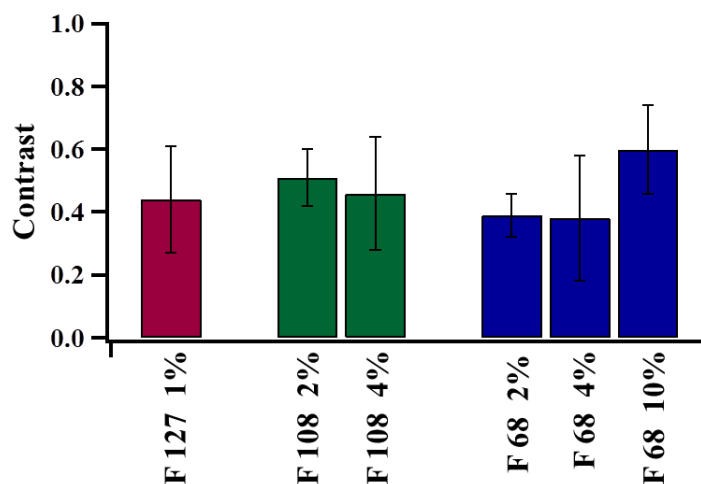
Figure 4.33 – **Contrast of Nav-TR nano-dots pattern on glass fabricated with different pluronic types and concentrations.**

As described in section 2.4, three types of poloxamer molecules (pluronic F-127, F-108 and F-68) were tried with different concentration to fabricate the glass master (Table 4.11). The pluronic was bound to the silane by hydrophobic interactions, and acted as repealer to prevent non-specific adsorption of proteins in between the holes, thus to passivate the glass master. In the ideal case, while making the glass master, there should be no protein absorbed on the regions passivated with the poloxamer and even if there is some protein absorbed, it should not be transferred to PDMS. The type of the pluronic and its concentration has a major influence on the amount of protein adsorbed and on the success and the quality of the transfer. To quantify and optimize the poloxamer solution parameters, Nav-TR patterns on glass were fabricated using several types of pluronic, either F-127, or F-108 or F-68. As F-127 has the longest polypropylene-oxide chain (PPO), we expect it to have the most efficient interaction with the surface in comparison with the two others. Instead F-108, having the highest number of polyethylene oxide chain (PEO), is expected to give the best repellent properties, thus, giving better contrast than the other pluronic types.

Figure 4.33 shows the contrast of Nav-TR patterns fabricated on glass with different pluronic types and concentrations. The values are averages calculated from at least 5 samples with at least 10 fields each, and hundreds of dots in each field. The best contrast is shown to be obtained with F 68 10%. However, on glass substrates, the quality of the pattern was most strongly influenced by the step of bead mask formation, where the presence of multilayer beads during the deposition instead of mono-layers give rise to unspecific interaction of the proteins (see section 4.2.2.1), and thus a lot of variation in the contrast which explains the high standard deviations.

Polymer	PEO (x)	PPO (y)	Concentration (in ultra-pure water)
F-68	75-85	25-40	2%,4%,6%,10%
F-108	137-146	42-47	2%,4%
F-127	95-105	54-67	1%

Table 4.11 – **Different types of poloxamer and their concentrations, used in this project.** X is the number of PEO monomers and y is the number of PPO monomers.

To study the influence of the pluronic type on the transfer, the Nav patterns fabricated on glass, were transfered to the surface of native or glu Q Gel. Figure 4.34, shows that when using the F-127 1% or F-108 2%, 4% and 6%, for the fabrication of the glass master, no or very low transfer was observed on native Q Gel, we think, this is due to the length of the PEO chain that was higher than that of the protein on the glass master, which prevented the possibility of the protein to interact with the PDMS surface. In the case of F 68 2%, 6% and 10%, the transfer is seen to be achieved easily, but the contrast was dependent on the concentration of the pluronic, better contrast is obtained when increasing the concentration. When transfer to glu Q gel, the type of pluronic did not affect the transfer. Protein patterns where obtained on the PDMS, both when using the F-127 and F-68. This can be due to the presence of the glutaraldhehyde on the Q gel surface, that create a very attractive surface to the proteins. Finally, the pluronic F-68 with a concentration of 10 % was chosen to be used for the fabrication of the pattern on the glass master.

Figure 4.34 – **Epi-fluorescence images of neutravidin transfered to native or glu Q Gel after a glass master fabricated with different pluronic type and/or concentrations.** Finally, the pluronic F-68 with a concentration of 10 % was chosen to be used for the fabrication of the pattern on the glass master. Insets display Fourier transforms of the corresponding images. Care was taken to ensure same camera and image display conditions for all images.

4.5 Understanding the transfer process

In order to understand the molecular factors governing the transfer process, we quantified the effective force of adhesion of the protein to glass and elastomer using atomic force microscopy. We used an AFM cantilever with a 6 μm spherical tip attached to its end. The proteins, either bBSA-Atto or bBSA-TR were covalently bound to the AFM tip. The protein covered tip was approached to touch a test surface which was either bare clean glass, or bare elastomer (native Sylgard or p Sylgard), or glass coated with the same protein (for protein-protein cohesion force-measurements), then force-distance curves were recorded. Since we are interested in the protein adhesion to different surfaces, we focused on the pull-off force curve of each force measurement (for more details about the measurements see section 2.8.6). All measurements were conducted in water, at room temperature.

4.5.1 Effect of tip functionalization on tip/substrate interaction

Fluorescent bBSA was covalently linked to the AFM tip using a procedure involving glutarald-hehyde as a cross-linking agent (see section 2.8.6.1). Figure 4.35 a, summarizes the tip functionalization procedure steps. Prior to start measuring the interaction between the protein and the substrates, force measurements were performed after each functionalization step of the AFM tip to asses the involvement of the introduced functional groups on the interaction between the tip and the substrate surface. First, hydroxyl groups (-OH) following the plasma treatment of the tip, second NH_3^+ coming from the amino-silanization step with APTES , finally carbonyl groups C=O for the glutaraldhehyde treated tip. Plasma treated silicon oxide (SiO) tip, shows large adhesion with the cleaned bare glass (Figure 4.35 b), this can be due to hydrogen bonding between oxygen atoms on the SiO tip and hydroxyl groups on the bare cleaned glass surface. The APTES treated tip, terminated with protonated NH_3^+ group at neutral pH, shows attraction during approach, followed by tip-surface adhesion when retraction of the tip from the surface (Figure 4.35 c). The observed attraction can be explained by the electrostatic interaction between the positively charged tip and the negatively charged surface. The glutaraldhehyde treated tip, bearing carbonyl groups shows small adhesion with the hydrophilic glass surface (Figure 4.35 d). Finally, the bBSA-TR functionalized tip shows at the retraction curve multiple adhesion peaks (Figure 4.35 e). These initial force measurements were important, to confirm the protein interaction with the substrate surface, which will be discussed in more details below. The same measurements were also conducted on native Sylgard (Figure 4.35 g). The curves show that Sylgard have very strong non specific interactions with the AFM tip, which makes these measurements not amenable to interpretation.

At least two samples were tested for every step, and 100 curves were recorded at different position for each sample at two distinct regions and under the same conditions. The force curves (b-e) in figure 4.35, shows one typical curve for the ensemble of the force curves acquired, and the curves in (f) and (g) shows the superposition of 100 curves recorded on a region of a typical sample.
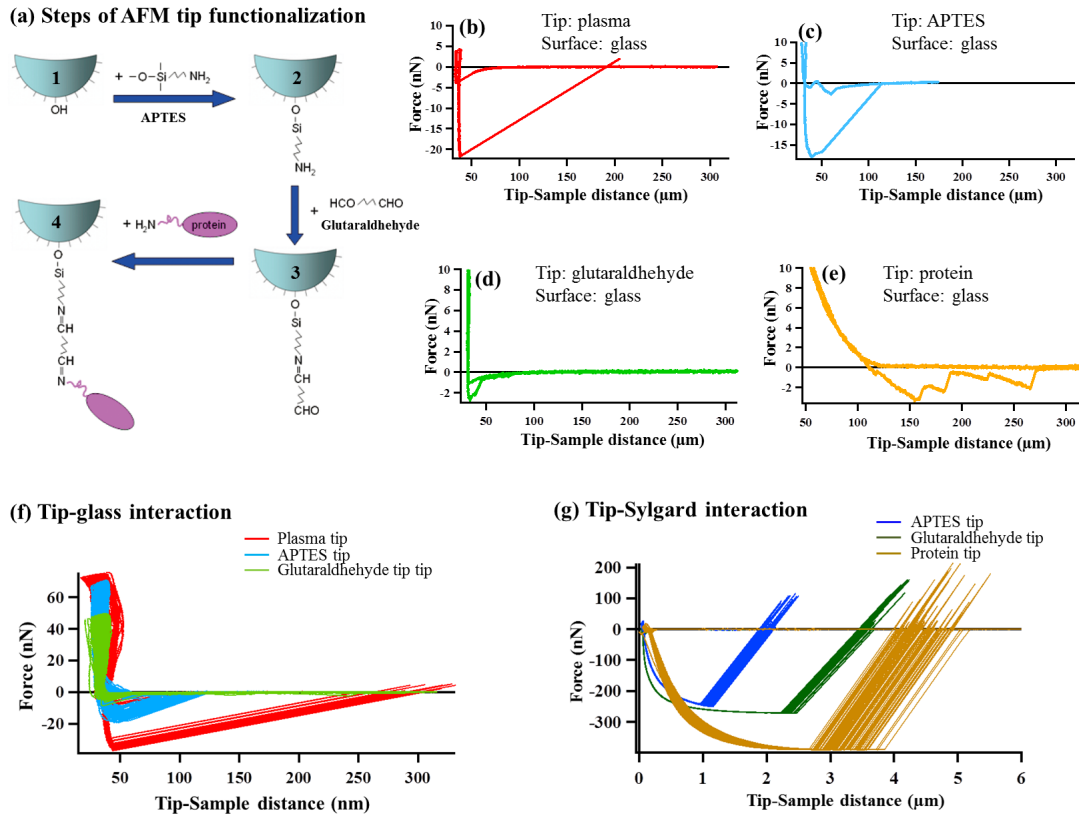
Figure 4.35 – **AFM measurement conducted on glass and Sylgard after each AFM tip-
functionalization step.** (a) Schematic of procedure for protein functionalization of the AFM
tip. (b-e) Force-curves conducted on bare cleaned glass at plasma treatment of the tip (step 1,
red curve), amino-silanization with APTES (step 2, blue curve), glutaraldhehyde treatment (step
3, green curve), and final coupling of the protein, here bBSA-TR (step 4, yellow curves). (f)
Overlay of 100 force-distance curves conducted on glass at step 1-3 of the tip-functionalisation.
(g) Overlay of 100 force-distance curves conducted on native Sylgard after amino-silanization with
APTES (dark blue curve), glutaraldhehyde treatment (dark green curve) and protein coupling
(dark yellow curve).

4.5.2 Pull-off force measurements of fluorescent bBSA on different surfaces

Depending on the interaction strength between the protein multilayers (called $F_{prt-prt}$), glass-
protein layer (called F_{g-prt}) and PDMS-protein layer (called $F_{PDMS-prt}$) (figure 4.36), the
transfer will or not occurs. Three different cases are possible:

1- If the glass-protein layer interaction (F_{g-prt}) is larger than PDMS-protein layer interaction
($F_{PDMS-prt}$), the proteins will stay on the glass substrate.

2- If the glass-protein layer interaction (F_{g-prt}) is smaller than PDMS-protein layer interaction
($F_{PDMS-prt}$), and the cohesion proteins-proteins ($F_{prt-prt}$) is larger than the glass-protein layer
interaction (F_{g-prt}) interaction, the proteins will transfer by peeling from the glass substrate.

3- If the glass-protein layer interaction (F_{g-prt}) is smaller than PDMS-protein layer interaction
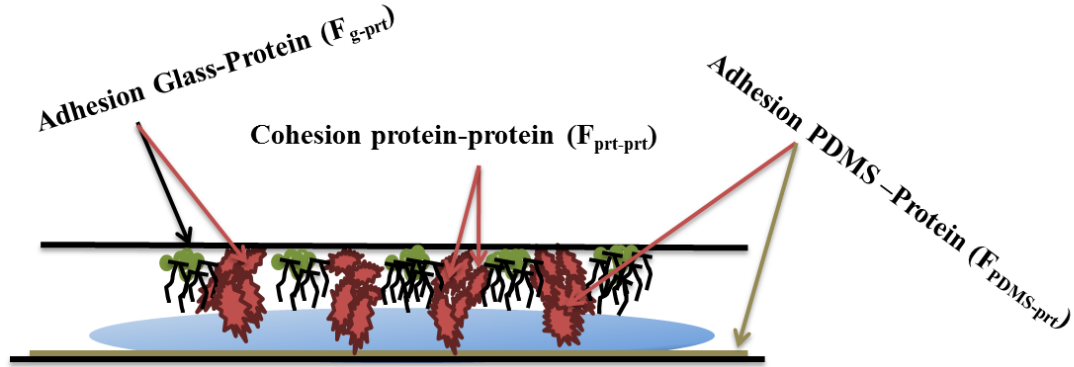
Figure 4.36 – **Schematic representation of the reverse contact printing process.**

$(F_{PDMS-prt})$, and the cohesion proteins-protein $(F_{prt-prt})$ is smaller than the glass-protein layer interaction (F_{g-prt}), just the top layers of the protein on the glass substrate will transfer to the PDMS surface.

In the following, force-curves were obtained in water, to quantify the cohesion force between layers of fluorescent bBSA and the interaction between glass-proteins layer (F_{g-prt}) and PDMS-proteins layer $(F_{PDMS-prt})$.

4.5.2.1 Protein-Protein interactions

AFM was used to measure the adhesion force between layer of fluorescent bBSA (either bBSA-Atto or bBSA-TR) immobilized on the AFM tip and fluorescent bBSA adsorbed on a glass surface. During AFM force measurements, the protein-coated cantilever is approached toward and then, after contact, retracted away from the substrate. The approach portion of the force curve gives informations about the attraction or the affinity that has the protein for the surface, the retraction portion represents, the pull-off force required to separate layers of proteins after contact.

Figure 4.37 shows representative curves of the force (nN) versus the relative distance of separation (nm) during the approach and retract of the fluorescent bBSA tip to the fluorescent bBSA coated surface. We observe, no attractive or repulsive interactions during the approach for both bBSA-Atto and bBSA-TR (Figure 4.37). The retraction curves corresponding to the pull-off forces seen in the figure, shows the breaking of the binding interaction between several proteins layers. After analysis of numerous force curves, the magnitude of the pull-off force for bBSA-Atto layers is found to be 9.5 ± 5 nN and for bBSA-TR, 4.6 ± 2.8 nN. Thus the force required to separate layers of bBSA-Atto is higher that that required to separate bBSA-TR layers. The dissipation energy, determined as the area between the approach and retract curves calculated to be $11 \pm 8 \ 10^{-16}$ N.m for bBSA-Atto and $8.6 \pm 7 \ 10^{-16}$ N.m for bBSA-TR.
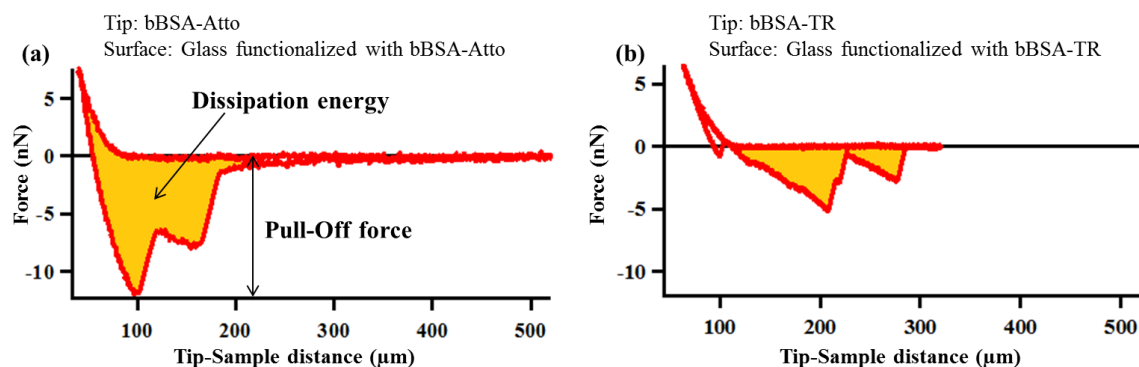
Figure 4.37 – **Representative force-curves of the interactions between fluorescent bBSA tip and fluorescent bBSA adsorbed on glass surface.** (a) bBSA-Atto. (b) bBSA-TR.

4.5.2.2 Protein-Substrate interactions

AFM force measurements, between the fluorescent bBSA coated tip and different substrates were carried out. During the measurements, the fluorescent bBSA functionalized tip, is brought repeatedly into contact with the substrate to initiate binding and the fluorescent bBSA/surface adhesion forces acting on the tip are detected as the tip is withdrawn from the substrate surface. Before each touch-down, the tip is displaced laterally by 2 μm. Typically, the initial 10 to 20 curves were non-reproducible and we interpret this as steps where protein layers were repeatedly transferred from the tip to the surface. Indeed, post experiment inspection of the surface with optical fluorescence microscopy clearly shows foot-print of the tip with diminishing fluorescence intensity. After these initial steps, the curves become highly reproducible and no more protein foot-prints are detectable on the surface. These curves are recorded for analysis. Overlay of 100 curves of force (nN) versus the relative distance of separation (nm) for fluorescent bBSA interacting with native Sylgard (Figure 4.38), bare cleaned glass (Figure 4.39 a,b) and plasma treated Sylgard (Figure 4.39 c,d) are shown.

Native Sylgard turned out to have a very strong non-specific adhesion with the tip functionalized either with bBSA-Atto or bBSA-TR (Figure 4.38), probably, this is due to van der Wall's interactions. These measurements were not amenable to interpretation.

In the case where the tip is functionalized with bBSA-Atto, interacts with a bare glass surface (Figure 4.39 a). On the approach curve, a repulsion is detectable, probably due to the negative charge on both the molecule and the bare glass. First, a soft contact is detectable before the hard contact with glass (slope vertical) is discerned. This is possibly due to formation of protein multilayers on the tip, which nevertheless are not shed on contact as verified with the procedure above. The adhesion force is determined from the retraction curve. When the tip is functionalized with bBSA-TR and interacts with a bare glass surface (Figure 4.39 b). On the approach curve, an attractive interaction is present and on contact, as expected for a monolayer of protein,

a slope corresponding to a hard surface is seen. As before, the adhesion force is determined from
the retraction curve. For a tip is functionalized with bBSA-Atto in contact with pPD surface
(Figure 4.39 c). Features are present on both the approach and the retraction curves, which
we interpret as corresponding to collective adhesion/de-adhesion of a protein-covered region on
the tip (which is a bead and therefore presents a large surface). As before, the adhesion force
is determined from the entire retraction curve, ignoring the fine features. Adhesion is strong.
Finally, when the tip is functionalized with bBSA-TR is in contact with pPD surface. Unlike
the previous case, fine features are absent and the adhesion is weak, as determined form the
retraction curve.

The adhesion forces calculated for bBSA-Atto and bBSA-TR with bare cleaned glass surface
and plasma treated Sylgard are summarized in table 4.12. The largest pull-off force and hence
strength of adhesion was observed between bBSA-Atto and p Sylgard (12.8 ± 1.7 nN), while less
adhesion was observed between bBSA-TR and p Sylgard (5.1 ± 0.6 nN). Instead, bBSA-Atto
and bBSA-TR show similar adhesion on bare cleaned glass (2.3 ± 0.8 nN and 2.7 ± 0.8 nN
respectively). Dissipation energies were calculated as the area between the retract and advance
curves. The values are shown in table 4.13.
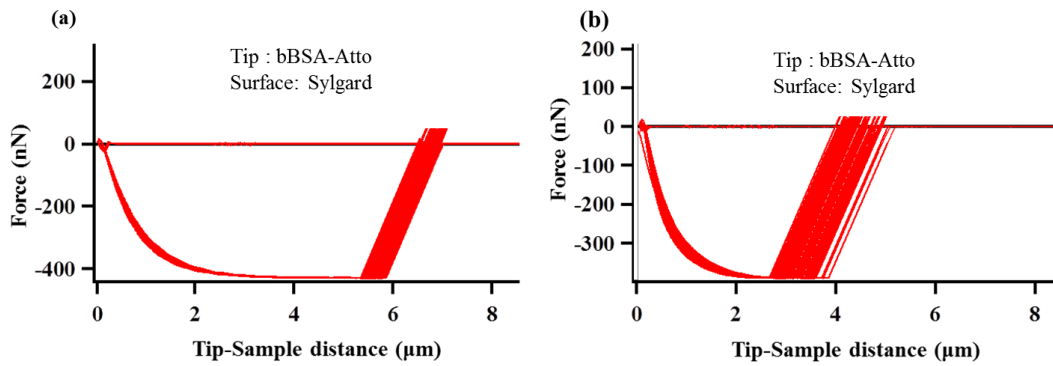
Figure 4.38 – **Force curves of the interaction between fluorescent bBSA and native
Sylgard.** (a) bBSA-Atto. (b) bBSA-TR.

	$F_{prt-prt}$ (nN)	F_{g-prt} (nN)	$F_{pSylgard-prt}$ (nN)
bBSA-Atto	9.5 ± 5	2.3 ± 0.8	12.8±1.7
bBSA-TR	4.6 ± 2.8	2.7±0.8	5.1±0.6

Table 4.12 – **Adhesion force measurements.** Each value is an average of 100 force curvesat
different location for each sample, at three distinct regions and for at least three different samples.
Errors are standard deviations.
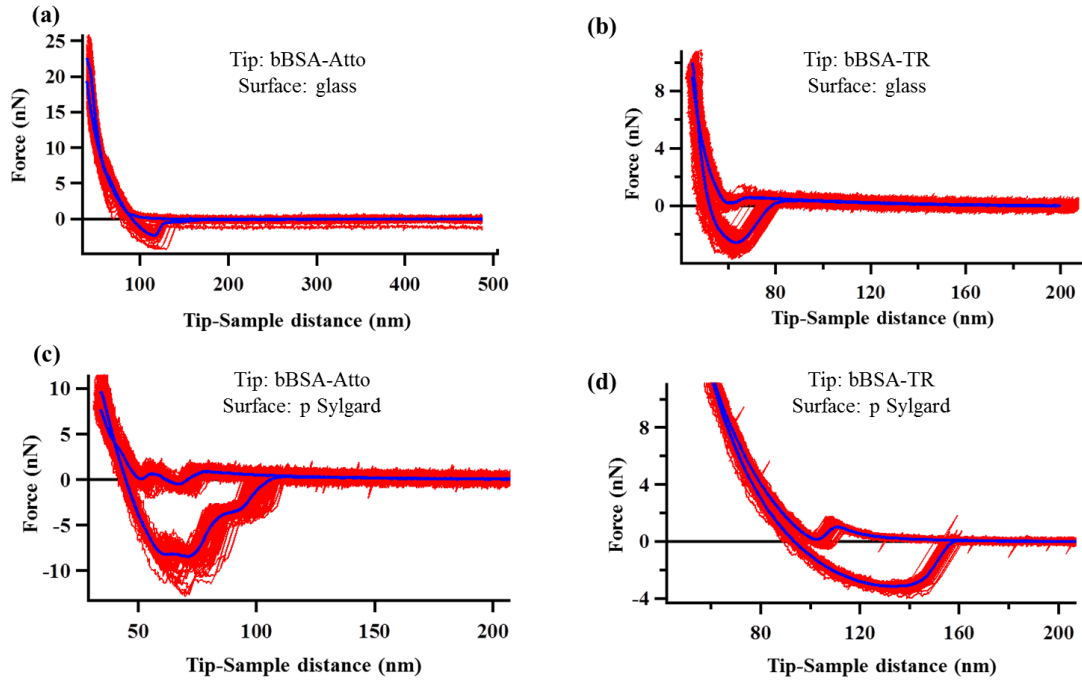
Figure 4.39 – **Force curves of the interaction between fluorescent bBSA and bare
cleaned glass or p Sylgard.** bBSA-Atto and bBSA-TR adhesion to : bare clean glass (a,b
respectively), plasma treated Sylgard (c,d respectively). Red lines are overlay of 100 force curves,
each at a different spot on the surface, and the blue lines are the median force curves.

	$E_{prt-prt}$	E_{g-prt}	$E_{pSylgard-prt}$
bBSA-Atto	11±8	0.35 ± 0.13	1.85±0.26
bBSA-TR	8.6 ±7	0.78±0.44	1.3±0.13

Table 4.13 – **Dissipation energy measurements.** Each value is an average of 100 force curves
at different location for each sample, at three distinct regions and for at least three different
samples. Errors are standard deviations. The value are in N.m 10^{-16}.

Protein	PDMS surface (Elasticity)	Width (nm)		Contrast		Tr ratio inside	Tr ratio outside
		Glass	PDMS	Glass	PDMS		
bBSA-Atto	Sylgard (2 MPa)	364 ± 27	353 ± 55	0.39 ± 0.04	≈ 0	≈ 0	≈ 0
bBSA-Atto	Q Gel (20 kPa)	365 ± 28	329 ± 82	0.47 ± 0.11	0.16 ± 0.041	0.38 ± 0.03	0.8 ± 0.018
bBSA-TR	Sylgard (2 MPa)	396 ± 7	377 ± 13	0.58 ± 0.055	0.49 ± 0.08	0.31 ± 0.066	0.57 ± 0.033
bBSA-TR	Sylgard (5 kPa)	472 ± 61	486 ± 100	0.35 ± 0.07	0.5 ± 0.16	0.52 ± 0.07	
bBSA-TR	Q Gel (20 kPa)	404.5 ± 26.6	349 ± 27	0.61 ± 0.07	0.59 ± 0.054	0.6 ± 0.14	0.6 ± 0.06
bBSA-Atto	p Sylgard (7 MPa)	380.44 ± 27.6	447.7 ± 29	0.46 ± 0.05	0.26 ± 0.09	0.6 ± 0.056	1
bBSA-Atto	p Q Gel (120 kPa)	467 ± 32	526 ± 101	0.46 ± 0.18	0.16 ± 0.06	0.46 ± 0.048	0.86 ± 0.027
bBSA-TR	p Sylgard (7 MPa)	377.14 ± 19	465.34 ± 25	0.67 ± 0.06	0.37 ± 0.044	0.36 ± 0.042	0.88 ± 0.082
bBSA-TR	p Q Gel (120 kPa)	410.8 ± 28	451 ± 86	0.44 ± 0.29	0.25 ± 0.024	0.33 ± 0.044	0.62 ± 0.046
Nav-TR	Q Gel (20 kPa)	406 ± 30	536 ± 85	0.55 ± 0.14	0.2 ± 0.05	0.24 ± 0.06	
Nav-TR	glu Q Gel	482 ± 33	495 ± 58	0.45 ± 0.1	0.25 ± 0.1	0.39 ± 0.24	

Table 4.14 – **Summary table of transfer ratio (Tr ratio), width and contrast of different proteins transferred from glass to different PDMS surfaces.** Fluorescent bBSA transferred to native PDMS (red rows), and to plasma treated PDMS (blue rows). Nav-TR transfer (green rows). Tr ratio inside: transfer ratio of proteins from the inside of the dot. Tr ratio outside: transfer ratio of proteins from the regions passivated with pluronic. p Sylgard: plasma treated sylgard, p Q gel: plasma treated Q Gel (see section 2.3.4). Q Gel+plasma+APTES+Glu: Q Gel chemically treated as described in section 3.2.2.1.

4.6 Mecanism of Transfer

The reverse contact printing technique developed in this study is characterized by direct printing of proteins from glass to a PDMS based polymer surface. To establish the technique, we characterized the transfer in terms of width, contrast and transfer ratio based on epi-fluorescence images of the protein patterns before and after the transfer (Table 4.14). We selected bBSA protein coupled to two different fluorophore either Atto 488 or Texas Red as a model for a detailed evaluation of the printed structures. We also demonstrated the versatility of our technique by printing different types of protein onto different PDMS surfaces and elasticity. Since understanding the transfer mechanism is essential to further develop the technique, we show that the success of reverse contact crucially depends on molecular parameters. The transfer can be strongly influenced by chemical modification of the core protein and/or the PDMS surface, and can be predicted from measuring the forces of adhesion and cohesion using atomic force microscopy. We show that the degree of hydrophobicity as well as the presence of ionic groups on both the PDMS and the protein are important molecular factors that govern the transfer.

AFM force measurements are done to understand the molecular factors that determine the transfer ratio. They provide information about the protein adhesion to different substrates and specifically, can give quantitative information on the magnitude of the adhesion forces. The adhesion force between the protein and the substrate surface is measured from the pull-off force of the retract curve, and is determined as the force required to mechanically detach the adhered protein from the surface. This measurements were difficult to be conducted on native Q gel PDMS, probably due to its extreme softness, and they show very strong non specific adhesion when interacting with native Sylgard (see section 4.5.2.2). These measurements were not amenable to explanation. However, force-curves could be consistently measured and interpreted for p Sylgard and bare cleaned glass.

Figure 4.39 shows the comparison of adhesion forces obtained for fluorescent bBSA tip interacting with a bare cleaned glass and fluorescent bBSA tip interacting with plasma treated Sylgard. A clear separation between the data of this two groups is observed. During the measurements, we used the same source of the AFM cantilever and the fluorescent bBSA, which indicates that the differences observed in the measured adhesion forces for this two groups, is due to the interaction between the proteins and the different surfaces, not to the interaction between the AFM tip and the proteins.

As seen in Table 4.12, we notice for both bBSA-Atto and bBSA-TR, the force required to separate a protein layer from glass (F_{g-prt}) is less than that required to pull apart two layers of protein ($F_{prt-prt}$). The dissipation energy goes into the same direction (Table 4.13). Therefore the protein multi-layers present on the dots on the glass master are transferred to the elastomer probably by peeling from glass instead of only the top most layer peeling off.

Comparing the adhesion forces of bBSA-TR and bBSA-Atto, we see that the latter has a stronger

interaction with p Sylgard; 12.8 ± 1.7 nN versus 5.1 ± 0.6 for bBSA-TR (Table 4.12). This is
consistent with the higher transfer ratio being 0.6 ± 0.056 for bBSA-Atto, and 0.36 ± 0.042 for
bBSA-TR (Table 4.14). From the molecular structure of Atto and TR (Figure 4.40), we expect
TR to be more hydrophobic than Atto, the latter having a net negative charge and an isolated
primary amine group that is prone to losing an anion. Therefore, the difference in the inter-
action of the two species with p Sylgard may be attributed to hydrophobic/hydrophilic forces.
We can also notice when looking on the force measurement curves in Figure 4.39, an attraction
of bBSA-Atto to the surface of p Sylgard in the approach curve, versus a slight repulsion from
the surface for bBSA-TR (Figure 4.39 c,d respectively). This means that bBSA-Atto has more
propensity to the p Sylgard than bBSA-TR.

Similar reasoning can be perused for all the transfer process reported in section 4.2. Table
4.15, represents a summary of section 4.2 describing the success or failing of the transfer of pro-
teins to the different PDMS substrates.
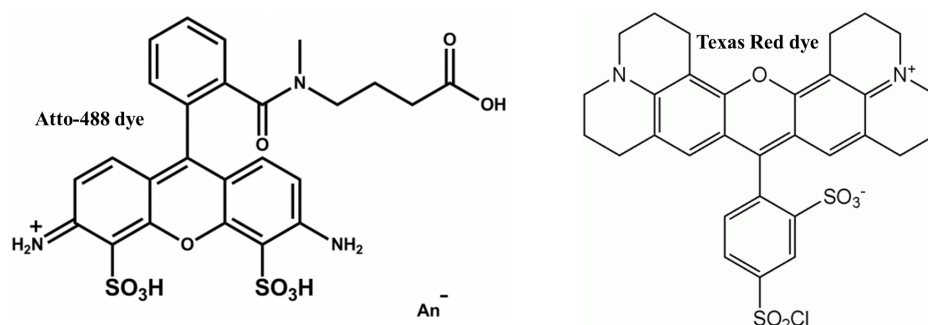
Figure 4.40 – **Chemical formula of Atto 488 and Texas red dyes.** Adapted from [278][280].

	Q Gel	p Q Gel	glu Q Gel	Sylgard	p Sylgard	CY	glu CY
bBSA-TR	ok	ok	NA	ok	ok	NA	NA
bBSA-Atto	ok	ok	NA	X	ok	NA	NA
bBSA	ok (very low)	NA	X	NA	NA	X	X
BSA-FITC	X	ok	X	X	NA	X	X
Nav-TR	ok	NA	ok	ok	NA	ok	ok
BSA-TR	ok	NA	NA	ok [215]	NA	NA	NA

Table 4.15 – **Protein Pattern Transfer from glass to different PDMS surfaces.** X
indicates that no transfer occurs, NA indicates data not available and ok refer to success of the
transfer.

As can be expected, lack of strong adhesion between the hydrophillic bBSA-Atto and the hy-
drophobic Sylgard is observed, which means that hydrophobic interaction does not play a major
role in bBSA-Atto interactions. The transfer to Sylgard is so feeble and can not be detected with
the standard camera settings, it can be detected with higher camera amplification (Figure 4.11) .
Furthermore, Sylgard is known to be slightly negatively charged in aqueous solution at neutral pH

[329], resulting in a additional electrostatic repulsion towards the negatively charged bBSA-Atto.

When in contact with Q Gel surface, bBSA-Atto does transfer to some extent (Transfer ratio = 0.38 ± 0.03). In fact, Q Gel is more hydrophobic than Sylgard as judged by contact angle measurements ($116° \pm 4$; $104° \pm 4$ for Q Gel and Sylgard respectively) and has phenyl groups in its chain which are not present for Sylgard. Thus, We can explain the success of transfer of bBSA-Atto to native Q Gel by noting that bBSA-Atto has many aromatic groups that may chemically interact with the phenyl groups on Q gel forming a $\pi - \pi$ interaction.

When looking on the transfer of bBSA-TR, we see that it transfers well on both hydrophobic native Sylgard and Q Gel, with transfer being better on the latter, Transfer ratio = 0.31 ± 0.067, 0.6 ± 0.14 on Sylgard and Q Gel respectively (Table 4.14). Hydrophobic interaction plays a central role in the transfer of bBSA-TR to Sylgard and Q Gel. Moreover, texas red dye holds more aromatic group than Atto (Figure 4.40), which explains its stronger interaction with Q gel. This is proved by the higher transfer ratio of bBSA-TR with Q Gel (0.6 ± 0.14) than that of bBSA-Atto (0.38 ± 0.03). Consistent with this, BSA (non biotinylated) conjugated to FITC dye (BSA-FITC) supposed to be hydrophilic, shows a good transfer to p Sylgard with a transfer ratio of 0.58, and fails to transfer to native Sylgard. BSA (non-biotinylated) conjugated to texas red dye (BSA-TR) shows successful transfer to native Sylgard.

The transfer of bBSA not conjugated to any fluorophore, can not be directly tested due to the absence of fluorophore (section 4.2.2.1), thus the transfer ratio of bBSA can not be reported. Its presence was revealed by functionalization with fluorescent neutravidin to asses the quality of the pattern. The experiments show that bBSA failed to transfer to CY, and have a very unreliable transfer to Q Gel. We can conclude that bBSA probably expose its hydrophilic groups when adsorbed to glass.

To confirm the general hypothesis that the inclusion of the texas red dye renders the protein more amenable to transfer on hydrophobic untreated elastomers, we checked that Nav-TR transferred well on all the elastomers studied here (Table 4.15). However, probably due to drying, the transferred neutravidin was not functional and failed to bind to a biotinylated protein.

In a related set of experiments we functionalized the plasma treated elastomer surface (p CY and p Q gel) with APTES ((3-Aminopropyl)triethoxysilane) and glutaraldehyde, which is known to render the surface hydrophobic and support strong and stable covalent linkage of the protein [318] [319][39]. The hydrophobic Nav-TR, transfered well on this type of surface, but hydrophilic bBSA and BSA-FITC showed a very low transfer, demonstrating that even when covalent bonds are eventually formed, the initial transfer is governed by physico-chemical affinity.

Chapter 5

Cells on homogeneous and patterned PDMS

This chapter deals with the response of T-cells to soft substrates. In section 1.1.5, the response of cells to soft substrates is discussed. Cells like fibroblasts, epithelial cells or myocytes adhere and spread more on harder than on softer substrates [66][28][330][331]. For T-cells however, there are very few studies and the evidence is contradictory. Using naive mouse T-cells on polyacrylamide (PAA) gels with elasticity ranging from 10 kPa to 200 kPa, shows that cells are more activated on stiffer substrates [126]. However experiments using the human cell line Jurkat on silicone rubber (PDMS) with stiffness ranging from 100 kPa to 5000 kPa, show the opposite trend [127]. In terms of force application, Bashour et al. show that forces of about 100 pN can be exerted through the TCR complex [128], and preliminary evidence suggested that on PAA at least, more force is exerted on harder substrates [129]. In all these experiments, the adhesion was fully or partly mediated by the TCR complex. Recently, it was shown that indeed the anti-CD3 domain of the TCR complex mediates mechano-sensing in T-cells [332] [333] [334]. Here, we shall first explore the interaction of Jurkat cells with PDMS of different stiffness and covered with anti-CD3[1]. Next, we shall choose one elasticity and explore the behavior of Jurkat T-cells on patterned PDMS .

5.1 T-Cell on homogeneously functionalized PDMS substrates

In this section, we describe the adhesion of T-cells to homogeneously functionalized PDMS. PDMS was chosen as substrate of interest based on the ability to readily modulate its elastic modulus. Several types of PDMS were used to achieve the experiments, which together cover the elastic modulus range from 1 kPa to 40 MPa. Table 5.1 summarizes all the PDMS used for these experiments and their relative elastic Modulus.

PDMS Type	Base:current agent; Ratio	Elasticity (kPa)
CY	1:1	3 ± 1
	1:2	300 ± 150
	1:4	40000 ± 8000
Sylgard	10:1	2440 ± 500
	35:1	130 ± 9 [71]
	58:1	5 [335]
Q Gel	1:2	20 ± 3
	1:1.1	3.7 [264]

Table 5.1 – **Summary table of PDMS used for cell studies and their relative elasticity.** The PDMS elasticity were either calculated from AFM force measurements (section 2.8.5), or taken from references indicated between bracket.

The different PDMS substrates were prepared as described in section 2.3.2, and biotinylated anti-CD3 was adsorbed to the surface of the PDMS after functionalization steps with bBSA and Nav (see section 2.6). This provides a system for activation of T-cells on substrates with

---

[1]This part of the work was done in close collaboration with Astrid Wahl.

varying elastic modulus. Cell adhesion area, actin organization, TCR and ZAP-70 distribution were studied on the different PDMS.

Prior to each experiment, quantitative measurements of adsorbed Nav-TR were done. The measurements indicate that the per-area amount of Nav-TR adsorbed onto PDMS substrates was 20 to 30 molecules/μm^2, as verified by relative fluorescence intensity. This amount is equivalent for all substrates, and independent of the substrate rigidity.

5.1.1   Effect of PDMS Elasticity on cellular Adhesion

We examined the contact area of Jurkat T-cells adhered to different types of PDMS with varying elasticity. Cells were allowed to interact with the different substrates for 20 minutes and were imaged with RICM (as explained in section 2.9.3), to determine the region of contact between the proximal surface of the cell and the substrate surface. The region of contact is called the contact zone, and the area of this zone is called the contact area and is a measure of cell spreading. Note that the cell membrane in the contact zone, may not be tightly adhered everywhere, but we consider that it potentially interacts closely with the substrate. The cell contact area is seen to be dependent on the elasticity of the PDMS, and the extent of cell spreading is quantified using a macro written in-house in ImageJ/Fiji (see section 2.10.2).

Figure 5.1 shows the adhesion area of cells on CY, Sylgard and Q gel of varying elasticity. In the case of **CY**, the cells adhering on the soft 3 kPa CY occupied 1.8 times larger area than cells adhering to the CY with a medium elasticity of 300 kPa, and 3.5 times larger area than those adhering to the hard CY owing an elasticity of 40 MPa (Figure 5.1 A). However, as we discussed in section 4.1.3, the CY (1:2; 300 kPa) and the CY (1:4; 40 MPa) show a viscoelastic behavior, and therefore we subsequently decided to not consider these two types of PDMS.

Cells adhering on **Sylgard** with varying elasticity show similar behavior as that of CY; the cell adhesion area decreases with increasing stiffness of the substrate: 330 ± 130 μm^2 for soft (5 kPa), 270 ± 110 μm^2 for the medium (140 kPa) and 200 ± 90 μm^2 for the hard Sylgard (2 MPa) (Figure 5.1 B).

Finally, on the third type of PDMS, **Q Gel** (1:2/ 20 kPa), cells show an adhesion area of 300 ± 110 μm^2 (Figure 5.1 C). Measurements on softer Q gel (1:1.1), with an elasticity of 3.7 kPa, show a higher adhesion area comparable to that on Sylgard 5 kPa and CY 3 kPa (data not shown).

We can hypothesize that cell adhesion is independent of the type of PDMS used, therefore of the chemical composition of the PDMS. It however depends on the substrate elasticity. Cells are seen to spread more on softer than on harder substrates when the cell-substrate interaction is mediated via the T-cell receptor. Figure 5.2 B shows a nearly similar spreading area on 3 and 5 kPa PDMS, this area decreases simultaneously when passing to the 20 kPa, 140 kPa and 2 MPa PDMS.
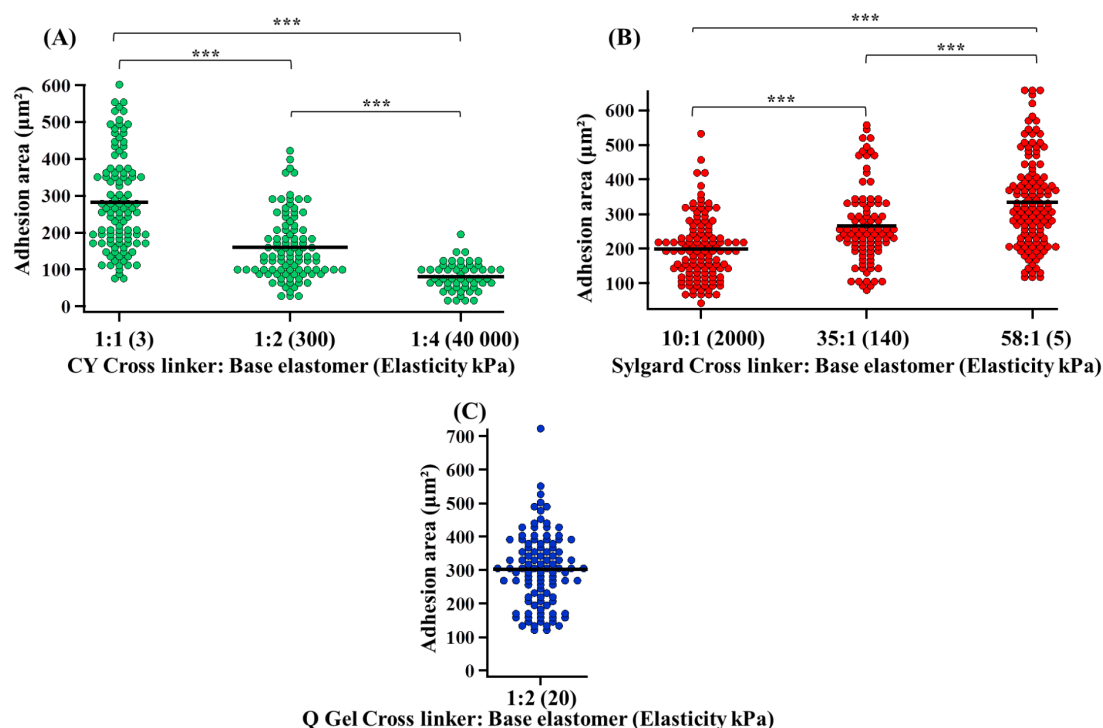
Figure 5.1 – **Scatter dot plots of cell adhesion area determined from segmentation of RICM images of cells adhering on three different types of PDMS with varying elasticity.** (A) On CY. (B) On Sylgard. (C) On Q Gel. The results of three independent experiments (with at least 30 cells) were pooled for each condition. Bar= median value. ***: P < 0.01.

5.1.2   Actin Cytoskeleton organisation, TCR and ZAP-70 distribution

Actin organization, TCR and ZAP-70 distribution were evaluated for cell spreading on different PDMS with varying elasticity. For this, cells were allowed to interact with the different substrates for 20 minutes, fixed and then labeled. FITC-conjugated phalloidin was used for actin cytoskeleton staining, TCR molecules were revealed by labeling with a fluorescent antibody against the β chain of the TCR molecules (anti human anti-Vβ8 TCR) and finally Alexa-Fluor 647 mouse anti ZAP-70 was used for labeling the ZAP-70 signaling kinase.

5.1.2.1   Actin Organisation

The architecture of actin cytoskeleton was imaged with TIRF-M on different substrates with varying elasticity. Visual inspection of the images shows an actin organization, which is depleted at the center and enriched at the periphery, independent of substrate rigidity (Figure 5.3-5.5). Cells spreading on CY (1:1; 3 kPa) and (1:2; 300 kPa) show strong enrichment of actin at the periphery of the contact zone, concomitant with a depletion at the center (Figure 5.3). This is also observed for cell spreading on Sylgard where a peripheral distribution of actin is noticed on the 2 MPa, 140 kPa and 5 kPa Sylgard (Figure 5.4). Similarly, cell spreading on Q Gel shows
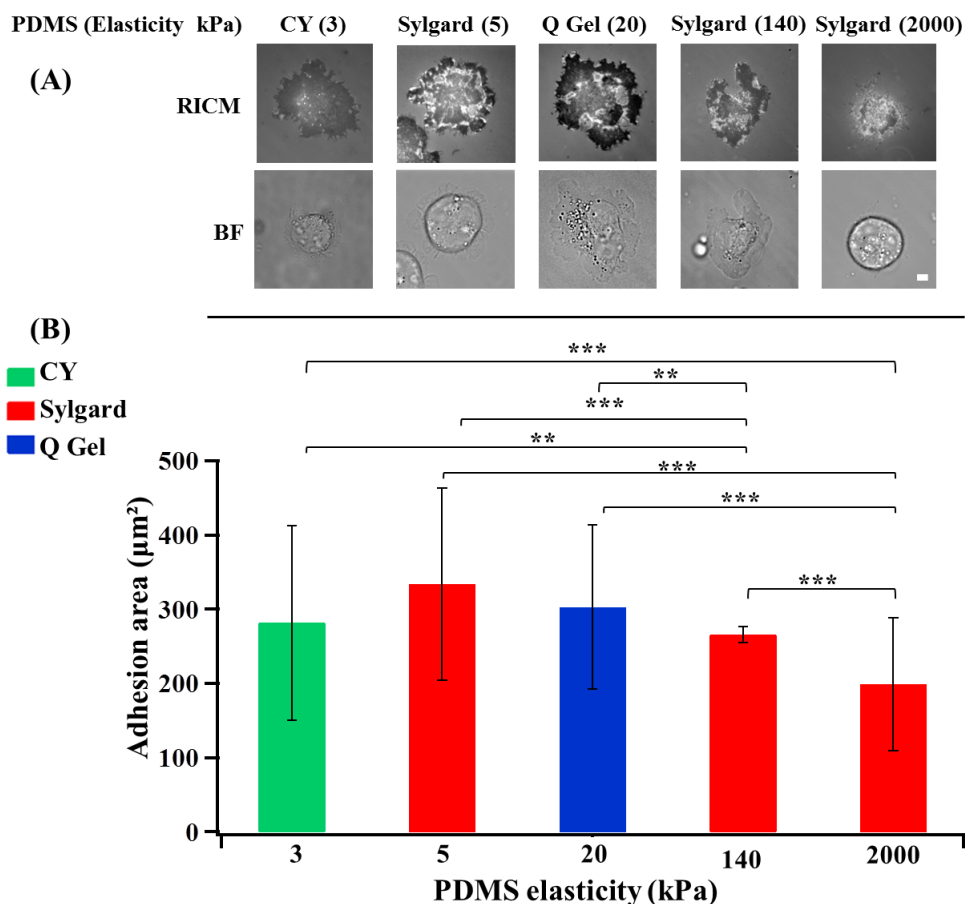
Figure 5.2 – **Cell adhesion area of cells adhering on different PDMS substrates of varying elasticity.**. (A) Bright-field (BF) and RICM images of cell spreading on PDMS of varying elasticity. Scale bar: 4 μm. (B) Mean cell adhesion area calculated from RICM images, error bar = standard deviation. ***: P < 0.01, ** P < 0.05.

actin located at the periphery (Figure 5.5). Structures resembling to lamellipod are observed on the different substrates, specially dominant on Q Gel, where they may be present along with filopodial structures.

5.1.2.2 TCR and ZAP-70 distribution

TCR and ZAP-70 distribution were imaged in TIRF-M for cell spreading on the different substrates (Figure 5.3-5.5). Visual inspection of the images shows TCR is distributed uniformly on all the different substrates. Individual μ-clusters are not detectable. Following the TCR distribution, we looked into the organization of the ZAP-70 which is one of the first molecules to be recruited by the TCR complex following activation. ZAP-70 is seen to be distributed homogeneously on the different substrates, similarly to the TCR and independently of the PDMS rigidity (Figure 5.3, 5.4). Nevertheless, we can note that the ZAP-70 distribution is more clustered than that of the TCR demonstrating the recruitment of ZAP-70 in form of clusters at the membrane.
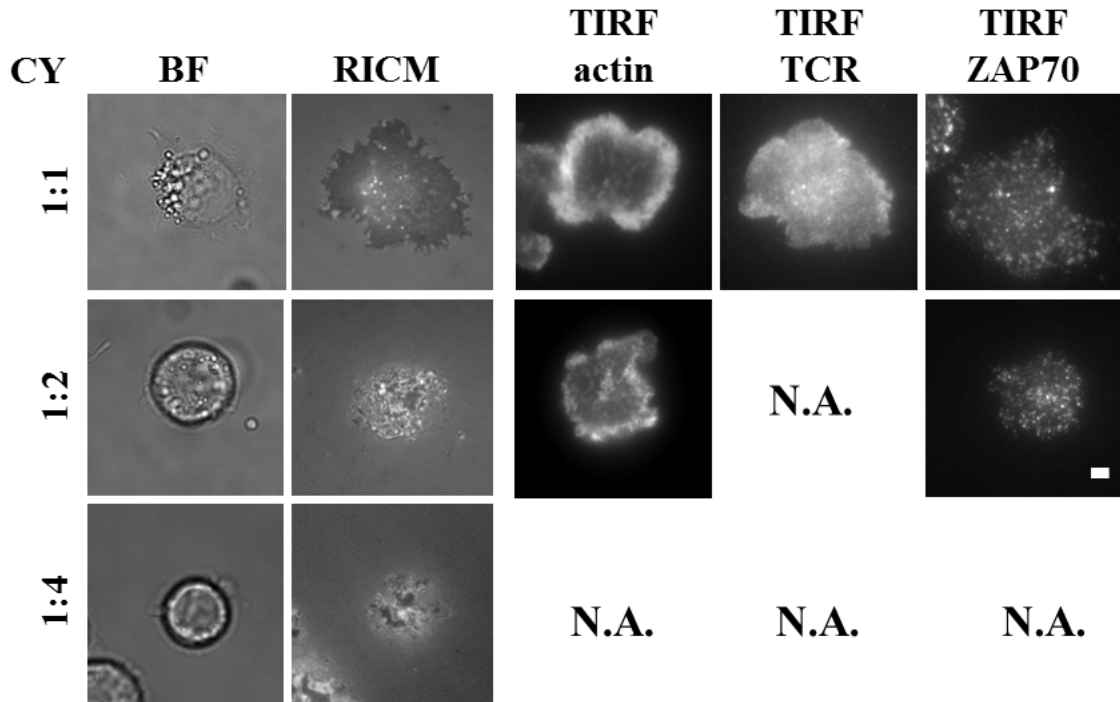
Figure 5.3 – **BF, RICM and TIRF-M images of cell spreading on CY with varying elasticity.** For TIRF-M images, TCR, ZAP-70 and actin were marked. Scale bar: 4 μm. N.A. indicates data not available.

5.1.3 Cell elasticity measurements

Inspired from the study done by Solon et al. on the elasticity of fibroblast cells as a function of the underlying substrate elasticity [28], we decided to measure the Jurkat T-cell elasticity on different substrates including glass and soft PDMS. For this, force measurements were done using a combined AFM/optical microscope system [2]. Figure 5.6 A, shows a scatter dot plot of the obtained T-cell elasticity as a function of the underlying substrate elasticity for experiments done during two different days. We observe that the elasticity of cells on glass substrate is higher than that on the soft PDMS substrates. This is correlated with results obtained by Solon et al. for fibroblast cells, which were harder on hard substrates. Figure 5.6 B, shows the variation of the cell elasticity as a function of the cell adhesion area. The stiffness is also seen to be weakly correlated with the cell adhesion area. We observe an increase in stiffness from 107 Pa to 216 Pa, for an increasing in the area from 217 μm^2 to 317 μm^2 (Table 5.2). However this measurements are just initial measurements done on one sample for each type of substrate. More experiments are required to confirm the results. It should also be noted that force measurements on hard PDMS, where cells adhere very weakly, could not be carried out correctly. In fact, AFM force curves on soft, weakly adhered objects is highly challenging. However, for a full understanding it is imperative to device a way to compare the soft PDMS with the hard PDMS (rather than

---

[2]This part of the work was done in close collaboration with Pierre Henri Puech, Laurant Limozin and Astrid Wahl in "Laboratoire Adhésion et Inflammation"
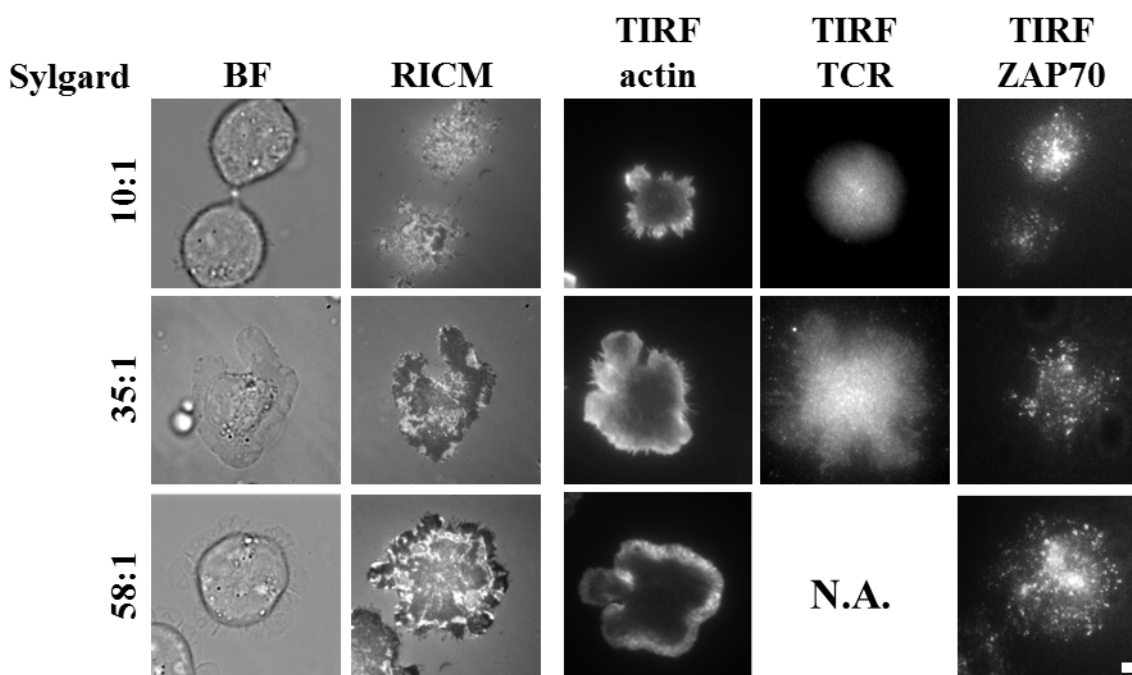
Figure 5.4 – **BF, RICM and TIRF-M images of cell spreading on Sylgard with varying elasticity.** For TIRF-M images, TCR, ZAP-70 and actin were marked. Scale bar: 4 μm. N.A. indicates data not available.
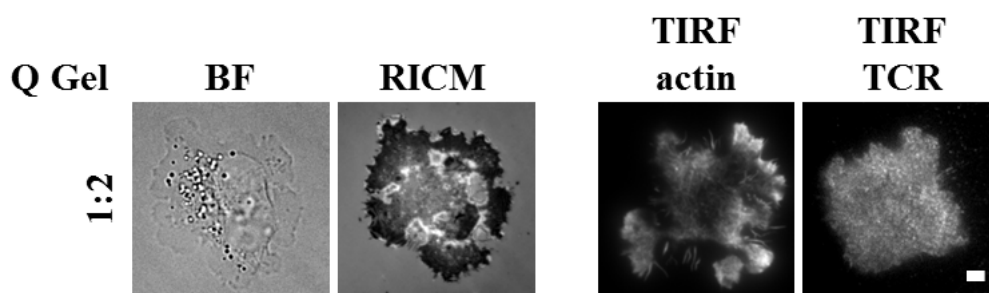
Figure 5.5 – **BF, RICM and TIRF-M images of cell spreading on Q Gel with varying elasticity.** For TIRF-M images, TCR, ZAP-70 and actin were marked. Scale bar: 4 μm.

glass). Our new experiments with optical tweezers[3] point to a promising alternative for such mechanical measurements.

---

[3]This part of the work was done in close collaboration with Pierre Henri Puech, Laurant Limozin and Astrid Wahl in "Laboratoire Adhésion et Inflammation"
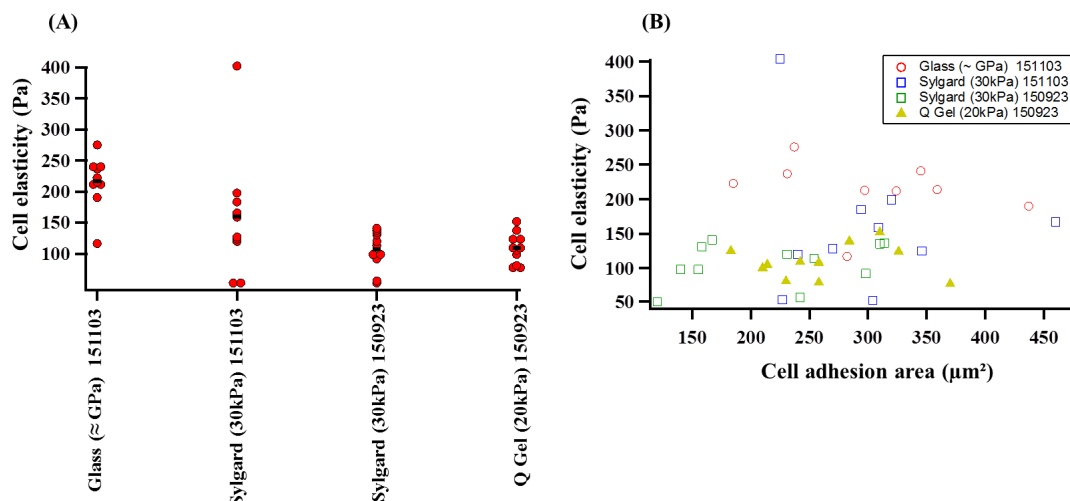
Figure 5.6 – **Cell elasticity as a function of substrate elasticity or cell adhesion area.**
(A) Cell elasticity as a function of substrate elasticity. The data in abscissa are represented as
follows: type of the substrate (elasticity) date of the experiment. Each point is the mean stiffness
of a single cell plotted against the underlying substrate. Bar = mean value. (B) Cell elasticity
as a function of cell adhesion area.

Substrate (elasticity) date of the experiment: year/month/day	Cell elasticity (Pa)	Cell adhesion area (μm^2)
Glass ($\sim$ GPa) 151103	216 $\pm$ 42	317 $\pm$ 92
Sylgard (30 kPa) 151103	159 $\pm$ 99	300 $\pm$ 66
Sylgard (30 kPa) 150923	107 $\pm$ 31	217 $\pm$ 72
Q Gel (20 kPa) 150923	118 $\pm$ 31	262 $\pm$ 53

Table 5.2 – **Cell elasticity and adhesion area on different substrates.** Values are averages
for measurements done on at least 10 cells.

5.2 T-Cell ON Patterned Substrate

PDMS substrates were often used, micropatterned with ECM proteins in order to control cell
adhesion and interaction [336]. However, patterning soft substrates such as gels, with an elastic
modulus < 100 kPa, presents an engineering challenge. This kind of substrates are shown to be
difficult to pattern with techniques such as microcontact-printing without requiring additional
fabrication steps [337, 158]. Here, we were able to pattern soft PDMS substrates (elasticity < 50
kPa) with different kinds of proteins at it was seen in chapters 3 and 4.

The patterned substrates are used as support for experiments on T-cells. Since Q gel (20 kPa)
patterned with bBSA-TR shows better transfer ratio (0.6 $\pm$ 0.14) in comparison with the one
patterned with bBSA-atto (0.4 $\pm$ 0.03) (see section 4.2.2.1), we chose to use it as system of
choice to study the influence of such patterns on T-cell behavior, and their compatibility with
advanced optical imaging (RICM and TIRF-M). For this, bBSA-TR patterned Q gel 20 kPa
substrate is subsequently functionalized with fluorescent neutravidin, after a blocking step with
pluronic F-127, then further incubated with biotinylated anti-CD3 (see section 3.2.4), which will
specifically bound to the neutravidin and targets the TCR at the same time. This substrate

will be called **soft pattern/pluronic**. We should note that the PDMS surface maintains the patterned proteins over a prolonged period (several days), even though the proteins were not covalently linked to the PDMS.

In addition to bBSA-TR patterned Q Gel substrate, four different substrates were used:

1- Positive control, called **POS**, composed of Q gel 20 kPa substrate with homogeneous ligand distribution without patterning (section 2.6.1).

2- bBSA-TR patterned Q gel substrate functionalized with non fluorescent bBSA outside the dots (after patterning the Q gel surface with bBSA-TR, non fluorescent bBSA was added all over the surface). This substrate shows therefore homogeneous distribution of ligands similar to the positive control. It will be called **soft pseudo-pattern/bBSA**.

3- Glass substrate patterned with anti-CD3 in a sea of pluronic acid as described in section 3.1.4.1. It will be called **glass pattern/pluronic**.

4- Negative control, called **NEG**, composed of Q gel 20 kPa substrate functionalized with pluronic F-127.

Cells were allowed to interact with these substrates, were then fixed after spreading, stained, observed and, imaged with RICM and TIRF-M.

The objective of this part is to compare cell adhesion on homogeneously functionalized and patterned soft Q Gel substrates, and also to compare the difference of cell behavior on glass patterned substrates and Q gel patterned substrates. Four major cell parameters are analyzed using the different substrates described above. These parameters include, average cell density, cell adhesion, actin cytoskeleton organization and overall TCR distribution.

5.2.1 Average Cell Density

The average density of cell on Q gel substrates was determined by enumerating the number of cells in a field view (Figure 5.7, a-c) divided to the total surface of the field selected (Figure 5.7, d). At least 25 fields view are analyzed for each sample case. As expected, the cell density on POS substrate ($0.25 \pm 0.15/1000 \ \mu m^2$) was higher than the soft pattern/pluronic ($0.2 \pm 0.08/1000 \ \mu m^2$). In fact, on POS substrate, anti-CD3 is distributed homogeneously all over the substrate which allow an effective adhesion thanks to TCR/anti-CD3 interaction.

The highest cell density was observed for the soft pseudo-pattern/bBSA ($0.4 \pm 0.2/1000 \ \mu m^2$). Here, non fluorescent bBSA was added to the substrate, covering all its surface, in addition to the bBSA-TR already present in a form of pattern. Thus, neutravidin and anti-CD3 should be distributed all over the surface. Therefore a surface similar to the positive control should be created with a higher ligand density than that of the POS and soft pattern/pluronic substrates. This could explain the higher cell density for soft pseudo-pattern/bBSA in comparison with the latter substrates.

The soft pattern/pluronic substrate, shows as expected, the lowest cell density ($0.2 \pm 0.08/1000 \ \mu m^2$). Here, neutravidin and anti-CD3 are grafted only on the bBSA-TR dots, forming a regular
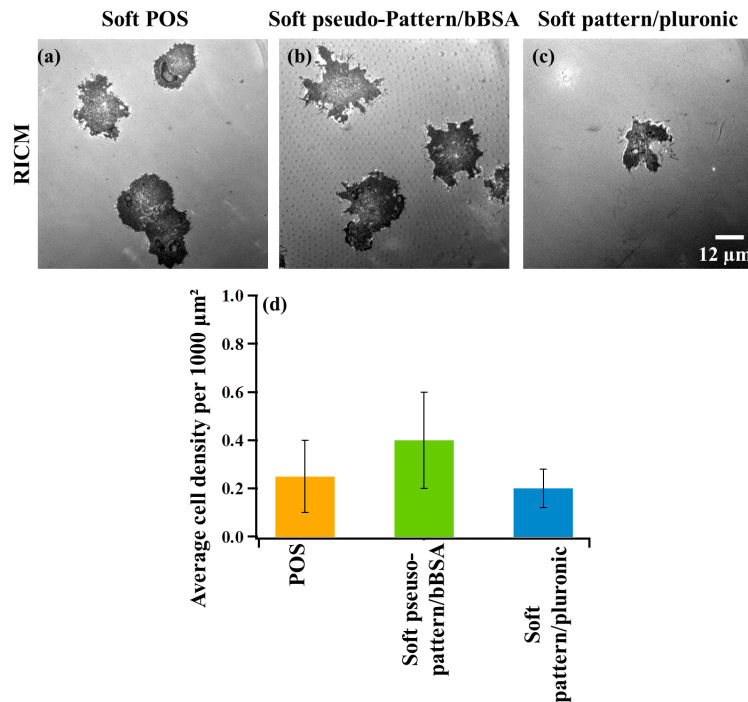
Figure 5.7 – **Average T-cell density on three different substrates.** (a) On homogeneous substrate. (b) On soft pseudo-pattern/bBSA substrate. (c) On soft pattern/pluronic substrate. (d) T-cell distribution per 1000 μm^2.

array of anti-CD3 pattern, separated by a sea of pluronic acid. Thus the ligand distribution here is lower than that of the POS and soft pseudo-pattern/bBSA substrates, which explains a lower cell adhesion mediated by the TCR/anti-CD3 interaction.

5.2.2 Cell Adhesion Area

Cells were allowed to interact with the different substrates, for 20 minutes on controls and 30 minutes on patterns (section 2.7.3), due to the slower dynamics of spreading on the patterns as compared to homogeneously coated substrates [113]. The cell is at its peak spread area at thirty minutes. The cells where then imaged with RICM, and the cell adhesion area was determined using a macro written in-house in ImageJ/Fiji (see section 2.10.2).

As described in section 5.1.1, the contact zone is imaged with RICM, and the contact area is quantified. Previous studies have demonstrated that the cell contact area depends strongly on the ligand density [113]. This was also observed in our experiments, where cells tend to spread better on substrates with higher ligand density. Quantification of the contact area (Figure 5.8) shows that the adhesion area on POS substrates (300 ± 20 μm^2) was similar to that for the soft pseudo-pattern/bBSA substrates (290 ± 35 μm^2). As expected, the soft pattern/pluronic substrates shows an adhesion area of cells (195 ± 20 μm^2) lower than the two previous substrates. The NEG control shows few cells adhering to the substrate with an adhesion area of 70 ± 40
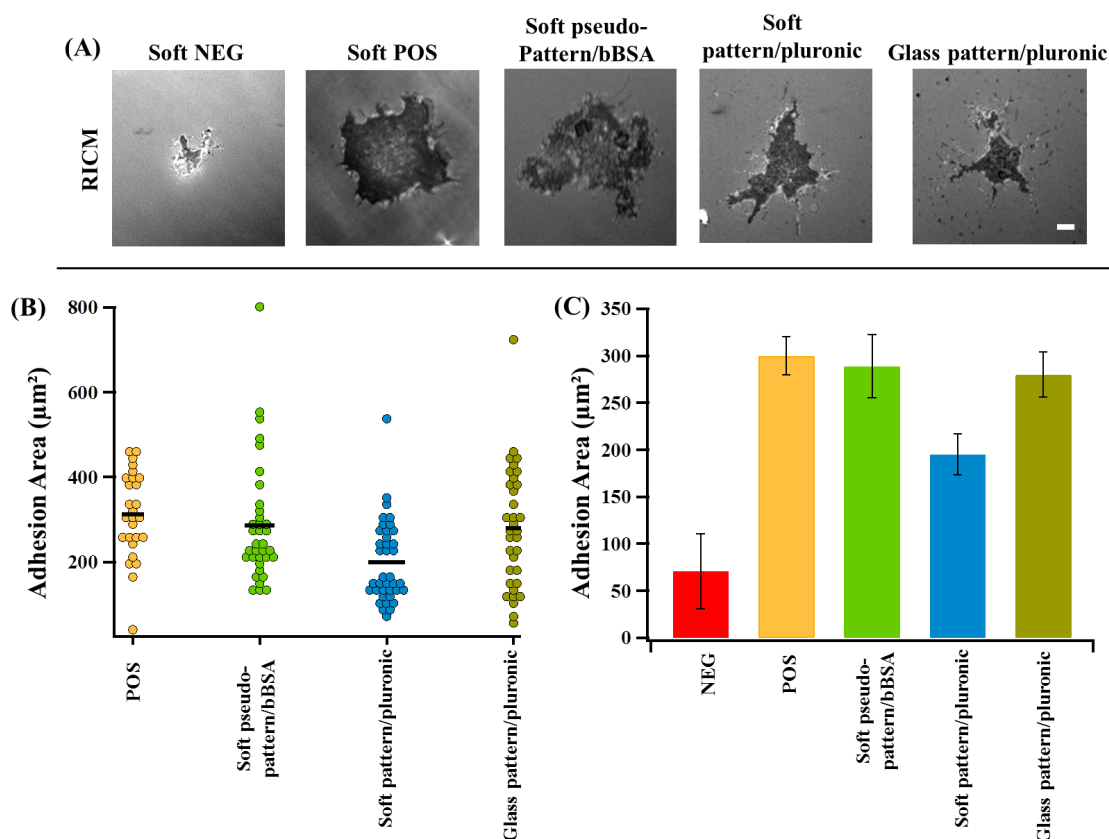
Figure 5.8 – **Cell adhesion area determined from segmentation of RICM images of T-cells adhering on different substrates.** (A) Examples of RICM images of cells spreading on different substrates. Scale bar = 4 μm. (B) Scatter dot plot of cell adhesion area on different substrates, bar = median value. (C) Mean cell adhesion area calculated from RICM images, error bar = standard deviation. At least two independent experiments were used for each case and at least 30 cells for each experiment.

μm^2, which confirms the repeating property of the pluronic and preventing cell adhesion.

When comparing the cell adhesion area on Q gel soft pattern/pluronic (195 $\pm$ 20 μm^2) to that of glass pattern/pluronic (280 $\pm$ 25 μm^2), we observe that it is higher on the latter. This can be explained by the greater ligand density on glass pattern/pluronic, seen that after the transfer of the protein from the glass pattern to the PDMS, the ligands density on PDMS is lower.

5.2.3 Actin cytoskeleton and TCR distribution

The influence of patterning soft substrates on actin organization and TCR distribution of T-cell is evaluated, and is compared with results obtained on homogeneously functionalized soft Q Gel substrate and glass patterned substrate. For this, cells are allowed to interact with the different substrates, fixed and then either labeled with phalloidine conjugated fluorescein, in order to mark the actin; or labeled with a fluorescent antibody against the β chain of the TCR molecules

(anti-human anti-Vβ8 TCR).
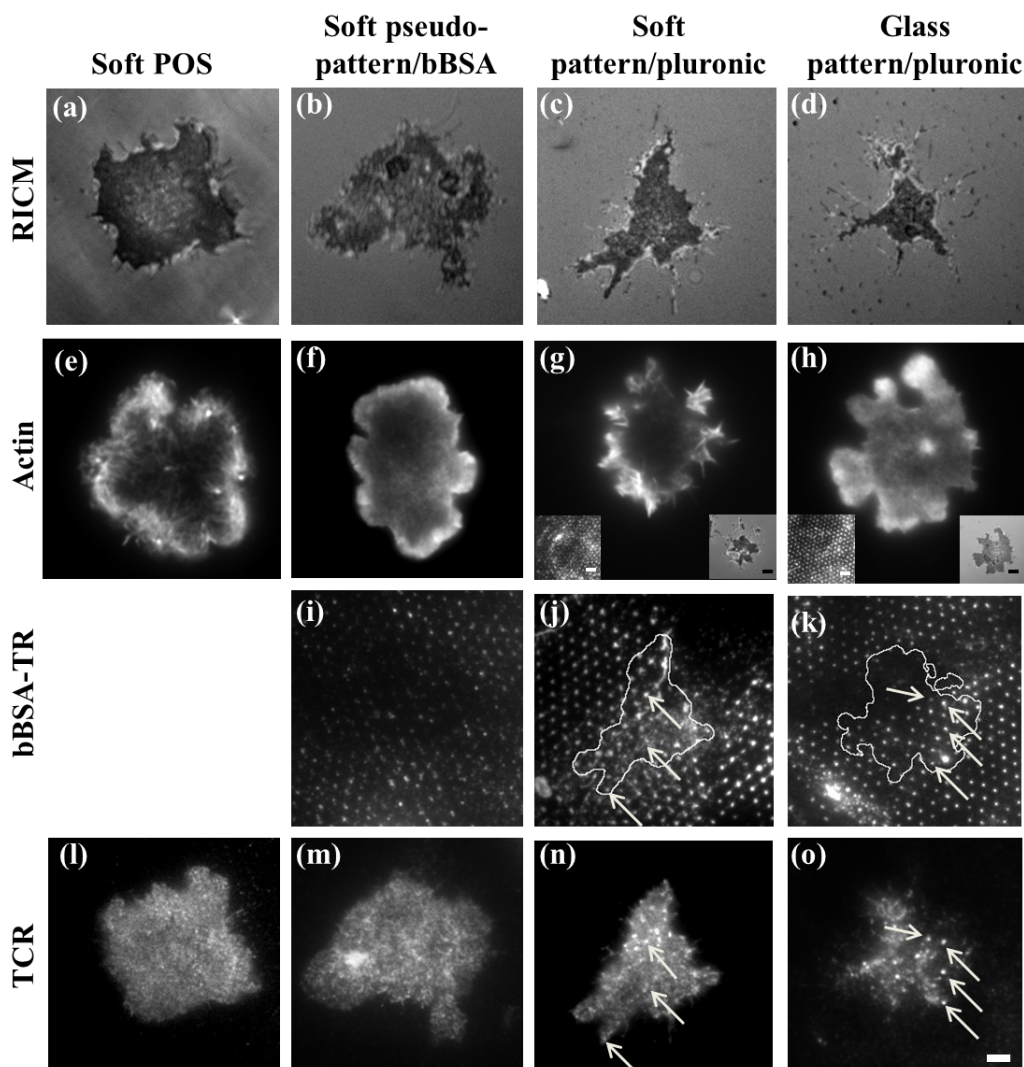
Figure 5.9 – **T-cells adhered to different surfaces, observed after 30 minutes of spreading followed by fixation.** (a-d) Examples of RICM images of cells adhering on different substrates. (e-h) TIRF-M of actin organisation on different substrates. Insets corresponds pattern (left) and RICM (right). Scale bar = 4 μm. (i-k) Epi-fluorescence images of bBSA-TR patterns. (l-o) TCR distribution on different substrates. Note that arrows point to TCR micro-clusters and corresponding anti-CD3 dot in the underlying pattern. Scale bar = 4 μm.

5.2.3.1 Actin Organisation

The architecture of the actin cytoskeleton was imaged with TIRF-M and observed on different substrates functionalized with anti-CD3 (Figure 5.9 e-h). Visual inspection of the images, shows on POS substrates, a strong enrichment in actin at the periphery of the contact zone, concomitant with a depletion at the center (Figure 5.9 e). On soft pseudo-pattern/bBSA substrates, the actin

shows also a peripheral distribution (Figure 5.9 f). Similarly, on the Q gel soft pattern/pluronic actin array was located at the periphery, and structures resembling to lamellipodia and filopodia are observed (Figure 5.9 g). We can conclude that actin cytoskeleton was similarly organized on patterned and homogeneously functionalized Q gel substrates. However, structures resembling to lamellipodes were seen for POS and soft pseudo-pattern/bBSA substrates while filopodial and lamellipodial resembling structures were equally observed on soft pattern/pluronic.

When comparing the Q gel soft pattern/pluronic (Figure 5.9 g) and the glass pattern/pluronic (Figure 5.9 h), the actin cytoskeleton is distributed at the periphery of the contact zone for both of them.

Previous studies realized in our group on T-cell interacting with glass substrates patterned with anti-CD3 in a sea of polyethylene-glycol coupled to poly-L-Lysin (PEGPLL) as a passivating material, have shown different behavior of the actin cytoskeleton organisation [253]. On these kind of substrates, we observed that T-cells presented a patterned actin distribution. Thus, the actin was colocalized with anti-CD3 proteins dots instead of a peripheral organization. In the current experiments, when using pluronic acid as a passivating material, actin did not appears to follows the structure of the pattern, instead it was similar to the experiment on POS substrate.

The mechanism of actin ring configuration in activated T-cells is still not fully understood. It has been reported in the literature for T-cells on anti-CD3 covered glass as well as on glass supported lipid bilayers (SLBs) carrying ligands of TCR as well as integrins. Here we observe the ring structure for all the substrates studied, which include the soft POS, patterned and pseudo-patterned, as well as glass patterned substrates. Specifically for the last case, based on previous studies [253], we had expected a different organization. The chemical differences between the previous experiments and current one was the use of pluronic acid instead of PEGPLL. Our characterization shows that more molecules of anti-CD3 are absorbed between the dots for pluronic case as compared to the PEGPLL case. This may explain why actin is in ring shape.

5.2.3.2 TCR distribution

The distribution of TCR was imaged in TIRF microscope on the different kinds of substrates (Figure 5.9 l-o). As expected, the images of soft POS and soft pseudo-pattern/bBSA substrates, show a homogeneous distribution of the TCR all over the contact zone (Figure 5.9 l,m). However, on the soft pattern/pluronic substrate, the TCR-microclusters partly co-localize with the underlying protein dots and seem to have nearly the same size (Figure 5.9 j,n). This was also observed on the glass pattern/pluronic substrate, with a slightly more pronounced co-localization (Figure 5.9 k,o). Thus a significant difference is established between the patterned and the homogeneous substrates. As expected TCR tended to be distributed uniformly following the homogeneous anti-CD3 ligands underneath (Figure 5.9 l,m), but when ligands were mainly concentrated within the dots on the pattern, TCR clusters were formed and seemed to partly co-localize with the dots (Figure 5.9 n,o). We can conclude that patterned substrates, which aimed to mimic the TCR ligands, naturally organized in clusters on APC surface, the TCR-microclusters distribution fol-

lowing the dots, might be similar to the microclusters formation in physiological state.

5.3 Discussion

The ECM is a diverse and instructional material that is critical to cell behavior and tissue function. It was reported that cells sense and respond to ECM elasticity and topography. However most previous reports have looked separately at these factors. In this study, surfaces with tunable elasticity were created, and were either functionalized homogeneously with specific protein targeting the T-cell receptor complex (anti-CD3), or imparted with controlled chemical features conjugated to anti-CD3, in order to decipher the role of substrate elasticity and/or patterning on T-cell adhesion and activation process.

Previous studies on T-cells spreading on planar glass surfaces, patterned or not, have shown that unlike other reported cell types (e.g. fibroblasts) where adhesion is modulated by the spacing between integrin ligands, globally T-lymphocytes adhesion depends on overall average surface density of the bioactive molecule. In case of patterned surfaces, the specific pattern distribution does strongly influence the local molecular distribution on the cell surface, as well as the architecture of the actin cytoskeleton. Following these findings, we were interested to develop a soft environment that mimics the mechanical properties of the in vivo cell-cell interaction, to see if the results obtained on hard glass substrates were also applicable for soft environment.

For this, we studied the behavior of T-cells on substrates with varying elasticity patterned or homogeneously functionalized with anti-CD3. We selected PDMS as material for our study, due to its biocompatibility, surface hydrophobicity, stability and facility to modulate its mechanical properties through variation of base to cross-linker ratio. We used three types of PDMS materials, CY , Sylgard and Q gel which together cover the elastic modulus range from 3 KPa to 2 MPa. Planar layer of PDMS supported on a glass substrate were fabricated and functionalized homogeneously, or patterned with anti-CD3 after functionalization steps with bBSA and Nav. T-cells were then allowed to interact with the surface for 20 minutes on homogeneously functionalized substrates and 30 minutes on patterned substrates. They were then fixed and labeled appropriately. Our main interest was to study the cell adhesion from quantification of the adhesion area. The other aspects under study were the actin cytoskeleton organization and distribution of the TCR and of a receptor kinase involved in the signaling (ZAP-70).

On homogeneously functionalized PDMS substrates, we demonstrated comparable amount of Nav adsorption to the surface, independently of the type of PDMS used and its elasticity. In general, protein adsorption to a surface is highly dependent upon both the hydrophibicity and electrostatic properties of the surface [338]. Since PDMS is known to be highly hydrophobic facilitated the protein adsorption to its surface.

We found that unlike other cell types, such as fibroblasts [28], T-cells spread more on soft PDMS

substrates (Young's modulus 5, 20 or 150 kPa), than on hard ones (2 MPa). We showed that on hard PDMS, the cell barely adhered whereas on soft PDMS substrates, a considerable adhesion is observed. Interestingly, on glass substrates (Young's modulus $\approx$ GPa), the cell adhere very well too. This results are in agreement with previous report which demonstrated that T-cells are more activated on softer PDMS (100 kPa), since they produce more interleukin-2 (IL-2) [127]. The results we obtained on patterned soft substrates (20 kPa) are consistent with this, since cells were seen to adhere well with an adhesion area of 195 ± 20 μm^2. The differences in area between homogeneously functionalized and patterned soft substrates could be attributed to the differences in the average ligand density, as was demonstrated for glass substrates [123]. Negative controls consisting of soft substrates with pluronic acid, show barely adhered cells. This confirms the repulsive property of the pluronic acid.

Cell elasticity measurements were done on glass and soft PDMS, and show as expected, a higher cell elasticity on hard glass than that on soft PDMS. However the results could not be conclusive because force measurements on hard PDMS , where cells adhere very weakly could not be carried out correctly.

Studies concerning the distribution of cell surface TCR molecules on glass substrates, show a random distribution on homogeneously coated anti-CD3 substrates [113] [117], while a specific rearrangement following the underlying antibody pattern is observed on patterned substrates [253]. Here, the same results were obtained on homogeneously coated PDMS substrates. Thus, we observed TCR molecules and even ZAP-70 homogeneously distributed on the PDMS substrates, independently of the elasticity. However, small population of sub-micron clusters are observed, whose are more significant for ZAP-70 than for the TCR demonstrating the recruitment of ZAP-70 in form of clusters at the membrane. In the case of patterned glass substrates, TCR is observed to partly co-localize with the underlying anti-CD3 dots. Thus, we reproduce the previous results concerning the TCR on patterned glass. Even though, we have to note the difference between our patterned substrates and the previous reported one, regarding the blocking material used for fabrication of the pattern. In the previous work, the space between the dots was filled with a di-block copolymer, poly-L-lysin/poly ethylene glycol (PEGPLL), whereas here, it is filled with the tri-block copolymer pluronic.
Our first results concerning the TCR on patterned soft PDMS substrates (20 kPa), show only a partial co-localization.

It is well known that actin cytoskeleton structure is related to cell adhesion mechanics, and many proteins involved in TCR and co-stimulatory receptor signal transduction interact directly or indirectly with the actin cytoskeleton. However, unlike the more frequently studied integrin mediated adhesion, the connection between the ligand molecule and actin is not clear for TCR. On homogeneously functionalized glass, actin architecture was observed to have a peripheral ring organization [108][113][117]. This was also the case on our PDMS substrates, where a strong enrichment in actin at the periphery of the contact zone is seen independently of the substrate

rigidity. While on patterned glass fabricated with PEGPLL as repellent material, a partial co-localization with the dots is seen [253], on our patterned soft PDMS substrates a peripheral ring organization is still always observed. We have to note that this was also reproduced on patterned glass using pluronic as a repellent material, which raises the question about the role of pluronic versus PEGPLL. It may be speculated that either pluronic is not as efficient as the other polymer in passivating the glass, or that the height of the two polymers on the glass are different and that may influence actin organization. In general, many questions still remain open on how the organization of the actin cytoskeleton impact the distribution and formation of the TCR micron cluster and vice versa. The current results add to the debate.

Chapter 6

Conclusion

Hard surfaces like glass and silicon are mechanically very different from the physiological environment of cells. For this reason, there is a great current interest in the cell biology domain, for the fabrication of patterned soft substrates, providing a surface that better mimics the real environment of the cell. So far, there is only one available technique to do so. It is based on patterning soft hydrogels using gold nanoparticles. However, this technique requires specialized chemistry and is limited by the chemical and optical properties of gold, as well as the mechanics of hydrogels. The overall aim of this thesis was to propose a novel approach to generate protein patterns over large area of soft elastomer, in order to explore cell responses, specially cell adhesion, activation and mechanics.

To do so, I developed the reverse contact printing technique (RCP), based on patterning glass substrates with nano-scale protein islands which are further transfered to the surface of a soft polydimethylsiloxane elastomer (PDMS) substrate by a simple physical contact (Figure 6.1).

Different types of PDMS with different chemical properties (Sylgard, CY, and Q Gel) were used, in their native form or were functionalized, and were characterized in terms of wettability and elasticity. Contact angle measurements show that in their native forms, the elastomers could be classified in order of hydrophobicity as CY > Q Gel > Sylgard, and following plasma treatment as p Q Gel > p CY > p Sylgard.
Elasticity measurements were performed using force measurements with atomic force microscopy, for native and plasma treated PDMS. The measurements show an increasing of PDMS stiffness following the plasma treatment. Overall, a range of Young's Moduli, from 3 kPa to 7 MPa were explored.

The RCP technique was validated for different types of proteins including BSA (un-conjugated or fluorescently labeled), biotin-BSA (bBSA, un-conjugated or fluorescently labeled), neutravidin Texas-red conjugated (Nav-TR), and fibronectin labeled with fluorescein isothiocyanate. The success of the transfer was also validated for different PDMS surfaces, native, plasma treated or chemically functionalized with a process involving the use of glutaraldhehyde. We also showed that a slightly different technique, involving the use of aluminum as place holder, can be used to create the glass-master [253]. This shows that RCP is a highly versatile, facile and reproducible method, for sub-micropatterning surfaces.

The quality of the patterns was characterized in terms of dot size and contrast on glass before the transfer and on PDMS after the transfer. The transfer ratio was also calculated. The results show that the success of the transfer was strongly influenced by the chemical nature of the fluorophore grafted to the protein, and/or the elastomer surface, and can be predicted from measuring the forces of adhesion and cohesion using atomic force microscopy (AFM). The degree of hydrophobicity, as well as the presence of ionic groups on both the PDMS and the protein are also important molecular factors governing the transfer.
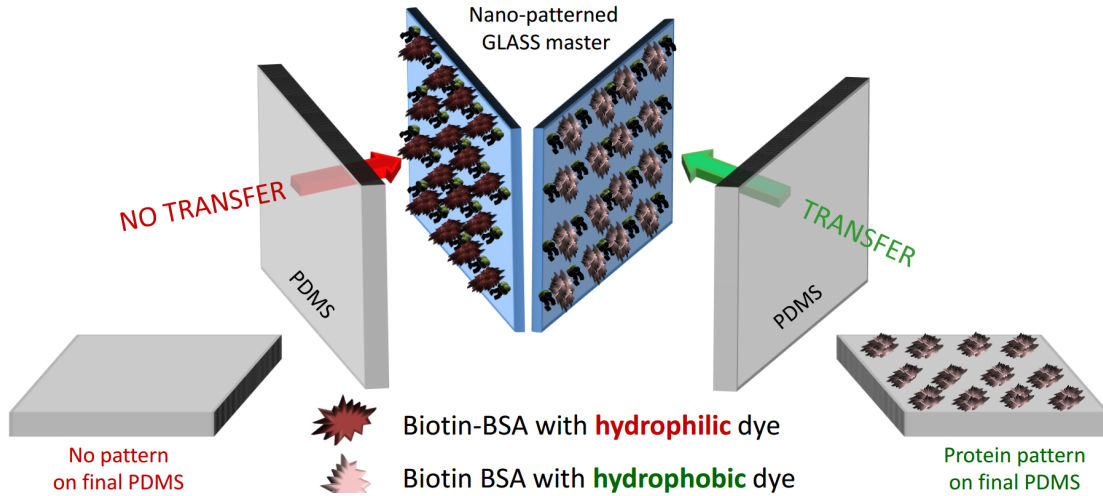
Figure 6.1 – **Graphical representation of the reverse contact printing technique.**

To understand this factors, I quantified the effective force of adhesion, as well as the adhesive energy of the protein on glass and PDMS using AFM force curves of the interaction between the protein functionalized tip and the different surfaces. Sylgard PDMS was chosen for these measurements. The measurement on native Sylgard were not amenable to interpretation since strong non specific adhesions were present. However, these measurements were conducted and interpreted on plasma treated Sylgard and clean bare glass. They show that the nature of the grafted fluorophore influence the transfer, the detailed protocol and mechanism is summarized in ref [339] (submitted). This was also proved by the higher transfer ratio obtained when transferring bBSA-TR in comparison to that obtained for bBSA-Atto (noting that TR is more hydrophobic than Atto). To confirm this finding, Nav-TR was transfered to the surface of native PDMS. Successful transfer was obtained on all the surfaces. We should note that in contrast to fluorescently labeled bBSA, Nav-TR could not be further functionalized after direct transfer to PDMS. We think that this is probably because it was denaturated due to drying.

In another set of experiments, proteins were transferred to the surface of PDMS chemically treated with a process involving the use of glutaraldhehyde. This process is known to render the surface hydrophobic and to support strong and stable covalent linkage of proteins. Hydrophobic Nav-TR were seen to transfer well, but hydrophilic bBSA and BSA-FITC failed to transfer. These findings argue the fact that even when covalent bonds are formed, the initial transfer is governed by physico-chemical affinity.

Separately, the influence of substrate elasticity on cell adhesion and activation was studied for Jurkat T-cell line. For this, different PDMS substrates with elasticity ranging from 3 kPa to 2 MPa, were prepared and homogeneously functionalized with specific ligands targeting the CD3 domain of the TCR complex. Following that, cells were allowed to interact with these substrates.

We found that contrary to other cell types, T-cells adhesion increases with decreasing elasticity. Thus, cells are found to have a considerable adhesion on soft substrate whereas they barely adhere on hard substrates. However, we found that elasticity seems to not influence actin organization which is seen to have the common peripheral organization. The distribution of TCR molecules and ZAP-70 was also independent from the elasticity. TCR and ZAP-70 were found to be homogeneously distributed on the different substrates, with a small population of sub-micron clusters observed. This study demonstrates that our PDMS support adhesion and that T-cell adhesion is sensitive to the differences in substrates elastic moduli.

Cell elasticity measurements were also done for T-Cells using force measurements with atomic force microscopy. Initial results show an elasticity for cell spreading on glass substrates higher than that corresponding to cell spreading on soft PDMS substrate. As well as a correlation between cell elasticity and cell adhesion area is observed. However, it should be noted that force measurements on hard PDMS, where cells adhere very weakly, could note be carried out correctly. In fact, force measurements on soft, weakly adhering objects are challenging. However, for a full understanding it is imperative to device a way to compare the soft with the hard PDMS (rather than glass). For this, optical tweezers measurements are in progress. The first results show a similar cell elasticity on hard and soft PDMS substrates.

To elucidate that our RCP approach could potentially be applied for cell studies, we choose the Q Gel (20 kPa) patterned with bBSA-TR as a model substrate. Next, the patterned soft substrate was functionalized with Nav and anti-CD3 after a pluronic blocking step. Thus, substrates with anti-CD3 pattern motifs, targeting the CD3 domain of the TCR complex are obtained. T-cells were then allowed to interact with these patterns, and also with a pseudo-pattern constituted of fluorescent dots but with presence of equivalent non-fluorescent protein outside the dots, which make the substrate, at the chemical level, almost equivalent to the positive control. Cell adhesion area, actin cytoskeleton organization and TCR distribution were the parameters under study on these substrates. Cells were seen to adhere well on the patterned soft Q Gel substrate, which is consistent with the previous elucidated results showing a considerable adhesion of cell on homogeneously functionalized soft substrates. However, the ring structure of actin cytoskeleton is still persistent. The TCR distribution shows a partial co-localization with the underlying pattern.

Overall, the proposed technique of RCP is a facile, inexpensive, efficient and flexible nanofabrication technique that can be accessible for chemist as well as biologist. It allows patterning of proteins over a variety of biocompatible substrates via a relatively simple processing route, and could eventually be used with any cell type. Moreover, since the PDMS elastomers used in this technique are characterized by high refractive indexes, ranging from 1.41 for Sylgard, 1.4 for CY and 1.49 for Q Gel, they represent excellent compatibility with surface sensitive microscopy, total internal reflection fluorescence microscopy (TIRF-M), reflection interference contrast microscoy (RICM) and super resolution, the first two techniques were demonstrated by me in ref [253]. The fabricated substrates could be expected to be used for traction force microscopy

in order to combine patterning and cell mechanics. RCP can covers a wide range of physiologically relevant stiffness to extend our understanding for cell mechanics and holds potential to be further developed and used to increase our knowledge of fundamental cell biology processes.

The problems and limitations of RCP also need to be taken into consideration. In fact, in some cases, as it was seen for BSA labeled with FITC, the success of the transfer required plasma treatment of the PDMS surface. This treatment increases the PDMS elasticity, changes its surface chemistry and can form cracks at the PDMS surface if care is not taken during the plasma treatment. Another drawback that should be ameliorated, is the protein transfer from outside the dots which influences the contrast of the pattern and may also affect the cell response. Another limitation of this technique is related to the limited range of PDMS elasticity. We have to note also that this technique is not usable with hydrogels at least for now.

Future work that might be done, consists in optimizing structural parameters such as the lateral size of the dots and the inter-spacing which is possible by changing the size of the beads used for the fabrication of the glass master. We could also try to ameliorate the contrast of the PDMS pattern, thus decrease the transfer outside the dots, by trying several blocking reagent. Also we should increase the range of PDMS stiffness to which the pattern could be transfered. Finally we also aim at recording the dynamics of cell adhesion, measure cell elasticity with AFM, and set up traction force microscopy to measure forces exerted by cells, in order to explore the effect of patterning versus elasticity on cell mechanics.

Chapter 7

Summary In French

Durant les dernières décennies, de plus en plus de types de cellules se sont révélées capables de sonder leur environnement mécanique par l'application de forces par l'intermédiaire de protéines d'adhésion sur leur surface. Ce phénomène appelé "Mecanosensing" est lié à l'adhésion et la mécanique cellulaire, et est souvent étudié grâce à l'interaction des cellules avec des substrats artificiels. Mecanosensing devient un domaine de recherche en pleine émergence, grâce au développement de techniques expérimentales permettant de changer l'élasticité de la matrice et de mesurer précisément les interactions cellules-substrats. Dans des études distinctes, les technologies de bio-nanostructuration ont fourni des outils pour mimer l'état physiologique et pathologique des cellules ainsi que pour les manipuler. Des surfaces chimiquement structurées avec une répartition des ligands spécifiques ont montré une forte influence sur l'adhésion et la mécanique cellulaire. Cependant, la relation entre les deux phénomènes n'a pas été beaucoup explorée, en partie parce que la fonctionnalisation de substrats mous s'est révélée être un défi technique.

Dans ce but, nous visons dans ce projet le développement d'une technique de structuration de substrats mous pour des applications dans le contexte de la biologie cellulaire et principalement dans le contexte des lymphocytes. Parmi les techniques de structuration les plus connus, on note la technique de microcontact printing développée par Georges Whitesides en 1993 [153]. Elle utilise un tampon en élastomère avec un motif de structure en relief, permettant le transfert de molécules à la surface de substrats en verre ou en or par exemple. Cette technique est actuellement un outil indispensable pour la structuration de substrats en verre avec des protéines pour des études cellulaires. Elle est connue pour son processus de fabrication simple et la facilité de son utilisation. Toutefois, vu que les cellules vivantes sont mécaniquement sensibles, l'élaboration d'une technique pour patterner des substrats mous est un besoin en pleine croissance.

Séparément, des études ont montré que les cellules ne répondent pas uniquement à la nature biochimique des protéines qui sont présentes sur la surface, mais aussi à la façon dont ces molécules sont organisées et présentées aux cellules. Les cellules du tissu conjonctif, comme les fibroblastes, se sont trouvées incapable d'adhérer, de s'étaler, de proliférer ou encore de croître sur des substrats patternés par des molécules uniques de ligand séparées par une distance supérieur à 100 nm. De manière surprenante, le comportement des lymphocytes s'est révélé différent, et dépend non seulement de la distance entre les ligands, mais aussi de la densité moyenne de ces derniers.

Les études des lymphocytes-T sur substrats mous sont intéressantes à cause des résultats contradictoires reportés sur leur adhésion et activation sur de tels substrats, mais aussi à cause de leur sensibilité mécanique qui, est-elle même très intéressante. En effet il a été montré que la capacité des lymphocytes à reconnaitre un antigène dépend de leur sensibilité mécanique et que les domaines CD3 du complexe récepteur des cellules T (TCR) est impliqué dans cette sensibilité.

Le but de cette thèse est de fabriquer des substrats mous chimiquement structurés avec des plots de protéines, et dont l'élasticité peut être facilement contrôlée afin de faire des études plus approfondies sur l'adhésion et l'activation cellulaire avec des lymphocytes-T. La thèse est

présentée en quatre chapitres principaux. Le **premier** chapitre montre une description détaillée de la technique d'impression que j'ai développée. Le **second**, rapporte l'efficacité de la méthode d'impression et propose un mécanisme moléculaire qui régit le transfert. Le **troisième**, concerne l'étude de la réponse des lymphocytes-T à des surfaces d'élastomères mous fonctionnalisés d'une façon homogène ou patterné. Des paramètres comme l'aire d'adhésion cellulaire, l'organisation du cytosquelette d'actine et la distribution du TCR et ZAP-70 sont étudiés. Le **dernier** chapitre conclut le manuscrit tout en évoquant les principaux points du projet ainsi que les limitations et les perspectives futures.

7.1 Protocole de transfert
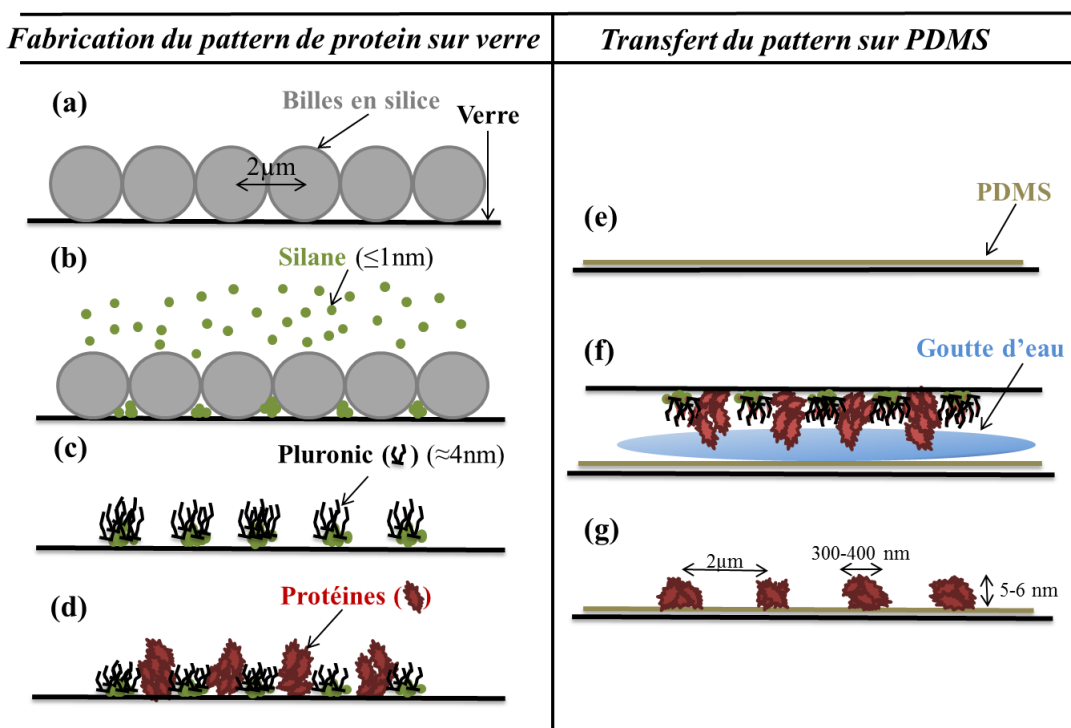
Figure 7.1 – **Représentation schématique des étapes de la fabrication des plots de protéines sur un substrat en verre et leur transfert sur un substrat mou.** (a) Auto-assemblage du masque de billes colloïdales en silice sur substrat en verre. (b) Déposition de molécules de fluorosilane (PFOTCS) à partir d'une phase gazeuse à travers le masque de billes. (c) Retrait des billes par ultra-sons et greffage d'un poloxamer (pluronic) afin de passiver la zone couverte de fluorosilane. (d) Incubation de la protéine. (e) Couche mince d'élastomère (PDMS) supportée sur une lamelle en verre. (f) Transfert des plots de protéines du verre à la surface de l'élastomère en présence d'une goutte d'eau. (g) Pattern de protéines à la surface du PDMS.

La technique de "reverse contact printing" que nous avons développée, est schématisée dans la figure 7.1. Elle est composée de deux parties. La première consiste à fabriquer des plots de protéines (pattern de protéines) submicroniques sur un substrat en verre, suivi dans la seconde partie de leur transfert sur un substrat de polydimethylsiloxane (PDMS) en présence d'une goutte

d'eau.

7.1.1 Fabrication du pattern de protéine sur verre

Le protocole de la fabrication du pattern de protéines sur un substrat en verre se divise en cinq étapes:

1- Une lamelle de verre lavée selon le protocole décrit précédemment (section 2.1) est posée selon un angle de 13°. Un volume de 80 à 100 μl de billes lavées y sont déposées puis laissées sur une surface plane afin que l'eau s'évapore (Figure 7.1 a).

2- Un dépôt de Trichloro (1H,1H,2H,2H-perfluorooctyl) silane (PFOTCS) est effectué sur le verre, à travers le masque de billes par évaporation sous vide a 35°C pendant une heure dans un dessiccateur (Figure 7.1 b). Durant ce processus le fluorosilane est immobilisé de façon covalente à la surface du verre. Le masque de billes est ensuite enlevé par ultrasons dans de l'eau. A ce stade une couche de silane hydrophobe est obtenue sous forme d'un pattern séparé par des trous exposant la surface du verre. La réussite de cette étape est testée par la mesure de l'angle de contact d'une goutte d'eau sur la lamelle de verre silanisée qui montre que la surface est devenue hydrophobe avec un angle de contact de 80°.

3- Les régions hydrophobes (silanisées) sont passivées par l'adsorption d'un poloxamer à trois block; le pluronic (Figure 7.1 c). En effet, le pluronic s'adsorbe à la surface du verre par interaction entre sa partie centrale apolaire hydrophobe (poly(oxyde de propylène)) et les groupements hydrophobes fluorés du silane. Par contre, les deux parties externes hydrophiles du pluronic (poly(oxyde d'éthylène)), vont être exposées à la surface permettant ainsi de diminuer ou limiter une fixation non spécifique des protéines.

4- Les trous exposant la surface du verre sont remplis avec la protéine de choix (Figure 7.1 d).

Suite à ses étapes, une lamelle de verre chimiquement patternée avec des plots de protéines est obtenue (Figure 7.2).
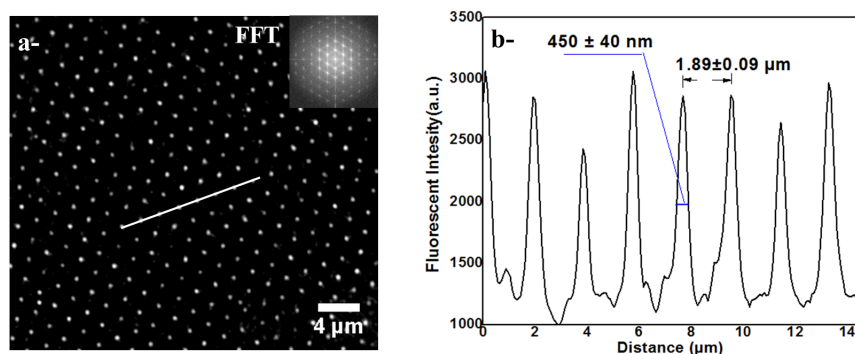
Figure 7.2 – **Image d'épi-fluorescence représentant un pattern de protéines (Nav-TR) sur substrat en verre.** a- Image d'épi-fluorescence. b- Profil d'intensité correspondant à la ligne tracée en (a). L'insert dans (a) représente la transformation de Fourier rapide indiquant l'organisation ordonnée du pattern.

Toutes les étapes de la fabrication du nanopattern sur verre à partir du greffage du fluorosilane

jusqu'à la fonctionnalisation avec la protéine, ont été vérifiées par imagerie avec le microscope à force atomique (Figure 7.3).
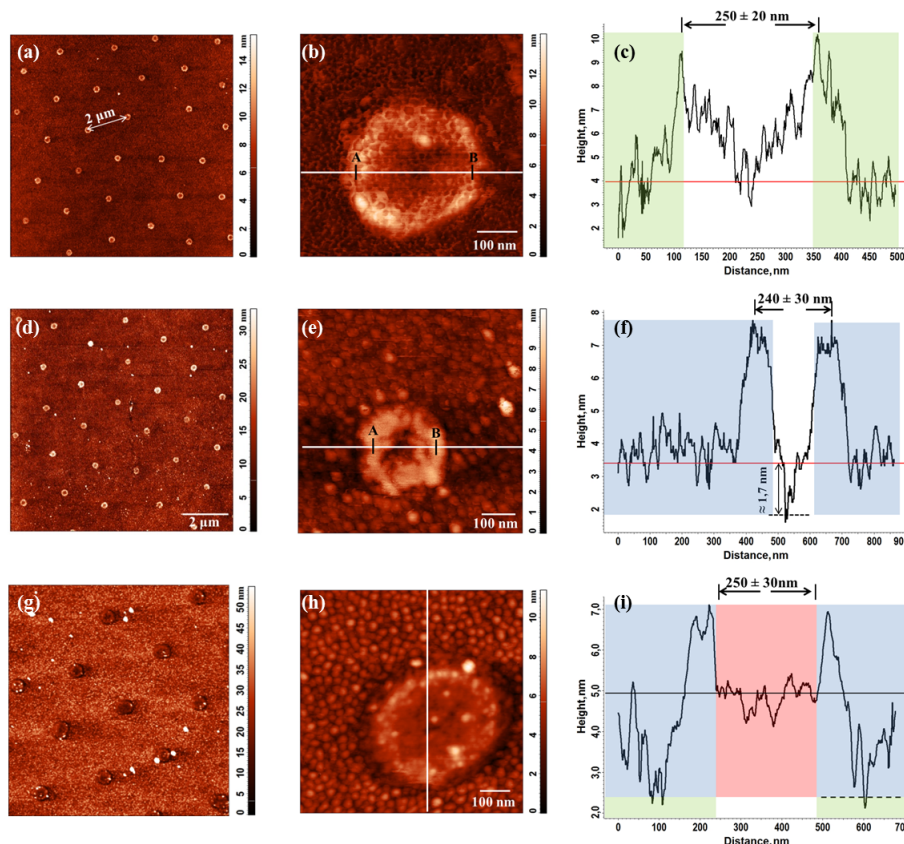
Figure 7.3 – **Image AFM en mode tapping à l'air pour suivre les étapes de greffage de molécules lors de la fabrication du pattern sur substrat en verre.** (a-c) Image AFM suite à l'étape de déposition du fluorosilane, Zoom-in et profil en z de la ligne tracée en (b). Comme prévu la distance entre deux cercles est de 2 μm. Le PFOTCS est préférentiellement absorbé au niveau du bord des cercles, ce qui se traduit par la formation des anneaux. Il est également prévu d'être absorbé partout à l'extérieur des anneaux (comme indiqué par les zones colorés en vert). A noté que la couche mince en dehors des anneaux n'est pas clairement détectable ici. (d-e) Image AFM suite à l'étape du greffage du pluronic sur le fluorosilane. L'élévation relative de la hauteur de la zone à l'extérieur des anneaux (zones colorées en bleu) indique la réussite de l'adsorption du pluronic. (g-i) Image AFM correspondant au greffage des protéines. L'élévation du niveau à l'intérieur des anneaux (Zone colorées en rouge) indique la présence des protéines. Le diamètre de l'anneau est mesuré à environ 250 nm. A noté que cette mesure présente une sous-estimation de la taille des plots.

7.1.2   Transfert du pattern sur PDMS

Une couche mince uniforme d'élastomère, supportée sur une lamelle de verre plate est fabriquée par enduction centrifuge. Un recuit du substrat est ensuite effectué à une température précise pour augmenter la vitesse de la réticulation de l'élastomère. Le polydimethylsiloxane ou PDMS

a été choisi comme élastomère de choix.

Pour effectuer le transfert, la surface du PDMS est mise en contact physique avec la surface du verre patternée en présence d'une goutte d'eau. En effet des études précédentes ont montré que la présence de l'eau facilite le transfert [161]. Une légère pression est appliquée manuellement pour assurer un contact conforme. Les deux surfaces sont laissées en contact pour la nuit, et sont soigneusement séparées le jour suivant. Après séparation, le pattern de protéines est bien transféré à la surface du PDMS.

7.2 Caractérisation et mécanisme du transfert.

7.2.1 Caractérisation des substrats de PDMS

Trois différents types de PDMS ont été utilisés; le sylgard 184, le Q Gel 920 et le CY 52-276. Les trois sont des polymères à base de dimethylsiloxane. Le Q Gel, possède en plus des groupements méthyl-phényles et des polymères de phényles. Les PDMS ont été utilisés directement après recuit, ou ont subi un traitement par plasma oxygène afin d'augmenter leur énergie de surface et donc, les rendre hydrophile.

Des mesures de force réalisées à l'aide d'un microscope à force atomique (AFM) ont été effectuées afin de déterminer l'élasticité des différents substrats de PDMS. Les mesures de forces montrent une gamme d'élasticité de PDMS allant de 3 kPa à 7 MPa (Table 7.1). Des mesures d'angle de contact ont été aussi effectuées afin de caractériser la surface des PDMS en termes de mouillabilité (Tableau 7.2).

	Native (kPa)	Plasma Treated (kPa)
Q gel (1:2)	20 ± 3	120 ± 4
Sylgard (10:1)	2440 ± 500	7300 ± 900
CY (1:1)	3 ± 1	260 ± 10

Table 7.1 – **Elasticité des différents PDMS mesurés à partir des courbes de forces d'AFM.** La valeur moyenne du module de Young (en kPa) et les écart-type correspondants sont indiqués. Au moins trois échantillons ont été testés pour chaque type de substrat et 100 courbes ont été enregistrées à différents endroits pour chaque échantillon, en au moins 4 régions distinctes à la surface de l'échantillon et ceci dans les mêmes conditions.

	Native	Plasma treated
Sylgard (10:1)	$104° \pm 4$	$3° \pm 1$
Q Gel (1:2)	$116° \pm 4$	$35° \pm 6$
CY(1:1)	$122° \pm 3$	$13° \pm 3$

Table 7.2 – **Mesure de l'angle de contact de l'eau pour différents substrats de PDMS avant et après traitement par plasma oxygène.**

7.2.2 Observation et caractérisation de pattern de BSA-biotine fluorescent sur des substrats en verre ou en PDMS

Les protéines de bovine sérum albumine attachées à de la biotine (bBSA), sont marquées avec du fluorophore, le Texas Red ou l'Atto 488 (indiquées respectivement par bBSA-TR et bBSA-atto 488). Ces protéines ont été utilisées comme protéines de choix pour la fabrication du pattern sur substrats en verre, suivi par leur transfert sur PDMS natif ou ayant subi un traitement de surface par plasma oxygène.

Les protéines bBSA-TR ou bBSA-Atto ont été transférées à la surface de deux types de PDMS différents; Sylgard 184 et Q gel 920, qui sont soit dans leur état natif (Q Gel (20 kPa), Sylgard (2 MPa)), ou ayant subi un traitement de surface par plasma oxygène (p Q Gel (120 kPa), p Sylgard (7 MPa)). Les substrats patternés ont été imagés à l'aide d'un microscope à épi-fluorescence avant et après le transfert (Figure 7.4, 7.6).
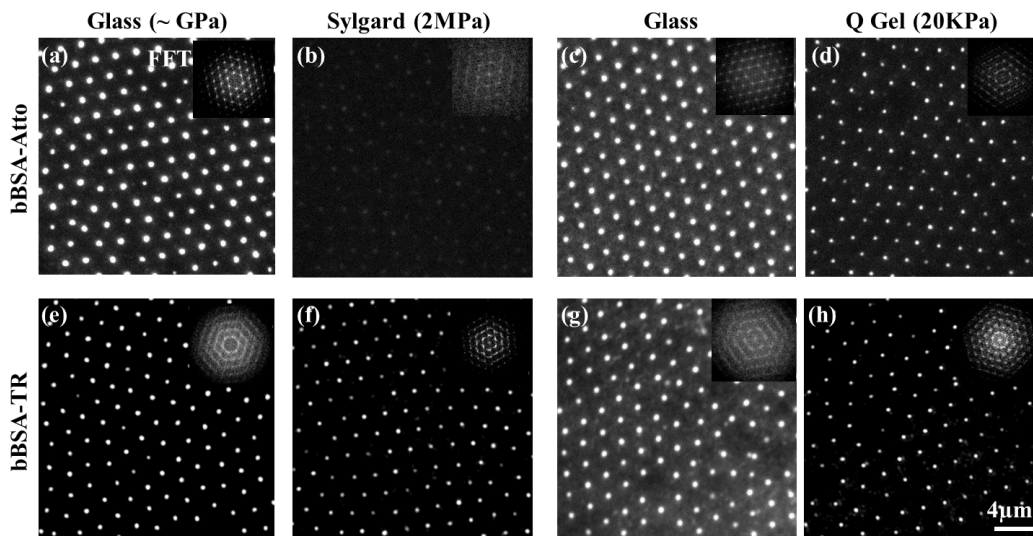
Figure 7.4 – **Images d'épi-fluorescence de pattern de bBSA marqué soit avec TR soit avec Atto 488, sur verre et sur Sylgard ou Q Gel natif.** Pattern de bBSA-Atto sur verre avant transfert (a, c), le même pattern transféré sur Sylgard et Q gel respectivement (b, d). Pattern de bBSA-TR sur verre avant transfert (e, g), le même pattern transféré sur Sylgard et Q gel respectivement (f, h). Les images insérées représentent la transformation de Fourrier rapide indiquant l'organisation ordonnée du pattern. A noter que toutes les images ont été prises avec le même paramètre de la caméra.

L'observation des images montrent que la bBSA-Atto s'est bien transférée sur le Q Gel (Figure 7.4 d), mais pas sur le Sylgard (Figure 7.4 b). En effet, le pattern de bBSA-Atto sur Sylgard ne peut être détecté que par amplification des paramètres de la caméra (Figure 7.5). Par contre, la bBSA-TR s'est bien transférée sur les deux PDMS (Figure 7.4 f, h). Néanmoins, les deux espèces moléculaires montrent un bon transfert sur p Sylgard et p Q gel (Figure 7.6).
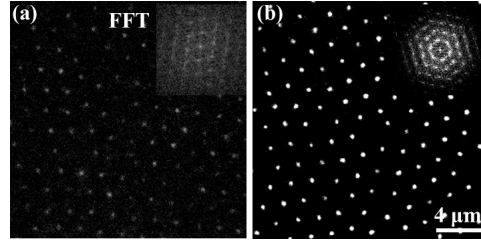
Figure 7.5 – **Transfert de bBSA-Atto sur Sylgard imagé avec deux paramètres différents de la caméra.** Avant et après amplification des paramètres de gain de la caméra (a, b respectivement).
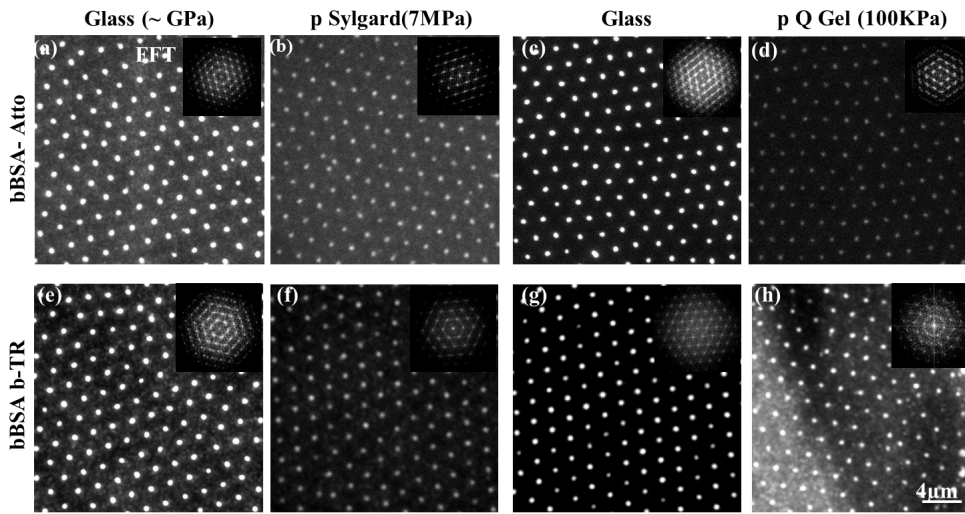
Figure 7.6 – **Images d'épi-fluorescence de pattern de bBSA marqué soit avec TR soit avec Atto 488, sur verre et sur Sylgard ou Q Gel traité par plasma oxygène.** Pattern de bBSA-Atto sur verre avant transfert (a, c), le même pattern transféré sur p Sylgard et p Q gel respectivement (b, d). Pattern de bBSA-TR sur verre avant transfert (e, g), le même pattern transféré sur p Sylgard et p Q gel respectivement (f, h). Les images insérées représentent la transformation de Fourrier rapide indiquant l'organisation ordonnée du pattern. A noter que tous les images ont été prises avec le même paramètre de la caméra.

Les différents patterns ont été caractérisés avant et après le transfert en termes de taille des agrégats, contraste et rapport de transfert.

Afin de déterminer la **taille des agrégats**, un agrégat médian est construit pour chaque type de surface patternée. Ensuite un profil d'intensité de l'agrégat médian est tracé. Sa taille est déterminé en mesurant la largeur du pic à mi-hauteur.

Le **contraste** correspond à la mesure de la quantité de protéines dans un agrégat, par rapport à celle à l'extérieur de l'agrégat. Il est définit par l'équation 7.1:

$$Contrast = \frac{I_{max} - I_{min}}{I_{max} + I_{min}} \qquad (7.1)$$

Ou I_{max} est le pic du profil d'intensité de l'agrégats médian.

I_{min} est l'intensité entre les agrégats, dans la région passivée avec le pluronic.

Le **rapport de transfert** à l'intérieur des agrégats est défini par l'équation:

$$Rapport de Transfert = \frac{I_{max}(elastomer)}{I_{max}(verre)}$$

(7.2)
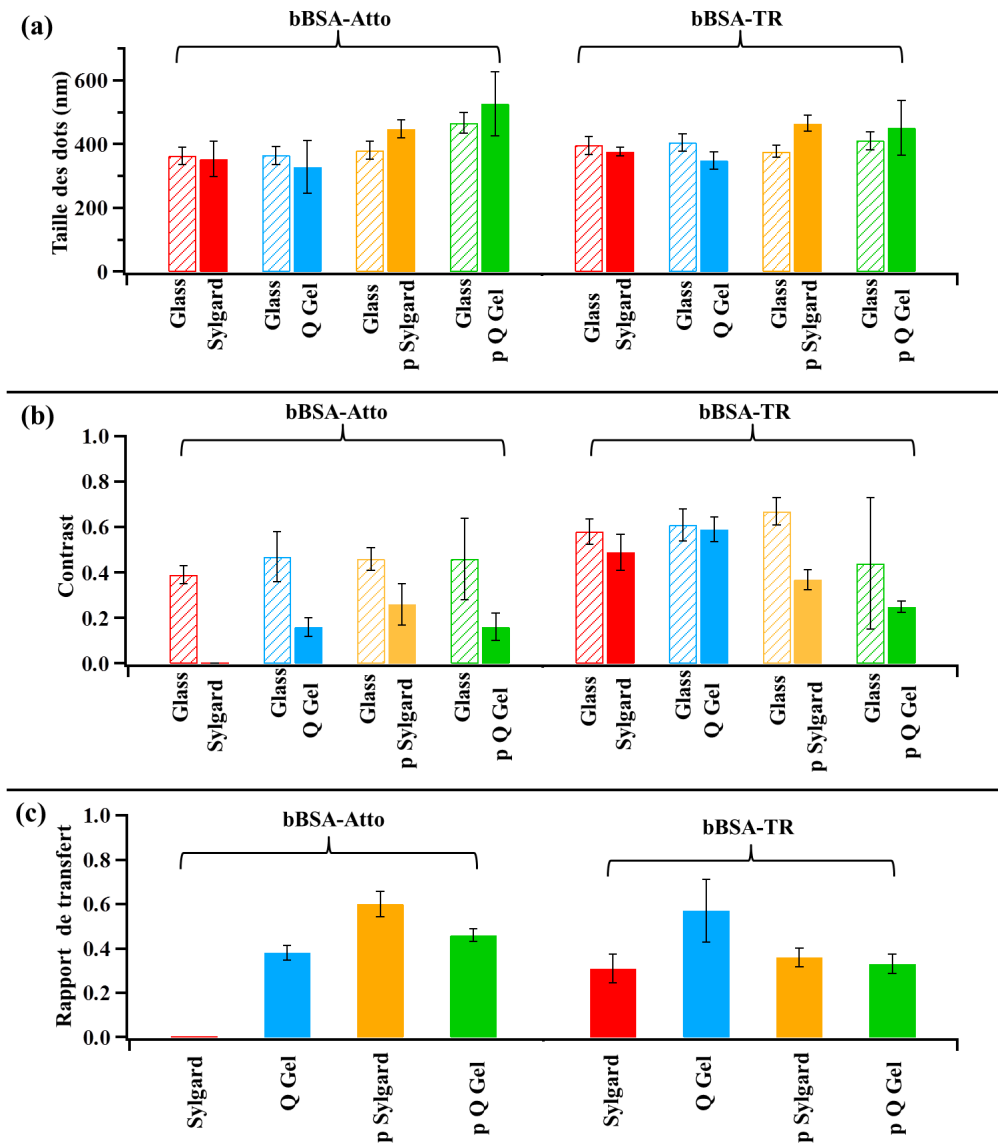
Figure 7.7 – **Analyse des images d'épi-fluorescence correspondant au transfert de bBSA fluorescent du verre à différents substrats de PDMS.** (a) Taille des agrégats et contraste avant et après transfert (a, b respectivement). (c) Rapport de transfert.

Figure 7.7 présente une quantification des agrégats de bBSA fluorescents, faite à partir des im-

ages d'épi-fluorescence avant et après le transfert du verre au PDMS. Toutes les valeurs obtenues représentent une moyenne d'au moins 6 agrégats médians pour chaque échantillon, obtenu sur des endroits distincts de l'échantillon. Au moins trois échantillons différents ont été caractérisés pour chaque cas.

On observe que **la taille des agrégats** est pratiquement conservée avant et après transfert des protéines du verre au PDMS dans leurs états natifs, que ce soit pour le Sylgard ou pour le Q gel. Par contre une légère augmentation de la taille des dots est remarquée après transfert sur p Sygard et p Q Gel (T-test < 0.001) (Figure 7.7 a).

Le **contraste** diminue systématiquement après le transfert que ce soit sur du PDMS natif ou traité par plasma oxygène (Figure 7.7 b). Ceci indique que la quantité de protéines transférée à l'intérieur des agrégats et différente de celle transférée à l'extérieur des agrégats. Dans le cas idéal, lors de la fabrication du pattern sur verre, il ne faudrait aucune adsorption de protéines dans les zones passivées avec le pluronic. Dans le cas où cela arrivent, il ne faut pas qu'ils se transfèrent sur le PDMS. Ce n'est pas notre cas ici.

Les mesures de contraste confirment que le transfert à bien réussit dans tous les cas sauf dans le cas de bBSA-Atto sur Sylgard.

Le **rapport de transfert** a aussi été calculé afin de caractériser le transfert. Des rapports variant entre 0 et 0.6 sont obtenus. Le meilleur transfert sur PDMS non traité étant pour bBSA-TR sur Q Gel (0.6 ± 0.14), et sur PDMS traité par oxygène plasma pour bBSA-Atto sur p Sylgard (0.6 ± 0.056). Les rapports de transfert montrent bien que la nature chimique du fluorophore attaché à la protéine, le type du PDMS, et le traitement de surface de ce dernier influent sur la réussite du transfert.

7.2.3 Compréhension du processus de transfert

Afin de comprendre les facteurs moléculaires qui régissent le transfert, des mesures de forces par AFM ont été réalisées. Ces mesures permettent de quantifier les forces d'adhésion et de cohésion effectives impliquées dans le processus. Afin de pouvoir réaliser ces mesures, la pointe d'AFM a été d'abord fonctionnalisée d'une façon covalente avec la protéine. Elle est ensuite approchée de la surface du substrat, qui est soit une lamelle en verre propre, soit une lamelle de verre fonctionnalisée avec la protéine, soit du PDMS natif ou traité par plasma oxygène. La pointe est ensuite retirée loin de la surface, et les courbes de forces sont enregistrées. La courbe de recul est analysée afin d'extraire les forces d'adhésion entre la protéine et les différents substrats, ou les forces de cohésion protéine-protéine. Ce type de mesure a été difficile a réaliser sur du Q Gel du fait de sa souplesse. Ainsi que les mesures sur du Sylgard natif, montrent de fortes adhésion non spécifiques avec la bille. Ces mesures n'ont donc pas été exploitées. Alors que les mesures réalisées sur du Sylgard traité par plasma oxygène ou sur des lamelles de verre propre ont bien été réalisées et traitées (Figure 7.8).

Le tableau 7.3 résume les forces d'adhésion des protéines avec la surface de p Sylgard (nommée
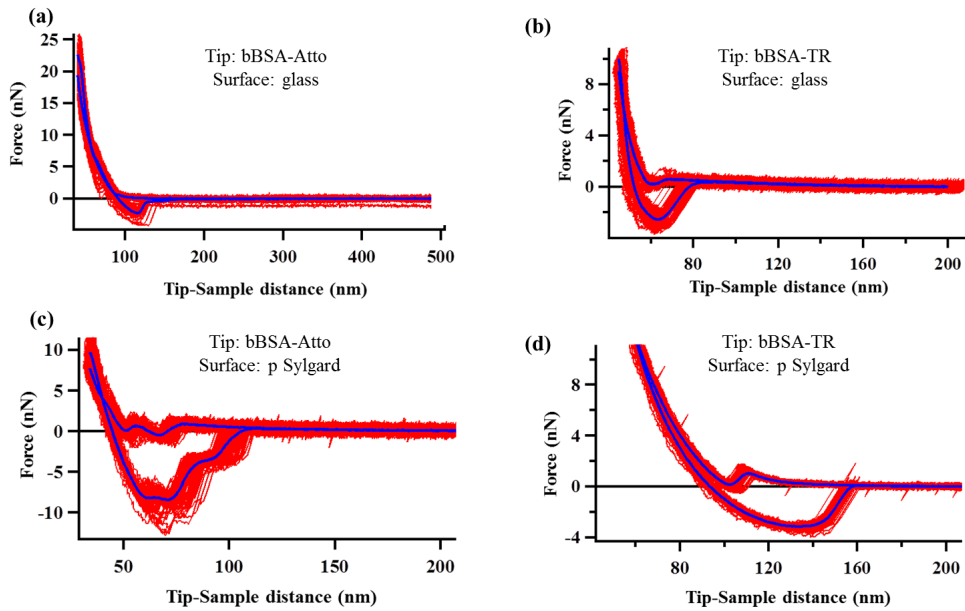
Figure 7.8 – **Courbes de forces correspondantes à l'interaction entre bBSA fluorescente et une surface de verre propre ou de Sylgard traité par plasma oxygène.** (a, b) Courbes de force correspondantes respectivement à l'adhésion de bBSA-Atto et bBSA-TR sur une surface de verre propre. (c, d) Courbes de force correspondantes respectivement à l'adhésion de bBSA-Atto et bBSA-TR sur une surface de p Sylgard. Les lignes rouges représentent la superposition de 100 courbes réalisées sur différents endroits de la surface. Les lignes bleues représentent la courbe médiane.

$F_{pSylgard-prt}$), de verre propre (nommée F_{g-prt}) et une surface de verre fonctionnalisée avec la protéine correspondante (nommée $F_{prt-prt}$).

D'après les forces d'adhésion calculées on remarque que pour bBSA-TR ainsi que pour bBSA-

	$F_{prt-prt}$ (nN)	F_{g-prt} (nN)	$F_{pSylgard-prt}$ (nN)
bBSA-Atto	9.5 ± 5	2.3 ± 0.8	12.8 ± 1.7
bBSA-TR	4.6 ± 2.8	2.7 ± 0.8	5.1 ± 0.6

Table 7.3 – **Mesure des forces d'adhésion.** Chaque valeur représente une moyenne calculée à partir de 100 courbes de forces réalisées sur des endroits différents de l'échantillon et sur au moins trois régions distincts et sous les même conditions. Au moins trois échantillons sont analysés pour chaque mesure. Les erreurs représentent les écarts-types.

Atto, la force nécessaire pour détacher une couche de protéine de la surface de verre (F_{g-prt}), est inférieure à celle nécessaire pour séparer deux couches de protéines ($F_{prt-prt}$) (Tableau 7.3). Par conséquent, les multicouches de protéines formant les agrégats du pattern sur verre sont transférées à l'élastomère probablement en se décollant entièrement de la surface de la lamelle en verre, plutôt qu'uniquement la couche supérieure des protéines soient.

En comparant les forces d'adhésion de bBSA-TR et bBSA-Atto avec le p Sylgard, on observe que

bBSA-Atto présente une plus forte interaction avec le p Sylgard (12.8 ± 1.7 nN pou bBSA-Atto et 5.1 ± 0.6 pour bBSA-TR) (Table 7.3). Ceci est consistant avec le rapport de transfert plus élevé pour ce dernier (0.6 ± 0.056 et 0.36 ± 0.042 pour bBSA-Atto et bBSA-TR respectivement). D'après la structure moléculaire d'Atto et de TR, nous attendons que TR soit plus hydrophobe qu'Atto vu que ce dernier possède une charge nette négative et un groupement amine capable de perdre un anion. Par conséquence, la différence d'interaction des deux espèces avec le p Sylgard peut être attribuée à des forces hydrophobes/hydrophiles. Ce même raisonnement peut être utilisé pour expliquer les autres transferts évoqués dans les figures 7.4 et 7.6.

On observe que le transfert de bBSA-Atto sur Sylgard hydrophobe a échoué. Le transfert était trop faible et ne pouvait être détecté que par amplification des paramètres de la caméra (Figure 7.5). De plus le Sylgard est connu pour avoir une légère charge négative en solution aqueuse et à pH neutre [329], ce qui résulte en une répulsion électrostatique envers la bBSA-Atto qui elle, possède une charge négative.

Par contre le transfert de bBSA-Atto à la surface du Q gel est réussi (rapport de transfert = 0.38 ± 0.03). A noté que ce dernier est plus hydrophobe que le Sylgard d'après les mesures d'angle de contact, et possède en plus, des groupements phényles dans sa chaine. Ainsi, on peut expliquer la réussite du transfert de bBSA-Atto sur Q gel par la formation d'interaction π-π entre les groupements aromatiques de bBSA-Atto et les groupements phényles du Q gel.
Dans le cas de bBSA-TR, le transfert est réussi à la fois sur Sylgard et sur Q gel, avec un rapport de transfert plus élevé pour ce dernier (Rapport de transfert = 0.6 ± 0.14 et 0.31 ± 0.067 sur Q gel et Sylgard respectivement). Les interactions hydrophobes jouent un rôle central dans le transfert de bBSA-TR sur Sylgard et Q gel natifs. De plus, on note que TR possède plus de groupement aromatique dans sa chaine que Atto, ce qui explique sa plus forte interaction avec le Q gel. Ceci est aussi confirmé par le rapport de transfert plus élevé pour bBSA-TR sur Q gel (0.6 ± 0.14) que celui de bBSA-Atto (0.38 ± 0.03). Consistent avec ces résultats, la BSA non biotinylée, et marquée avec un fluorophore hydrophile (BSA-FITC) se transfère bien à la surface de p Sylgard avec un rapport de transfert de 0.58, par contre son transfert sur du Sylgard natif ne réussit pas. D'autre part, la BSA non biotinylée et marquée avec TR (BSA-TR), se transfère bien à la surface du Sylgard natif.

Nous avons aussi essayé de transférer de la bBSA non marqué avec de fluorophore. Les résultats montrent que le transfert échoue que ce soit sur le PDMS de type CY ou Q Gel. On peut alors conclure que la bBSA expose son groupement hydrophile quand elle est adsorbée sur le verre.
Pour confirmer notre hypothèse que le marquage de la protéine avec le TR comme fluorophore, augmente la possibilité de transfert de cette dernière à la surface du PDMS hydrophobe non traité, on a essayé de transférer la neutravidin marqué avec texas red (Nav-TR). Le transfert réussi sur les différents types de PDMS. Néanmoins, probablement à cause du séchage, on n'a pas réussi à fonctionnalisé la neutravidin transférée, avec une protéine biotinylée.

Dans un autre ensemble d'expériences, nous avons fonctionnalisé la surface du PDMS traité par plasma oxygène avec de l'APTES ((3-aminopropyl)triethoxysilne) et de la glutaraldhéhyde. Ce traitement est connu pour rendre la surface hydrophobe et permettre des liaisons covalentes stable avec la protéine [39] [318][319]. Le transfert de Nav-TR sur ce type de surface est bien réussit, par contre le transfert de bBSA et du BSA-FITC est trop faible et presque inaperçu. Ceci montre que même quand des liaisons covalentes peuvent être formées, le transfert initial est régi par l'affinité physico-chimique.

7.3 Cellules sur PDMS fonctionnalisé d'une façon homogène ou patterné

Il a été montré que les cellules ont la capacité de sonder leur environnement mécanique et aussi topographique. Or, la plupart des études faites dans ce domaine ont regardé séparément l'influence de ces facteurs sur le comportement cellulaire. Dans ce projet, nous avons choisi les lymphocytes-T de type Jurkat afin d'étudier l'influence de ces deux facteurs sur le comportement de ces derniers et spécialement sur leur adhésion et leur activation.

Des études précédentes faites sur des lymphocytes-T adhérentes sur une surface de verre plane, patternée ou homogène, ont montrées que contrairement à d'autres types de cellules (par exemple les fibroblastes), où l'adhésion est modulée par l'espacement entre les ligands d'intégrines, pour les cellules T, elle dépend de la densité moyenne globale des molécules bioactive présentes sur la surface. Dans le cas de substrats patternés, la distribution spécifique du pattern influence fortement la distribution locale des molécules à la surface de la cellule. Vu ces découvertes, nous avons été intéressé par le développement de substrats mous qui miment les propriétés mécaniques in-vivo des interactions cellule-cellule, dans le but de voir si les résultats obtenus sur des substrats en verre durs peuvent être aussi appliqués pour des environnements mous.

Pour cela, nous avons commencé par l'étude de l'adhésion des cellules-T sur des substrats d'élasticité contrôlée fonctionnalisés de façon homogène avec des anticorps spécifiques qui ciblent la molécule CD3 du complexe TCR (anti-CD3). Puis, sur des substrats de PDMS mous (Q Gel 20 kPa) patternés avec ce même anticorps.

Nos résultats sur les substrats mous homogènes ont montré que contrairement à d'autres types de cellules, comme les fibroblastes par exemple [28], les cellules T s'étalent d'avantage sur substrats mous (module de Young: 5, 20 ou 150 kPa) que sur substrats durs (module de Young: 2 MPa) (Figure 7.9). En effet, nous avons vu que sur du PDMS dur, les cellules adhèrent à peine alors que sur des substrats de PDMS mou, une adhésion considérable est observée. De manière surprenante, sur des substrats en verre (Module de Young: $\approx$ GPa), les cellules présentent aussi une forte adhésion. Ces résultats sont en accord avec des résultats précédents qui montrent que les cellules T sont plus activées sur du PDMS mou (100 kPa), vu qu'elle sont capables de produire plus d'interlukin-2 [127]. Ces résultats sont aussi en accord avec ceux obtenus sur les substrats mous patternés qui ont aussi montrés une aire d'adhésion élevée pour les cellules.
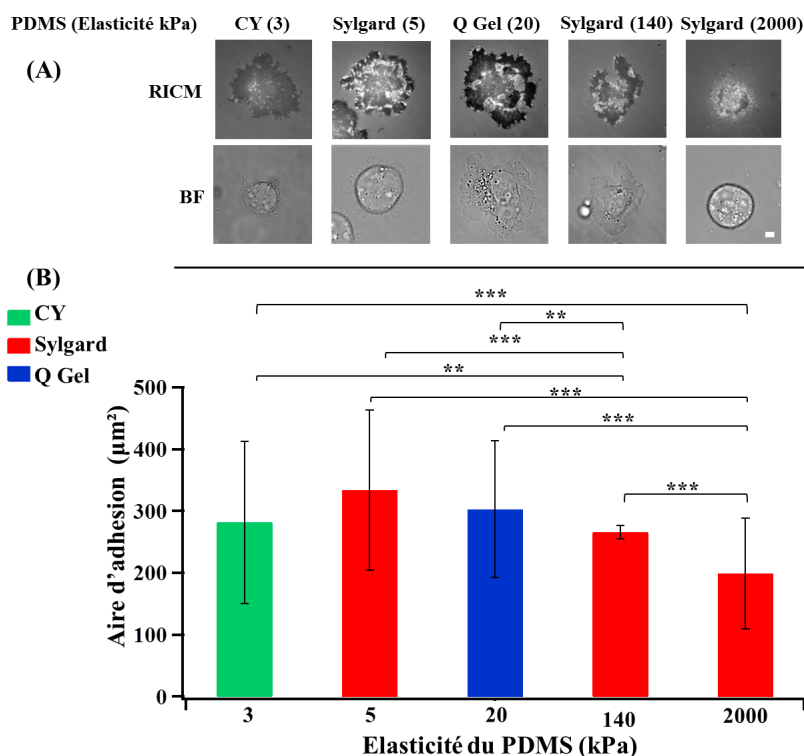
Figure 7.9 – **Aire d'adhésion de cellules adhérentes sur des substrats de PDMS de différentes élasticités.** (A) Images en Bright-field (BF) et en RICM de cellules qui s'étalent sur différents substrats de PDMS d'élasticité variés. Barre d'échelle: 4 μm. (B) L'aire d'adhésion moyen des cellules calculés à partir d'image de RICM, barre d'erreur = écarts-type. ***: P < 0.01, ** P < 0.001.

Des études sur la distribution de TCR et de ZAP-70 (protéine kinase qui joue un rôle dans la signalisation), ainsi que sur l'organisation du cytosquelette d'actine ont été menées. Les résultats montrent que sur des substrats de PDMS fonctionnalisés d'une façon homogène, une distribution homogène des molécules de TCR et de ZAP-70 est observée et ceci indépendamment de l'élasticité du PDMS. Le cytosquelette d'actine se présente sous forme d'anneau. Ces résultats sont en accord avec ceux obtenus pour des cellules-T qui s'étalent sur des substrats en verre fonctionnalisé d'une façon homogène.

Sur les substrats de Q gel 20 kPa patternés, on observe que le cytosquelette d'actine des cellules conservent sa forme en anneau. Des clusters de TCR sont détectables et co-localisent partiellement avec les agrégats d'anti-CD3.

Dans des études séparées des mesures de forces par AFM ont été faites afin de mesurer l'élasticité des cellules sur des substrats en verre ou en PDMS mou. Comme prévu, les résultats montrent que l'élasticité des cellules sur du verre est plus élevée que celle sur PDMS. Cependant, ces résultats n'ont pas été concluante, parce que nous n'avons pas pu faire correctement les mesures
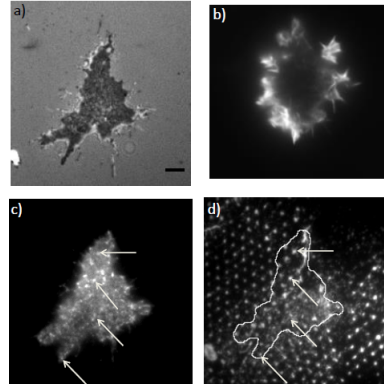
Figure 7.10 – **Cellules-T adhérentes sur élastomère mou (Q Gel 20 kPa) patterné avec des anticorps d'anti-CD3. Les cellules sont observées après 30 minutes d'étalement suivi de fixation.** (a) Image en RICM montrant une topographie plane de la membrane cellulaire dans la zone de contact. (b) Image en TIRF montrant une organisation en anneau du cytosquelette d'actine. (c) Image en TIRF du TCR sur la surface de la cellule. (d) Image d'épi-fluorescence des dots d'anti-CD3. Les flèches dans (c) et (d) indiquent une co-localisation partielle du TCR avec les dots d'anti-CD3.

de force sur du PDMS dur, où les cellules adhèrent très faiblement.

7.4 Conclusion

Nous avons développé dans ce projet une technique simple, facile, peu couteuse et rentable que nous avons nommé "reverse contact printing" permettant de structurer des substrats en verre avec des plots de protéines submicroniques et de les transférées sur des substrats d'élastomère mou (PDMS) par un simple contact physique.

Nous avons montré que notre technique peut être appliquée pour différents types de protéines, y compris, la Bovine sérum albumine (BSA), la biotine-BSA et la neutravidine. Nous avons aussi montré la réussite du transfert sur différents types de PDMS (Sylgard 184, Q gel 920 et CY52-276) d'élasticité allant de 3 kPa à 7 MPa.

Nous avons cherché à standardiser et comprendre le processus de transfert en montrant que le greffage d'une espèce moléculaire, telle qu'un fluorophore, sur la protéine à transférer, ainsi que la nature chimique de la surface du PDMS peuvent influencer fortement le succès du transfert. Le degré d'hydrophobicité, ainsi que la présence de groupes ioniques à la fois sur l'élastomère et la protéine sont des facteurs moléculaires importants qui régissent le transfert.

A l'aide de mesures de forces réalisées par AFM nous avons mesuré l'élasticité du PDMS, ainsi que les forces de cohésion et d'adhésion effectives impliquées dans le processus. Nous avons identifié que la réussite du reverse contact printing technique est facilitée par le greffage de groupes chimiques appropriés sur la protéine, et dépend du traitement de la surface du PDMS ainsi que de son élasticité.

D'autres parts, nous avons étudié l'adhésion cellulaire avec des lymphocytes-T sur des surfaces de PDMS d'élasticité variable. Nous avons montré que contrairement à la plupart d'autres types

de cellules, les cellules-T s'étalent davantage sur substrat mou (5 et 140 kPa) que sur dur (2 MPa), sur la gamme de dureté étudiée.

Finalement nous avons réalisé des expériences pilotes d'adhésion cellulaire sur PDMS structuré, que nous avons comparé à d'autres réalisées sur du verre structuré et sur surfaces de PDMS fonctionnalisées de manière homogène.

Dans la suite, nous visons à utiliser des techniques bien adaptées dans le but de mesurer les forces exercées par les cellules sur nos substrats.

Abbreviations List

μ-clusters micro-clusters

μCP   Microcontact printing

Anti-CD3 Anti-cluster of differentiation 3

APC   Antigen Presenting Cell

APTES (3-AminoPropyl)-TriEthoxySilane

bBSA   Bovine serum albumin coupled to biotin

bBSA-Atto biotin-bovin serum albumin, Atto 488 conjugated

bBSA-TR biotin-bovin serum albumin, texas red conjugated

BCML Block Copolymer Micelles Nanolithography

BF   Bright-field

BSA   Bovine serum albumin

BSA-FITC Bovine serum albumin fluorescein isothiocyanate conjugated

BSA-TR Bovine serum albumin texas-red conjugated

CAMs Cell adhesion molecules

CD3   Cluster of differentiation 3

CD3   cluster of differentiation 3

CY   CY 52-276 A and B

DPN   Dip-pen nanolithography

ECM   Extra Cellular Matrix

Glu   Glutaraldhehyde

glu CY CY after curing chemically treated with a process involving glutaraldhehyde

glu Q gel Q Gel after curing chemically treated with a process involving glutaraldhehyde

ICAM-1 Intercellular Adhesion Molecule 1

IS Immune synapse

LFA-1 Lymphocyte function-associated antigen 1

MHC Major Histocompatibility Complex

Nav Neutravidin (un-conjugated)

Nav-dylight Neutravidin dylight conjugated

Nav-FITC Neutravidin fluorescein isothiocyanate conjugated

Nav-TR Neutravidin texas-red conjugated

NIL Nanoimprint lithography

NSL Nanosphere lithography

p CY CY after curing exposed to plasma

p Q Gel Q Gel after curing exposed to plasma

p Sylgard Sylgard after curing exposed to plasma

PAA Polyacrilamide

PBS Phosphate buffer saline

PEG Polyethylene glycol

PEGPLL Polyethylene-glycol coupled to poly-L-Lysin

PEO Polyethylene oxide

PFOTCS 1H, 1H, 2H, 2H PerFluoroOctyl-TriChloroSilane

pMHC peptide MHC complex

PPO Polypropylene oxide

Q Gel Q Gel 920 A and B

RICM Reflection interference contrast microscopy

RIE Reactive ion etching

SAM Self-assembled monolayer

SLB Supported lipid bilayer

SMAC supramolecular activation cluster

Sylgard Sylgard 184 A and B

T-Cell T lymphocytes cell

TCR   T-cell receptor

TIRF-M Total internal reflection fluorescence microscopy

Appendix A

Annexes

A.1 Protocols

A.1.1 PDMS Sample Preparation

In this appendix, we will be describing step by step the technique of creating PDMS layer on clean glass substrate. It involves the following steps:

1- A plastic petri dish is placed on a digital analytical balance, and the balance is tared.

2- A certain mass of Part A (base) of the PDMS is poured in the petri dish using a plastic pipette, the balance is tared again and another mass of the part B (current agent) is then added to the part A using another clean plastic pipette. The mass of the A and B part depend of the ratio A to B of the PDMS that we want to prepare (e.g. to prepare Q gel with A to B ratio = 1/2, we need for every 1 gramme of the part A, 2 grammes of the part B). This step define the cross-linking degree.

3- The solution is mixed, in order to spread homogeneously, the curring agent in the base.

4- The bubbles formed during the mixing step, are eliminated.

This step depend on the type of the PDMS that we are preparing, in the case of Q Gel and CY PDMS ,the petri dish filled with the mixture solution is kept for some minutes at room temperature until the bubbles disappear. In the case of Sylgard, the sample need to be kept in a vacuum desiccator for around 30 minutes to eliminate the bubbles.

5- At this point, the mixture is ready to use. A glass substrate cleaned using the surfactant cleaning procedure (see section 2.1.1) is fixed on the spin coater holder (chuck) and well centered on this holder.

6- 2 ml of the polymer mixture is dispensed in the middle of the substrate using a plastic pipette.

7- The substrate is spinned at 2000 rpm for 60s with an acceleration of 300 rpm/s.

8- The polymer solution will flows radially, owing to the action of centrifugal force, and the excess is ejected off the edge of the substrate.

9- The substrate is cured on a hot plate for a certain time and a certain temperature depending on the PDMS type that we are preparing (Table 2.2). Curing the substrate is not mandatory but is required in order to decrease the polymerization time.

Bibliography

[1] B. Alberts, D. Bray, K. Hopkin, A. Johnson, J. Lewis, M. Raff, K. Roberts, and P. Walter, *Essential cell biology*. Garland Science, 2013.

[2] "Cell structure 1: Basics of cellular structures and functions." `http://biologicalphysics.iop.org/cws/article/lectures/52854`.

[3] G. Karp, "The structure and function of the plasma membrane," *Cell and Molecular Biology: Concepts and Experiments, 3rd edn. New York: John Wiley and Sons*, pp. 122–82, 2002.

[4] R. A. Freitas, *Nanomedicine, volume I: basic capabilities*. Landes Bioscience Georgetown, TX, 1999.

[5] A. Chen and V. T. Moy, "Cross-linking of cell surface receptors enhances cooperativity of molecular adhesion," *Biophysical Journal*, vol. 78, no. 6, pp. 2814–2820, 2000.

[6] S. Singer and G. L. Nicolson, "The fluid mosaic model of the structure of cell membranes," *Membranes and Viruses in Immunopathology; Day, SB, Good, RA, Eds*, pp. 7–47, 1972.

[7] "Cell membrane." `http://aisdvs.aldine.k12.tx.us/mod/book/view.php?id=179201`.

[8] B. Alberts, A. Johnson, J. Lewis, M. Raff, K. Roberts, and P. Walter, "Cell junctions, cell adhesion, and the extracellular matrix," 2002.

[9] D. A. Fletcher and R. D. Mullins, "Cell mechanics and the cytoskeleton," *Nature*, vol. 463, no. 7280, pp. 485–492, 2010.

[10] G. Michel, T. Tonon, D. Scornet, J. M. Cock, and B. Kloareg, "The cell wall polysaccharide metabolism of the brown alga ectocarpus siliculosus. insights into the evolution of extracellular matrix polysaccharides in eukaryotes," *New Phytologist*, vol. 188, no. 1, pp. 82–97, 2010.

[11] M. Abedin and N. King, "Diverse evolutionary paths to cell adhesion," *Trends in cell biology*, vol. 20, no. 12, pp. 734–742, 2010.

[12] D. S. Harburger and D. A. Calderwood, "Integrin signalling at a glance," *Journal of cell science*, vol. 122, no. 2, pp. 159–163, 2009.

[13] E. A. Cavalcanti-Adam, T. Volberg, A. Micoulet, H. Kessler, B. Geiger, and J. P. Spatz, "Cell spreading and focal adhesion dynamics are regulated by spacing of integrin ligands," *Biophysical journal*, vol. 92, no. 8, pp. 2964–2974, 2007.

[14] H. Delanoë-Ayari, J. Rieu, and M. Sano, "4d traction force microscopy reveals asymmetric cortical forces in migrating dictyostelium cells," *Physical Review Letters*, vol. 105, no. 24, p. 248103, 2010.

[15] S. Schmidt and P. Friedl, "Interstitial cell migration: integrin-dependent and alternative adhesion mechanisms," *Cell and tissue research*, vol. 339, no. 1, pp. 83–92, 2010.

[16] W. Walz, *The neuronal environment: brain homeostasis in health and disease.* Springer Science & Business Media, 2001.

[17] R. Merkel, N. Kirchgeßner, C. M. Cesa, and B. Hoffmann, "Cell force microscopy on elastic layers of finite thickness," *Biophysical journal*, vol. 93, no. 9, pp. 3314–3323, 2007.

[18] R. G. Wells, "The role of matrix stiffness in regulating cell behavior," *Hepatology*, vol. 47, no. 4, pp. 1394–1400, 2008.

[19] S. Johansson, G. Svineng, K. Wennerberg, A. Armulik, and L. Lohikangas, "Fibronectin-integrin interactions," *Front Biosci*, vol. 2, pp. d126–d146, 1997.

[20] B. Geiger, J. P. Spatz, and A. D. Bershadsky, "Environmental sensing through focal adhesions," *Nature reviews Molecular cell biology*, vol. 10, no. 1, pp. 21–33, 2009.

[21] M. D. Mager, V. LaPointe, and M. M. Stevens, "Exploring and exploiting chemistry at the cell surface," *Nature Chemistry*, vol. 3, no. 8, pp. 582–589, 2011.

[22] S. W. Moore, P. Roca-Cusachs, and M. P. Sheetz, "Stretchy proteins on stretchy substrates: the important elements of integrin-mediated rigidity sensing," *Developmental cell*, vol. 19, no. 2, pp. 194–206, 2010.

[23] A. A. Khalili and M. R. Ahmad, "A review of cell adhesion studies for biomedical and biological applications," *International journal of molecular sciences*, vol. 16, no. 8, pp. 18149–18184, 2015.

[24] J. H. Lee and H. B. Lee, "A wettability gradient as a tool to study protein adsorption and cell adhesion on polymer surfaces," *Journal of Biomaterials Science, Polymer Edition*, vol. 4, no. 5, pp. 467–481, 1993.

[25] G. Maheshwari, A. Wells, L. G. Griffith, and D. A. Lauffenburger, "Biophysical integration of effects of epidermal growth factor and fibronectin on fibroblast migration," *Biophysical Journal*, vol. 76, no. 5, pp. 2814–2823, 1999.

[26] A. Curtis, B. Casey, J. Gallagher, D. Pasqui, M. Wood, and C. Wilkinson, "Substratum nanotopography and the adhesion of biological cells. are symmetry or regularity of nanotopography important?," *Biophysical chemistry*, vol. 94, no. 3, pp. 275–283, 2001.

[27] K. Anselme, "Osteoblast adhesion on biomaterials," *Biomaterials*, vol. 21, no. 7, pp. 667–681, 2000.

[28] J. Solon, I. Levental, K. Sengupta, P. C. Georges, and P. A. Janmey, "Fibroblast adaptation and stiffness matching to soft elastic substrates," *Biophysical journal*, vol. 93, no. 12, pp. 4453–4461, 2007.

[29] L.-C. Xu and C. A. Siedlecki, "Effects of surface wettability and contact time on protein adhesion to biomaterial surfaces," *Biomaterials*, vol. 28, no. 22, pp. 3273–3283, 2007.

[30] A. Sethuraman, M. Han, R. S. Kane, and G. Belfort, "Effect of surface wettability on the adhesion of proteins," *Langmuir*, vol. 20, no. 18, pp. 7779–7788, 2004.

[31] G. Altankov and T. Groth, "Reorganization of substratum-bound fibronectin on hydrophilic and hydrophobic materials is related to biocompatibility," *Journal of Materials Science: Materials in Medicine*, vol. 5, no. 9-10, pp. 732–737, 1994.

[32] C. A. Haynes and W. Norde, "Globular proteins at solid/liquid interfaces," *Colloids and Surfaces B: Biointerfaces*, vol. 2, no. 6, pp. 517–566, 1994.

[33] M. S. Wang, L. B. Palmer, J. D. Schwartz, and A. Razatos, "Evaluating protein attraction and adhesion to biomaterials with the atomic force microscope," *Langmuir*, vol. 20, no. 18, pp. 7753–7759, 2004.

[34] J. M. Dechene, *Surface Modifications of Poly (dimethylsiloxane) for Biological Application of Microfluidic Devices*. PhD thesis, The University of Western Ontario, 2010.

[35] K. B. McClary, T. Ugarova, and D. W. Grainger, "Modulating fibroblast adhesion, spreading, and proliferation using self-assembled monolayer films of alkylthiolates on gold," *Journal of biomedical materials research*, vol. 50, no. 3, pp. 428–439, 2000.

[36] C. C. Barrias, M. C. L. Martins, G. Almeida-Porada, M. A. Barbosa, and P. L. Granja, "The correlation between the adsorption of adhesive proteins and cell behaviour on hydroxyl-methyl mixed self-assembled monolayers," *Biomaterials*, vol. 30, no. 3, pp. 307–316, 2009.

[37] Y.-W. Wang, Q. Wu, and G.-Q. Chen, "Reduced mouse fibroblast cell growth by increased hydrophilicity of microbial polyhydroxyalkanoates via hyaluronan coating," *Biomaterials*, vol. 24, no. 25, pp. 4621–4629, 2003.

[38] D. P. Dowling, I. S. Miller, M. Ardhaoui, and W. M. Gallagher, "Effect of surface wettability and topography on the adhesion of osteosarcoma cells on plasma-modified polystyrene," *Journal of biomaterials applications*, 2010.

[39] S. Kuddannaya, Y. J. Chuah, M. H. A. Lee, N. V. Menon, Y. Kang, and Y. Zhang, "Surface chemical modification of poly (dimethylsiloxane) for the enhanced adhesion and proliferation of mesenchymal stem cells," *ACS applied materials & interfaces*, vol. 5, no. 19, pp. 9777–9784, 2013.

[40] B. A. Dalton, C. D. McFarland, T. R. Gengenbach, H. J. Griesser, and J. G. Steele, "Polymer surface chemistry and bone cell migration," *Journal of Biomaterials Science, Polymer Edition*, vol. 9, no. 8, pp. 781–799, 1998.

[41] Z. Yang, J. A. Galloway, and H. Yu, "Protein interactions with poly (ethylene glycol) self-assembled monolayers on glass substrates: diffusion and adsorption," *Langmuir*, vol. 15, no. 24, pp. 8405–8411, 1999.

[42] E. Tziampazis, J. Kohn, and P. V. Moghe, "Peg-variant biomaterials as selectively adhesive protein templates: model surfaces for controlled cell adhesion and migration," *Biomaterials*, vol. 21, no. 5, pp. 511–520, 2000.

[43] D. D. Deligianni, N. D. Katsala, P. G. Koutsoukos, and Y. F. Missirlis, "Effect of surface roughness of hydroxyapatite on human bone marrow cell adhesion, proliferation, differentiation and detachment strength," *Biomaterials*, vol. 22, no. 1, pp. 87–96, 2000.

[44] B. D. Boyan, T. W. Hummert, D. D. Dean, and Z. Schwartz, "Role of material surfaces in regulating bone and cartilage cell response," *Biomaterials*, vol. 17, no. 2, pp. 137–146, 1996.

[45] K. C. Dee, D. A. Puleo, and R. Bizios, *An introduction to tissue-biomaterial interactions*. John Wiley & Sons, 2003.

[46] E. C. Martínez, J. C. R. Hernández, M. Machado, J. F. Mano, J. L. G. Ribelles, M. M. Pradas, and M. S. Sánchez, "Human chondrocyte morphology, its dedifferentiation, and fibronectin conformation on different plla microtopographies," *Tissue Engineering Part A*, vol. 14, no. 10, pp. 1751–1762, 2008.

[47] K. Hatano, H. Inoue, T. Kojo, T. Matsunaga, T. Tsujisawa, C. Uchiyama, and Y. Uchida, "Effect of surface roughness on proliferation and alkaline phosphatase expression of rat calvarial cells cultured on polystyrene," *Bone*, vol. 25, no. 4, pp. 439–445, 1999.

[48] J. Y. Lim, J. C. Hansen, C. A. Siedlecki, J. Runt, and H. J. Donahue, "Human foetal osteoblastic cell response to polymer-demixed nanotopographic interfaces," *Journal of the Royal Society Interface*, vol. 2, no. 2, pp. 97–108, 2005.

[49] J. Martin, Z. Schwartz, T. Hummert, D. Schraub, J. Simpson, J. Lankford, D. Dean, D. Cochran, and B. Boyan, "Effect of titanium surface roughness on proliferation, differentiation, and protein synthesis of human osteoblast-like cells (mg63)," *Journal of biomedical materials research*, vol. 29, no. 3, pp. 389–401, 1995.

[50] K. Anselme, P. Linez, M. Bigerelle, D. Le Maguer, A. Le Maguer, P. Hardouin, H. Hildebrand, A. Iost, and J. Leroy, "The relative influence of the topography and chemistry of tial6v4 surfaces on osteoblastic cell behaviour," *Biomaterials*, vol. 21, no. 15, pp. 1567–1577, 2000.

[51] M. Arnold, E. A. Cavalcanti-Adam, R. Glass, J. Blümmel, W. Eck, M. Kantlehner, H. Kessler, and J. P. Spatz, "Activation of integrin function by nanopatterned adhesive interfaces," *ChemPhysChem*, vol. 5, no. 3, pp. 383–388, 2004.

[52] A. Curtis and C. Wilkinson, "Topographical control of cells," *Biomaterials*, vol. 18, no. 24, pp. 1573–1583, 1997.

[53] C. S. Chen, M. Mrksich, S. Huang, G. M. Whitesides, and D. E. Ingber, "Geometric control of cell life and death," *Science*, vol. 276, no. 5317, pp. 1425–1428, 1997.

[54] M. Arnold, M. Schwieder, J. Blümmel, E. A. Cavalcanti-Adam, M. López-Garcia, H. Kessler, B. Geiger, and J. P. Spatz, "Cell interactions with hierarchically structured nano-patterned adhesive surfaces," *Soft Matter*, vol. 5, no. 1, pp. 72–77, 2009.

[55] M. Théry, "Micropatterning as a tool to decipher cell morphogenesis and functions," *J Cell Sci*, vol. 123, no. 24, pp. 4201–4213, 2010.

[56] M. Théry, V. Racine, A. Pépin, M. Piel, Y. Chen, J.-B. Sibarita, and M. Bornens, "The extracellular matrix guides the orientation of the cell division axis," *Nature cell biology*, vol. 7, no. 10, pp. 947–953, 2005.

[57] M. Thery, A. Jiménez-Dalmaroni, V. Racine, M. Bornens, and F. Jülicher, "Experimental and theoretical study of mitotic spindle orientation," *Nature*, vol. 447, no. 7143, pp. 493–496, 2007.

[58] M. Bailly, L. Yan, G. M. Whitesides, J. S. Condeelis, and J. E. Segall, "Regulation of protrusion shape and adhesion to the substratum during chemotactic responses of mammalian carcinoma cells," *Experimental cell research*, vol. 241, no. 2, pp. 285–299, 1998.

[59] R. Glass, M. Möller, and J. P. Spatz, "Block copolymer micelle nanolithography," *Nanotechnology*, vol. 14, no. 10, p. 1153, 2003.

[60] C. Selhuber-Unkel, T. Erdmann, M. Lopez-Garcia, H. Kessler, U. Schwarz, and J. Spatz, "Cell adhesion strength is controlled by intermolecular spacing of adhesion receptors," *Biophysical Journal*, vol. 98, no. 4, pp. 543–551, 2010.

[61] M. S. Niepel, B. Fuhrmann, H. S. Leipner, and T. Groth, "Nanoscaled surface patterns influence adhesion and growth of human dermal fibroblasts," *Langmuir*, vol. 29, no. 43, pp. 13278–13290, 2013.

[62] B. N. Mason, J. P. Califano, and C. A. Reinhart-King, "Matrix stiffness: A regulator of cellular behavior and tissue formation," in *Engineering Biomaterials for Regenerative Medicine*, pp. 19–37, Springer, 2012.

[63] P. A. Janmey, J. P. Winer, M. E. Murray, and Q. Wen, "The hard life of soft cells," *Cell motility and the cytoskeleton*, vol. 66, no. 8, pp. 597–605, 2009.

[64] V. Vogel and M. Sheetz, "Local force and geometry sensing regulate cell functions," *Nature reviews Molecular cell biology*, vol. 7, no. 4, pp. 265–275, 2006.

[65] D. Ingber, "Mechanobiology and diseases of mechanotransduction," *Annals of medicine*, vol. 35, no. 8, pp. 564–577, 2003.

[66] R. J. Pelham and Y.-l. Wang, "Cell locomotion and focal adhesions are regulated by substrate flexibility," *Proceedings of the National Academy of Sciences*, vol. 94, no. 25, pp. 13661–13665, 1997.

[67] A. K. Harris, P. Wild, D. Stopak, *et al.*, "Silicone rubber substrata: a new wrinkle in the study of cell locomotion," *Science*, vol. 208, no. 4440, pp. 177–179, 1980.

[68] U. S. Schwarz and J. R. Soiné, "Traction force microscopy on soft elastic substrates: a guide to recent computational advances," *Biochimica et Biophysica Acta (BBA)-Molecular Cell Research*, vol. 1853, no. 11, pp. 3095–3104, 2015.

[69] M. Dembo, T. Oliver, A. Ishihara, and K. Jacobson, "Imaging the traction stresses exerted by locomoting cells with the elastic substratum method," *Biophysical journal*, vol. 70, no. 4, pp. 2008–2022, 1996.

[70] M. Dembo and Y.-L. Wang, "Stresses at the cell-to-substrate interface during locomotion of fibroblasts," *Biophysical journal*, vol. 76, no. 4, pp. 2307–2316, 1999.

[71] C. M. Cesa, N. Kirchgeßner, D. Mayer, U. S. Schwarz, B. Hoffmann, and R. Merkel, "Micropatterned silicone elastomer substrates for high resolution analysis of cellular force patterns," *Review of scientific instruments*, vol. 78, no. 3, p. 034301, 2007.

[72] J. R. Soine, N. Hersch, G. Dreissen, N. Hampe, B. Hoffmann, R. Merkel, and U. S. Schwarz, "Measuring cellular traction forces on non-planar substrates," *arXiv preprint arXiv:1605.08373*, 2016.

[73] N. Q. Balaban, U. S. Schwarz, D. Riveline, P. Goichberg, G. Tzur, I. Sabanay, D. Mahalu, S. Safran, A. Bershadsky, L. Addadi, *et al.*, "Force and focal adhesion assembly: a close relationship studied using elastic micropatterned substrates," *Nature cell biology*, vol. 3, no. 5, pp. 466–472, 2001.

[74] N. J. Sniadecki and C. S. Chen, "Microfabricated silicone elastomeric post arrays for measuring traction forces of adherent cells," *Methods in cell biology*, vol. 83, pp. 313–328, 2007.

[75] S. Ghassemi, G. Meacci, S. Liu, A. A. Gondarenko, A. Mathur, P. Roca-Cusachs, M. P. Sheetz, and J. Hone, "Cells test substrate rigidity by local contractions on submicrometer pillars," *Proceedings of the National Academy of Sciences*, vol. 109, no. 14, pp. 5328–5333, 2012.

[76] O. Du Roure, A. Saez, A. Buguin, R. H. Austin, P. Chavrier, P. Siberzan, and B. Ladoux, "Force mapping in epithelial cell migration," *Proceedings of the National Academy of Sciences of the United States of America*, vol. 102, no. 7, pp. 2390–2395, 2005.

[77] L. Trichet, J. Le Digabel, R. J. Hawkins, S. R. K. Vedula, M. Gupta, C. Ribrault, P. Hersen, R. Voituriez, and B. Ladoux, "Evidence of a large-scale mechanosensing mechanism for cellular adaptation to substrate stiffness," *Proceedings of the National Academy of Sciences*, vol. 109, no. 18, pp. 6933–6938, 2012.

[78] R. De, A. Zemel, and S. A. Safran, "Do cells sense stress or strain? measurement of cellular orientation can provide a clue," *Biophysical journal*, vol. 94, no. 5, pp. L29–L31, 2008.

[79] A. K. Yip, K. Iwasaki, C. Ursekar, H. Machiyama, M. Saxena, H. Chen, I. Harada, K.-H. Chiam, and Y. Sawada, "Cellular response to substrate rigidity is governed by either stress or strain," *Biophysical journal*, vol. 104, no. 1, pp. 19–29, 2013.

[80] K. A. Jansen, D. M. Donato, H. E. Balcioglu, T. Schmidt, E. H. Danen, and G. H. Koenderink, "A guide to mechanobiology: where biology and physics meet," *Biochimica et Biophysica Acta (BBA)-Molecular Cell Research*, vol. 1853, no. 11, pp. 3043–3052, 2015.

[81] B. Trappmann, J. E. Gautrot, J. T. Connelly, D. G. Strange, Y. Li, M. L. Oyen, M. A. C. Stuart, H. Boehm, B. Li, V. Vogel, *et al.*, "Extracellular-matrix tethering regulates stem-cell fate," *Nature materials*, vol. 11, no. 7, pp. 642–649, 2012.

[82] A. Buxboim, K. Rajagopal, B. Andre'EX, and D. E. Discher, "How deeply cells feel: methods for thin gels," *Journal of Physics: Condensed Matter*, vol. 22, no. 19, p. 194116, 2010.

[83] A. J. Engler, S. Sen, H. L. Sweeney, and D. E. Discher, "Matrix elasticity directs stem cell lineage specification," *Cell*, vol. 126, no. 4, pp. 677–689, 2006.

[84] C. Yang, M. W. Tibbitt, L. Basta, and K. S. Anseth, "Mechanical memory and dosing influence stem cell fate," *Nature materials*, vol. 13, no. 6, p. 645, 2014.

[85] D. Missirlis and J. P. Spatz, "Combined effects of peg hydrogel elasticity and cell-adhesive coating on fibroblast adhesion and persistent migration," *Biomacromolecules*, vol. 15, no. 1, pp. 195–205, 2013.

[86] I. Levental, P. C. Georges, and P. A. Janmey, "Soft biological materials and their impact on cell function," *Soft Matter*, vol. 3, no. 3, pp. 299–306, 2007.

[87] A. J. Engler, M. A. Griffin, S. Sen, C. G. Bönnemann, H. L. Sweeney, and D. E. Discher, "Myotubes differentiate optimally on substrates with tissue-like stiffness pathological implications for soft or stiff microenvironments," *The Journal of cell biology*, vol. 166, no. 6, pp. 877–887, 2004.

[88] A. J. Engler, C. Carag-Krieger, C. P. Johnson, M. Raab, H.-Y. Tang, D. W. Speicher, J. W. Sanger, J. M. Sanger, and D. E. Discher, "Embryonic cardiomyocytes beat best on a matrix with heart-like elasticity: scar-like rigidity inhibits beating," *Journal of cell science*, vol. 121, no. 22, pp. 3794–3802, 2008.

[89] M. R. Ng and J. S. Brugge, "A stiff blow from the stroma: collagen crosslinking drives tumor progression," *Cancer cell*, vol. 16, no. 6, pp. 455–457, 2009.

[90] R. G. Wells, "Cellular sources of extracellular matrix in hepatic fibrosis," *Clinics in liver disease*, vol. 12, no. 4, pp. 759–768, 2008.

[91] C. A. Janeway, P. Travers, M. Walport, and M. J. Shlomchik, *Immunobiology: the immune system in health and disease*, vol. 1. Current Biology, 1997.

[92] K. D. Elgert, *Immunology: understanding the immune system*. John Wiley & Sons, 2009.

[93] B. H. Rimawi, "Infectious comorbidities encountered in obstetrics and neonatology," *OMICS Group eBooks. Foster city, California, USA*, 2014.

[94] R. Clark and T. Kupper, "Old meets new: the interaction between innate and adaptive immunity," *Journal of investigative dermatology*, vol. 125, no. 4, pp. 629–637, 2005.

[95] J. Sprent, "Antigen-presenting cells: professionals and amateurs," *Current Biology*, vol. 5, no. 10, pp. 1095–1097, 1995.

[96] T. Kambayashi and T. M. Laufer, "Atypical mhc class ii-expressing antigen-presenting cells: can anything replace a dendritic cell?," *Nature Reviews Immunology*, vol. 14, no. 11, pp. 719–730, 2014.

[97] M. O. Butler and N. Hirano, "Human cell-based artificial antigen-presenting cells for cancer immunotherapy," *Immunological reviews*, vol. 257, no. 1, pp. 191–209, 2014.

[98] L. J. Eggermont, L. E. Paulis, J. Tel, and C. G. Figdor, "Towards efficient cancer immunotherapy: advances in developing artificial antigen-presenting cells," *Trends in biotechnology*, vol. 32, no. 9, pp. 456–465, 2014.

[99] "Immune system." `http://slideplayer.com/slide/10780579/`. Accessed june 5, 2016.

[100] X. Lu, J. S. Gibbs, H. D. Hickman, A. David, B. P. Dolan, Y. Jin, D. M. Kranz, J. R. Bennink, J. W. Yewdell, and R. Varma, "Endogenous viral antigen processing generates peptide-specific mhc class i cell-surface clusters," *Proceedings of the National Academy of Sciences*, vol. 109, no. 38, pp. 15407–15412, 2012.

[101] M. Ferez, M. Castro, B. Alarcon, and H. M. van Santen, "Cognate peptide–mhc complexes are expressed as tightly apposed nanoclusters in virus-infected cells to allow tcr crosslinking," *The Journal of Immunology*, vol. 192, no. 1, pp. 52–58, 2014.

[102] K. P. Menard, *Dynamic mechanical analysis: a practical introduction*. CRC press, 2008.

[103] N. Bufi, M. Saitakis, S. Dogniaux, O. Buschinger, A. Bohineust, A. Richert, M. Maurin, C. Hivroz, and A. Asnacios, "Human primary immune cells exhibit distinct mechanical properties that are modified by inflammation," *Biophysical journal*, vol. 108, no. 9, pp. 2181–2190, 2015.

[104] "T-cells." `https://www.studyblue.com/notes/note/n/exam-1-tables-and-diagrams/deck/3727242`. Accessed june 5, 2016.

[105] M. J. Miller, A. S. Hejazi, S. H. Wei, M. D. Cahalan, and I. Parker, "T cell repertoire scanning is promoted by dynamic dendritic cell behavior and random t cell motility in the lymph node," *Proceedings of the National Academy of Sciences of the United States of America*, vol. 101, no. 4, pp. 998–1003, 2004.

[106] J. Delon and R. N. Germain, "Information transfer at the immunological synapse," *Current Biology*, vol. 10, no. 24, pp. R923–R933, 2000.

[107] D. R. Fooksman, S. Vardhana, G. Vasiliver-Shamis, J. Liese, D. Blair, J. Waite, C. Sacristán, G. Victora, A. Zanin-Zhorov, and M. L. Dustin, "Functional anatomy of t cell activation and synapse formation," *Annual review of immunology*, vol. 28, p. 79, 2010.

[108] A. Grakoui, S. K. Bromley, C. Sumen, M. M. Davis, A. S. Shaw, P. M. Allen, and M. L. Dustin, "The immunological synapse: a molecular machine controlling t cell activation," *Science*, vol. 285, no. 5425, pp. 221–227, 1999.

[109] M. L. Dustin and J. T. Groves, "Receptor signaling clusters in the immune synapse," *Annual review of biophysics*, vol. 41, p. 543, 2012.

[110] C. P. Semba and T. R. Gadek, "Development of lifitegrast: a novel t-cell inhibitor for the treatment of dry eye disease," *Clinical Ophthalmology (Auckland, NZ)*, vol. 10, p. 1083, 2016.

[111] M. Norcross, "A synaptic basis for t-lymphocyte activation," in *Annales de l'Institut Pasteur/Immunologie*, vol. 135, pp. 113–134, Elsevier, 1984.

[112] C. R. Monks, B. A. Freiberg, H. Kupfer, N. Sciaky, and A. Kupfer, "Three-dimensional segregation of supramolecular activation clusters in t cells," *Nature*, vol. 395, no. 6697, pp. 82–86, 1998.

[113] P. Dillard, R. Varma, K. Sengupta, and L. Limozin, "Ligand-mediated friction determines morphodynamics of spreading t cells," *Biophysical journal*, vol. 107, no. 11, pp. 2629–2638, 2014.

[114] J. T. Groves, N. Ulman, and S. G. Boxer, "Micropatterning fluid lipid bilayers on solid supports," *Science*, vol. 275, no. 5300, pp. 651–653, 1997.

[115] K. D. Mossman, G. Campi, J. T. Groves, and M. L. Dustin, "Altered tcr signaling from geometrically repatterned immunological synapses," *Science*, vol. 310, no. 5751, pp. 1191–1193, 2005.

[116] G. Campi, R. Varma, and M. L. Dustin, "Actin and agonist mhc–peptide complex–dependent t cell receptor microclusters as scaffolds for signaling," *The Journal of experimental medicine*, vol. 202, no. 8, pp. 1031–1036, 2005.

[117] Y. Kaizuka, A. D. Douglass, R. Varma, M. L. Dustin, and R. D. Vale, "Mechanisms for segregating t cell receptor and adhesion molecules during immunological synapse formation in jurkat t cells," *Proceedings of the National Academy of Sciences*, vol. 104, no. 51, pp. 20296–20301, 2007.

[118] R. Varma, G. Campi, T. Yokosuka, T. Saito, and M. L. Dustin, "T cell receptor-proximal signals are sustained in peripheral microclusters and terminated in the central supramolecular activation cluster," *Immunity*, vol. 25, no. 1, pp. 117–127, 2006.

[119] T. Yokosuka, K. Sakata-Sogawa, W. Kobayashi, M. Hiroshima, A. Hashimoto-Tane, M. Tokunaga, M. L. Dustin, and T. Saito, "Newly generated t cell receptor microclusters initiate and sustain t cell activation by recruitment of zap70 and slp-76," *Nature immunology*, vol. 6, no. 12, pp. 1253–1262, 2005.

[120] S. C. Bunnell, "Multiple microclusters: diverse compartments within the immune synapse," in *Immunological Synapse*, pp. 123–154, Springer, 2010.

[121] K. Beck-García, E. Beck-García, S. Bohler, C. Zorzin, E. Sezgin, I. Levental, B. Alarcón, and W. W. Schamel, "Nanoclusters of the resting t cell antigen receptor (tcr) localize to non-raft domains," *Biochimica et Biophysica Acta (BBA)-Molecular Cell Research*, vol. 1853, no. 4, pp. 802–809, 2015.

[122] T. J. Crites, K. Padhan, J. Muller, M. Krogsgaard, P. R. Gudla, S. J. Lockett, and R. Varma, "Tcr microclusters pre-exist and contain molecules necessary for tcr signal transduction," *The Journal of Immunology*, vol. 193, no. 1, pp. 56–67, 2014.

[123] P. Dillard, F. Pi, A. C. Lellouch, L. Limozin, and K. Sengupta, "Nano-clustering of ligands on surrogate antigen presenting cells modulates t cell membrane adhesion and organization," *Integrative Biology*, vol. 8, no. 3, pp. 287–301, 2016.

[124] J. Deeg, M. Axmann, J. Matic, A. Liapis, D. Depoil, J. Afrose, S. Curado, M. L. Dustin, and J. P. Spatz, "T cell activation is determined by the number of presented antigens," *Nano letters*, vol. 13, no. 11, pp. 5619–5626, 2013.

[125] J. Matic, J. Deeg, A. Scheffold, I. Goldstein, and J. P. Spatz, "Fine tuning and efficient t cell activation with stimulatory acd3 nanoarrays," *Nano letters*, vol. 13, no. 11, pp. 5090–5097, 2013.

[126] E. Judokusumo, E. Tabdanov, S. Kumari, M. L. Dustin, and L. C. Kam, "Mechanosensing in t lymphocyte activation," *Biophysical journal*, vol. 102, no. 2, pp. L5–L7, 2012.

[127] R. S. O'Connor, X. Hao, K. Shen, K. Bashour, T. Akimova, W. W. Hancock, L. C. Kam, and M. C. Milone, "Substrate rigidity regulates human t cell activation and proliferation," *The Journal of Immunology*, vol. 189, no. 3, pp. 1330–1339, 2012.

[128] K. T. Bashour, A. Gondarenko, H. Chen, K. Shen, X. Liu, M. Huse, J. C. Hone, and L. C. Kam, "Cd28 and cd3 have complementary roles in t-cell traction forces," *Proceedings of the National Academy of Sciences*, vol. 111, no. 6, pp. 2241–2246, 2014.

[129] K. L. Hui, L. Balagopalan, L. E. Samelson, and A. Upadhyaya, "Cytoskeletal forces during signaling activation in jurkat t-cells," *Molecular biology of the cell*, vol. 26, no. 4, pp. 685–695, 2015.

[130] H. Chen, L. Yuan, W. Song, Z. Wu, and D. Li, "Biocompatible polymer materials: role of protein–surface interactions," *Progress in Polymer Science*, vol. 33, no. 11, pp. 1059–1087, 2008.

[131] E. A. Vogler, "Protein adsorption in three dimensions," *Biomaterials*, vol. 33, no. 5, pp. 1201–1237, 2012.

[132] G. M. Whitesides, E. Ostuni, S. Takayama, X. Jiang, and D. E. Ingber, "Soft lithography in biology and biochemistry," *Annual review of biomedical engineering*, vol. 3, no. 1, pp. 335–373, 2001.

[133] S. A. Ruiz and C. S. Chen, "Microcontact printing: a tool to pattern," *Soft Matter*, vol. 3, no. 2, pp. 168–177, 2007.

[134] J. J. Moon, B. Huang, and D. J. Irvine, "Engineering nano-and microparticles to tune immunity," *Advanced materials*, vol. 24, no. 28, pp. 3724–3746, 2012.

[135] I. Platzman, K. M. Gadomska, J.-W. Janiesch, I. Louban, E. A. Cavalcanti-Adam, and J. P. Spatz, "Soft/elastic nanopatterned biointerfaces in the service of cell biology.," *Methods in cell biology*, vol. 119, pp. 237–260, 2013.

[136] A. Biswas, I. S. Bayer, A. S. Biris, T. Wang, E. Dervishi, and F. Faupel, "Advances in top–down and bottom–up surface nanofabrication: Techniques, applications & future prospects," *Advances in colloid and interface science*, vol. 170, no. 1, pp. 2–27, 2012.

[137] D. Falconnet, G. Csucs, H. M. Grandin, and M. Textor, "Surface engineering approaches to micropattern surfaces for cell-based assays," *Biomaterials*, vol. 27, no. 16, pp. 3044–3063, 2006.

[138] L. Filipponi, D. Sutherland, and I. N. Center, "Nanoyou teachers training kit in nanotechnologies," *European Commision Document, Denmark*, 2010.

[139] P. Rodgers, "Nanofabrication: Top down, bottom up," *Nature Nanotechnology, DOI*, vol. 10, 2006.

[140] M. J. P. Roldan, *Chemical patterning of surfaces for the development of biofunctional interfaces*. PhD thesis, Universidad Autónoma de Madrid, 2011.

[141] "Photolithography." `http://cnx.org/contents/KZdIG-zX@2/Composition-and-Photochemical-`. Accessed August 19, 2016.

[142] B. Spargo, M. Testoff, T. Nielsen, D. Stenger, J. Hickman, and A. Rudolph, "Spatially controlled adhesion, spreading, and differentiation of endothelial cells on self-assembled molecular monolayers," *Proceedings of the National Academy of Sciences*, vol. 91, no. 23, pp. 11070–11074, 1994.

[143] S. K. Bhatia, J. J. Hickman, and F. S. Ligler, "New approach to producing patterned biomolecular assemblies," *Journal of the American Chemical Society*, vol. 114, no. 11, pp. 4432–4433, 1992.

[144] T. Matsuda, K. Inoue, and N. Tani, "Control of cell arrangement," Apr. 13 1993. US Patent 5,202,227.

[145] M. Veiseh, B. T. Wickes, D. G. Castner, and M. Zhang, "Guided cell patterning on gold–silicon dioxide substrates by surface molecular engineering," *Biomaterials*, vol. 25, no. 16, pp. 3315–3324, 2004.

[146] F. Yap and Y. Zhang, "Protein and cell micropatterning and its integration with micro/nanoparticles assembly," *Biosensors and Bioelectronics*, vol. 22, no. 6, pp. 775–788, 2007.

[147] G. M. Whitesides and A. D. Stroock, "Flexible methods for microfluidics," *Phys. Today*, vol. 54, no. 6, pp. 42–48, 2001.

[148] H. Schmid and B. Michel, "Siloxane polymers for high-resolution, high-accuracy soft lithography," *Macromolecules*, vol. 33, no. 8, pp. 3042–3049, 2000.

[149] T. W. Odom, J. C. Love, D. B. Wolfe, K. E. Paul, and G. M. Whitesides, "Improved pattern transfer in soft lithography using composite stamps," *Langmuir*, vol. 18, no. 13, pp. 5314–5320, 2002.

[150] X. Jiang, S. Takayama, R. G. Chapman, R. S. Kane, and G. M. Whitesides, "Micro-scale patterning of cells and their environment," 2007.

[151] A. Bernard, J. P. Renault, B. Michel, H. R. Bosshard, E. Delamarche, *et al.*, "Microcontact printing of proteins," *Advanced Materials*, vol. 12, no. 14, pp. 1067–1070, 2000.

[152] Y. Xia and G. M. Whitesides, "Soft lithography," *Annual review of materials science*, vol. 28, no. 1, pp. 153–184, 1998.

[153] A. Kumar and G. M. Whitesides, "Features of gold having micrometer to centimeter dimensions can be formed through a combination of stamping with an elastomeric stamp and an alkanethiol "ink" followed by chemical etching," *Applied Physics Letters*, vol. 63, no. 14, pp. 2002–2004, 1993.

[154] M. Mrksich and G. M. Whitesides, "Patterning self-assembled monolayers using microcontact printing: a new technology for biosensors?," *Trends in biotechnology*, vol. 13, no. 6, pp. 228–235, 1995.

[155] M. Geissler, A. Bernard, A. Bietsch, H. Schmid, B. Michel, and E. Delamarche, "Microcontact-printing chemical patterns with flat stamps," *Journal of the American Chemical Society*, vol. 122, no. 26, pp. 6303–6304, 2000.

[156] L. Filipponi, P. Livingston, O. Kašpar, V. Tokárová, and D. V. Nicolau, "Protein patterning by microcontact printing using pyramidal pdms stamps," *Biomedical microdevices*, vol. 18, no. 1, pp. 1–7, 2016.

[157] N. Hampe, T. Jonas, B. Wolters, N. Hersch, B. Hoffmann, and R. Merkel, "Defined 2-d microtissues on soft elastomeric silicone rubber using lift-off epoxy-membranes for biomechanical analyses," *Soft matter*, vol. 10, no. 14, pp. 2431–2443, 2014.

[158] A. Perl, D. N. Reinhoudt, and J. Huskens, "Microcontact printing: limitations and achievements," *Advanced Materials*, vol. 21, no. 22, pp. 2257–2268, 2009.

[159] X. Yan, J. Yao, G. Lu, X. Chen, K. Zhang, and B. Yang, "Microcontact printing of colloidal crystals," *Journal of the American Chemical Society*, vol. 126, no. 34, pp. 10510–10511, 2004.

[160] D. Trimbach, K. Feldman, N. D. Spencer, D. J. Broer, and C. W. Bastiaansen, "Block copolymer thermoplastic elastomers for microcontact printing," *Langmuir*, vol. 19, no. 26, pp. 10957–10961, 2003.

[161] S. G. Ricoult, A. Sanati Nezhad, M. Knapp-Mohammady, T. E. Kennedy, and D. Juncker, "Humidified microcontact printing of proteins: universal patterning of proteins on both low and high energy surfaces," *Langmuir*, vol. 30, no. 40, pp. 12002–12010, 2014.

[162] P. C. Hidber, W. Helbig, E. Kim, and G. M. Whitesides, "Microcontact printing of palladium colloids: micron-scale patterning by electroless deposition of copper," *Langmuir*, vol. 12, no. 5, pp. 1375–1380, 1996.

[163] M. Gai, J. Frueh, A. Girard-Egrot, S. Rebaud, B. Doumeche, and Q. He, "Micro-contact printing of pem thin films: effect of line tension and surface energies," *RSC Advances*, vol. 5, no. 64, pp. 51891–51899, 2015.

[164] A. Alexanian, A. Yeremyan, and G. Pluzian, "Possibility of self-induced transparency in multi-layer semiconductor heterostructure placed in a quantizing magnetic field," *International Journal of Infrared and Millimeter Waves*, vol. 21, no. 11, pp. 1851–1857, 2000.

[165] Z. Wang, *Development of microcontact printing techniques for fabricating functional micropatterns and microparticles for biomedical applications.* PhD thesis, THE FLORIDA STATE UNIVERSITY, 2015.

[166] S. Bhatia, U. Balis, M. Yarmush, and M. Toner, "Effect of cell–cell interactions in preservation of cellular phenotype: cocultivation of hepatocytes and nonparenchymal cells," *The FASEB Journal*, vol. 13, no. 14, pp. 1883–1900, 1999.

[167] H.-D. Kim and S. R. Peyton, "Bio-inspired materials for parsing matrix physicochemical control of cell migration: a review," *Integrative biology*, vol. 4, no. 1, pp. 37–52, 2012.

[168] C. S. Chen, M. Mrksich, S. Huang, G. M. Whitesides, and D. E. Ingber, "Micropatterned surfaces for control of cell shape, position, and function," *Biotechnology progress*, vol. 14, no. 3, pp. 356–363, 1998.

[169] A. Bernard, E. Delamarche, H. Schmid, B. Michel, H. R. Bosshard, and H. Biebuyck, "Printing patterns of proteins," *Langmuir*, vol. 14, no. 9, pp. 2225–2229, 1998.

[170] J. Renault, A. Bernard, A. Bietsch, B. Michel, H. Bosshard, E. Delamarche, M. Kreiter, B. Hecht, and U. Wild, "Fabricating arrays of single protein molecules on glass using microcontact printing," *The Journal of Physical Chemistry B*, vol. 107, no. 3, pp. 703–711, 2003.

[171] J. L. Tan, J. Tien, and C. S. Chen, "Microcontact printing of proteins on mixed self-assembled monolayers," *Langmuir*, vol. 18, no. 2, pp. 519–523, 2002.

[172] R. S. Kane, S. Takayama, E. Ostuni, D. E. Ingber, and G. M. Whitesides, "Patterning proteins and cells using soft lithography," *Biomaterials*, vol. 20, no. 23, pp. 2363–2376, 1999.

[173] Y. Chen and A. Pépin, "Emerging nanolithographic methods," in *Nanoscience*, pp. 157–175, Springer, 2007.

[174] B. Michel, A. Bernard, A. Bietsch, E. Delamarche, M. Geissler, D. Juncker, H. Kind, J.-P. Renault, H. Rothuizen, H. Schmid, *et al.*, "Printing meets lithography: soft approaches to high-resolution patterning," *IBM Journal of Research and Development*, vol. 45, no. 5, pp. 697–719, 2001.

[175] A. Cerf, X. Dollat, J. Chalmeau, A. Coutable, and C. Vieu, "A versatile method for generating single dna molecule patterns: Through the combination of directed capillary assembly and (micro/nano) contact printing," *Journal of Materials Research*, vol. 26, no. 02, pp. 336–346, 2011.

[176] S. G. Ricoult, M. Pla-Roca, R. Safavieh, G. M. Lopez-Ayon, P. Grütter, T. E. Kennedy, and D. Juncker, "Large dynamic range digital nanodot gradients of biomolecules made by low-cost nanocontact printing for cell haptotaxis," *Small*, vol. 9, no. 19, pp. 3308–3313, 2013.

[177] H. Tran, K. L. Killops, and L. M. Campos, "Advancements and challenges of patterning biomolecules with sub-50 nm features," *Soft Matter*, vol. 9, no. 29, pp. 6578–6586, 2013.

[178] J. C. Love, L. A. Estroff, J. K. Kriebel, R. G. Nuzzo, and G. M. Whitesides, "Self-assembled monolayers of thiolates on metals as a form of nanotechnology," *Chemical reviews*, vol. 105, no. 4, pp. 1103–1170, 2005.

[179] F. Schreiber, "Structure and growth of self-assembling monolayers," *Progress in surface science*, vol. 65, no. 5, pp. 151–257, 2000.

[180] P. E. Laibinis, G. M. Whitesides, D. L. Allara, Y. T. Tao, A. N. Parikh, and R. G. Nuzzo, "Comparison of the structures and wetting properties of self-assembled monolayers of n-alkanethiols on the coinage metal surfaces, copper, silver, and gold," *Journal of the American Chemical Society*, vol. 113, no. 19, pp. 7152–7167, 1991.

[181] A. Ulman, "Formation and structure of self-assembled monolayers," *Chemical reviews*, vol. 96, no. 4, pp. 1533–1554, 1996.

[182] Y. Arima and H. Iwata, "Effect of wettability and surface functional groups on protein adsorption and cell adhesion using well-defined mixed self-assembled monolayers," *Biomaterials*, vol. 28, no. 20, pp. 3074–3082, 2007.

[183] S. Y. Chou, P. R. Krauss, and P. J. Renstrom, "Nanoimprint lithography," *Journal of Vacuum Science & Technology B*, vol. 14, no. 6, pp. 4129–4133, 1996.

[184] F. Hua, Y. Sun, A. Gaur, M. A. Meitl, L. Bilhaut, L. Rotkina, J. Wang, P. Geil, M. Shim, J. A. Rogers, *et al.*, "Polymer imprint lithography with molecular-scale resolution," *Nano letters*, vol. 4, no. 12, pp. 2467–2471, 2004.

[185] L. J. Guo, "Recent progress in nanoimprint technology and its applications," *Journal of Physics D: Applied Physics*, vol. 37, no. 11, p. R123, 2004.

[186] M. Schvartzman, M. Palma, J. Sable, J. Abramson, X. Hu, M. P. Sheetz, and S. J. Wind, "Nanolithographic control of the spatial organization of cellular adhesion receptors at the single-molecule level," *Nano letters*, vol. 11, no. 3, pp. 1306–1312, 2011.

[187] M. Schvartzman, K. Nguyen, M. Palma, J. Abramson, J. Sable, J. Hone, M. Sheetz, and S. Wind, "Fabrication of nanoscale bioarrays for the study of cytoskeletal protein binding interactions using nanoimprint lithography," *Journal of Vacuum Science & Technology B*, vol. 27, no. 1, pp. 61–65, 2009.

[188] R. D. Piner, J. Zhu, F. Xu, S. Hong, and C. A. Mirkin, "" dip-pen" nanolithography," *science*, vol. 283, no. 5402, pp. 661–663, 1999.

[189] F. Huo, Z. Zheng, G. Zheng, L. R. Giam, H. Zhang, and C. A. Mirkin, "Polymer pen lithography," *Science*, vol. 321, no. 5896, pp. 1658–1660, 2008.

[190] K.-B. Lee, S.-J. Park, C. A. Mirkin, J. C. Smith, and M. Mrksich, "Protein nanoarrays generated by dip-pen nanolithography," *Science*, vol. 295, no. 5560, pp. 1702–1705, 2002.

[191] S.-W. Chung, D. S. Ginger, M. W. Morales, Z. Zhang, V. Chandrasekhar, M. A. Ratner, and C. A. Mirkin, "Top-down meets bottom-up: Dip-pen nanolithography and dna-directed assembly of nanoscale electrical circuits," *small*, vol. 1, no. 1, pp. 64–69, 2005.

[192] R. Sistiabudi and A. Ivanisevic, "Dip-pen nanolithography of bioactive peptides on collagen-terminated retinal membrane," *Advanced Materials*, vol. 20, no. 19, pp. 3678–3681, 2008.

[193] S. Rozhok, C. K.-F. Shen, P.-L. H. Littler, Z. Fan, C. Liu, C. A. Mirkin, and R. C. Holz, "Methods for fabricating microarrays of motile bacteria," *Small*, vol. 1, no. 4, pp. 445–451, 2005.

[194] A. Pimpin and W. Srituravanich, "Review on micro-and nanolithography techniques and their applications," *Engineering Journal*, vol. 16, no. 1, pp. 37–56, 2011.

[195] J.-R. Li, L. Shi, Z. Deng, S. H. Lo, and G.-y. Liu, "Nanostructures of designed geometry and functionality enable regulation of cellular signaling processes," *Biochemistry*, vol. 51, no. 30, pp. 5876–5893, 2012.

[196] Z. Deng, I.-C. Weng, J.-R. Li, H.-Y. Chen, F.-T. Liu, and G.-y. Liu, "Engineered nanostructures of antigen provide an effective means for regulating mast cell activation," *ACS nano*, vol. 5, no. 11, pp. 8672–8683, 2011.

[197] A. Pulsipher and M. N. Yousaf, "Surface chemistry and cell biological tools for the analysis of cell adhesion and migration," *ChemBioChem*, vol. 11, no. 6, pp. 745–753, 2010.

[198] J. P. Spatz, "Nano-and micropatterning by organic–inorganic templating of hierarchical self-assembled structures," *Angewandte Chemie International Edition*, vol. 41, no. 18, pp. 3359–3362, 2002.

[199] M. Park, C. Harrison, P. M. Chaikin, R. A. Register, and D. H. Adamson, "Block copolymer lithography: periodic arrays of~ 1011 holes in 1 square centimeter," *Science*, vol. 276, no. 5317, pp. 1401–1404, 1997.

[200] G. Kästle, H.-G. Boyen, F. Weigl, G. Lengl, T. Herzog, P. Ziemann, S. Riethmüller, O. Mayer, C. Hartmann, J. P. Spatz, *et al.*, "Micellar nanoreactors—preparation and characterization of hexagonally ordered arrays of metallic nanodots," *Advanced Functional Materials*, vol. 13, no. 11, pp. 853–861, 2003.

[201] R. Glass, M. Arnold, J. Bluemmel, A. Kueller, M. Moeller, and J. P. Spatz, "Micro-nanostructured interfaces fabricated by the use of inorganic block copolymer micellar monolayers as negative resist for electron-beam lithography," *Advanced Functional Materials*, vol. 13, no. 7, pp. 569–575, 2003.

[202] J. P. Spatz, A. Roescher, S. Sheiko, G. Krausch, and M. Möller, "Noble metal loaded block lonomers: micelle organization, adsorption of free chains and formation of thin films," *Advanced Materials*, vol. 7, no. 8, pp. 731–735, 1995.

[203] T. Lohmueller, E. Bock, and J. P. Spatz, "Synthesis of quasi-hexagonal ordered arrays of metallic nanoparticles with tuneable particle size," *Advanced Materials*, vol. 20, no. 12, pp. 2297–2302, 2008.

[204] J. P. Spatz, S. Mössmer, C. Hartmann, M. Möller, T. Herzog, M. Krieger, H.-G. Boyen, P. Ziemann, and B. Kabius, "Ordered deposition of inorganic clusters from micellar block copolymer films," *Langmuir*, vol. 16, no. 2, pp. 407–415, 2000.

[205] Y. Cao, R. Jin, and C. A. Mirkin, "Dna-modified core-shell ag/au nanoparticles," *Journal of the American Chemical Society*, vol. 123, no. 32, pp. 7961–7962, 2001.

[206] M. Arnold, V. C. Hirschfeld-Warneken, T. Lohmuuller, P. Heil, J. Bluummel, E. A. Cavalcanti-Adam, M. López-García, P. Walther, H. Kessler, B. Geiger, *et al.*, "Induction of cell polarization and migration by a gradient of nanoscale variations in adhesive ligand spacing," *Nano letters*, vol. 8, no. 7, pp. 2063–2069, 2008.

[207] L. Purwaningsih, "Fabrication of nano-structured materials and their applications," tech. rep., Lehrstuhl für Textilchemie und Makromolekulare Chemie, 2011.

[208] S. V. Graeter, J. Huang, N. Perschmann, M. López-García, H. Kessler, J. Ding, and J. P. Spatz, "Mimicking cellular environments by nanostructured soft interfaces," *Nano letters*, vol. 7, no. 5, pp. 1413–1418, 2007.

[209] D. Aydin, I. Louban, N. Perschmann, J. Blummel, T. Lohmuller, E. A. Cavalcanti-Adam, T. L. Haas, H. Walczak, H. Kessler, R. Fiammengo, *et al.*, "Polymeric substrates with tunable elasticity and nanoscopically controlled biomolecule presentation," *Langmuir*, vol. 26, no. 19, pp. 15472–15480, 2010.

[210] H. Deckman and J. Dunsmuir, "Natural lithography," *Applied Physics Letters*, vol. 41, no. 4, pp. 377–379, 1982.

[211] S.-M. Yang, S. G. Jang, D.-G. Choi, S. Kim, and H. K. Yu, "Nanomachining by colloidal lithography," *small*, vol. 2, no. 4, pp. 458–475, 2006.

[212] A. Kosiorek, W. Kandulski, H. Glaczynska, and M. Giersig, "Fabrication of nanoscale rings, dots, and rods by combining shadow nanosphere lithography and annealed polystyrene nanosphere masks," *Small*, vol. 1, no. 4, pp. 439–444, 2005.

[213] U. C. Fischer and H. Zingsheim, "Submicroscopic pattern replication with visible light," *Journal of Vacuum Science & Technology*, vol. 19, no. 4, pp. 881–885, 1981.

[214] P. Colson, C. Henrist, and R. Cloots, "Nanosphere lithography: a powerful method for the controlled manufacturing of nanomaterials," *Journal of Nanomaterials*, vol. 2013, p. 21, 2013.

[215] F. Pi, P. Dillard, L. Limozin, A. Charrier, and K. Sengupta, "Nanometric protein-patch arrays on glass and polydimethylsiloxane for cell adhesion studies," *Nano letters*, vol. 13, no. 7, pp. 3372–3378, 2013.

[216] Z. R. Taylor, J. C. Keay, E. S. Sanchez, M. B. Johnson, and D. W. Schmidtke, "Independently controlling protein dot size and spacing in particle lithography," *Langmuir*, vol. 28, no. 25, pp. 9656–9663, 2012.

[217] O. Wichterle and D. Lim, "Hydrophilic gels for biological use," 1960.

[218] N. Peppas, P. Bures, W. Leobandung, and H. Ichikawa, "Hydrogels in pharmaceutical formulations," *European journal of pharmaceutics and biopharmaceutics*, vol. 50, no. 1, pp. 27–46, 2000.

[219] P. H. Corkhill, C. J. Hamilton, and B. J. Tighe, "Synthetic hydrogels vi. hydrogel composites as wound dressings and implant materials," *Biomaterials*, vol. 10, no. 1, pp. 3–10, 1989.

[220] K. Y. Lee and D. J. Mooney, "Hydrogels for tissue engineering," *Chemical reviews*, vol. 101, no. 7, pp. 1869–1880, 2001.

[221] K. N. Plunkett and J. S. Moore, "Patterned dual ph-responsive core-shell hydrogels with controllable swelling kinetics and volumes," *Langmuir*, vol. 20, no. 16, pp. 6535–6537, 2004.

[222] X. Chen, B. Martin, T. Neubauer, R. Linhardt, J. Dordick, and D. Rethwisch, "Enzymatic and chemoenzymatic approaches to synthesis of sugar-based polymer and hydrogels," *Carbohydrate Polymers*, vol. 28, no. 1, pp. 15–21, 1995.

[223] S. W. Kim, Y. H. Bae, and T. Okano, "Hydrogels: swelling, drug loading, and release," *Pharmaceutical Research*, vol. 9, no. 3, pp. 283–290, 1992.

[224] S. L. Bennett, D. A. Melanson, D. F. Torchiana, D. M. Wiseman, and A. S. Sawhney, "Next-generation hydrogel films as tissue sealants and adhesion barriers," *Journal of cardiac surgery*, vol. 18, no. 6, pp. 494–499, 2003.

[225] V. Compan, A. Andrio, A. Lopez-Alemany, E. Riande, and M. Refojo, "Oxygen permeability of hydrogel contact lenses with organosilicon moieties," *Biomaterials*, vol. 23, no. 13, pp. 2767–2772, 2002.

[226] S. R. Caliari and J. A. Burdick, "A practical guide to hydrogels for cell culture," *Nature methods*, vol. 13, no. 5, pp. 405–414, 2016.

[227] Y.-L. Wang and R. J. Pelham, "Preparation of a flexible, porous polyacrylamide substrate for mechanical studies of cultured cells," *Methods in enzymology*, vol. 298, pp. 489–496, 1998.

[228] F. Chowdhury, Y. Li, Y.-C. Poh, T. Yokohama-Tamaki, N. Wang, and T. S. Tanaka, "Soft substrates promote homogeneous self-renewal of embryonic stem cells via downregulating cell-matrix tractions," *PloS one*, vol. 5, no. 12, p. e15655, 2010.

[229] O. Shebanova and D. A. Hammer, "Biochemical and mechanical extracellular matrix properties dictate mammary epithelial cell motility and assembly," *Biotechnology journal*, vol. 7, no. 3, pp. 397–408, 2012.

[230] K. A. Beningo, C.-M. Lo, and Y.-L. Wang, "Flexible polyacrylamide substrata for the analysis of mechanical interactions at cell-substratum adhesions," *Methods in cell biology*, vol. 69, pp. 325–339, 2002.

[231] N. J. Sniadecki, A. Anguelouch, M. T. Yang, C. M. Lamb, Z. Liu, S. B. Kirschner, Y. Liu, D. H. Reich, and C. S. Chen, "Magnetic microposts as an approach to apply forces to living cells," *Proceedings of the National Academy of Sciences*, vol. 104, no. 37, pp. 14553–14558, 2007.

[232] A. Saez, A. Buguin, P. Silberzan, and B. Ladoux, "Is the mechanical activity of epithelial cells controlled by deformations or forces?," *Biophysical journal*, vol. 89, no. 6, pp. L52–L54, 2005.

[233] Y. Zhao and X. Zhang, "Adaptation of flexible polymer fabrication to cellular mechanics study," *Applied Physics Letters*, vol. 87, no. 14, p. 144101, 2005.

[234] B. G. Ricart, M. T. Yang, C. A. Hunter, C. S. Chen, and D. A. Hammer, "Measuring traction forces of motile dendritic cells on micropost arrays," *Biophysical journal*, vol. 101, no. 11, pp. 2620–2628, 2011.

[235] E. K. Yim, R. M. Reano, S. W. Pang, A. F. Yee, C. S. Chen, and K. W. Leong, "Nanopattern-induced changes in morphology and motility of smooth muscle cells," *Biomaterials*, vol. 26, no. 26, pp. 5405–5413, 2005.

[236] M. Murrell, R. Kamm, and P. Matsudaira, "Substrate viscosity enhances correlation in epithelial sheet movement," *Biophysical journal*, vol. 101, no. 2, pp. 297–306, 2011.

[237] H.-j. Song, G.-l. Ming, and M.-m. Poo, "camp-induced switching in turning direction of nerve growth cones," *Nature*, vol. 388, no. 6639, pp. 275–279, 1997.

[238] A. Folch, A. Ayon, O. Hurtado, M. Schmidt, and M. Toner, "Molding of deep polydimethylsiloxane microstructures for microfluidics and biological applications," *Journal of Biomechanical Engineering*, vol. 121, no. 1, pp. 28–34, 1999.

[239] J. C. McDonald, M. L. Chabinyc, S. J. Metallo, J. R. Anderson, A. D. Stroock, and G. M. Whitesides, "Prototyping of microfluidic devices in poly (dimethylsiloxane) using solid-object printing," *Analytical chemistry*, vol. 74, no. 7, pp. 1537–1545, 2002.

[240] L. Malaquin, F. Carcenac, C. Vieu, and M. Mauzac, "Using polydimethylsiloxane as a thermocurable resist for a soft imprint lithography process," *Microelectronic engineering*, vol. 61, pp. 379–384, 2002.

[241] J. Zhou, A. V. Ellis, and N. H. Voelcker, "Recent developments in pdms surface modification for microfluidic devices," *Electrophoresis*, vol. 31, no. 1, pp. 2–16, 2010.

[242] J. Li, M. Wang, and Y. Shen, "Chemical modification on top of nanotopography to enhance surface properties of pdms," *Surface and Coatings Technology*, vol. 206, no. 8, pp. 2161–2167, 2012.

[243] J. C. McDonald and G. M. Whitesides, "Poly (dimethylsiloxane) as a material for fabricating microfluidic devices," *Accounts of chemical research*, vol. 35, no. 7, pp. 491–499, 2002.

[244] I. Wong and C.-M. Ho, "Surface molecular property modifications for poly (dimethyl-siloxane)(pdms) based microfluidic devices," *Microfluidics and nanofluidics*, vol. 7, no. 3, pp. 291–306, 2009.

[245] R. D. Lovchik, H. Wolf, and E. Delamarche, "High-grade optical polydimethylsiloxane for microfluidic applications," *Biomedical microdevices*, vol. 13, no. 6, pp. 1027–1032, 2011.

[246] M. C. Jo and R. Guldiken, "Effects of polydimethylsiloxane (pdms) microchannels on surface acoustic wave-based microfluidic devices," *Microelectronic Engineering*, vol. 113, pp. 98–104, 2014.

[247] A. Tserepi, E. Gogolides, K. Tsougeni, V. Constantoudis, and E. S. Valamontes, "Tailoring the surface topography and wetting properties of oxygen-plasma treated polydimethylsilox-ane," *Journal of applied physics*, vol. 98, no. 11, p. 113502, 2005.

[248] D. C. Duffy, J. C. McDonald, O. J. Schueller, and G. M. Whitesides, "Rapid prototyping of microfluidic systems in poly (dimethylsiloxane)," *Analytical chemistry*, vol. 70, no. 23, pp. 4974–4984, 1998.

[249] J. Lahann, M. Balcells, H. Lu, T. Rodon, K. F. Jensen, and R. Langer, "Reactive poly-mer coatings: a first step toward surface engineering of microfluidic devices," *Analytical chemistry*, vol. 75, no. 9, pp. 2117–2122, 2003.

[250] H. Makamba, J. H. Kim, K. Lim, N. Park, and J. H. Hahn, "Surface modification of poly (dimethylsiloxane) microchannels," *Electrophoresis*, vol. 24, no. 21, pp. 3607–3619, 2003.

[251] K. Ye, X. Wang, L. Cao, S. Li, Z. Li, L. Yu, and J. Ding, "Matrix stiffness and nanoscale spatial organization of cell-adhesive ligands direct stem cell fate," *Nano letters*, vol. 15, no. 7, pp. 4720–4729, 2015.

[252] P. Liu, J. Sun, J. Huang, R. Peng, J. Tang, and J. Ding, "Fabrication of micropatterns of nanoarrays on a polymeric gel surface," *Nanoscale*, vol. 2, no. 1, pp. 122–127, 2010.

[253] F. Pi, P. Dillard, R. Alameddine, E. Benard, A. Wahl, I. Ozerov, A. Charrier, L. Limozin, and K. Sengupta, "Size-tunable organic nanodot arrays: A versatile platform for manipu-lating and imaging cells," *Nano letters*, vol. 15, no. 8, pp. 5178–5184, 2015.

[254] "Silane chemistry." `http://www.dowcorning.com/content/discover/discoverchem/silanes.aspx/`. Accessed june 5, 2016.

[255] J. R. Cox, L. A. Ferris, and V. R. Thalladi, "Selective growth of a stable drug polymorph by suppressing the nucleation of corresponding metastable polymorphs," *Angewandte Chemie International Edition*, vol. 46, no. 23, pp. 4333–4336, 2007.

[256] N. S. K. Gunda, M. Singh, L. Norman, K. Kaur, and S. K. Mitra, "Optimization and char-acterization of biomolecule immobilization on silicon substrates using (3-aminopropyl) tri-ethoxysilane (aptes) and glutaraldehyde linker," *Applied Surface Science*, vol. 305, pp. 522–530, 2014.

[257] "siloxane." `https://en.wikipedia.org/wiki/Siloxane`.

[258] A. Colas, "Silicones: Preparation, properties and performance," *Dow Corning, Life Sciences*, 2005.

[259] A. Colas and J. Curtis, "Silicone biomaterials: history and chemistry," *Biomaterials science: An introduction to materials in medicine*, vol. 2, pp. 80–85, 2004.

[260] F. Wisser, B. Schumm, G. Mondin, J. Grothe, and S. Kaskel, "Precursor strategies for metallic nano-and micropatterns using soft lithography," *Journal of Materials Chemistry C*, vol. 3, no. 12, pp. 2717–2731, 2015.

[261] D. B. Hall, P. Underhill, and J. M. Torkelson, "Spin coating of thin and ultrathin polymer films," *Polymer Engineering & Science*, vol. 38, no. 12, pp. 2039–2045, 1998.

[262] L. Nguyen, M. Hang, W. Wang, Y. Tian, L. Wang, T. J. McCarthy, and W. Chen, "Simple and improved approaches to long-lasting, hydrophilic silicones derived from commercially available precursors," *ACS applied materials & interfaces*, vol. 6, no. 24, pp. 22876–22883, 2014.

[263] "Silicone materials for optical applications." `http://www.dowcorning.com.cn/zh_CN/content/publishedlit/75-1007-01_single.pdf`. Accessed july 10, 2016.

[264] E. Gutierrez, E. Tkachenko, A. Besser, P. Sundd, K. Ley, G. Danuser, M. H. Ginsberg, and A. Groisman, "High refractive index silicone gels for simultaneous total internal reflection fluorescence and traction force microscopy of adherent cells," *PLoS One*, vol. 6, no. 9, p. e23807, 2011.

[265] "Dow corning cy52-276, product inormation.." `http://DOW_CORNING_ELECTRONICS_FT_CY52-276%20(2).pdf`.

[266] Y. Iwadate and S. Yumura, "Molecular dynamics and forces of a motile cell simultaneously visualized by tirf and force microscopies," *Biotechniques*, vol. 44, no. 6, pp. 739–50, 2008.

[267] "Sylgard 184 silicone elastomer." `http://www.dowcorning.com/DataFiles/090276fe80190b08.pdf`. Accessed september 11, 2016.

[268] http://www.quantumsilicones.com/wp-content/uploads/2012/02/QGel-9204.pdf.

[269] http://www.dowcorning.com/applications/search/default.aspx?R=1709EN.

[270] S. H. Tan, N.-T. Nguyen, Y. C. Chua, and T. G. Kang, "Oxygen plasma treatment for reducing hydrophobicity of a sealed polydimethylsiloxane microchannel," *Biomicrofluidics*, vol. 4, no. 3, p. 032204, 2010.

[271] M. Morra, E. Occhiello, R. Marola, F. Garbassi, P. Humphrey, and D. Johnson, "On the aging of oxygen plasma-treated polydimethylsiloxane surfaces," *Journal of Colloid and Interface Science*, vol. 137, no. 1, pp. 11–24, 1990.

[272] A. Tóth, I. Bertóti, M. Blazsó, G. Bánhegyi, A. Bognar, and P. Szaplonczay, "Oxidative damage and recovery of silicone rubber surfaces. i. x-ray photoelectron spectroscopic study," *Journal of applied polymer science*, vol. 52, no. 9, pp. 1293–1307, 1994.

[273] J. J. Escobar-Chávez, M. López-Cervantes, A. Naik, Y. Kalia, D. Quintanar-Guerrero, and A. Ganem-Quintanar, "Applications of thermo-reversible pluronic f-127 gels in pharmaceutical formulations," *Journal of Pharmacy & Pharmaceutical Sciences*, vol. 9, no. 3, pp. 339–58, 2006.

[274] D. R. Devi, P. Sandhya, and B. V. Hari, "Poloxamer: A novel functional molecule for drug delivery and gene therapy," *J. Pharm. Sci. Res*, vol. 5, pp. 159–165, 2013.

[275] C.-Z. Sun, C.-T. Lu, Y.-Z. Zhao, P. Guo, J.-L. Tian, L. Zhang, X.-K. Li, H.-F. Lv, D.-D. Dai, and X. Li, "Characterization of the doxorubicin-pluronic f68 conjugate micelles and their effect on doxorubicin resistant human erythroleukemic cancer cells," *Journal of Nanomedicine & Nanotechnology*, vol. 2011, 2012.

[276] P. Dillard, *Impact de la présentation des ligands sur la biophysique de l'adhésion des lymphocytes T*. PhD thesis, Aix-Marseille, 2014.

[277] "Principles of fluorescence." `http://www.blizard.qmul.ac.uk/flow-cytometry/what-is-flow-cytometry/principles-of-fluorescence.html`.

[278] "Fluorescent labels and dyes." `http://www.atto-tec.com/index.php?id=222&L=1`.

[279] "Primary antibody fluorescent conjugates." `https://www.biomol.com/primary-antibody-conjugates.html?id=1288`.

[280] "Texas reds." `https://fr.wikipedia.org/wiki/Texas_Red`.

[281] "Fluorescein." `http://www.wikiwand.com/en/Fluorescein`.

[282] "Amine-reactive crosslinker chemistry." `https://www.thermofisher.com/fr/fr/home/life-science/protein-biology/protein-biology-learning-center/protein-biology-resource-library/pierce-protein-methods/amine-reactive-crosslinker-chemistry.html`.

[283] "Fluorecent labelling of proteins.." http://www.sigmaaldrich.com/life-science/learning-center/biofiles/biofiles-5-2/protein-labeling.html.

[284] G. Binnig, C. F. Quate, and C. Gerber, "Atomic force microscope," *Physical review letters*, vol. 56, no. 9, p. 930, 1986.

[285] G. Binnig, H. Rohrer, C. Gerber, and E. Weibel, "Tunneling through a controllable vacuum gap," *Applied Physics Letters*, vol. 40, no. 2, pp. 178–180, 1982.

[286] J. A. Last, P. Russell, P. F. Nealey, and C. J. Murphy, "The applications of atomic force microscopy to vision science," *Investigative ophthalmology & visual science*, vol. 51, no. 12, pp. 6083–6094, 2010.

[287] "Atomic force microscopy.." `http://lnf-wiki.eecs.umich.edu/wiki/Atomic_force_microscopy`.

[288] F. L. Leite, C. C. Bueno, A. L. Da Róz, E. C. Ziemath, and O. N. Oliveira, "Theoretical models for surface forces and adhesion and their measurement using atomic force microscopy," *International journal of molecular sciences*, vol. 13, no. 10, pp. 12773–12856, 2012.

[289] H.-J. Butt and M. Jaschke, "Calculation of thermal noise in atomic force microscopy," *Nanotechnology*, vol. 6, no. 1, p. 1, 1995.

[290] C. A. Clifford and M. P. Seah, "The determination of atomic force microscope cantilever spring constants via dimensional methods for nanomechanical analysis," *Nanotechnology*, vol. 16, no. 9, p. 1666, 2005.

[291] J. Cleveland, S. Manne, D. Bocek, and P. Hansma, "A nondestructive method for determining the spring constant of cantilevers for scanning force microscopy," *Review of Scientific Instruments*, vol. 64, no. 2, pp. 403–405, 1993.

[292] A. Torii, M. Sasaki, K. Hane, and S. Okuma, "A method for determining the spring constant of cantilevers for atomic force microscopy," *Measurement Science and Technology*, vol. 7, no. 2, p. 179, 1996.

[293] H.-J. Butt, B. Cappella, and M. Kappl, "Force measurements with the atomic force microscope: Technique, interpretation and applications," *Surface science reports*, vol. 59, no. 1, pp. 1–152, 2005.

[294] "Summary note: Force spectroscopy measurement and processing.." `file:///C:/Users/rara/Downloads/jpk-note-force-spectroscopy%20(3).pdf`.

[295] J. F. G. Martínez, I. Nieto-Carvajal, and J. Colchero, "Calibration of oscillation amplitude in dynamic scanning force microscopy," *Nanotechnology*, vol. 24, no. 18, p. 185701, 2013.

[296] J. J Roa, G. Oncins, J. Diaz, F. Sanz, and M. Segarra, "Calculation of young's modulus value by means of afm," *Recent patents on nanotechnology*, vol. 5, no. 1, pp. 27–36, 2011.

[297] H. Hertz, "On the contact of elastic solids," *J. reine angew. Math*, vol. 92, no. 110, pp. 156–171, 1881.

[298] F. Variola, "Atomic force microscopy in biomaterials surface science," *Physical Chemistry Chemical Physics*, vol. 17, no. 5, pp. 2950–2959, 2015.

[299] D. Axelrod, "Cell-substrate contacts illuminated by total internal reflection fluorescence.," *The Journal of cell biology*, vol. 89, no. 1, pp. 141–145, 1981.

[300] D. Axelrod, "Total internal reflection fluorescence microscopy in cell biology," *Traffic*, vol. 2, no. 11, pp. 764–774, 2001.

[301] A. L. Mattheyses, S. M. Simon, and J. Z. Rappoport, "Imaging with total internal reflection fluorescence microscopy for the cell biologist," *J Cell Sci*, vol. 123, no. 21, pp. 3621–3628, 2010.

[302] J. S. Burmeister, L. A. Olivier, W. Reichert, and G. A. Truskey, "Application of total internal reflection fluorescence microscopy to study cell adhesion to biomaterials," *Biomaterials*, vol. 19, no. 4, pp. 307–325, 1998.

[303] "Introduction and theoritical aspects to tirf microscope.." http://www.olympusmicro.com/primer/techniques/fluorescence/tirf/tirfintro.html.

[304] N. L. Thompson and B. C. Lagerholm, "Total internal reflection fluorescence: applications in cellular biophysics," *Current opinion in biotechnology*, vol. 8, no. 1, pp. 58–64, 1997.

[305] U. Silván, J. Hyotyla, H.-G. Mannherz, P. Ringler, S. A. Müller, U. Aebi, T. Maier, and C.-A. Schoenenberger, "Contributions of the lower dimer to supramolecular actin patterning revealed by tirf microscopy," *Journal of structural biology*, 2016.

[306] A. Curtis, "The mechanism of adhesion of cells to glass a study by interference reflection microscopy," *The Journal of cell biology*, vol. 20, no. 2, pp. 199–215, 1964.

[307] M. Kühner and E. Sackmann, "Ultrathin hydrated dextran films grafted on glass: preparation and characterization of structural, viscous, and elastic properties by quantitative microinterferometry," *Langmuir*, vol. 12, no. 20, pp. 4866–4876, 1996.

[308] J. Rädler and E. Sackmann, "Imaging optical thicknesses and separation distances of phospholipid vesicles at solid surfaces," *Journal de Physique II*, vol. 3, no. 5, pp. 727–748, 1993.

[309] J. Schilling, K. Sengupta, S. Goennenwein, A. R. Bausch, and E. Sackmann, "Absolute interfacial distance measurements by dual-wavelength reflection interference contrast microscopy," *Physical Review E*, vol. 69, no. 2, p. 021901, 2004.

[310] L. Limozin and K. Sengupta, "Quantitative reflection interference contrast microscopy (ricm) in soft matter and cell adhesion," *ChemPhysChem*, vol. 10, no. 16, pp. 2752–2768, 2009.

[311] J. Ploem, *Reflection-contrast microscopy as a tool for investigation of the attachment of living cells to a glass surface.* Blackwell, Oxford, 1975.

[312] L. Lochner and C. Izzard, "Dynamic aspects of cell-substrate contact in fibroblast motility," in *JOURNAL OF CELL BIOLOGY*, vol. 59, pp. A199–A199, ROCKEFELLER UNIV PRESS 1114 FIRST AVE, 4TH FL, NEW YORK, NY 10021 USA, 1973.

[313] J. Bereiter-Hahn, C. H. Fox, and B. Thorell, "Quantitative reflection contrast microscopy of living cells.," *The Journal of cell biology*, vol. 82, no. 3, pp. 767–779, 1979.

[314] C. A. Schneider, W. S. Rasband, K. W. Eliceiri, *et al.*, "Nih image to imagej: 25 years of image analysis," *Nat methods*, vol. 9, no. 7, pp. 671–675, 2012.

[315] G.-Y. Jung, Z. Li, W. Wu, Y. Chen, D. L. Olynick, S.-Y. Wang, W. M. Tong, and R. S. Williams, "Vapor-phase self-assembled monolayer for improved mold release in nanoimprint lithography," *Langmuir*, vol. 21, no. 4, pp. 1158–1161, 2005.

[316] Y.-C. Tai, P. Joshi, J. McGuire, and J. A. Neff, "Nisin adsorption to hydrophobic surfaces coated with the peo–ppo–peo triblock surfactant pluronic® f108," *Journal of colloid and interface science*, vol. 322, no. 1, pp. 112–118, 2008.

[317] J. H. Lee, J. Kopecek, and J. D. Andrade, "Protein-resistant surfaces prepared by peo-containing block copolymer surfactants," *Journal of biomedical materials research*, vol. 23, no. 3, pp. 351–368, 1989.

[318] L. M. Lee, R. L. Heimark, R. Guzman, J. C. Baygents, and Y. Zohar, "Low melting point agarose as a protection layer in photolithographic patterning of aligned binary proteins," *Lab on a Chip*, vol. 6, no. 8, pp. 1080–1085, 2006.

[319] C.-H. Chao, K.-L. Li, C.-S. Wu, C.-C. Lee, H.-P. Chiang, Y.-S. Yang, T.-M. Pan, F.-H. Ko, *et al.*, "Surface effect of assembling enzyme and modulation of surface enzyme activity with electric potential stress," *Int. J. Electrochem. Sci*, vol. 7, pp. 5100–5114, 2012.

[320] V. Pinto, G. Minas, and M. Correia-Neves, "Pdms biofunctionalization study for the development of a microfluidic device: Application to salivary cortisol," in *Bioengineering (ENBENG), 2015 IEEE 4th Portuguese Meeting on*, pp. 1–5, IEEE, 2015.

[321] J. Juárez-Moreno, A. Ávila-Ortega, A. Oliva, F. Avilés, and J. Cauich-Rodríguez, "Effect of wettability and surface roughness on the adhesion properties of collagen on pdms films treated by capacitively coupled oxygen plasma," *Applied Surface Science*, vol. 349, pp. 763–773, 2015.

[322] E. G. Rochow, *An introduction chemistry of the silicones*. Read Books Ltd, 2013.

[323] R. W. Style, R. Boltyanskiy, G. K. German, C. Hyland, C. W. MacMinn, A. F. Mertz, L. A. Wilen, Y. Xu, and E. R. Dufresne, "Traction force microscopy in physics and biology," *Soft matter*, vol. 10, no. 23, pp. 4047–4055, 2014.

[324] R. W. Style, C. Hyland, R. Boltyanskiy, J. S. Wettlaufer, and E. R. Dufresne, "Surface tension and contact with soft elastic solids," *Nature communications*, vol. 4, 2013.

[325] D. Fuard, T. Tzvetkova-Chevolleau, S. Decossas, P. Tracqui, and P. Schiavone, "Optimization of poly-di-methyl-siloxane (pdms) substrates for studying cellular adhesion and motility," *Microelectronic Engineering*, vol. 85, no. 5, pp. 1289–1293, 2008.

[326] G. Bar, L. Delineau, A. Häfele, and M.-H. Whangbo, "Investigation of the stiffness change in, the indentation force and the hydrophobic recovery of plasma-oxidized polydimethylsiloxane surfaces by tapping mode atomic force microscopy," *Polymer*, vol. 42, no. 8, pp. 3627–3632, 2001.

[327] S. Béfahy, P. Lipnik, T. Pardoen, C. Nascimento, B. Patris, P. Bertrand, and S. Yunus, "Thickness and elastic modulus of plasma treated pdms silica-like surface layer," *Langmuir*, vol. 26, no. 5, pp. 3372–3375, 2009.

[328] T. Kaufmann and B. J. Ravoo, "Stamps, inks and substrates: polymers in microcontact printing," *Polymer Chemistry*, vol. 1, no. 4, pp. 371–387, 2010.

[329] Y. Kazoe and Y. Sato, "Effect of ion motion on zeta-potential distribution at microchannel wall obtained from nanoscale laser-induced fluorescence," *Analytical chemistry*, vol. 79, no. 17, pp. 6727–6733, 2007.

[330] J. Li, D. Han, and Y.-P. Zhao, "Kinetic behaviour of the cells touching substrate: the interfacial stiffness guides cell spreading," *Scientific reports*, vol. 4, p. 3910, 2014.

[331] N. Hersch, B. Wolters, G. Dreissen, R. Springer, N. Kirchgeßner, R. Merkel, and B. Hoffmann, "The constant beat: cardiomyocytes adapt their forces by equal contraction upon environmental stiffening," *Biology open*, vol. 2, no. 3, pp. 351–361, 2013.

[332] S. T. Kim, M. Touma, K. Takeuchi, Z.-Y. J. Sun, V. P. Dave, D. J. Kappes, G. Wagner, and E. L. Reinherz, "Distinctive cd3 heterodimeric ectodomain topologies maximize antigen-triggered activation of $\alpha\beta$ t cell receptors," *The Journal of Immunology*, vol. 185, no. 5, pp. 2951–2959, 2010.

[333] S. T. Kim, K. Takeuchi, Z.-Y. J. Sun, M. Touma, C. E. Castro, A. Fahmy, M. J. Lang, G. Wagner, and E. L. Reinherz, "The $\alpha\beta$ t cell receptor is an anisotropic mechanosensor," *Journal of Biological Chemistry*, vol. 284, no. 45, pp. 31028–31037, 2009.

[334] S. T. Kim, Y. Shin, K. Brazin, R. J. Mallis, J. Sun, G. Wagner, M. Lang, and E. L. Reinherz, "Tcr mechanobiology: torques and tunable structures linked to early t cell signaling," *Frontiers in immunology*, vol. 3, p. 76, 2012.

[335] M. Ochsner, M. R. Dusseiller, H. M. Grandin, S. Luna-Morris, M. Textor, V. Vogel, and M. L. Smith, "Micro-well arrays for 3d shape control and high resolution analysis of single cells," *Lab on a Chip*, vol. 7, no. 8, pp. 1074–1077, 2007.

[336] A. Ranjan and T. J. Webster, "Increased endothelial cell adhesion and elongation on micron-patterned nano-rough poly (dimethylsiloxane) films," *Nanotechnology*, vol. 20, no. 30, p. 305102, 2009.

[337] H. Yu, S. Xiong, C. Y. Tay, W. S. Leong, and L. P. Tan, "A novel and simple microcontact printing technique for tacky, soft substrates and/or complex surfaces in soft tissue engineering," *Acta biomaterialia*, vol. 8, no. 3, pp. 1267–1272, 2012.

[338] D. R. Schmidt, H. Waldeck, and W. J. Kao, "Protein adsorption to biomaterials," in *Biological interactions on materials surfaces*, pp. 1–18, Springer, 2009.

[339] F. P. K. B. L. L. A. C. Ranime Alameddine, Astrid Wahl and K. Sengupta, "Reverse contact printing of protein patterns for cell mechanotransduction studies,"